THE UNIVERSITY OF CHICAGO

SINGLE CRYSTAL DIAMOND MEMBRANE FOR QUANTUM TECHNOLOGIES

A DISSERTATION SUBMITTED TO
THE FACULTY OF THE PRITZKER SCHOOL OF MOLECULAR ENGINEERING
IN CANDIDACY FOR THE DEGREE OF
DOCTOR OF PHILOSOPHY

BY
XINGHAN GUO

CHICAGO, ILLINOIS
JUNE 2024

TABLE OF CONTENTS

LIST OF FIGURES

LIST OF TABLES

ACKNOWLEDGEMENTS

This thesis is more than a description of my work in the past 7 years. It represents a team effort on the diamond membrane projects, especially at the University of Chicago and Argonne National Laboratory. I am fortunate to witness the development of the platform from day one. I want to thank advisors, professors, scientists, colleagues, collaborators, family members, and friends who have provided generous support, both technically and emotionally, during my challenging and rewarding Ph. D. journey.

First and foremost, I wish to thank my adviser, Prof. Alexander High, who took me as his second student in 2017. There is no other mentor as critical as Alex is to my research journey, intellectual pursuits, and professional growth. Back in 2017, I was a first-year Ph. D. student freshly out of my undergraduate who had a very strong preference for topics despite having little knowledge about the whole quantum research landscape. Alex encouraged me to be brave and explore my interests by taking an entirely new, interdisciplinary research topic with four precious electronic grade diamonds. Ever since Alex has provided the highest level of trust and support I can imagine. His positive way of thinking has saved me countless times from my own negative thoughts when "something new" happened. I learned a tremendous amount from Alex, including passion for innovation, general curiosity for new physics, and pursuit of collaborations. Most importantly, I am now brave enough to explore the unknown, which is an invaluable gift for a scientific research career.

Excellent research always comes from teamwork, and this holds particularly true for diamond membrane studies. We have a great diamond team: Zixi Li, Anchita Addhya, Chun Tung Cheung, Tanvi Deshmukh, Tianle Liu, Avery Linder, Jonathan Colen, and more. In particular, I am fortunate to have Zixi on the team, who is always motivated and capable of expanding the frontier of the diamond membrane world. In addition, Anchita, Tung, and Tanvi are critical members of the team and have made significant progress in various aspects of the research. I am also grateful to work with Tianle and Avery for their outsized contribution to the platform as undergraduates.

They brought with them creative spirits and demonstrated an inspiring commitment to research. Although I have not had a chance to work with Jon for a long time, I have always been inspired by his expertise in coding and creative ways of thinking.

From 2017 to 2024, it was also a 7 year journey for the High Lab. Starting from 3 members, we now have over 20 members and alumni, and the number keeps growing. I am grateful to work with so many excellent colleagues in High Lab. First of all, I would like to thank Dr. Amy Butcher and Dr. Rob Shreiner, my long-time friends and our first generation. I have fond memories of building the lab from the ground up: training, lab setup, device fabrications, and optical measurements. In addition, I am grateful to have Dr. Kai Hao in the lab. He started in my second year, is quite an expert on optics and also my good friend. I am also happy to work with Anil Bilgin, Ian Hammock, Dr. Clayton DeVault, and Andrew Kindseth, who were great lab mates and friends I would cherish.

This work could not even start without the collaboration from the Material Sciences Division (MSD) and the Center for Nanoscale Materials (CNM), Argonne National Laboratory. Specifically, I could not have asked for better guidance, support, and friendship from Dr. F. Joseph Heremans and Dr. Nazar Delegan. They helped me throughout my Ph. D. in material synthesis, characterizations, data analysis, equipment, project developments, manuscripts, presentations, and more. Without their knowledge and support, I wouldn't have been able to make continuous progress in building the diamond membrane platform. In addition, I want to thank Dr. Benjamin Pingault, our group IV and cavity expert who has contributed a lot to understanding our exotic SnV centers, Dr. Alan Dibos, who is quite knowledgeable in materials transfers, and Dr. Yuzi Liu, who took arguably the best TEM image of our diamond membranes.

Unlike many research topics, diamond membrane is a platform technology requiring numerous collaborative efforts for continuous development. Inside PME, I am grateful to collaborate with Prof. David Awschalom and the Awschalom group on NV characterizations. I want to thank Jonathan Marcks, particularly, for his expertise in optical measurements and spin physics. Working with Jonathan is nothing but joy. I would also like to thank Prof. Giulia Galli, Dr. Yu Jin, and

Benchen Huang in the Galli group for supporting our group IV center studies with fruitful DFT calculations and discussions. I have always admired Giulia, Yu, and Benchen for their curiosity and dedication to understanding microscopic physical processes. For the NV sensing project, I really appreciate the opportunity to work with Prof. Peter Maurer, Dr. (now Prof.) Mouzhe Xie, Xiaofei Yu, Uri Zvi and Stella Wang from Maurer Lab, and Prof. Aaron Esser-Kahn. Without your effort, I would never have had a chance to see cells and live bacteria on top of the diamond membrane. Outside of Chicagoland, I want to thank our theoretical collaborators, Prof. Darrick Chang and Dr. Francesco Andreoli from ICFO. During the collaboration, Francesco has shown great commitment and expertise in quantum optics. I am often encouraged by his confidence in our project, especially during manuscript reviewing cycles.

From all collaborations, I would like to thank the labs I visited (and stayed) in the past three years. First, thank you, Prof. Mete Atatüre, for providing me with a lab away from the lab in Chicago. You play an exemplary role in showing dedication to research, teaching, lab culture, and student life all at once. In Atatüre lab, I really enjoyed working with my collaborators in Cambridge, including but not limited to Alexander Stramma (thanks for the formal!) and William Roth. In particular, Alex's dedication to excellence and commitment to research has deeply influenced me ever since. It was also my first trip to the U.K., and I will definitely come back again.

And thank you, Prof. Marko Lončar, for hosting me at Harvard University. I am really impressed by your genuine leadership, dedication to mentorship, and kindness. Since we collaborated in 2021, your support of diamond nanophotonics has been a critical part of our membrane platform. I am grateful for the opportunity that helps me connect with the broader quantum community in Cambridge, MA. I look forward to continuing the dialogue in the future. In Lončar Lab, I am fortunate to work with Dr. (now Prof.) Kazuhiro Kuruma, Sophie Ding, Michael Hass, and Jin Chang are being treated as one of yours. You are an amazing group of people to work with and I learned a lot from you during my visit.

Building a lab from scratch is non-trivial, and it would have become more difficult if we had not

received strong support from the PME. I want to thank Dr. (Now Prof.) Christopher Anderson, Dr. Paul Jerger, Dr. Alexandre Bourassa, and Dr. Kevin Miao from Awschalom Lab for generously sharing the information on sample preparation, device fabrication, measurements, and programming. I also appreciate the help from Dr. Youpeng Zhong, Dr. Ming-Han Chou, Hong Qiao, and Haoxiong Yan from Cleland Lab on microwave design and characterizations, Dr. Shobhit Gupta and Dr. Yizhong Huang from Zhong Lab on signal analysis, Dr. Yuxin Wang on theoretical discussions, Peter Duda and Sally Wolcott on cleanroom support. In addition, I am so happy to have David Taylor and Rovana Popoff in PME, who always provide us with unconditional support in many ways. I am also grateful to receive support and assistance from Mary Pat McCullough, Ozge Kocak Hemmat, Jennifer White, Amanda Dennis, Preeti Chalsani, and Briana Konnick regarding reservations, appointments, reports, reimbursements, scientific outreaches, and career developments. I also enjoyed my time in the University wind ensemble in the first three years of my Ph. D. life. I always felt at home when sitting in the rehearsal room of the Logan Center.

Lastly, I would like to thank my family and friends. I am so grateful to receive unconditional support and understanding from my parents. That means a lot to me, especially during this special period full of turbulence and uncertainty. In the past 7 years, there were only a handful of days that we could meet, and I was busy in most cases. I really hope to have more chances to spend time with you in the future. I'm fortunate to have my cat, Lao Tie, who is cute, affectionate, and a true life companion. You must have a great time with my parents now. I also enjoyed my time in the lovely 2017 cohort of PME, and I am so lucky to have many great friends at UChicago. Finally, I would like to thank my partner, Pei Gong, who is always by my side and provides constant care, love, humor, and support.

ABSTRACT

Optically active spin defects in diamond, often named color centers, are prime candidates for quantum technologies, including quantum networking, computing, sensing, and photonics. Integrating single-crystal diamond with heterogeneous materials unlocks numerous research directions that are non-trivial for bulk diamond or nanodiamond. This thesis describes a deterministic method for diamond membrane synthesis and integration to expand integration options for hosted color centers. This heterogeneous material platform enables efficient spin-photon interfaces and improves the coherence of color centers, two key elements of quantum networking. The platform also offers a versatile and practical interface for quantum sensing and provides an opportunity to explore atomic-scale optical interaction in solids. Chapter 1 introduces the fundamentals of quantum technology, diamond color centers for quantum applications, and material properties of diamond with synthesis methods. Chapter 2 provides the research background of low-dimensional diamond fabrication and details our approaches to generating high-quality diamond films and integrating them with a wide selection of materials. Chapter 3 demonstrates multiple fabrication methods of nanophotonic cavities with diamond-based heterostructures and their coupling to color centers. Chapter 4 presents our work on strain generation in thin-film diamonds and modification of the spin dynamics for tin-vacancy centers using strain. Chapter 5 discusses the spin coherence of nitrogen-vacancy centers in diamond membranes and their applications for quantum bio-sensing. Chapter 6 describes our study on near-field enhancement of germanium-vacancy centers based on the behavior of nearby carbon vacancies. Chapter 7 concludes the thesis and provides an outlook on this platform in quantum technologies.

CHAPTER 1

INTRODUCTION

1.1 Quantum technology and physical implementations

Information science and technology developments, including information collection, processing, storage, and transmission, have always been tightly bonded with fundamental science and technology innovations in physics. Modern information science originates from the Digital Revolution—often called the Third Industrial Revolution—that translates the handwritten, mechanical, or analog information into a series of "bits", which can be chosen from two discrete numbers: 0 and 1. The incredible fact about the realization of this basic information unit is that, in principle, any separate and distinguishable physical value pairs can be defined as a "bit". Therefore, there is no physical limitation to defining zeros and ones as long as there are distinguishable differences and deterministic transitions between the two statuses. The freedom of definition unleashes researchers' and engineers' endless imagination and creativity in seeking the most suitable forms of bits for different application scenarios. It can take the form of dark and bright pixels in quick-response (QR) codes [1], high and low voltage of transistors in processors [2], charge/discharge of capacitors in computer memories [3], magnetization direction of ferromagnetic materials in hard disks [4], and amplitude, frequency or phase modulation of carrier signals for communication systems [5].

In the meantime, advances in quantum physics in the 20th century have not only brought hardware revolution to traditional information science but also stimulated the emergence of quantum computation and quantum information concepts. Instead of using quantum mechanics to obtain a deeper understanding of traditional devices and improve their performance accordingly, quantum information science takes a more straightforward approach: treat quantum objects in a quantum manner and build technologies based on pure quantum effects. Therefore, the basic information unit switches from a pair of number options (0 or 1) to a more quantum mechanical description: a superposition of two physical states, written as $|0\rangle$ and $|1\rangle$. This quantum bit, with a simpler name

"qubit", can then be written as: $|\psi\rangle = \alpha|0\rangle + \beta|1\rangle$, where $\{\alpha, \beta\}$ are a pair of complex numbers with $\sqrt{\alpha^2 + \beta^2} = 1$ after normalization.

The difference between bits and qubits may not look apparent as quantum states $|0\rangle$ and $|1\rangle$ are also a pair of distinct physical statuses. However, since the two statuses belong to the quantum objects, an additional term appears: phase. After normalization, the phase information is included in the $\{\alpha, \beta\}$ pair for any qubit state $|\psi\rangle$. This phase term is a unique feature that separates quantum and classic objects and forms the foundation of quantum information science and technology. Clever utilization of the phase information from multiple qubits leads to the real attractive aspects of quantum technology, including unique quantum algorithms for quantum computing, hack-free quantum communication with quantum key distribution, and high sensitivity quantum sensing [6]. Echoing the traditional information science, the current quantum information research covers almost every significant aspect of information, including signal collection (quantum sensing), processing (quantum computation, quantum simulation), storage (quantum memory), and transmission (quantum networking, quantum transduction, quantum repeaters). Fortunately, like the definition of classical bits, the definition of qubits is not bonded by the physical implementation either. In recent decades, numerous inspiring proposals and landmark demonstrations of new qubit platforms have emerged in every aspect of quantum information science. The qubit can take microscopic or mesoscopic form, operate at microwave or optical frequency, live in solid state matters, liquids, optical or electrical traps, optical cavities, or travel freely in space (photon). Even in a single physical platform, the definition of "qubit" can vary due to the much larger Hilbert space the system obtains than the qubit subspace. It is worth noting that there is no universal definition of a good "qubit". Instead, the evaluation is determined by the application scenarios. For instance, DiVincenzo's criteria are ideal for evaluating quantum computation and quantum communication systems [7]. Instead, qubits for quantum sensing are encouraged to improve the coupling with targets instead of pursuing longer coherence time.

After several decades of exploration of practical quantum systems, several promising candidates

have emerged and have been extensively studied for quantum technologies. For quantum computation and simulation studies, the quantum system is required to obtain many qubits with high-fidelity initialization, readout, multi-qubit gate operations, and long coherence time. Therefore, individually manipulated qubits that are well isolated from the environment are preferred. A few examples include superconducting qubits in the microwave frequency domain [8], cold atoms and molecules in optical tweezer arrays [9, 10], trapped ions [11, 12], electrons in neon [13], donor electron spins in silicon [14], and purely photonics [15]. For quantum memory, long qubit coherence time with deterministic quantum state transfer is the primary factor in choosing candidates. Some demonstrations include nuclear spins in semiconductors [16], rare earth ions in solid state hosts [17], and atomic vapor cells [18]. In the quantum communication and networking domain, correct choices of flying qubits and efficient transition between local and flying qubits are of primary concern. For free space communication, near-infrared (NIR) or infrared (IR) photons are prime flying qubit candidates [19]. For optical fiber communications, low-loss transmission only happens when the operating wavelength is within specific telecommunication windows, such as O ($1260\,\mathrm{nm}$ to $1360\,\mathrm{nm}$), E ($1360\,\mathrm{nm}$ to $1460\,\mathrm{nm}$) or C ($1530\,\mathrm{nm}$ to $1565\,\mathrm{nm}$) bands. Choices of the flying qubit wavelength also affect the stationary qubit's physical platform. For instance, rare earth ion erbium (Er^{3+})-doped crystals and carefully designed quantum dots are natural choices for fiber-based quantum communication due to their well-matched wavelength ranges with telecom windows [20, 21], while other candidates have to incorporate wavelength conversion modules before being transmitted through optical fibers [22, 23]. Another approach to interconnecting stationary and flying qubits is to build quantum transduction systems that do not require qubits with both microwave and optical access. These systems typically utilize optomechanics or electro-optics to link qubits from very different wavelength ranges and are considered critical for distributed quantum computing [24, 25]. In quantum sensing, the qubit has to interact with some physical quantities with a measurable response. This requirement indicates some compromise of the qubit coherence to improve the total sensitivity, which differs from the criteria for quantum computation and com-

munication qubits [26]. Some great examples of quantum sensors include nitrogen-vacancy (NV^-) centers in diamond for biomedical applications [27], atomic vapor cells for microwave electrical and magnetic field sensing [28], superconducting qubits for cosmology [29], and trapped atoms for gravitational studies [30]. We note that it is a mutual selection between qubit platforms and quantum technologies. A physical qubit platform can have multiple application scenarios, and sometimes, an underperforming qubit for one usage can be a perfect choice for another.

Here, we will mainly discuss one physical platform—optically active spin defects in diamond. Technically speaking, defects in diamond are solid-state platforms. However, these defects only have the atomic scale and thus share many properties with trapped atoms or ions regarding fundamental understanding and operation mechanisms. The electron spin of the defects also serves as a good qubit candidate, which can interact with surrounding environments or serve as quantum memories. Furthermore, it is a rare solid-state system with both optical and microwave access, which significantly enhances the manipulation flexibility and versatility. In the meantime, these defects are "eternally trapped" in solid-state substrates, which requires no additional trapping mechanism compared with atoms or ions and enables on-chip photonic, electric, and microwave integration possibilities. We will start by describing the spin defects we work with, then discuss the diamond's properties as the material host.

1.2 Color centers in diamond for quantum technology

For crystalline solid state matters, all atoms (or ions) are periodically arranged in a three-dimensional position space, which can be classified into different groups depending on the microscopic structure of the primitive unit cell [31]. We know that an infinite, periodic arrangement in the position space can be translated via Fourier transform to a series of de-localized traveling waves in the momentum space (k-space). Therefore, no *localized* quantum feature can be defined as qubits in a perfect single crystalline matter. Instead, the only physical property that can be quantized is the traveling waves in the k-space—the collective motion of atoms or ions that can be quantitatively

described as *phonons*. Although phonon is not the central topic of this work, we will soon find that phonon modes and distributions play an essential role in understanding and utilizing solid-state defects.

Spatially (and spectrally) localized quantum objects require microscopic arrangements that deviate from a perfect lattice. In the world of solid-state physics, this deviation refers to crystal defects. The most interesting quantum phenomena originate from the tiniest defects in crystals: point defects. Point defects are atomic-scale structures associated with added, missing, or dislocation of native atoms or external impurities. Like other single crystalline lattices, diamond contains numerous point defects. From quantum technology's perspective, we would like to investigate the point defects that are magneto-optically active, which means that they (1) are optically accessible, (2) have non-zero electron spin ($|\ \mathbf{S}\ | \neq 0$). Point defects that satisfy the first criteria are often called color centers due to their distinct emission profile when optically excited. The name originates from the coloration of the crystal when a large density of optically active emitters is present. There have been several decades of studies regarding the color centers in diamond, and several hundreds of luminescent configurations have been found [32]. Here, we note that optical access is not required for a point defect to be a qubit. A commonly-known example is the nuclear spin of the phosphorus defect in silicon [33], which only allows microwave manipulation. Some reasons for the pursuit of optical access may include (1) color centers in diamond have been well-studied for their optical properties, and some color centers have been proven to be promising candidates for quantum technologies; (2) the optical access provides a way of utilizing qubits for quantum networking, which is quite challenging in the microwave frequency; and (3) the coherence and manipulation of optically inactive defects in diamond have not been well understood. Therefore, the current quantum research remains focusing on color centers in diamond, which includes more than two dozen candidates [34]. Some of them do not meet the second criteria, such as nitrogen-vacancy center and single vacancy center in a neutral charge state (NV^0 and V^0), which can be used as single photon sources instead due to the lack of energy levels to store quantum infor-

mation. Some other centers have poorly understood electronic configurations, unknown creation mechanisms, low yield, or inconvenient operation frequency, which keep them away from practical applications until future progress. In this work, we focus on the two groups of color centers that satisfy both criteria, which are negatively-charged substitutional nitrogen-vacancy center (NV^- center or NV center), and negatively-charged interstitial group IV centers, including silicon-vacancy center (SiV^- center, SiV), germanium-vacancy center (GeV^- center, GeV), tin-vacancy center (SnV^- center, SnV), and lead-vacancy center (PbV^- center, PbV). They have well-understood electronic structures, deterministic creation methods with a decent yield, addressable through both optical and microwave controls, and relatively long electron spin coherence time when combined with careful material engineering. In the rest of the work, we use the term *color center* to represent these two types of color centers unless specified.

1.2.1 NV^- centers

Unlike optically or electrically trapped atoms and ions, the understanding of species and molecular configurations of color centers is not straightforward and often requires a combination of experimental characterizations (spectroscopy, ion implantation, annealing, etc.), theoretical analysis (group theory), and *ab initio* calculations (often performed via density-functional theory calculation, DFT) [35]. In the early stages, the speculation of a molecular structure is tightly connected to the experimental observations. For instance, the first proposal linked the photoluminescence (PL) to the nitrogen-vacancy compound due to the excessive presence of nitrogen atoms and vacancies in the diamond crystal [36]. The confirmation of the NV^0 center came from the correlation between its signature PL and the charge state transition from the known NV^- center [37]. After about five decades of studying, we now have a pretty clear picture of the molecular structure and electronic configuration of the NV^- center, as well as its optical, spin properties and operation mechanisms.

Molecular structure and electronic configuration The molecular structure of a NV^- center is shown in Figure 1.1 (a). The NV^- contains one substitutional nitrogen atom and one vacancy, taking two adjacent sites of sp^3 carbon atoms along the $[111]$ crystal axis. Here, sp^3 refers to carbon-carbon covalent bonds with the sp^3 hybridization orbitals (the diamond lattice), which is in contrast to graphite, another carbon-formed material with sp^2 bonds. According to the group symmetry classification [35], NV center belongs to the C_{3v} group. This group indicates that the center is symmetric under C_3 rotation to the $N-V$ axis: $120°$, $240°$, $360°$ and three mirror operations with respect to the vertical plane containing the $N-V$ axis: σ_v. The molecular structure of the NV^- center is slightly complicated compared with some simple defects, such as ND1 (V^-), GR1 (V^0), or P1 (N). Therefore, the formation of NV^- is usually determined by the energy difference between the complex (NV^0) and separated simple defects (a V^0 and a N^0) compared with other possible formation mechanisms (such as V_2^0 or $N-V-N$). Previous research shows that although forming NV^0 is less energetically favorable than forming V_2^0, introducing extra vacancy is easier in substitutional N sites and form NV compared with regular carbon vacancies [38]. This preferential NV formation is due to one less covalent bond the carbon atoms have when neighboring a nitrogen atom. The observation not only explains the formation mechanism of NV center but also points out the creation methods: introducing external vacancies through ion implantation or electron radiation. Both of these methods are used in our work.

Unlike the determination of the molecular structure, NV^- center's electronic configuration has been an arguable topic for a long time. According to the current understanding, the NV^- has a non-zero electron spin. The NV^- has an extra electron from the crystal, possibly from other donors such as substitutional [N]. This defect has six electrons; two always occupy an energy level below the valence band. The other four live in the bandgap, with their configuration labeled by A_1, A_2, and E. The energy level diagram is shown in Figure 1.1 (b). Both ground and excited states are triplet states, while a standalone pair of singlet states are also optically active. Ground ($^3A_2$) and excited (^3E) triplet states are connected by a direct (no phonon participation) optical transition at $1.945\,\mathrm{eV}$

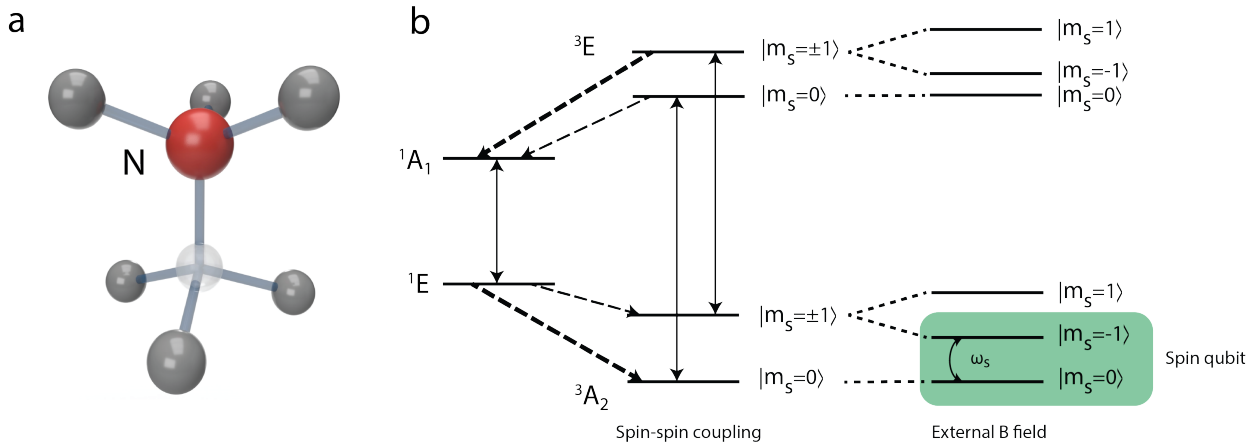

Figure 1.1: Negatively-charged nitrogen-vacancy center (NV^-) in diamond. (a) The molecular structure of the NV^- center. The red atom stands for the substitutional nitrogen, and the dark grey atoms are sp^3 carbon. The missing carbon vacancy is right next to the nitrogen atom. (b) Energy level diagram of NV^-. The spin-triplet states are $^3A_2$ and ^3E, each with a zero-field splitting. The state $|m_s = 0\rangle$ is unchanged with the external magnetic field while the states $|m_s = \pm 1\rangle$ shift accordingly due to the Zeeman effect, forming a qubit pair $|m_s = 0\rangle$ and $|m_s = -1\rangle$. NV^- also has a singlet state pair $^1A_1$ and ^1E, mainly used for spin initialization due to the much stronger non-radiative decay between ^3E $|m_s = \pm 1\rangle$ to $^1A_1$ compared with $|m_s = 0\rangle$ to $^1A_1$, and stronger decay between ^1E to $^3A_2$ $|m_s = 0\rangle$ compared with ^1E to $|m_s = \pm 1\rangle$. The widths of the non-radiative decay arrows indicate the relative rate.

(637 nm), which is often called the primary zero phonon line (ZPL) of NV^-. The two singlet states (^1E, $^1A_1$) are connected by another ZPL transition at 1.190 eV (1042 nm), which can be named as the secondary ZPL. Triplet and singlet states are connected via non-radiative transitions with spin-dependent intensity and are primarily used for spin initialization and readout in most NV^- studies. Here A_1, A_2, and E are irreducible representations of coordinate components, quadratic components, and rotations of NV^- categorized by their symmetry under operations of the C_{3v} group. A detailed explanation can be found in Ref [35].

Optical and spin properties The optical and spin properties of NV^- are tightly related to its molecular and electronic structures. As mentioned before, NV^- center has two ZPL peaks, the primary one at 637 nm and the secondary one at 1042 nm. However, due to its relatively less symmetric molecular and electronic structures (compared with group IV centers, as discussed in the

next section), optical transitions are strongly coupled to the vibrational modes of the diamond lattice (phonons), with only $\approx 3\,\%$ of the optical emission belonging to the ZPL wavelength and $97\,\%$ of the emission spanning across a broad phonon sideband from $640\,\mathrm{nm}$ to $800\,\mathrm{nm}$. On the plus side, this broad phonon sideband emission (ZPL energy $\rightarrow$ photon + phonon) indicates a similar broadband excitation spectrum (excitation energy $\rightarrow$ ZPL energy + phonon), which relaxes the wavelength requirement to excite NV^- centers. In the meantime, this also indicates that most emitted photons from NV^- have very different energies, which makes it hard to form entanglements using the Hong-Ou-Mandel protocol, a primary method used for quantum networking applications that require identical photons [39]. In addition, the broadband signal collection requires a relatively low fluorescence background (optical signal noise), especially for individual NV^- center measurements.

Both ground and excited states of NV^- center are triplet states. Each triplet state has two spin sub-levels: $m_s = 0$ and $m_s = \pm 1$. Two sub-levels are distinguishable due to the presence of zero field splittings with $2.87\,\mathrm{GHz}$ transition frequency for the ground state and $1.42\,\mathrm{GHz}$ for the excited state, primarily due to the spin-spin interactions. $m_s = \pm 1$ within a sub-level degenerate unless an external magnetic field is present. Zero field splittings can be observed by a special technique called optically detected magnetic resonance (ODMR) [35], which is an important operation mechanism and will be discussed in the next paragraph. The magnetic g factor of the electron spin is ≈ 2, indicating a free-electron-like Zeeman splitting in the presence of an external magnetic field. Depending on the nuclear spin of the nitrogen isotope, hyperfine interactions can also affect the energy levels (and thus resonances) of the NV^- center. For instance, [^{14}N] has a nuclear spin of $I = 1$, which leads to three ODMR resonances when the external magnetic field is present, while [^{15}N] contains a $I = 1/2$ nuclear spin which only results in two ODMR resonances. This difference is a straightforward method to distinguish the isotope of the nitrogen, which is a key step in identifying δ-doped $^{15}NV^-$ from the naturally present $^{14}NV^-$ [40].

One special property of the NV^- center is the secondary ZPL emission connecting two singlet

states. This optical transition, combined with non-radiative decays linking the triplet states, provides a state-dependent overall decay rate between ground and excited triplets and can be used for initializing the NV$^-$ qubit state. The schematic of the feature is called *state-selective intersystem crossing* (state-selective ISC) and is also shown in Figure 1.1 (b) [41]. In short, non-radiative decay $|^3E, m_s = \pm 1\rangle \rightarrow |^1A1\rangle$ is faster than $|^3E, m_s = 0\rangle \rightarrow |^1A1\rangle$, and decay $|^1E\rangle \rightarrow |^3A_2, m_s = 0\rangle$ is faster than $|^1E\rangle \rightarrow |^3A_2, m_s = \pm 1\rangle$, leading to a net spin flow from $m_s = \pm 1$ to $m_s = 0$. Also due to a considerable portion of emission from state $|^3E, m_s = \pm 1\rangle$ undergoing non-radiative path, signals collected from the radiative transition $|^3E, m_s = \pm 1\rangle \rightarrow |^3A_2, m_s = \pm 1\rangle$ has fewer counts. Therefore, off-resonance excitations such as commonly used green lasers ($520\,\mathrm{nm}$ or $532\,\mathrm{nm}$) can simultaneously readout and initialize the spin state of the NV$^-$ center. This simple operation is valid at both cryogenic and room temperatures and has been a basis of the quantum operation of NV$^-$.

Operation mechanism Since the sub-level pair $|m_s = 0\rangle$ and $|m_s = \pm 1\rangle$ are orbital singlet and spin-triplet for both $^3A_2$ and ^3E, microwave manipulation of the NV$^-$ spin is very efficient due to negligible orbit change. This efficiency can be observed by looking at the g factor $g = 2 \times \langle m_s = \pm 1 | H^{ac}_{Zeeman} | m_s = 0\rangle \approx 2$, where H^{ac}_{Zeeman} refers to a unit AC magnetic field (unit microwave drive). Therefore, a combination of optical initialization, readout, and microwave manipulation is sufficient for utilizing NV$^-$ centers as qubits. The first step of the spin control is to search for the qubit resonance with or without an external magnetic field. When the microwave driving is on-resonance with the energy difference between $|m_s = \pm 1\rangle$ and $|m_s = 0\rangle$, NV$^-$ centers prepared at the state $|m_s = 0\rangle$ will be driven to the state $m_s = 1$ or $m_s = -1$, which can be captured via a weaker optical readout signal (a dip). This technique is called ODMR. The resonance frequency shift from the zero-field splitting and energy separation between two or three ODMR peaks indicate the magnitude of the magnetic field. Furthermore, microwave driving can be used for coherent quantum state transfer (single qubit gates). By varying the duration of the microwave drive for $|m_s = 0\rangle \leftrightarrow |m_s = -1\rangle$, one can prepare the NV$^-$ to $|m_s = 0\rangle$ (no pulse, 2π pulse),

$|m_s = -1\rangle$ (π pulse), $(|m_s = -1\rangle + |m_s = 0\rangle)/\sqrt{(}2)$ ($\pi/2$ pulse), or any other superpositions. The π pulse duration can be characterized via Rabi oscillation measurements. Once the parameters for the single qubit gates are set, other measurements regarding the qubit lifetime (T_1), coherence (T_2^*), and dynamical decoupling coherence (T_2, $T_{2,XY}$, $T_{2,CPMG}$) can be performed, to reduce the qubit decoherence from environment, or study the interaction between NV^- and other spins in the system [42]. Furthermore, a similar radio frequency (RF) drive can be applied to the system if nearby nuclear spins are used for long coherence quantum registers [16], and some additional optical pulses can be added to help maintain the charge state of NV^- [43].

Applications in quantum technology NV^- centers have been proposed for three main applications in quantum technology: quantum computation, quantum networking, and quantum sensing. The idea of quantum computation originates from the fact that a single NV^- center can effectively communicate with multiple nuclear spins, which may serve as quantum registers. This multi-qubit cluster can then be used for logical operations and even error corrections [44]. To date, the maximum quantum registers that can be accessed via a single NV^- center reaches 27, which could serve as a logical qubit [45]. Although NV^- and ^{13}C obtain long coherence times, the scalability of such a system still needs to be improved compared with other systems [8, 46]. Therefore, only small-scale quantum computing can be performed at this moment. NV^- center also pioneered quantum networking research, with the study of remote entanglement between matter qubits over ten years ago [43]. To date, a multi-node quantum network with entanglement delivery has been demonstrated using NV^- center at remote locations [47]. Although the state-of-the-art quantum network using NV^- faces several issues, including low signal collection efficiency due to the lack of cavity enhancements, spectral drift, and low ZPL ratio compared with total counts, NV^- remains one of the prime candidates for future quantum networking nodes. Unlike quantum computation and networking which mostly rely on the optical and spin coherence of NV^- centers, the third application, quantum sensing, primarily utilizes the sensitivity of NV^- spin for external magnetic field, temperature, and electric field changes. The use of NV^- only requires sufficient spin coherence, which

is well preserved even at room temperature. Therefore, the operation mechanism is considerably simpler than the quantum computation and networking protocols, using only green excitation laser and microwave delivery instead of cryogenic temperature, charge re-pump, ZPL narrow bandwidth signal collection, etc. NV^- has unique advantages in nanoscale sensing, that NV^- can detect local signals that are only a few nanometers away. In addition, the size of the diamond that hosts NV^- centers can be sub-micrometer, such as commercially available nanodiamonds [48] and scanning NV^- tips [49], which greatly improves the versatility of the sensing platform. In this work, we will also introduce our nanoscale diamond host—diamond membrane—in Chapter 3. To date, NV^- sensing has widely spread to many sensing applications. A few examples include nuclear magnetic resonance (NMR) [50], understanding of superconductors and strongly correlated electronic systems [51], and biological sensing and imaging [27].

1.2.2 Group IV centers

Due to the limited natural abundance, the history of group IV center studies is less than four decades. The SiV^- emission spectrum was first observed when investigating spectra of lab-grown diamonds using the chemical vapor deposition (CVD) technique [52]. The emission profile was later assigned to the silicon defects in diamond without ambiguity [53]. Ten years later, individual-level SiV^- defects have been observed, which could serve as single photon sources for quantum applications [54]. Later, people observed other defects in this family, all on the single center level: germanium-vacancy center (GeV^-) [55], tin-vacancy center (SnV^-) [56], and lead-vacancy center (PbV^-) [57]. Although the field of group IV centers is still young with lots of arguable phenomena in their detailed electronic structures, these centers have been proven to be prime candidates for quantum networking applications [23].

Molecular structure and electronic configuration Group IV centers share a lot of similarities in molecular structures, electronic configurations, and energy levels, with only minor differences

in specific parameters, such as ZPL emission wavelength and spin-orbit coupling strength. Here, we take the silicon-vacancy center as an example. Chapter 4 will discuss the difference between group IV centers and their implications for quantum networking applications.

The molecular structure of a SiV^- center is shown in Figure 1.2 (a). Similar to NV^-, the SiV^- also occupies two adjacent sites of sp^3 carbon atoms along the $[111]$ crystal axis. However, the silicon atom is placed in an interstitial site instead of a substitutional site between the two vacancies. This placement also holds for other group IV centers (GeV^-, SnV^-, PbV^-), mostly due to the significant size of the atom compared with nitrogen which makes the interstitial defect more energetically favorable [58]. The split-vacancy configuration grants a different point group symmetry, D_{3d} for group IV defects. Compared with C_{3v}, this point group includes an additional symmetry operation, inversion with respect to the central atom (Si, Ge, Sn, Pb). This inversion symmetry profoundly impacts its electronic configuration and optical properties, which will be discussed in the next paragraph. DFT calculations show that the $\mathrm{Si}-\mathrm{V}$ structure is stable at high temperatures against dissociation towards substitutional silicon and vacancy [59], indicating that SiV is a thermally stable molecular state.

The electronic configuration of SiV^- is relatively simpler than NV^-. The D_{3d} group symmetry leaves two groups of orbits for the excessive electron to choose: E_g and E_u. Each group includes two axes x and y. Taking the spin freedom of the electron into consideration, both the optical ground and the excited state have four energy levels. The four levels form two branches, split by the spin-orbit coupling λ_g (λ_e). Unlike NV^-, group IV centers do not have zero field splitting. Therefore, they all require an additional static magnetic field to remove the degeneracy inside each branch and form resolvable qubit levels. Figure 1.2 (b) shows the energy level of the SiV with spin-orbit coupling (left) and external magnetic field (right). When the magnetic field is absent, there are four ZPL transitions between two branches in ${}^2E_g$ and the other two in ${}^2E_u$. The number of peaks can increase to 16 when the external field is present, with fitting parameters revealing the detailed electronic structure of the SiV^- [60]. All the ZPL wavelengths are around $738\,\mathrm{nm}$,

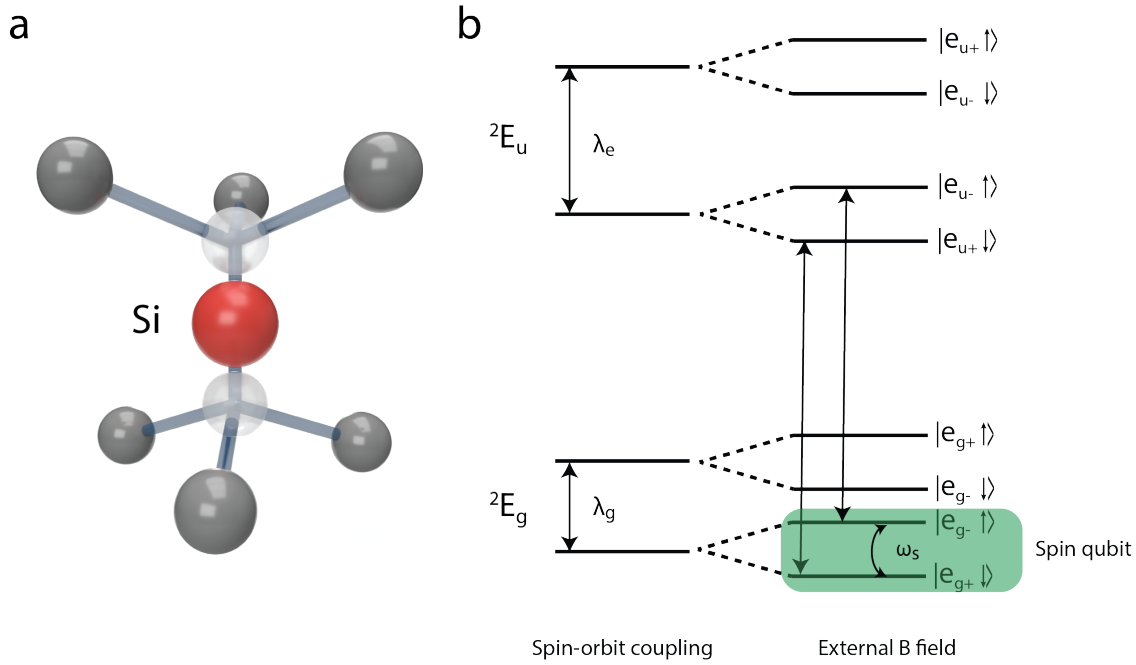

Figure 1.2: Negatively-charged silicon-vacancy center (SiV^-) in diamond. (a) The molecular structure of the SiV^- center. The red atom is the interstitial silicon between two vacancies, and the dark grey atoms are sp^3 carbon. Two carbon vacancies are right next to the silicon atom. (b) Energy level diagram of SiV^-. The optical ground state is ^2E_g, and the excited state is ^2E_u. Both states are spin $1/2$ with orbital degeneracy. The spin-orbit coupling (λ_g, λ_e) creates two branches, and the lowest branch is used as the qubit when an external magnetic field is present (no zero field splitting). Spin up ($|\uparrow\rangle$) and down ($|\downarrow\rangle$) are simplified labels to the $|m_s\rangle$ states, with $|\uparrow\rangle = |m_s = 1/2\rangle$, $|\downarrow\rangle = |m_s = -1/2\rangle$ The arrows between energy levels indicate spin-conserving transitions of SiV^-, detected as one of the ZPL emissions (C line) mostly used for spin qubit initialization.

a relatively accessible wavelength for tunable Ti: Sa lasers. In addition, due to the lack of zero-field splitting. SiV^- and other group IV defects don't have the privilege of using the off-resonant excitation for spin initialization.

Optical and spin properties All group IV centers obtain inversion symmetry for the molecular structure. The electronic configuration follows this high symmetry, with a small displacement of electron wavefunctions between ground and excited states [35]. This indicates a weak electron-phonon coupling for optical transitions and, thus, a large ZPL (small phonon sideband) portion in the total emission profile. In the case of SiV^-, the ZPL ratio can be as high as $80\,\%$ [61]. According to our discussion of NV^-, indistinguishable ZPL photons from separate emitters can be used for

entanglement generation, and SiV^- is a much brighter single emitter in terms of ZPL photon emission. In addition, because of the inversion symmetry, the electron wavefunctions of SiV^- (and other group IVs) have a negligible permanent electric dipole. Therefore, they are insensitive to electric field fluctuation, which protects their spectral stability against noises. The spectral robustness enhances the compatibility of the group IV centers to diamond nanostructures—nanophotonic cavities and waveguides—that improve the coupling between color centers and photons and increase the entanglement generation rate [62]. In contrast, the optical coherence of NV^- centers is strongly impacted by the nanofabrication devices. Therefore, many quantum networking demonstrations rely on solid immersion lenses [43], a less invasive method.

The optical ground state of SiV is a degenerate spin $S = 1/2$ system with two branches, with $\approx 48\,\mathrm{GHz}$ energy difference between branches due to spin-orbit coupling [60]. The spin qubit is normally defined as the two spin states in the lowest energy branch, with qubit frequency entirely dependent on the external magnetic field (no zero-field splitting). When we take a brief look at the qubit states $|e_{g+}\downarrow\rangle$ and $|e_{g-}\uparrow\rangle$, we might (falsely) conclude that the qubit coherence has to be excellent since different orbit and spin values of qubit states lead to more difficult transition. In fact, the major decoherence path is through the other two quantum states in the upper branch outside of the qubit subspace. For instance, phonon-related spin depolarization (spin decay T_1^{orbit}) between states $|e_{g+}\downarrow\rangle \leftrightarrow |e_{g+}\uparrow\rangle$ and $|e_{g-}\downarrow\rangle \leftrightarrow |e_{g-}\uparrow\rangle$ are the dominant decoherence sources [63]. This depolarization can be understood as a loss of phase information when the qubit population is bounced back and forth between two quantum states with the same spins but different orbits. The feature can hardly be captured by directly measuring the traditional T_1^{spin} depolarization between qubit states [64]. We will discuss the details of our findings in Chapter 4. In short, phonons in diamond lattice are the dominant spin decoherence source, which ultimately limits the operation of SiV^- and all group IV centers at cryogenic temperature [65].

Unlike NV^-, the lack of the secondary ZPL emission leaves no spin-selective, non-radiative path (intersystem crossing) for spin initialization through off-resonant excitation. As a result, the spin

initialization has to be performed via resonant excitation at one of the ZPL wavelengths. The fidelity of the spin initialization depends on the spectral distance between two spin-conserving transitions, labeled as arrows in Figure 1.2 (b). This distance is determined by the magnitude and orientation of the external magnetic field. The initialization efficiency depends on the optical cyclicity of SiV^-, which is a function of the magnetic field orientation with respect to the quantization axis (crystal axis $[111]$) and the excitation laser power. Similarly, the spin readout is performed via resonant excitation at one of the spin-conserving transitions and signal collection at the phonon sideband.

Operation mechanism The two qubit states of SiV^- are $|e_{g+}\downarrow\rangle$ and $|e_{g-}\uparrow\rangle$. They are energetically distinguishable due to the spin-dependent Zeeman effect. In addition to the spin difference, these qubit states also belong to separate orbits: $|e_{g+}\rangle = -(|e_{gx}\rangle + i\,|e_{gy}\rangle)/\sqrt{2}$ and $|e_{g-}\rangle = (|e_{gx}\rangle - i\,|e_{gy}\rangle)/\sqrt{2}$. Two orbits are orthogonal, leading to inefficient coherent spin manipulation via microwave. Therefore, some early-stage manipulations utilized all-optical, Raman-based methods for spin manipulation and coherence characterization [65, 66]. Fortunately, SiV^- (and all other group IVs) have large strain susceptibility. As a result, an anisotropic strain profile can essentially generate orbit mixing between qubit states and enable coherent spin control via microwave [63, 67]. For group IV qubits with small spin-orbit coupling (SiV^-, GeV^-), ion-implantation induced random strain profile would be sufficient to generate some highly-strained defects [68, 69]. However, this is not a viable approach for large spin-orbit coupling defects (SnV^-, PbV^-), which require a much larger strain magnitude for efficient microwave manipulation [70]. Therefore, those heavy defects are still manipulated via all-optical methods [71], which are relatively slow with low gate fidelity. The elegant solution is to introduce a large strain profile to the diamond crystal, which will be discussed in detail in Chapter 4.

Applications in quantum technology The application of group IV centers in quantum technology largely resides in the quantum networking sector, mainly due to the phonon-limited operation

temperature. Similar to the NV^- center, although group IVs have shown their potential in interacting with nuclear spins [68], the scalability of such a system for quantum computing still needs to be improved. In quantum networking applications, group IVs have a much larger ZPL emission ratio, excellent robustness against nanophotonic cavities and waveguides fabrication, high fidelity initialization, readout, and quantum control [67], and low spectral drifts. Therefore, group IV centers have been regarded as the next generation of quantum networking nodes after NV^-. Recent demonstrations integrating frequency tuning and wavelength conversion unlock the realization of quantum networking via telecommunication fibers [23, 72, 73], which opens the pathways of telecom-frequency networking for other visible or near-infrared (NIR) defects [74] in addition to the existed candidates [75]. Furthermore, group IVs have shown a strong correlation between ZPL linewidth and temperature [76], indicating their potential as cryogenic temperature sensors [77]. In general, exploring the usage of group IV centers is an active research project, and we shall see more applications shortly.

1.3 Material properties and synthesis of diamond

After introducing the solid state qubits—NV^- and group IV centers—for quantum technology, we focus on their host material: diamond. Although point defects have a similar operation philosophy as neutral atoms, molecules, or trapped ions, living in a solid-state material has fundamentally changed the investigation perspective, characterization approaches, manipulation methods, and usage scenarios. Arguably, while atomic defects can be regarded as *pseudo atoms*, the host material and other objects in the vicinity introduce unique properties to the defects and make them different enough from atoms studied in atomic, molecular, and optical (AMO) physics. In this section, we will discuss a few properties of the host material, diamond, and other objects in diamond that affect the behavior of color centers. As we will see, these properties provide both challenges and opportunities for defect studies.

1.3.1 Material properties of diamond

Diamond has been quite a unique material since its discovery. The perfect diamond crystal is composed of only one chemical element—carbon. Strictly speaking, graphite is the chemically stable form of crystalline carbon at room temperature and atmosphere instead of diamond. However, diamond is a meta-stable state in such a condition, and a much higher temperature (at least $\geq 400\,^{\circ}\mathrm{C}$, slightly higher than the oxygen-termination temperature [78]) is required to allow for a visible transition between diamond and graphite. Carbon atoms inside diamond form covalent sp^3 bonds, and each carbon atom is bonded to four other carbons, forming a typical Bravais lattice called diamond lattice [31]. Due to small atomic sizes and short, rigid sp^3 bonds ($0.154\,\mathrm{nm}$), diamond has a very high atomic density, leading to the highest hardness as a natural material. In addition, diamond is chemically inert at room temperature against most acids and solvents. Although these features preserve the properties of color centers and make them compatible with numerous operation environments, the hardness and inertness make the diamond incompatible with many nanofabrication processes, either physical or chemical. The hardness also makes it quite challenging for strain engineering except in nanoscale forms [79].

Optical properties Diamond is a wide bandgap material ($5.5\,\mathrm{eV}$). Therefore, diamond is transparent for lights at the visible wavelength ($\leq 3.3\,\mathrm{eV}$). The refractive index of diamond is ≈ 2.4, which is relatively high compared with many materials. Some certain crystals obtain even higher refractive indexes that can confine light and enhance the interaction with diamond color centers through evanescent coupling [80]. The mainstream of color center research, however, still relies on fabricating diamond nanostructures for photon-emitter interactions. Our efforts on this topic will be discussed in Chapter 3.

Isotopes and bulk spin bath Many elements have multiple isotopes; some isotopes include nuclear spins. The nuclear spin bath is one of solid-state spin qubits' most important environmental properties due to their considerable total interaction strength. The perfect diamond crystal only

includes carbon atoms. For natural abundance the majority of carbon ($\approx 99\,\%$) is ^{12}C which does not have nuclear spin ($I = 0$), and ^{13}C with non-zero nuclear spin ($I = 1/2$) only takes a small portion ($1\,\%$). ^{14}C is radioactive and extremely rare, which are mostly used for radiocarbon dating and will not be discussed here [81]. In synthetic diamond (discussed in the next section), the isotopes can be engineered for different purposes. For instance, an isotopically purified diamond with negligible ^{13}C concentration has a very quiet spin bath, which is ideal for hosting coherent color centers [67, 82].

In addition to the native carbon nuclear spin bath, impurities such as $[N]$ introduce excessive electron and nuclear spins ($I = 1$ for ^{14}N, $I = 1/2$ for ^{15}N). These $[N]$ often exist as substitutional defects in diamond called P1 centers, which also include a non-zero electron spin ($S = 1/2$). P1 centers become one of the main decoherence sources of NV$^-$ [83] at a non-negligible concentration. Therefore, for NV$^-$ studies requiring dense ensembles, the creation yield of NV$^-$ has to be high to limit P1 concentration and improve the qubit coherence [84].

Surface spins and treatments Like all solid-state systems, the bulk spin bath is not the only source of the spin environment. For shallow implanted color centers, especially NV$^-$ centers for nanoscale sensing, surface spins tend to have more significant impacts compared to bulk spins. A systematic study reveals that the surface roughness of diamond greatly impacts the dangling bond density, and surface spin-induced decoherence [78]. For diamond nanostructures, a combination of the front surface and sidewall morphology determines the overall decoherence magnitude. Compared with the well-polished front surface, the sidewall is typically defined via plasma etching, which obtains a much weaker roughness control. Therefore, the plasma etching profile becomes the dominant decoherence source.

Some surface terminations, such as oxygen termination and hydrogen termination, could improve the spin environment by replacing dangling bonds with uniform covalent bonds [78]. They also shift the Fermi level and affect the charge state of near-surface color centers. A well-accepted treatment is performing oxygen termination to improve the charge stability of NV$^-$ over NV^0,

which is beneficial for sensing and networking purposes [78]. In contrast, hydrogen termination will prefer the NV^0 and is thus undesirable. Group IV centers, especially heavy group IVs (GeV^-, SnV^-, PbV^-) are predicted to have a higher defect level closer to the middle of the bandgap [85]. Therefore, they are not in favor of either termination.

Discussion Due to its unique material properties, diamond has been used for many applications. Before the emergence of quantum science and technology, diamonds were mostly used for fashion and decoration. Diamond is also ideal for cutting hard crystals thanks to its exceptional hardness. Besides, the wide band gap and high breakdown voltage make diamond an ideal material for power electronics [86]. The excellent thermal conductivity of diamond leads to heat dissipation studies for the semiconductor industry [87]. Although we only focus on color centers and quantum technologies in this work, we are aware of other exciting possibilities this material platform brings.

1.3.2 Formation of diamond

Natural diamond Before the invention of high-pressure, high-temperature (HPHT), and chemical vapor deposition (CVD) processes, all diamond research and applications were conducted via natural diamonds from diamond mines in many places. Natural diamonds are formed in the mantle, a perfect place with high pressure and temperature. Although natural diamonds are great for industry and fashion purposes, there are large fluctuations in crystal defect concentration between stones. The inconsistency of diamond quality is not ideal for electronic and quantum applications. Therefore, these studies have turned to a more controllable and scalable source—synthetic diamond.

HPHT diamond HPHT process is designed to imitate the earth condition that created diamond billions of years ago. The process requires a relatively high temperature (often surpasses $1300\,^{\circ}\mathrm{C}$) and pressure (several GPa) [88]. This process can produce diamonds at scale and has naturally become the main method to generate synthetic diamonds. The HPHT method is a chemical process

with seed crystals and a few catalysts, which introduces impurities and limits the purity of the crystal. Since the process utilizes the phase transition of carbon, HPHT diamonds typically have excellent crystal quality with minimal strain. In addition to diamond growth, higher temperature processes can release the local strain variations post large ion implantation, as discussed in the PbV^- center creation study [89].

CVD diamond The CVD process is the other primary method to create synthetic diamonds. One major type of CVD, microwave plasma CVD (MPCVD), takes place in a chamber with dense hydrogen plasma generated via strong microwave power. The added precursor gas—methane (CH_4)—is dissociated by the hydrogen plasma, with carbon atoms falling onto the seed crystal. These carbon ad-atoms can form either sp^2 or sp^3 bonds, but the hydrogen plasma selectively etches the sp^2 carbon, leaving only sp^3 carbons behind if the correct growth condition is met. Therefore, there is a positive rate of diamond growth. Multiple diamond growth regimes can be achieved depending on the plasma power and precursor flow. In this work, we focus on the slowest but cleanest regime, one-dimensional step-flow growth, which can provide the highest crystal quality with minimal impurity concentration [90, 91]. Traditionally, only diamond seed crystals can allow single-crystal diamond growth (homoepitaxy). However, recently, some wafer-scale diamonds have been grown using heteroepitaxy methods [92], which is promising for future scalable diamond devices. Compared with the HPHT method, the CVD process offers more precise layer control on the vertical structure due to its layer-by-layer growth mechanism. Therefore, other impurities can be intentionally incorporated at growth stages to generate *in situ* point defects [93]. Defects that can be generated at a certain depth with a narrow distribution profile are called δ doping, which has been applied to NV^- studies [90]. The work presented in the next chapter is entirely based on the MPCVD diamond that offers pristine crystal quality and versatile impurity control over different growth layers, which is critical for the rest of the study.

CHAPTER 2

DIAMOND MEMBRANE SYNTHESIS AND INTEGRATION†

Abstract

Nitrogen-vacancy and group IV centers in diamond have shown great potential in quantum technologies. These advances can turn into practical quantum systems if their host—single crystal diamond—is integrated with heterogeneous materials platforms. In this chapter, we introduce the fabrication details and material characterizations of our state-of-the-art diamond membrane platform, which sets the foundation for the demonstrations in quantum photonics, quantum networking, and quantum sensing, as discussed in the following chapters. We start with an introduction of the efforts in generating low-dimensional diamond structures for quantum applications. After a process overview of the "smart-cut" based method, we introduce our approach to synthesizing diamond membranes and generating color centers, followed by individual membrane patterning and undercut. Starting from ready-to-transfer diamond membranes, we present two different methods to integrate them with heterogeneous materials, either by bonding agents such as photoresist or plasma-activated bonding. We conclude the section by discussing the usage scenarios of the two transfer methods and summarizing the material properties of the diamond membrane platform.

2.1 Wafer-scale diamond substrates and diamond-based heterostructures

Color centers in diamond, such as NV^- and group IV centers, are promising candidates for quantum technologies. However, due to the diamond's scarcity and unique material properties, including extreme hardness, inert chemical properties, and high refractive index, on-chip integration of color centers with other functional devices remains challenging. In response, manufacturing wafer-scale single-crystal diamond substrates or integrating diamond with heterogeneous material platforms

†. The work discussed in this section was reported in [40, 94]

has become one of the primary focuses of diamond research. Here, we briefly introduce some exemplary works related to quantum applications, including heteroepitaxial diamond growth, diamond slabs and membranes from laser cutting and thinning, diamond beams and frames formed by angle etching or isotropic etching, integrated diamond AFM tips, and diamond membranes fabricated via the "smart-cut" method.

Heteroepitaxial growth A natural approach to address material scarcity is the heteroepitaxial growth of diamond. This has historically been challenging due to significant lattice mismatch between single-crystal diamond and seed substrates, leading to grain boundaries and polycrystalline diamond. Recent progress based on the ion bombardment-induced buried lateral growth (IBI-BLG) method [92] shows the state-of-the-art growth effort on wafer-scale, single-crystal diamond substrates. Although impressive, the lattice mismatch leads to large strain distribution across the thickness of the substrates, which are normally hundreds of micrometers. The inevitable strain presence could lead to excess growth defects and compromised emitter properties. Therefore, it has to be eliminated or largely suppressed before the actual usage of quantum applications.

Plasma-etched diamond slabs The most straightforward material integration of diamond substrates utilizes commercially available single-crystal diamond slabs. However, most laser-cut diamond slabs' thickness is beyond $30\,\mu\mathrm{m}$. Membranes with such a thickness is compatible for some bio-sensing applications [95], but not ideal for integration with distributed Bragg reflector (DBR) mirrors or other on-chip devices. Therefore, an appropriate thinning process must be applied before material integration. Due to the extreme hardness and chemical inertness of single-crystal diamond, inductively-coupled plasma reactive ion etching (ICP-RIE) becomes the only etching option with a consistent etching rate while maintaining the surface morphology [96]. This method offers a straightforward fabrication process and minimum requirements on nanofabrication facilities and has thus been used for color center integration with micro-cavities [97] and fabrication of two-dimensional photonic crystal with decent quality factors [98]. However, since the ICP-RIE

etching removes the majority of the material (from $\approx 30\,\mu\mathrm{m}$ to $\approx 1\,\mu\mathrm{m}$), any etching rate deviation across the membrane would result in a considerable difference to the height profile of the final diamond membrane. The relatively long etching sequence also posts strict requirements for the control of the plasma chamber environment. The variation of the membrane thickness limits the bonding uniformity, which is not ideal for photonic applications such as microcavities and nanophotonic integration.

Angled etching of diamond An alternative method to integrate diamond with other on-chip devices is generating freestanding diamond nanostructures. Although not designed for heterogeneous integration, angled ICP etching via a Faraday cage or focused ion beam (FIB) milling [99] draws lots of inspiration and has a profound impact on the diamond nanofabrication community. Angled etching is a promising method for fabricating beams with strain control [63], waveguides, nanophotonic crystals, and cavities [100], phononic crystals and cavities [101], and tapered fiber couplers [102]. As an important figure of merit for diamond nanofabrication, the quality factors of nanophotonic cavities can reach 3×10^4, which exceeds the threshold of generating strong cavity-emitter coupling [103] and therefore has been used for some landmark demonstrations [62]. However, this fabrication method is tailored for diamond photonics, and the final devices remain on diamond substrates. Therefore, the possibility of integration with other on-chip structures from heterogeneous materials remains limited. Moreover, this method is suitable for thin, one-dimensional geometries [104] but is not applicable for wide, two-dimensional (2D) structures such as 2D photonic cavities and waveguides. The Faraday cage and FIB methods also lack precise sidewall control, which introduces additional optical loss to the system. Nonetheless, angled etching remains one of the mainstream etching methods to create suspended diamond nanostructures.

Isotropically etched diamond frames The diamond angled etching process posts unique requirements for nanofabrication facilities, such as Faraday cage-compatible ICP etching chambers or angled FIB tools, which may not be applicable to many places. In 2017, an alternative

method combining anisotropic etching with isotropic etching to fabricate diamond structures has been demonstrated [105]. Compared with angled etching, this method does not rely on sophisticated nanofabrication equipment and has shown reproducible results at various cleanroom facilities [101, 106, 107]. More importantly, this method is suitable for generating standalone diamond waveguides and frames, which can be transferred and bonded to heterogeneous material platforms via Van der Waals forces [108, 109]. However, as this method heavily depends on the isotropic etching to perform undercut, the structural profile on the back side of the device is weakly controlled, which often introduces additional optical loss. The uneven backside also reduces the quality factor, making it unsuitable for 2D photonic crystal fabrications. Furthermore, the Van der Waals bonding is relatively weak, which reduces the device yield and limits the strain tuning range. Future optimizations on device integration should be able to address this issue.

Integrated diamond AFM tips Sharp diamond pillars containing single or ensemble NV^- centers are promising candidates for scanning probe magnetometry due to their high spatial resolution and magnetic field sensitivity [110]. After over ten years of development, this proof-of-concept demonstration has evolved into a fast-growing market with a few companies (Qnami, QZabre, etc.), providing high-quality NV^- AFM tips for scanning NV magnetometry with various targets. This application is and will be one of the primary usage scenarios for NV-based quantum sensing. However, due to its highly specialized focus, the diamond tips are unsuitable for large-scale integration with other on-chip devices.

Diamond membrane via the "smart-cut" method "Smart-cut" is a common method in the semiconducting industry with applications well beyond diamond substrates. Demonstrations of silicon-on-insulator (SOI) wafer [111], silicon carbide-on-insulator [112], and lithium niobate (LN) [113] unveils the strong potential of this universal method in integrating heterogeneous materials at wafer scales. Although this method can generate large-scale thin film with precise thickness, the implanted species (often H or He) introduce excess crystal damage that might be

undesirable for quantum applications. Specifically, in one of the earliest demonstrations regarding thin film diamond generation [114], a shifted and much broader Raman linewidth was observed on the smart-cut diamond membranes. This crystal damage can be partially recovered by a subsequent diamond overgrowth via the chemical vapor deposition (CVD) method [115]. By introducing external chemical elements (nitrogen, silicon, germanium, tin), these diamond membranes are decent hosts for ensemble-level NV^-, SiV^-, GeV^-, and SnV^- centers [116, 117]. Although the diamond membrane fabrication shares many commonalities with other “smart-cut "-based material integrations, this quantum application-oriented method is unique in several aspects. First, as a rare material with great scarcity, all demonstrations are based on millimeter-scale diamond substrates with limited scalability. Second, ion bombardment of diamond generates a graphitic layer (amorphous graphite) that cannot be separated naturally (like SOI) or be removed via pure chemical etching (like thin film LN). Alternatively, as a conductive layer, the amorphous graphite can be removed via a relatively time-consuming process called electrochemical (EC) etching in water. Although this method provides clean undercut with smooth surfaces, this fabrication step is relatively slow even with additional optimizations (high voltage, chemical solutions) [118, 119], which remains the bottleneck of the diamond membrane generation. Third, ion-implanted diamond membranes contain numerous crystal damages and defects that are not compatible with quantum applications. Therefore, an additional homoepitaxial overgrowth step is necessary to recover the crystal quality. Lastly, diamond is one of the hardest materials, thus pure mechanical polish post membrane bonding is not a feasible option. Therefore, an ICP-RIE etching step has to be implemented to remove the damaged layer and improve the surface morphology. Compared with other diamond-based heterogeneous materials integration, the “smart-cut” method obtains the best scalability with the most flexible user scenarios. Unfortunately, the previous demonstrations suffered from limited material quality [115] and non-deterministic transfer method [120], posting needs for in-depth investigations.

Starting from the next section, we will introduce our diamond membrane synthesis and integration

methods based on the "smart-cut" technology. We will emphasize several key steps of our process and explain our logic to improve the crystal quality and realize deterministic membrane transfer and bonding.

2.2 Process overview

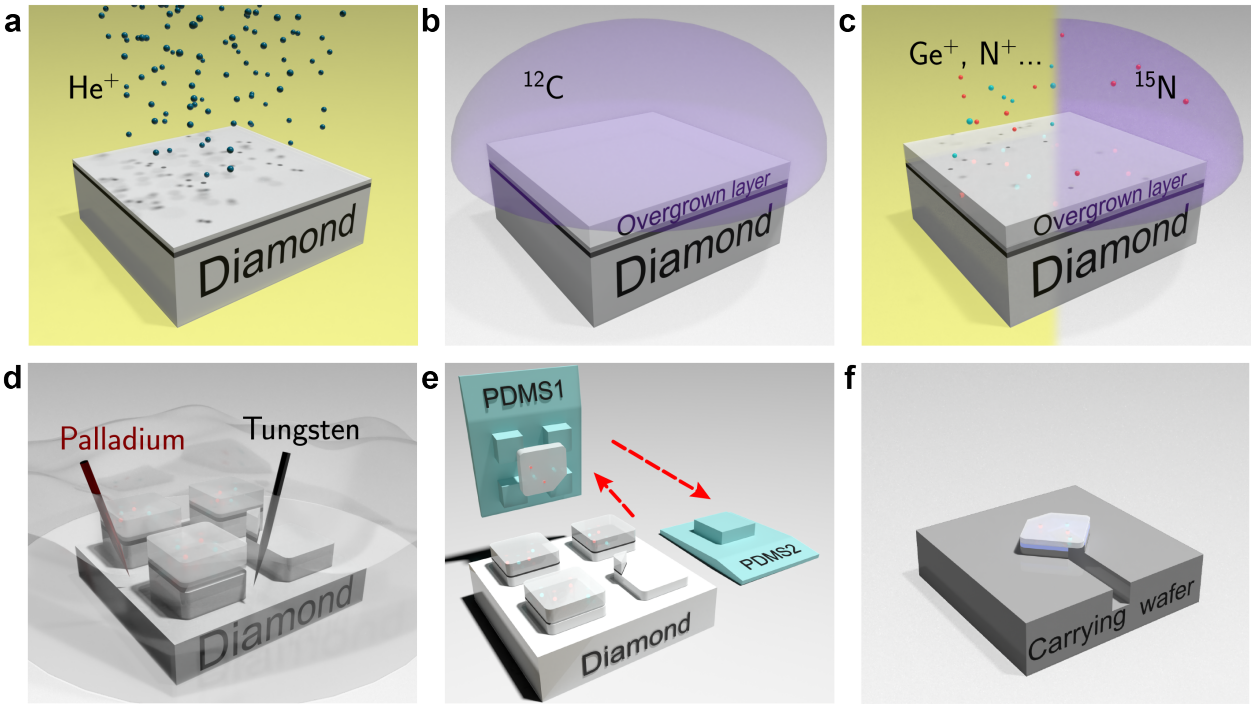

Figure 2.1: Schematics of the diamond fabrication process. (a) Formation of the diamond membrane via the "smart-cut" method. (b) Diamond overgrowth with isotopic purification. (c) Color centers incorporation via either ion implantation or *in-situ* doping. (d) Individual membrane patterning and undercut using electrochemical etching. (e) Membrane transfer by patterned PDMS stamps. (f) Membrane bonding with resist and damaged layer removal via plasma etching.

Integrating diamond membranes with pristine quality with heterogeneous materials involves many nanofabrication steps, which can be categorized into several stages: original diamond membrane formation, synthesis of pristine quality diamond membranes, generation of color centers, patterning of transferable membranes, membrane undercut, stamp transfer, damaged layer removal, and bonding to target carriers. Depending on the device's purpose, the bonding step involves either an additional bonding agent or surface functionalization via plasma. Figure 2.1 displays the

process overview of the bonding agent-based method. The schematics of the plasma-activated bonding will be introduced in the following sections.

2.3 Diamond membrane formation and overgrowth

2.3.1 Formation of the diamond membrane

The schematics of the diamond membrane formation via "smart-cut" is shown in Figure 2.2 (a). The process starts with a heavy ion implantation. In this work, we use He^+ as the primary dopant, but other species such as Ne^+ are also proved to be effective[121]. Crystal damage in diamond membranes is believed to be associated with growth defect concentration during the subsequent diamond CVD growth step. Therefore, we reduce the implantation energy ($150\,\mathrm{keV}$) with a slightly lower dose ($5 \times 10^{16}\,\mathrm{cm}^{-2}$) compared with previous demonstrations [115] to minimize the crystal damage. The simulated depth of the implanted He^+ is $\approx 410\,\mathrm{nm}$ using the SRIM software [122]. The implanted diamond substrates have a dark finish, indicating a phase transition of the carbon bonds from sp^3 to sp^2, often called the graphitization process. We note that the diamond remains transparent, indicating that no graphitized layer is formed if the implantation dose is less than $2 \times 10^{16}\,\mathrm{cm}^{-2}$.

One key step post He^+ implantation is the diamond annealing. This step helps recover the crystal quality of the diamond layer above the implantation depth. Although the recovered diamond membrane has imperfect crystal quality to host color centers, it is sufficient for the homoepitaxial diamond overgrowth. In principle, high-temperature annealing allows for the mobilization and subsequent annihilation of implantation-induced crystal damage in the top diamond layer [78, 123]. In our work, we employ a three-step annealing process: a $400\,^\circ\mathrm{C}$ soak for $8\,\mathrm{h}$, followed by a $800\,^\circ\mathrm{C}$ soak for $8\,\mathrm{h}$ and a finish of a $1200\,^\circ\mathrm{C}$ anneal for $2\,\mathrm{h}$, adopted from the fabrication process to generate SiV centers [124]. The annealing is performed in an argon forming gas environment (Ar:H_2 of $96:4$) to prevent interaction and surface damage from oxygen molecules. We notice in practice

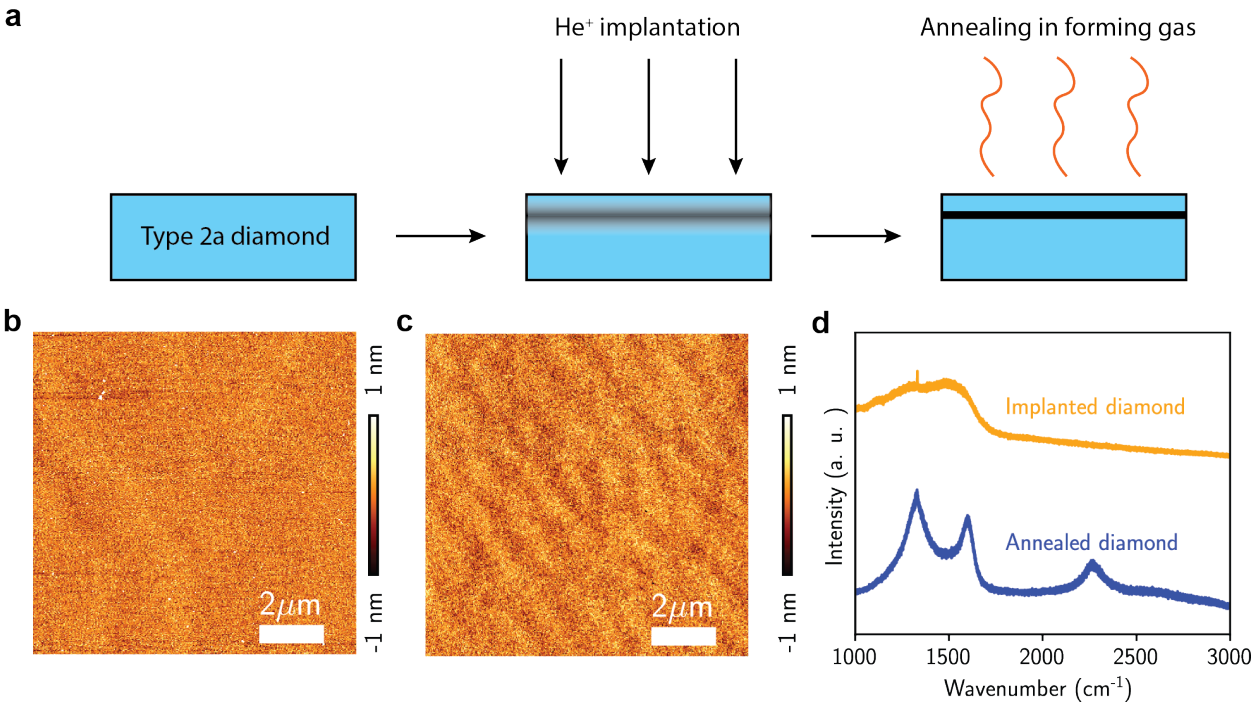

Figure 2.2: Diamond membrane formation. (a) Schematics of the original diamond membrane formation via the "smart-cut" method. (b) AFM of the initial diamond substrate, showing an R_q of $\leq 0.30\,\mathrm{nm}$. (c) AFM of the diamond substrate post implantation and annealing, with an R_q of $0.27\,\mathrm{nm}$. (d) Raman spectroscopy of the He^+ implanted and annealed diamond substrates.

that the protection gas—argon forming gas—prevents the formation of the surface graphitization layer ($\approx 3\,\mathrm{nm}$), which is in contrast with the traditional high vacuum annealing [125]. The lack of surface graphitization eliminates the necessity of applying strong tri-acid cleaning ($1:1:1$ sulfuric acid, nitric acid, perchloric acid at $\approx 225\,^{\circ}\mathrm{C}$) and thus prevents the diamond membrane from undercut and undesirable etching pits before the diamond overgrowth. We apply a mild surface cleaning with only two acids ($1:1$ sulfuric acid and nitric acid at boiling temperature) to prepare the surface for diamond growth. In contrast to the dark finish, the annealed substrates have a distinct pink color with reflective surfaces, indicating an interference effect between the top diamond layer and the graphitic layer underneath. In principle, this color varies depending on the implantation depth (energy). Figure 2.3 (b) shows a micrograph of the diamond substrate post annealing.

We apply atomic force microscopy (AFM) and Raman spectroscopy to quantitatively character-

ize the surface and crystal quality of diamond membrane substrates. The results are shown in Figure 2.2 (b-d). We note that the surface roughness remains less than $0.3\,\mathrm{nm}$, indicating an atomically smooth surface profile throughout the membrane formation process. Prior to annealing, only a weak diamond peak from the back substrate and low sp^3 amorphous carbon features are observed at $\approx 1500\,\mathrm{cm}^{-1}$ [126]. Post annealing, three peaks are observed. The $\approx 1595\,\mathrm{cm}^{-1}$ and $\approx 2268\,\mathrm{cm}^{-1}$ peaks are strongly correlated with high sp^3 amorphous carbon composite [126], while the $\approx 1325\,\mathrm{cm}^{-1}$ peak represents the partially recovered top membrane layer [114].

2.3.2 Diamond overgrowth via microwave plasma CVD

Due to the imperfect crystal quality of the original diamond membrane layer, we perform diamond overgrowth to the membrane substrate after annealing. This overgrown layer serves as the host for the coherent color centers. Similar to the previous method [115], the diamond overgrowth is performed via microwave plasma chemical vapor deposition (MP-CVD). A photo of an active plasma chamber is shown in Figure 2.3 (a).

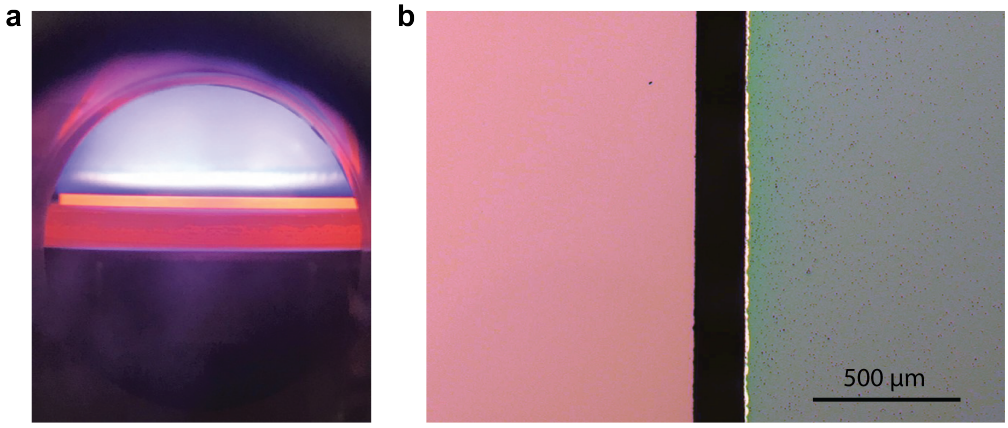

Figure 2.3: Diamond membrane overgrowth via MPCVD. (a) A photo of a running MPCVD chamber for diamond overgrowth. (b) The microscope image of an original diamond membrane (left) and an overgrown diamond membrane (right).

Unlike bulk diamond, diamond membrane substrates have imperfect surface and crystal quality, which could turn to excess growth defects if the growth recipe is not fully optimized. To min-

imize the defects from propagating during growth and fully recover the crystal quality, we use a slow growth recipe to ensure the 1D step growth regime [90, 91]. The limited methane concentration induces much lower growth rates ($3\,\mathrm{nm\,h^{-1}}$ to $10\,\mathrm{nm\,h^{-1}}$) compared with previous demonstrations($1\,\mu\mathrm{m\,h^{-1}}$ [127]). The maintained low growth rate also helps ensure a more accurate depth-localization of dopant layers, i.e., δ-doping precision, which will be discussed in the next section.

To further reduce the growth defect concentration, we apply di-acid cleaning ($1:1$ sulfuric acid and nitric acid at boiling temperature) to diamond substrates right before loading them into the CVD chamber. Inside the chamber, the target diamond substrate is placed on a grooved molybdenum substrate to keep it flat with the rest of the plasma-exposed surface, allowing for a uniform growth rate across the sample with minimized edge effects.

The chamber is first pumped down to a base pressure of $2\times10^{-8}\,\mathrm{Torr}$ to $5\times10^{-8}\,\mathrm{Torr}$ to reduce background contamination. Thereafter, high purity H_2 ($99.999\,999\,\%$ chemical purity, generated via hydrogen generator and purifier) is introduced into the chamber, with the gas flow rate kept constant to maintain a process pressure of $25\,\mathrm{Torr}$. Throughout the CVD process, the microwave power is maintained at $900\,\mathrm{W}$ ($11.5\,\mathrm{W\,mm^{-2}}$). The diamond substrate has to reach a certain temperature range to allow for proper growth conditions. In this work, the substrate is heated to either $500\,^{\circ}\mathrm{C}$ or $700\,^{\circ}\mathrm{C}$ which translates to a pyrometer assessed plasma temperature of $540(10)\,^{\circ}\mathrm{C}$ or $740(10)\,^{\circ}\mathrm{C}$. Prior to introducing the carbon precursor, the H_2-only plasma conditions are maintained for $20\,\mathrm{min}$ ($500\,^{\circ}\mathrm{C}$) and $1\,\mathrm{h}$ ($700\,^{\circ}\mathrm{C}$) to etch away residual surface carbonaceous contaminants. According to previous estimations [128], the approximate etching depth of diamond is $\leq1\,\mathrm{nm}$.

The diamond growth starts by introducing the methane into the chamber. In contrast with the natural abundance carbon precursor, we use ^{12}C-purified methane ($99.999\,99\,\%$ chemical purity, $99.99\,\mathrm{at.}\%$ isotopic purity $^{12}CH_4$) in our process to grow isotopically purified diamond membranes. Although carbon nuclear spins can be used as quantum registers via hyperfine interactions

with nearby nitrogen vacancies [129, 130], the natural abundance of ^{13}C forms a spin bath that limits the spin coherence of the color centers. Therefore, a ^{12}C-isotopic purification of the diamond crystal could tremendously improve the electron spin coherence, which is crucial for quantum applications [131]. The injection of methane is verified *in-situ* via the increase of the pyrometer temperature reading: $765(10)\,^{\circ}\mathrm{C}$ for the $700\,^{\circ}\mathrm{C}$ set-point ($580(10)\,^{\circ}\mathrm{C}$ for the $500\,^{\circ}\mathrm{C}$ set-point). We note that the nitrogen and carbon isotope concentrations in overgrown diamond membranes are determined by the growth process instead of the seed substrate. Therefore, we choose more budget-friendly optical grade single crystal diamonds as seed substrates for membrane synthesis.

2.4 Color center formation, membrane patterning and undercut

2.4.1 Color center formation

The work uses two methods to generate color centers in diamond membranes. We perform ion implantation for some NV characterizations and all group IV centers work, and *in-situ* doping during growth for many other NV-related studies. Recent demonstrations focus on the *in-situ* doping of group IV centers that obtain uniform emitter properties [132]. That research could be integrated with the diamond membrane platform for more exciting directions.

Ion implantation We use the Stopping and Range of Ions in Matter software (SRIM) [122] to estimate the ion implantation depth and straggle. The incidence angle is set to 7° to avoid ion channeling. For color center incorporations, we implant $^{14}N^{+}$, $^{28}Si^{+}$, $^{74}Ge^{+}$ and $^{120}Sn^{+}$ at a dose of $2 \times 10^{8}\,\mathrm{cm}^{-2}$ into the membrane to achieve an individual-level color center density. Such a low density level allows us to accurately characterize the optical and spin coherence and estimate the conversion yield. Table 2.1 shows details about the implantation parameters and simulated depths and straggles. All of the implantation steps are followed with the three-step $1200\,^{\circ}\mathrm{C}$ anneal [124] to form color centers.

We estimate a creation yield of color centers by counting the number of fluorescent centers in a

Species	Energy [keV]	Dose [cm^{-2}]	Target depth [nm]	Straggle [nm]
$^{4}He^{+}$	150	5×10^{16}	413	39
$^{14}N^{+}$	48	2×10^{8}	60	15
$^{28}Si^{+}$	58	2×10^{8}	40	11
$^{74}Ge^{+}$	98	2×10^{8}	40	10
$^{120}Sn^{+}$	150	2×10^{8}	42	8

Table 2.1: Implantation parameters and SRIM simulation results for diamond membrane formation and color center generation.

certain area. For a $40\,\mathrm{h}$-growth sample which obtains a overgrowth thickness of $350\,\mathrm{nm}$ to $400\,\mathrm{nm}$, we reach a conversion yield of $6.6(4)\,\%$ for GeV^{-}, which is higher than the previous reported value [108]. The yield of SnV^{-} is $\approx 1\,\%$, indicating a less effective activation, which could be further improved by extending the annealing duration at $1200\,^{\circ}\mathrm{C}$ or increasing the annealing temperature [56].

***In-situ* doping and electron radiation** In addition to the ion implantation, *in-situ* doping is one of the most common methods for color center generation. Luckily, the diamond membrane fabrication technique is also amendable to *in-situ* δ-doping of ^{15}N [90]. δ-doping allows deterministic incorporation of dopants (N, Ge, Si, etc.) at a specific depth during membrane overgrowth. The incorporated species also provide a valuable distinction from the intrinsic, naturally abundant defects (i.e., isotopically incorporating ^{15}N during growth to be distinguished from the ^{14}N), which is beneficial for background growth impurity (^{14}N) estimation. This δ-doping method can also be utilized to generate group IV centers such as SiV^{-} or GeV^{-} via additional gas input, such as silane or germane [93, 133].

In this work, we perform a proof-of-concept growth by generating a $\approx 2\,\mathrm{nm}$-thick δ-doped layer of ^{15}N. This *in-situ* nitrogen doping is accomplished by introducing $^{15}N_2$ gas ($99.99\,\%$ chemical purity, $99.99\,\mathrm{at.}\%$ isotopic purity) for $2\,\mathrm{min}$ during the growth phase. The doped layer is covered by a $\approx 36\,\mathrm{nm}$-thick cap layer to protect the NV– coherence from surface noises. To convert doped nitrogen into NV^{-} centers, an electron radiation of $10 \times 10^{18}\,\mathrm{cm}^{-2}$ at $2\,\mathrm{MeV}$ is performed to form

vacancies throughout the diamond crystal. This is followed by a $6\,\mathrm{h}$ vacancy mobilization anneal at $850\,^{\circ}\mathrm{C}$ in forming gas ($96:4$ of Ar:H_2) to form the δ-doped $^{15}NV^{-}$ layer.

The concentrations of the overgrowth background [^{14}N] and *in-situ* doped [^{15}N] are determined via a separate quantitative secondary ion mass spectroscopy (SIMS) characterization. The nitrogen doping effectiveness ^{15}N for a triple delta-doped overgrowth sample is shown in Figure 2.4. The full-width-half-maximum (FWHM) of the Gaussian-fit curves is used as an approximation of the δ-doping layer thickness, whereas the amplitude is used as an approximation of the atomic density (cm^{-3}) within that layer. The SIMS detection limit of [^{14}N] places an upper bound on the background nitrogen contamination $4.5(2) \times 10^{15}\,\mathrm{cm}^{-3}$ ($\leq 26(1)\,\mathrm{ppb}$). For the $^{15}N_2$ flow rate used in our case, we obtain a [^{15}N] of $5.1(10) \times 10^{15}\,\mathrm{cm}^{-3}$ ($30.8(57)\,\mathrm{ppb}$) with a quoted ^{15}N detection limit of $1 \times 10^{15}\,\mathrm{cm}^{-3}$ ($5.7\,\mathrm{ppb}$).

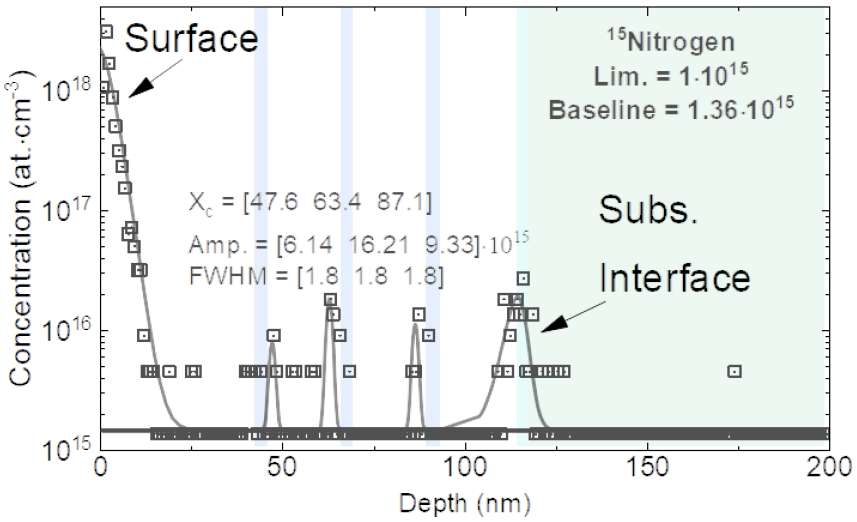

Figure 2.4: Nitrogen doping effectiveness ^{15}N for a triple δ-doped overgrowth sample. Fitting of the Gaussians is used to quantify the nitrogen density. The FWHM is used as an approximation of the delta-doping layer thickness, whereas the amplitude is used as an approximation of the atomic density (cm^{-3}) within that layer. The detection limit is shown in the graph. We also note a significant amount of nitrogen at the substrate/overgrowth and surface interfaces with ratios consistent with the natural abundance of ^{15}N in atmospheric nitrogen (measured via peak area ratio).

2.4.2 *Membrane patterning*

Diamond membrane substrates are patterned into many smaller membranes ($200\,\mu\mathrm{m}$ by $200\,\mu\mathrm{m}$ in size) before the undercut. This patterning step ensures short processing time per membrane and accelerates the optimization of the nanofabrication processes. The size of individual membranes is also sufficient for many cases, including color center characterizations, nanophotonic fabrications, and some quantum applications. We note that the size is not fundamentally limited, and membranes with various shapes and sizes (even the same size as the seed substrate [118]) can be generated via the same method.

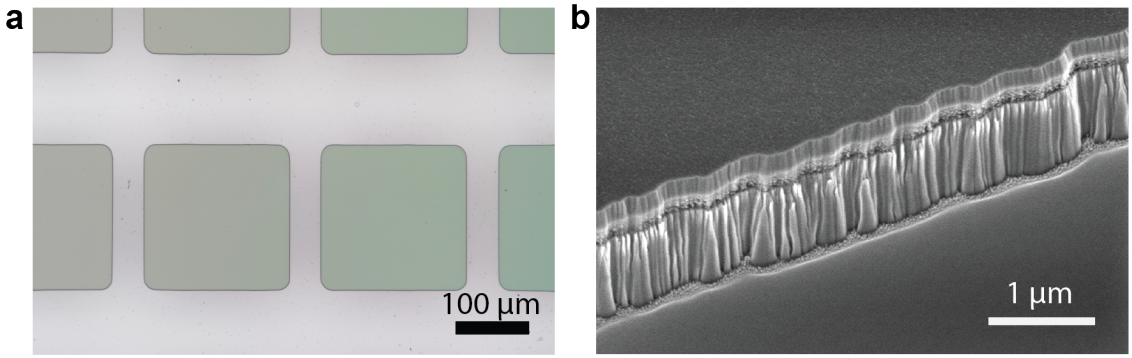

Figure 2.5: Individual membrane patterning. (a) Microscope image of a patterned diamond membrane. The graphitic layer at the area between membranes is etched through and thus transparent. (b) SEM image of a diamond sidewall post ICP etching. The amorphous graphitic layer is sandwiched between the crystal-like diamond membranes and substrates.

Individual membrane patterns are defined via photolithography. Before applying the photoresist, the membranes are deposited with alumina (Al_2O_3) via atomic layer deposition (ALD), which serves as the hard mask for diamond etching. To reduce the edge bead of the photoresist, we mount four sapphire substrates with a thickness comparable to that of the diamond to compensate for the height variation during resist spinning. After exposure and development steps, the pattern is transferred to the hard mask via Al_2O_3 etching in a chlorine-based ICP RIE chamber. Individual membranes are then patterned by applying O_2 plasma in the same chamber. The etching depth is deeper than the He^+ implantation depth to ensure that the graphitic layer underneath the membranes is exposed. The Al_2O_3 layer is then removed via acid cleaning, which also thoroughly cleans the

substrate, preparing for the electrochemical (EC) etching. The microscope image of the patterned membranes is shown in Figure 2.5 (a). Figure 2.5 (b) shows the scanning electron microscopy (SEM) image of the sidewall post ICP etching, with clear boundaries between the top diamond membrane, the graphitic layer, and the bottom diamond substrate.

2.4.3 Electrochemical etching

The central idea of the "smart-cut" method is to generate a uniform underneath layer with different material properties (mechanical/chemical, etc.) using ion implantation, which has been known to generate most vacancies at the end of the implantation trajectory. This underneath layer enables the detachment of the top layer from the substrate for subsequent material integration. In the context of diamond, the heavy He^+ implantation induces a phase transition of the carbon bonds from sp^3 to sp^2 (amorphous graphite), and this graphitic layer can be selectively removed via tri-acid cleaning or electrochemical (EC) etching. Compared with acid cleaning, EC etching offers an efficient undercut with better etching profile control, as the etching takes place at the region near the cathode.

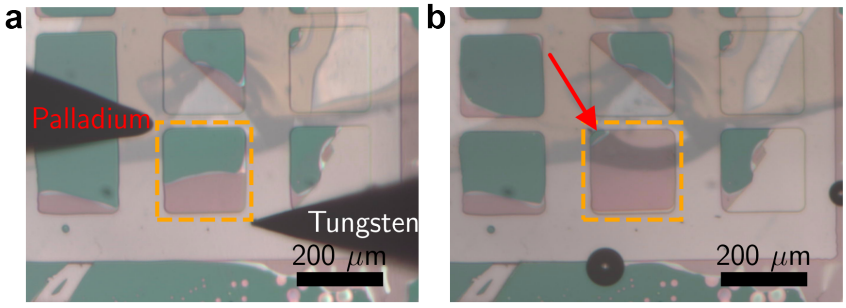

Figure 2.6: Electrochemical etching of a half- (almost) undercut membrane (dashed orange square) at the EC etching step. Both microscope images are taken when the membrane is in DI water. The left (right) electrode in (a) represents the palladium (tungsten) tip used as an anode and a cathode, respectively. The red arrow in (b) points to the membrane tether. The opaque graphitic layer exhibits interference colors (green), while the undercut region is almost transparent. The plate on the upper right indicates a leftover tether where the membrane has been picked up.

The mechanism of the EC etching has been thoroughly studied in previous literature [134, 135].

Most studies chose noble metals such as gold or platinum for the anode to avoid tip oxidation and deterioration. We utilize palladium for anodes due to its commercial availability. Tungsten tips are used as cathodes throughout the study. Typical microscope images of an ongoing EC etching are shown in Figure 2.6 (a)-(b). There are a few possible chemical reactions to describe the EC etching process [119]. Some chemical reactions are described as follows:

$$C_{(s)} + 2\,H_2O_{(aq)} \longrightarrow CO_{2(g)} + 4\,H^+_{(aq)} + 4\,e^-$$

$$C_{(s)} + H_2O_{(aq)} \longrightarrow CO_{(g)} + 2\,H^+_{(aq)} + 2\,e^-$$

$$C_{(s)} + 4\,H^+_{(aq)} + 4\,e^- \longrightarrow CH_{4(g)}$$

$$H_2O_{(aq)} \longrightarrow HO^{\bullet}_{(aq)} + e^- + H^+$$

Here, the "s", "aq", and "g" letters refer to solid (amorphous graphite), aqueous (liquid), and gaseous instances. As shown in the chemical equation, the EC etching generates gas, which has been observed as "bubbles" generated in water. The presence of air bubbles would typically block the view of the diamond membranes and raise the difficulty of estimating the etching progress. To circumvent this, we use freshly prepared de-ionized (DI) water for EC etching. Fresh DI water tends to have low carbon dioxide concentration, which can be utilized to absorb the EC etching-induced CO_2.

Unlike previous studies utilizing wet membrane transfer post EC etching [120], we apply dry etching to improve the transfer yield and precision, which will be discussed in the next section. To prevent membranes from total detachment during the EC etching, we always leave a tether on each membrane untouched to secure them in place when transferring the diamond substrate out of the water, as shown in Figure 2.6 (b).

2.5 Membrane transfer via bonding agents

Strong, high-yield material integration enables numerous post-fabrication possibilities and is thus crucial for a heterogeneous material platform. There are three main approaches to integrating thin films with carrier substrates. Small footprint material layers and devices, including two-

dimensional transition metal dichalcogenides (TMD), graphene, hexagonal boron nitride (hBN), and nanophotonic waveguides or cavities [108, 136, 137], benefit from Van der Waals forces between layers for heterostructure fabrications. However, the Van der Waals forces-based method is incompatible with devices with larger geometries, significant thicknesses, or built-in strain. Therefore, various bonding agents (photoresists, epoxy, fused oxides, etc.) are applied to generate stronger bonds between layers [95, 120, 138]. The third method, often called direct bonding or plasma-activated bonding, generates chemical bonds (in most cases, covalent bonds) at the bonding interface to enhance the bonding quality [139]. This method often requires pristine surface morphology at the bonding interface, which is challenging for nanostructures. Therefore, most demonstrations are focused on featureless plane film integration. With more than hundreds of micrometers in lateral sizes, the diamond membranes are not suitable for Van der Waals heterostructure fabrication but ideal for other bonding methods. The bonding agent-based transfer is discussed in this section, while the plasma-activated bonding will be described in the next section.

2.5.1 Diamond membrane pick-up and flipping

PDMS/PC method As discussed in the previous section, dry transfer could significantly improve the process yield and precision. Inspired by standard TMD materials integration [136], we develop a method based on polydimethylsiloxane (PDMS) - polycarbonate (PC) stacks. The stacks are mounted on a micropositioner which enables angle and position precision of 0.001° and $5\,\mu\mathrm{m}$, respectively. The PDMS is formed via a standard curing process, which involves mixing Sylgard 184 PDMS base and its curing agent, vacuum pumping, and subsequent baking, all taking place in a shallow Petri dish. Individual stamps are cut from the cured PDMS and placed on glass microscope slides. PC films are prepared from a PC solution (Sigma Aldrich Poly(Bisphenol A carbonate), $7\,\%$ solution in chloroform) and a pair of glass slides, which are then cut into small pieces and placed on PDMS stamps. The prepared PDMS/PC stacks are then mounted onto a computer-aided micropositioner (Signatone CAP - 946). As for the membrane pick-up process,

we slowly bring the stamp down and allow it to fully adhere to the target membrane. With a quick movement of the now-adhered stamp, we break the membrane from the tether. Then, we flip the membrane by replacing the substrate on the chuck with a second PDMS stamp on a glass slide (no PC film). The detached membrane can be deterministically transferred to this second stamp by slowly bringing the PDMS/PC stamp into contact with the “stickier" PDMS-only stamp and lifting the PDMS/PC stamp afterward. The schematic of this transfer process is shown in 2.7 (a), and the microscope images are shown in Figure 2.7 (b)-(c).

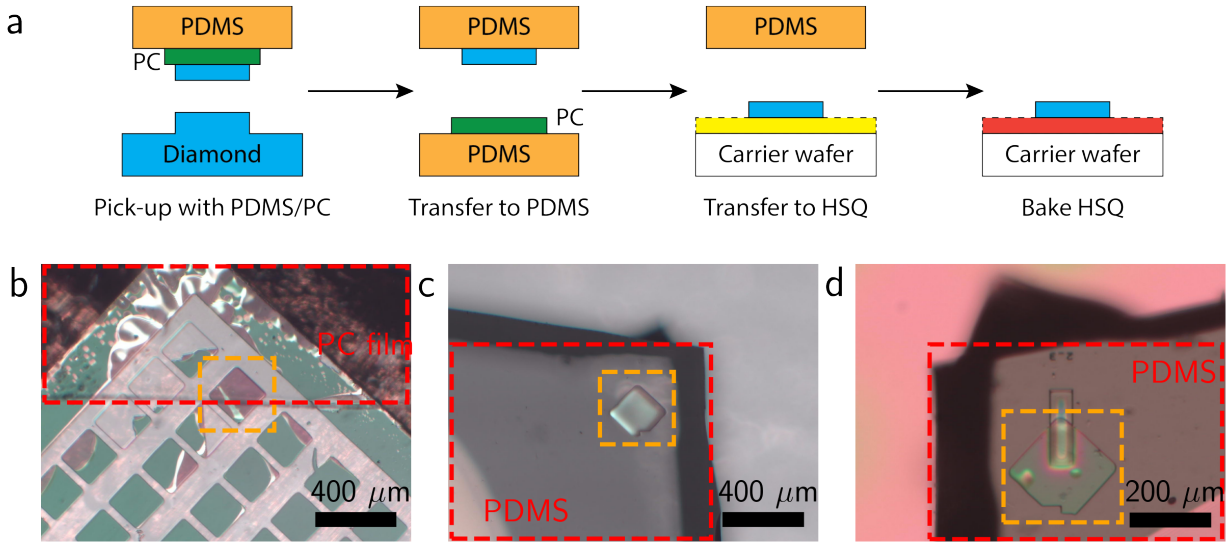

Figure 2.7: Diamond membrane transfer via the PDMS/PC method. (a) Schematics of the general membrane transfer process. The diamond is flipped during the process to remove the original membrane afterward. (b) The PDMS/PC stamp approaches the diamond membrane. The PC film (red dashed rectangle) is under a PDMS stamp, spanning beyond this image. The target membrane (orange dashed square) is linked to the diamond substrate via a small tether (see 2.6 (b)). (c) The membrane is transferred to a second, PDMS-only stamp (red dashed rectangle). (d) The membrane is attached to a resist-coated trench on a thermal oxide wafer. Contaminations under the membrane can be avoided by a cleaner PDMS/PC stamp preparation.

Patterned PDMS method The considerable size of membranes (over hundreds of micrometers) enables an alternative method for the pick-up and flipping processes. Instead of playing with the adhesion difference between PDMS and PC films, we can generate templated PDMS stamps with different footprints to ensure a deterministic transfer [137]. We start by depositing and patterning a

thick photoresist layer (SU-8 3050, $\approx 55\,\mu\mathrm{m}$ thick after baking) on a 4-inch silicon wafer. Then, we pour the mixed PDMS base and the curing agent on the patterned and baked silicon wafer, followed by the same PDMS-making process. The pattern is thus transferred from the SU-8 to each PDMS stamp. We can generate over 200 PDMS stamps with two different patterns in a single batch. The PDMS1-stamp consists of four little square-shaped contacting fingers with $70\,\mu\mathrm{m}$ spacing in order to break the diamond tether and pick up the membrane. The PDMS2-stamp contains a single large square with $300\,\mu\mathrm{m}$ length to flip and place the membrane. The schematic of the transfer process is shown in Figure 2.8 (a), with microscope images of the two stamps shown in Figure 2.8 (b)-(c).

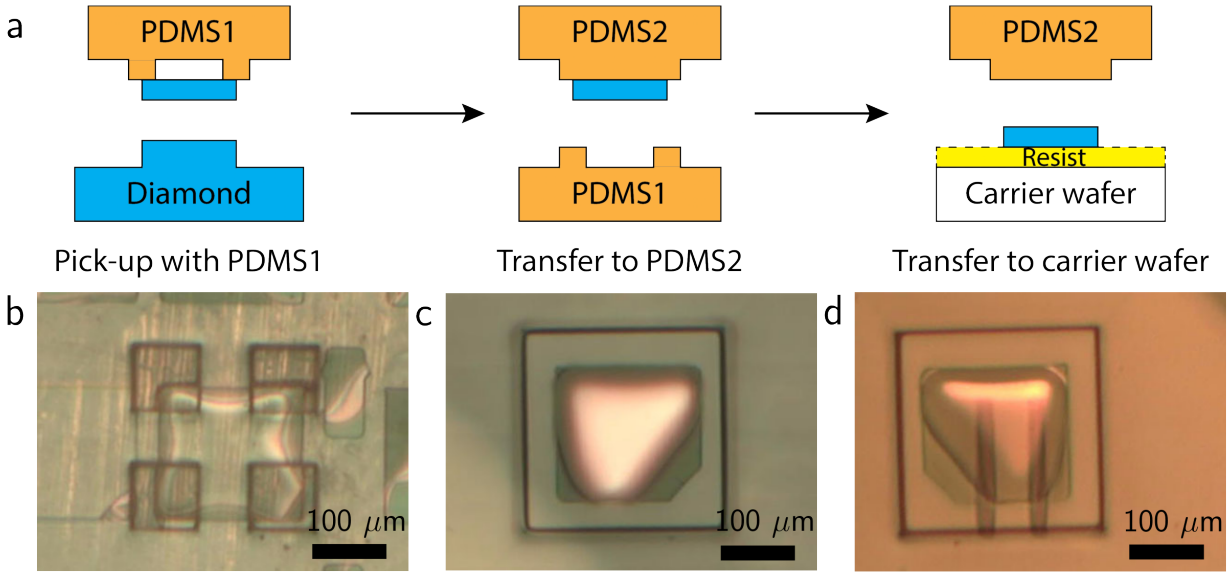

Figure 2.8: Diamond membrane transfer via patterned PDMS stamps. (a) Schematics of the membrane transfer with PDMS1-stamp and PDMS2-stamp. PDMS1-stamp is used to break the diamond tether and pick up the membrane, whereas PDMS2-stamp is used for flipping the diamond membrane from PDMS1-stamp and subsequent placement. (b-d) Microscope images of (b) alignment and pick-up of the diamond membrane using PDMS1-stamp, (c) the membrane flipping using PDMS2-stamp, (d) membrane placement onto a patterned carrier wafer coated with resist.

Compared with the PDMS/PC method, patterned PDMS stamps offer a few advantages. First, The shape and, thus, the contact region are defined lithographically instead of manually, which significantly improves the yield and accelerates the transfer process. Second, patterned PDMS stamps obtain limited contact areas. The prominence of the adhesion region, which is $50\,\mu\mathrm{m}$

taller than the rest of the stamp, ensures only the targeted membrane is contacted. This feature applies to both the diamond membrane substrate and the final target wafer, which prevents the "by-caught" issue induced by the PDMS/PC method (pick up undesired membranes or break half-etched membranes). Third, by only contacting the target membrane, this method enables multiple membrane transfers following EC etching, which, in the future, can be automated into a single step for picking up all membranes on the entire diamond substrate.

2.5.2 Membrane bonding with electron beam resist

Following the membrane pick-up and flipping, the next step is bonding diamond membranes with carrier wafers. In a previous study [120], polymethyl methacrylate (PMMA) was used as the bonding agent. Despite excellent adhesion, which assists bonding, PMMA is not chemically inert, preventing the bonded structure from being used for subsequent nanofabrication processes. Here, we use another electron beam resist, hydrogen silsesquioxane (HSQ), as the bonding agent, which forms strong bonds post baking [98]. To ensure deterministic membrane placement, we prepare the carrier wafer with a freshly spin-coated HSQ layer ($14\,\%$ or $14\,\%$ HSQ in methyl isobutyl ketone (MIBK) solution, DisChem Inc.) right before bonding. The schematics and microscope images for both PDMS/PC and patterned PDMS methods are detailed in Figure 2.7 (a), 2.7 (d), 2.8 (a) and 2.8 (d). We note that the bonding process is compatible with pre-patterned substrates. Therefore, some carrier wafers are patterned and etched to create suspended regions on diamond membranes. The suspension can effectively reduce the optical background from HSQ and enable double-sided surface termination via wet-chemical or dry processes using acid cleaning and oxygen annealing. To improve the bonding quality, the carrying wafer is annealed at $600\,^{\circ}\mathrm{C}$ for $8\,\mathrm{h}$ in argon environment post membrane transfer. The HSQ layer fully collapses during annealing, forming a nearly strain-free layer. The thickness of the HSQ can be tuned via the concentration of the HSQ solvents or resist spinning parameters. If the diamond membrane is partially suspended, the fluorescence background of the suspended region can be further reduced by introducing an additional vapor HF

treatment (Memsstar ORBIS ALPHA) to remove the HSQ in the trench. Finally, in order to etch the original damaged underlayer (the etched side of the membrane), improve surface morphology, and tune the final thickness, we apply a three-step ICP-RIE process to the mounted membrane. The ICP parameters are detailed in Table 2.2 [124]. We start with the "Ar/Cl_2" recipe ($2\,\mathrm{min}$ to $5\,\mathrm{min}$, depending on the target thickness) to improve the surface morphology. Then we use the "O_2/Cl_2" recipe ($30\,\mathrm{s}$ to $90\,\mathrm{s}$) to remove most of the chlorine-based compounds from the diamond surface. Finally, we apply a $30\,\mathrm{s}$ "O_2" etch to further remove the residual chlorine compounds and correctly terminate the surface while preventing the formation of micromasks [96]. To avoid chemical contamination, etching steps are separated by multiple pump-purge cycles. The microscope image of a bonded membrane on a pre-patterned fused silica substrate is shown in Figure 2.9.

Recipe name	Ar/Cl_2	O_2/Cl_2	O_2	Al_2O_3 etching
ICP power [W]	400	700	700	400
Bias power [W]	250	100	100	50
Pressure [mTorr]	8	10	10	5
Cl_2 flow [sccm]	40	2	0	0
Ar flow [sccm]	25	0	0	10
BCl_3 flow [sccm]	0	0	0	30
O_2 flow [sccm]	0	30	30	0
Etching rate [$\mathrm{nm\,min^{-1}}$]	≈73	≈177	≈175	≈63 (Al_2O_3)

Table 2.2: Cl-based ICP etching recipe for diamond. The last recipe, Al_2O_3 etching, is used for hard mask (ALD Al_2O_3) removal during the membrane patterning.

2.6 Direct bonding of diamond membrane

2.6.1 Direct bonding process overview

Direct wafer bonding is a mainstream method for integrating heterogeneous materials that are difficult to grow in heteroepitaxially. Since developed, this method has been widely utilized in silicon-based semiconductor industry and has been used to produce silicon-on-insulator (SOI) wafers [140], III-V-on-Si devices [141, 142], nitride materials [143], lithium niobate-on-insulator

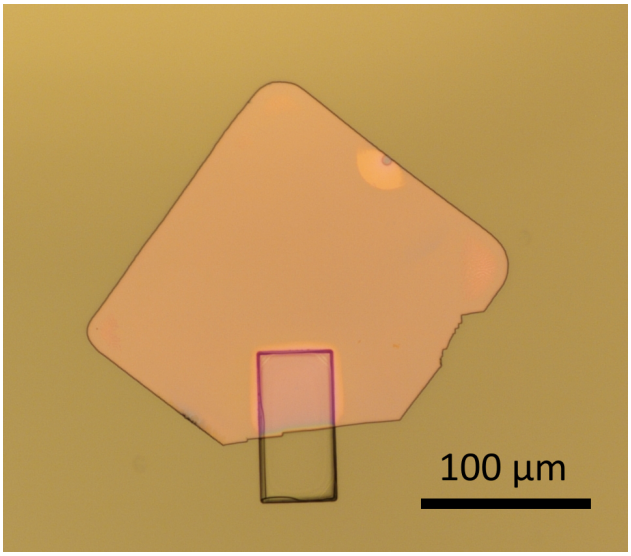

Figure 2.9: Microscope images of a transferred and back etched membrane on a fused silica wafer.

(LNOI) [144] and more. Compared with the fused oxide method [138], direct bonding features low-temperature operation with much more flexible material choices beyond oxides. Specifically, the direct bonding of diamond with various materials has been explored, mostly via wet surface functionalization [145, 146]. However, diamond membranes have huge aspect ratios and must be handled via carrier wafers to prevent bending and folding. This handling requirement precludes wet chemical processes (mainly acids) for surface functionalization. Alternatively, we utilize the all-dry plasma-activated bonding method to bond membranes. The overall schematics of the process are shown in Figure 2.10 (a)-(c), with the microscope images of the final bonded membranes shown in 2.10 (d). The membranes used for direct bonding share the same diamond membrane substrates for HSQ-based bonding purposes and thus obtain the same surface and material properties.

Membrane transfer to intermediate wafer Due to strictly better yield and performance, we use the patterned PDMS method for all membrane transfers in this section. However, instead of directly transferring the membrane to the HSQ-coated target wafer, now we transfer it to a photoresist-coated carrier substrate called “intermediate wafer”. The added intermediate wafer

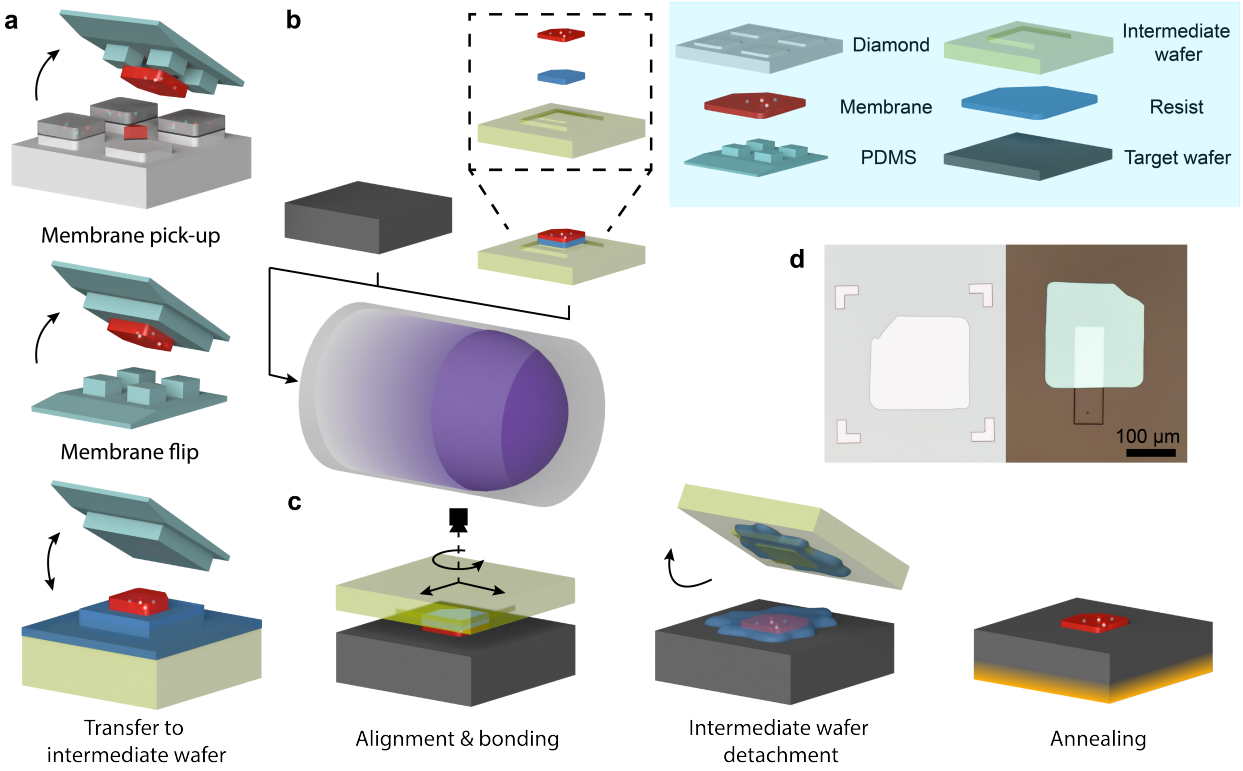

Figure 2.10: Overview of the membrane direct bonding. (a) Diamond membrane transfer to the intermediate wafer. From top to down: membrane pick-up from the diamond substrate using PDMS1-stamp, membrane flipping with PDMS2-stamp, membrane placement to a photoresist or electron beam resist covered intermediate wafer. (b) Diamond back etching and downstream oxygen plasma treatment. Inset: the detailed layer stack of the ICP-etched intermediate wafer. (c) Plasma-activated membrane bonding. Left to right: membrane alignment and bonding, temperature-controlled intermediate wafer detachment, and post-bonding annealing. (d) Microscope images of $155\,\mathrm{nm}$-thick diamond membranes bonded to a thermal oxide substrate with markers (left) and a fused silica substrate with a $5\,\mu\mathrm{m}$-deep trench etched before bonding (right).

offers a unique chance to remove the damaged layer before the final membrane bonding, which can also be applied to HSQ-based membrane transfer. The added flipping also results in a growth-side-up device, which eliminates growth-side morphology constraints for bonding and enables precise depth control for near-surface and δ-doped color centers. The schematic similar to Figure 2.8 (a) is shown in Figure 2.11 (a), with microscope images shown in Figure 2.11 (b)-(d). We note that the intermediate wafer is pre-patterned with a large central square to limit the bonding footprint and compensate for the residual approaching angle. Although intermediate wafers in this work are fabricated from fused silica substrates, in principle, any transparent substrates that

allow optical wafer alignment could serve as the intermediate wafer. The photoresists used to transfer membranes from PDMS2-stamps to intermediate wafers are AZ1505 and PMMA. They have different thermal and chemical properties, which will be discussed later in the section.

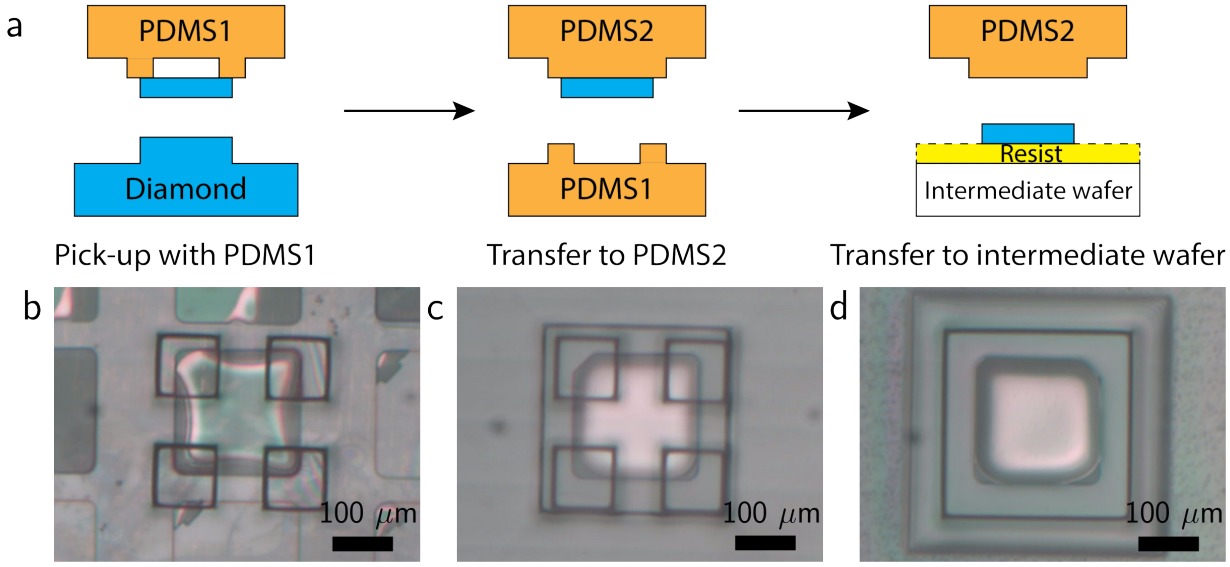

Figure 2.11: Deterministic diamond membrane transfer for direct bonding. (a) Schematics of the membrane transfer with PDMS1-stamp and PDMS2-stamp. (b-d) Microscope images of (b) alignment and pick-up of the diamond membrane using PDMS1-stamp, (c) membrane flipping using PDMS2-stamp, and (d) membrane placement onto the intermediate wafer coated with photoresist.

Prior to the surface functionalization, we first remove the underlying diamond layer that was damaged by the He^+ implantation. Unlike isotropically-etched diamond frames [108] or ICP-etched diamond slabs [96], smart-cut diamond membranes naturally contain out-of-plane strain originating from the lattice mismatch between the damaged layer generated from He^+ implantation and the subsequent overgrowth layer. This strain brings a curvature to freestanding membranes due to their high geometry aspect ratio (usually beyond 500) and has been observed in previous works [120]. The strain magnitude can be estimated by observing Raman features from both the damaged layer and the overgrowth layer ($100\,\mathrm{nm}$-thick here), as shown in Figure 2.12 (a). The experimental data is displayed as individual points, which can be fit by two Lorentzian curves. The original membrane (He^+ damaged layer) is indicated as the dashed blue curve with a center wave number

of $1326\,\mathrm{cm}^{-1}$, while the overgrowth layer obtains a center wave number of $1332\,\mathrm{cm}^{-1}$, labeled as the dashed orange curve. Differences in wave number indicate a $\approx 0.5\,\%$ lattice mismatch. In Figure 2.12 (b), a test membrane partially attached to a PDMS2-stamp is shown, with the upper and lower parts floated, as pointed by the red arrow. From the interference pattern, we can observe the extension of the original layer and the compression of the overgrowth layer, leading the membrane to be curved up.

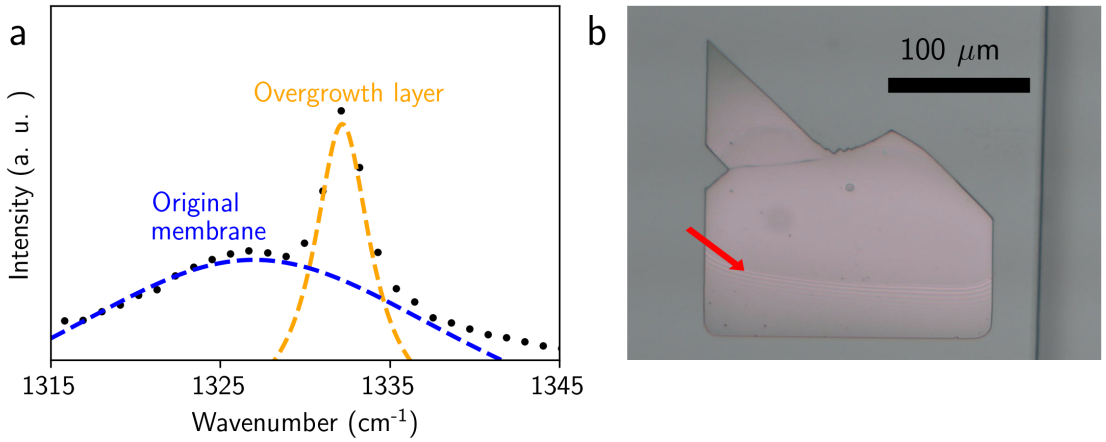

Figure 2.12: The out-of-plane strain in smart-cut diamond membranes. (a) Raman spectroscopy of a transferred membrane prior to the ICP etching. The raw data (black dots) can be qualitatively fitted by two separate peaks, the damaged (dashed blue line) and the overgrown (dashed orange line) layers. (b) A microscope image of a curved membrane on a PDMS2-stamp. The interference pattern is pointed out by the red arrow, which originates from the air gap between a curved membrane and a flat PDMS surface.

In addition, the removal of the damaged layer improves the overall crystallographic quality and fully decouples the final membranes—isotopically purified with controlled doping—from the low-cost type-IIa diamond substrate, which reduces a considerable fluorescence background from the damaged layer and improves the signal to noise ratio for most optical measurements. This step also defines the final membrane thickness. The actual thinning is performed via multi-cycle ICP-RIE, a similar process for etching HSQ-bonded membranes but with etching duration limited to $15\,\mathrm{s}$ per cycle to prevent the resist from overheating, crosslinking, or softening.

Surface plasma activation Unlike ICP-RIE plasma etching which is dominantly used for substrate etching with no sign of surface functionalization, surface activation utilizes downstream plasma ashing that has negligible etching rates due to the remote plasma generation mechanism. There are multiple gas options for surface plasma activation, including N_2, Ar, and O_2 [147–149]. We choose O_2-based plasma due to their better performance on diamond and other materials [150, 151]. Both diamond membranes and target substrates receive plasma treatments at room temperature to prevent degradation from elevated temperatures and enhance the bonding quality. Temperature dependence on plasma treatment effectiveness can be quantitatively measured via contact angle measurements, which will be discussed in the following subsection.

In this work, we investigate two recipes of downstream plasma ashing for surface activation. One recipe is the standard O_2 descum (gas flow $100\,\mathrm{sccm}$, RF power $200\,\mathrm{W}$ for $25\,\mathrm{s}$) which is usually used for photoresist clean-up post developing. The second recipe is a customized high-power ashing (gas flow $200\,\mathrm{sccm}$, RF power $600\,\mathrm{W}$ for $150\,\mathrm{s}$) to enhance the plasma effectiveness, with doubled or tripled process duration for some inert materials (sapphire, lithium niobate, Yttrium iron garnet, etc.). Although surface activation of only one bonding interface is viable, we prefer to prepare both interfaces for most device preparations. Diamond membranes are usually treated with the O_2 descum to minimize the contamination from the chamber, while carrier substrates receive the high power process to improve the plasma effectiveness (hydrophilicity). Detailed analysis of plasma treatments on surface morphology, hydrophilicity, and chemical elements are discussed in the following subsection. We note that plasma treatments also affect the optical background and the charge stability of the color centers hosted in the diamond membranes. They will be further discussed in Chapter 5.

Bonding process of diamond membranes In contrast to the diamond membrane transfer based on the adhesion difference between PDMS stamps and HSQ-coated substrates, the direct bonding involves two substrates—intermediate and target wafers—with limited adhesion flexibility. Alternatively, we realize the bonding process by utilizing the material properties of photoresists at

different temperature stages. Specifically, we spin-coat intermediate wafers with a thin layer of positive resists, which obtains much-reduced viscosity after reaching the softening temperature. The softening process grants a smooth detachment in heated environments after the membrane bonding. Two types of resists are used in this work. The photoresist is AZ1505 (Microchemicals GmbH) with $500\,\mathrm{nm}$ thickness which obtains a softening temperature (glass transition temperature T_g) between $100\,^{\circ}\mathrm{C}$ and $110\,^{\circ}\mathrm{C}$. The other is the 950 K PMMA A4 (Microchemicals GmbH) which has a T_g between $95\,^{\circ}\mathrm{C}$ to $106\,^{\circ}\mathrm{C}$. The resists are interchangeable for most bonding scenarios, but removing AZ 1505 after the bonding process requires acid cleaning, which is incompatible with some specific substrates and devices.

With both the intermediate wafer carrying ICP-etched diamond membrane and the target wafer treated with plasma, we continue and perform the bonding process. The schematics are shown in Figure 2.13 (a). First, we mount the patterned intermediate wafer onto a micropositioner-controlled glass slide via a flat, chip-size PDMS stamp. We secure the target substrate to a temperature-controlled stage. Due to the configuration of the micropositioner, only one tilting angle can be set to 0°. Therefore, the overall approaching angle is a small ($\leq 2^{\circ}$) but weakly defined value. Future utilization of dedicated wafer-bonding equipment will significantly improve the precision, tolerance, and device yield of all transfer steps. Leveraging optical access through the transparent intermediate wafer for alignment using a bright-field camera, we move the membrane to the target location and bring it close to the substrate. The alignment precision is $30\,\mu\mathrm{m}$, and the in-plane angle precision is 0.1°, both limited by the micropositioner tilt angle mentioned above. Post alignment, we slowly bring down the intermediate wafer until part of the membrane is in contact with the target substrate, indicated by the appearance of an interference pattern as exemplified in Figure 2.13 (b). We then step-wise increase the temperature beyond the T_g ($75\,^{\circ}\mathrm{C}$, $95\,^{\circ}\mathrm{C}$, and $125\,^{\circ}\mathrm{C}$ for AZ 1505, $90\,^{\circ}\mathrm{C}$, $130\,^{\circ}\mathrm{C}$, and $170\,^{\circ}\mathrm{C}$ for PMMA), allowing the resist to reach thermal equilibrium at each stage to enable a smooth resist re-flow. We note that abrupt temperature changes can cause undesirable resist re-flow across regions and impact the bonding quality. Once the temperature

reaches the highest stage, the resist layer thoroughly softens, and the intermediate wafer tends to shift translationally to release the stress, as shown in Figure 2.13 (c). Next, the intermediate wafer is slowly moved away from the membrane and lifted via the motorized stage, leaving the membrane on the target substrate covered by some residual resist, as shown in Figure 2.13 (d). Finally, the bonded heterostructure is left to cool down till room temperature, preparing for the subsequent annealing to enhance the bonding strength. Stripping the resist before annealing could potentially cause the membrane to detach due to the poor bonding quality at this point.

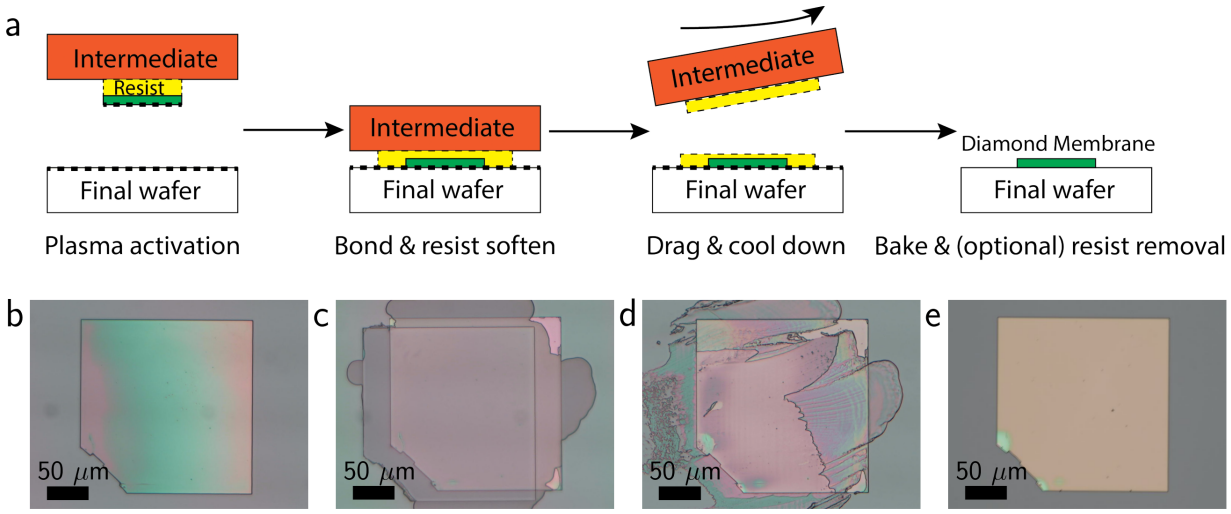

Figure 2.13: Plasma-activated membrane bonding. (a) Schematics of the direct bonding process. (b)-(e) Microscope images of (b) membrane alignment and initial contact. The interference pattern is induced by a non-zero approaching angle. (c) The membrane is bonded to the target wafer with resist re-flow at or above glass transition temperatures. (d) The bonded membrane with residual resist after lifting the intermediate wafer. (e) The membrane post baking and (optional) resist removal. Here, the AZ 1505 photoresist was applied, which requires a di-acid clean, but the PMMA-based bonded membrane requires no further cleaning post annealing.

Post bonding treatments The quality of the plasma-activated bonding highly depends on the formation of the covalent bonds, which can be greatly strengthened by additional annealing. The annealing can also remove the $-$OH bonds inside the bonded interface if present [150, 151]. Here We anneal the heterostructure at $550\,^{\circ}\mathrm{C}$ for $8\,\mathrm{h}$ to $14\,\mathrm{h}$ under argon forming gas environment ($96\,\%$ of Ar, $4\,\%$ of H_2 at atmosphere) to minimize undesired oxidation. We note that the bonding

strength when annealed at $450\,^{\circ}\mathrm{C}$ is insufficient, showing membrane detachment from the carrier substrate during the acid cleaning. This phenomenon might be explained by a less inert diamond surface to oxygen when the temperature exceeds $450\,^{\circ}\mathrm{C}$, which is approximately the temperature for standard diamond oxygen termination [78].

For the case of PMMA-based bonding, this annealing also removes the residual resist and leaves a clean direct-bonded membrane as the final product [152], which is gentle and compatible with acid-sensitive substrates. Microscope images of diamond membranes bonded to thermal oxide and fused silica wafers are shown in Figure 2.10 (d), revealing a high alignment accuracy and the compatibility of bonding membranes to structured materials. A regular bonded device using AZ1505 is shown in Figure 2.13 (e). The overall process yield stands above $95\,\%$, limited by inconsistent plasma ashing chamber conditions and the poorly controlled approach angle of the transfer station, which can be readily improved by transitioning to process-specific tooling.

The compatibility of post-nanofabrication is an important aspect of the bonded structures. We observe that our bonded membranes are compatible with isopropyl alcohol, acetone, potassium, or tetramethylammonium hydroxide (TMAH) based developers (such as AZ 300 MIF or AZ 400K), heated ($80\,^{\circ}\mathrm{C}$) N-Methyl-2-pyrrolidone (NMP), and room temperature NanoStrip. However, the tri-acid cleaning (1:1:1 H_2SO_4:HNO_3:$HClO_4$ at refluxing temperature), hot ($\geq 80\,^{\circ}\mathrm{C}$) Piranha (3:1 H_2SO_4:H_2O_2), and hot NanoStrip may damage the bonds and loosen the membranes from the target wafer. Future process development is needed to be compatible with these strong chemicals.

2.6.2 Plasma treatment analysis

Contact angle The effectiveness of the plasma surface activation can be characterized by tracking the change in surface hydrophilicity of the bonding interfaces via contact angle measurements [153, 154] on diamond and target wafer surfaces (Kruss DSA100A dropped shape analyzer). We use single crystal diamond substrates ($3\,\mathrm{mm}$ by $3\,\mathrm{mm}$) in this experiment due to the limited resolution of the water drops and the camera. To be consistent with the footprint of measured substrates,

the dispense rate is set to $2.67\,\mu L\,s^{-1}$, which translates to a typical droplet size between $4\,\mu L$ to $5\,\mu L$. Figure 2.14 (a)-(b) show the contact angle analysis of diamond and thermal oxide substrates before and after high-power plasma ashing. For the diamond surface, the contact angle reduces from $52.4° \pm 0.7°$ to $6.1°$. Similarly, the thermal oxide shows a reduction of contact angle from $101.15° \pm 0.05°$ to $8.2°$, indicating a considerable increase of hydrophilicity and thus better plasma-activated bonding quality [155]. In contrast, there is no noticeable change in the contact angle post ICP-RIE etching, demonstrating fundamental differences in surface preparation between the two methods.

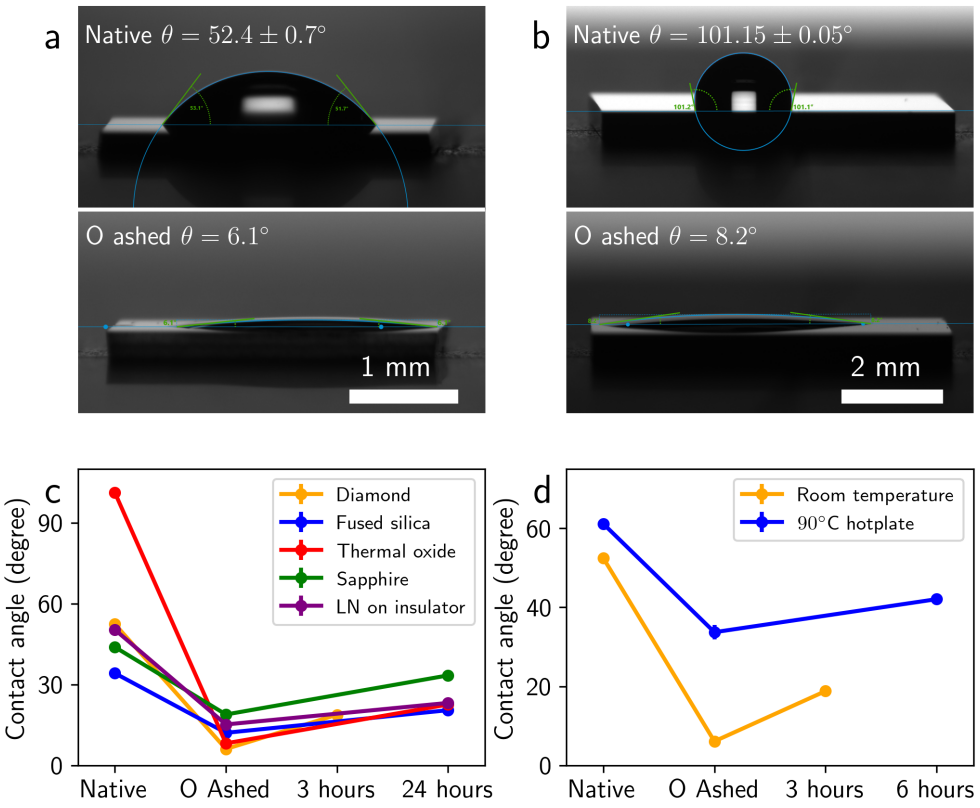

Figure 2.14: Surface hydrophilicity characterization via contact angle measurements. (a)-(b) Contact angles of native (top) and high-power plasma-treated (bottom) diamond and thermal oxide substrates. (c) Aging of hydrophilicity on various substrates. (d) The hydrophilicity of diamond surface with (blue) or without (orange) $30\,s$ baking on a $90\,°C$ hotplate.

We characterize the aging of the plasma treatment by tracking the contact angle of various substrates over time. The substrate list includes diamond, fused silica, thermal oxide, sapphire, and

lithium niobate on insulator (LNOI). The degradation of hydrophilicity shown in Figure 2.14 (c) indicates the need for a timely bonding process. In addition, we tested the temperature dependence of the hydrophilicity by baking the plasma-treated diamond sample on a $90\,^{\circ}\mathrm{C}$ hotplate for $30\,\mathrm{s}$ before the contact angle measurements. Contact angles in Figure 2.14 (d) show a hydrophilicity decay, possibly due to the loss of surface-absorbed water molecules. Guided by this observation, all plasma treatments are performed at room temperature.

X-ray photoelectron spectroscopy (XPS) XPS is another method to quantitatively characterize the plasma treatment by detecting the near-surface chemical bonds. First, we note that the plasma treatment results in a reduction of surface amorphous carbon sp^2 bonds as quantified by the more reliable D-parameter extrapolation of the C KLL line [156, 157]. Furthermore, the decrease from the raw C 1s quantification (likely an increase of ether-like terminations [78]) and an increase of surface available sapphire-O bonds indicate an effective surface preparation and oxygen termination to both surfaces, as shown in Figure 2.15. Similar behavior is confirmed on all other target bonding materials with observed contact angles below 20° post treatments.

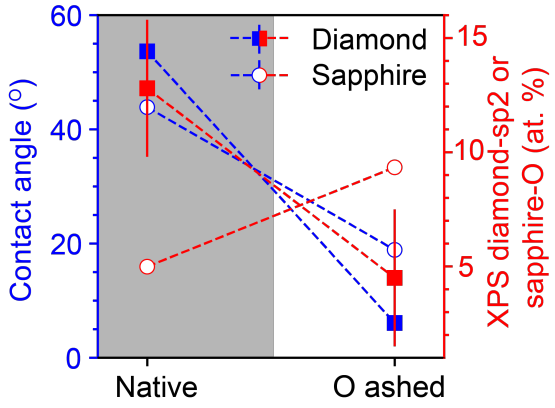

Figure 2.15: The contact angle and XPS of diamond and sapphire pre- and post-high-power plasma treatments. An increase in hydrophilicity is observed via the decrease in the contact angle. The effect of oxygen termination is observed through the reduction of the carbon sp^2 as obtained from C KLL extrapolation of the sp^2/sp^3 ratio and the enhancement of the sapphire-O signals as obtained from the O 1s peak quantification.

Surface morphology of carrier wafers Another critical factor for successful bonding is the surface morphology on both the diamond membrane and the carrier wafer. Ideally, both surfaces would obtain a roughness of less than $1\,\mathrm{nm}$. In this paragraph, we focus on the impact of downstream plasma asher recipes on carrier wafers. The diamond membrane side will be discussed in the next section. The surface morphology is investigated via AFM. Both small ($200\,\mathrm{nm}$ by $200\,\mathrm{nm}$) and large ($10\,\mu\mathrm{m}$ by $10\,\mu\mathrm{m}$) scale scans are applied to capture features of various sizes. Here, two widely used carrier substrates are analyzed: fused silica and thermal oxide silicon. Values of surface roughness R_q are shown in Table 2.3. Both wafers exhibit sub-nm R_q out of the box, and their surface morphology is maintained after the ashing step with no correlation to power or duration settings. Therefore, we conclude that our plasma recipe has no significant effect on the surface morphology of these carrier wafers.

Carrier wafer type	AFM area	No plasma	O_2 descum	Custom O_2 plasma
Fused silica	200 nm x 200 nm	0.324 nm	0.281 nm	0.366 nm
	10 µm x 10 µm	0.685 nm	0.581 nm	0.528 nm
Thermal oxide	200 nm x 200 nm	0.257 nm	0.290 nm	0.352 nm
	10 µm x 10 µm	0.270 nm	0.427 nm	0.293 nm

Table 2.3: Surface roughness R_q of fused silica and thermal oxide wafers under various plasma recipes.

2.6.3 Bonded interface analysis

The quality of the bonded diamond can be directly studied using high-resolution transmission electron microscopy (HRTEM), which obtains an atomic-level understanding of the bonding interface. Figure 2.16 (a) shows a cross-sectional image of a $10 \pm 0.3\,\mathrm{nm}$-thick diamond membrane bonded to a C-axis (0001) sapphire substrate. The diamond membrane is ICP-thinned from $\approx$309 nm post bonding. The thinness and uniformity shown in the figure reflect the high level of process control and allow the single field-of-view characterization of both diamond membrane interfaces. The image reveals several critical features. First, the membrane exhibits uniform crystallinity and morphology throughout its thickness. Second, we observe a sharp, sub-$0.5\,\mathrm{nm}$ interface between the

crystalline diamond and sapphire. Third, there is a repeating atomic arrangement throughout the interface profile, strongly indicating a covalently crosslinked interface [158–161].

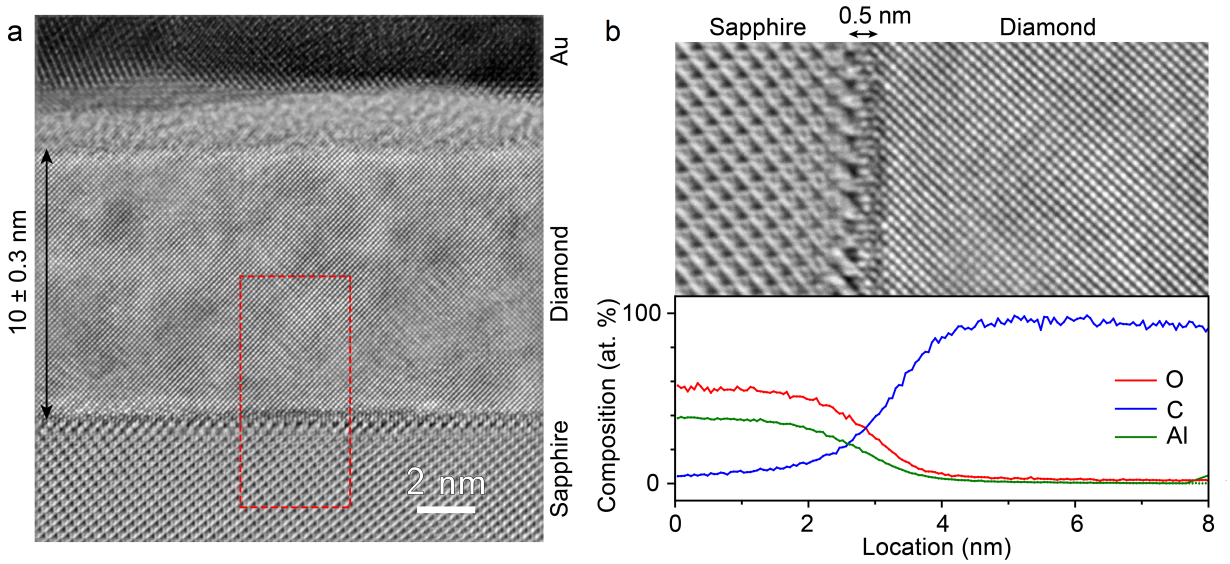

Figure 2.16: HRTEM of the bonded diamond interface. (a) HRTEM image of a $10\,\mathrm{nm}$-thick membrane bonded to a c-plane sapphire substrate. The $2\,\mathrm{nm}$ intermediate layer on top of the diamond comes from the lack of surface control before gold deposition, which is designed to protect the diamond membrane from being damaged by the Ga ion beam used for specimen preparation. (b) Top: the zoomed-in HRTEM image of the diamond-sapphire bonding interface, the red dashed rectangle region in (a), showing a sub-$0.5\,\mathrm{nm}$ thickness of the bonding intersection. Bottom: EDS elemental analysis across the bonding interface.

An alternative method to characterize the bonding interface is the Energy Dispersive X-ray Spectroscopy (EDS) analysis, which detects various elements associated with the intersection. In our case, we focus on C, Al, and O. The scanning transmission electron microscope (STEM) image and the STEM-EDS mapping are shown in Figure 2.17, with the summary figure shown in Figure 2.16 (b). The analysis places an upper limit on the bonding interface to be less than $2\,\mathrm{nm}$. We note that the EDS analysis artificially broadens the interface due to the slight angular mismatch between the electron beam depth projection and the actual physical interface.

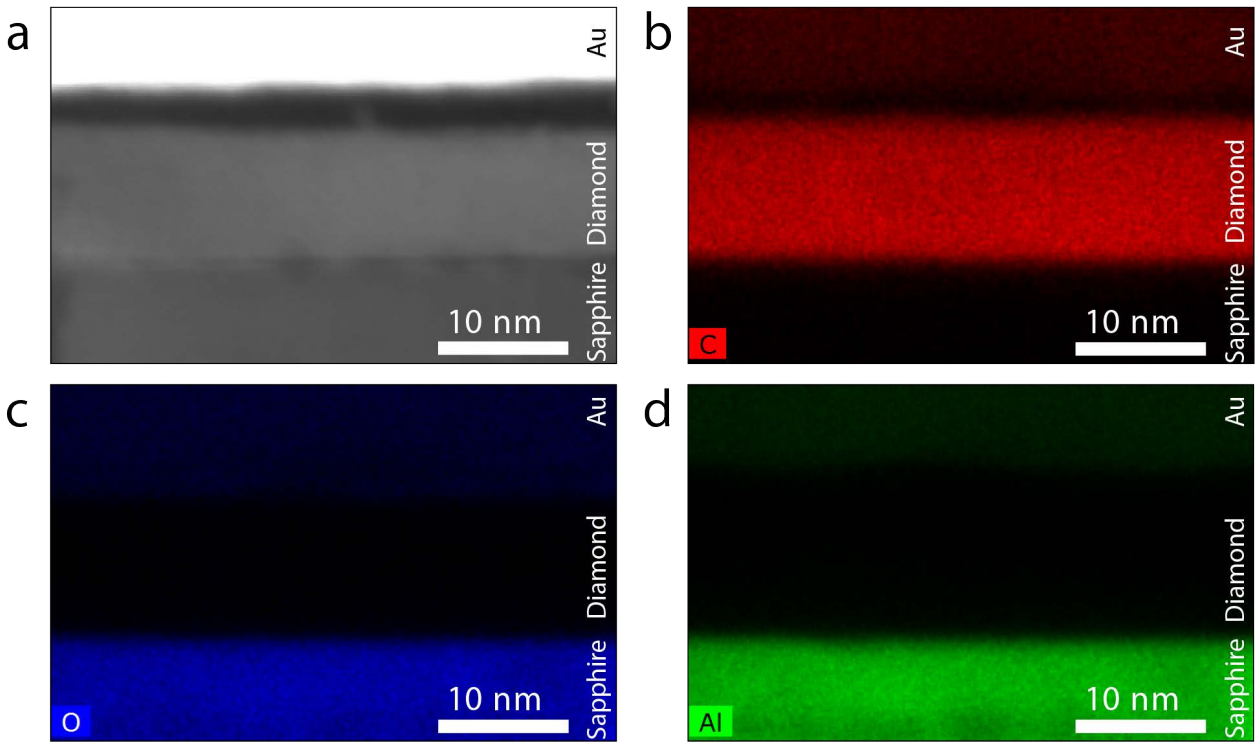

Figure 2.17: Additional atomic scale analysis of the bonded membrane. (a) HAADF-STEM of the diamond-sapphire heterostructure. (b)-(d) STEM-EDS elemental analysis of the diamond-sapphire heterostructure. The intensity plots of carbon, oxygen, and aluminum elements at the cross-section are shown in (a), (b), and (c), respectively.

2.7 Material characterization

2.7.1 Isotopically-purified overgrowth

The isotope engineering of diamond is realized by managing the ratio of methane gases with different carbon isotopes ($^{12}CH_4$ and $^{13}CH_4$) during the growth process. The concentration of the ^{13}C nuclear spin bath in diamond can have multiple implications for quantum technology studies. Firstly, the nuclear spin bath induces spin-spin interactions with the target qubits—NV^- or SiV^-—and reduces their spin coherence time [67]. Secondly, the ^{13}C nuclear spin in the vicinity can serve as quantum memory [129], which can be further utilized for error correction purposes [45]. The research performed in this work focuses on the limit of the minimal nuclear spin environment by using only $^{12}CH_4$ during the membrane overgrowth to realize the highest achievable qubit coher-

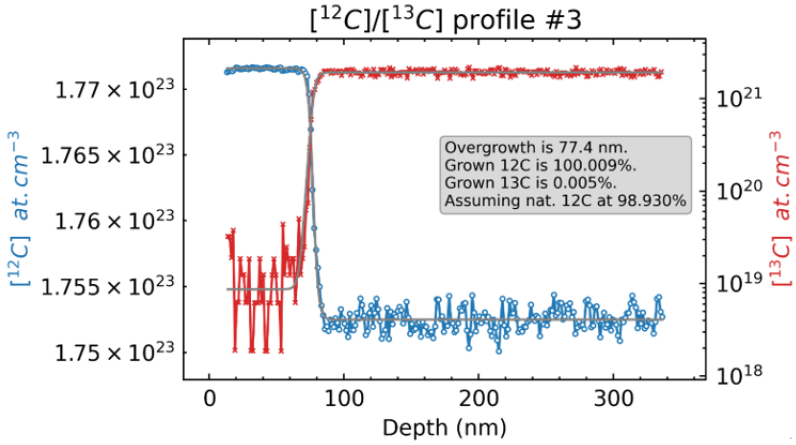

Figure 2.18: SIMS characterizations of a typical isotopically enriched diamond growth showing $99.99\,\mathrm{at.\%}$ ^{12}C diamond.

ence as a metric of the diamond membrane quality for quantum applications. Other nuclear spin concentrations for various purposes are achievable and will be investigated in subsequent studies. The quality of the ^{12}C enrichment is characterized via secondary ion mass spectrometry (SIMS). A typical carbon isotope scan of an overgrown layer on bulk diamond using $^{12}CH_4$ is shown in Figure 2.18 (a). We note that $99.99\,\mathrm{at.\%}$ ^{12}C concentration can be achieved reproducibly during growth, which is two orders of magnitude reduction of ^{13}C compared to natural abundance. This number is currently limited only by the isotopic enrichment of the precursor CH_4 gas and can be further improved.

2.7.2 *crystal quality*

The crystal quality of diamond can be characterized via room temperature Raman spectroscopy. As discussed in Figure 2.12 (a), He^+ implantation introduces crystal strain and lattice damage to the diamond, showing as downshifted and broadened Raman peaks. Through careful CVD growth parameters calibration, the overgrown diamond can have much better crystallinity, as shown by the narrow and upshifted Raman peaks compared with the damaged layer. In our characterization, a $633\,\mathrm{nm}$ excitation laser is used instead of the more popular $532\,\mathrm{nm}$ to avoid broad fluorescence

from NV^- centers in the substrates. The finest grating ($1800\,\mathrm{gr\,mm^{-1}}$) is used for data collection, which acquires a quoted resolution of $\approx 0.3\,\mathrm{cm^{-1}}$.

An appropriate reference diamond is critical for the crystal quality characterization. The reference we use is an electronic grade, single-crystal diamond from Element Six, which obtains pristine crystal quality with minimal impurity concentration. Furthermore, we ICP-etch the top $\approx 5\,\mu\mathrm{m}$ of the diamond substrate and subsequently anneal it to remove the residual strain induced by surface polish [78, 124]. The absence of strain variation provides the narrowest possible Raman linewidth ($1.570(1)\,\mathrm{cm^{-1}}$ at $1331.65\,\mathrm{cm^{-1}}$) for the subsequent crystallinity comparison, shown as the yellow curve in Figure 2.19.

The Raman features of overgrown membranes are shown in the same figure. The membrane with an $\approx 185\,\mathrm{nm}$ overgrowth layer ($20\,\mathrm{h}$ growth in $500\,^\circ\mathrm{C}$, back-etched down to $100\,\mathrm{nm}$) presents a Raman linewidth of $1.779(5)\,\mathrm{cm^{-1}}$ (green curve), slightly larger than the reference value. Remarkably, the isotopically purified, $\approx 370\,\mathrm{nm}$ overgrowth membrane ($40\,\mathrm{h}$ growth in $500\,^\circ\mathrm{C}$, back-etched down to $110\,\mathrm{nm}$) obtains a linewidth of $1.375(2)\,\mathrm{cm^{-1}}$, which is significantly lower than anything (including the reference bulk diamond) reported previously [118]. This ultra-narrow Raman peak indicates the crystal is free of impurities and defects. Additionally, the up-shifted and narrow peak, in comparison with the bulk spectra, is consistent with the change of the Raman transition via isotopic purification of a high-quality diamond structure [162]. Therefore, the Raman spectra indicate that these diamond membranes are of ideal crystal quality to host coherent color centers for quantum applications.

2.7.3 surface morphology

Another material property of diamond membranes is surface morphology. Uneven surfaces can form various dangling bonds and charge traps that significantly impact the surface termination and the spin coherence of near-surface color centers [78]. The surface roughness also determines the bonding quality of direct-bonded diamond membranes. To systematically characterize the surface

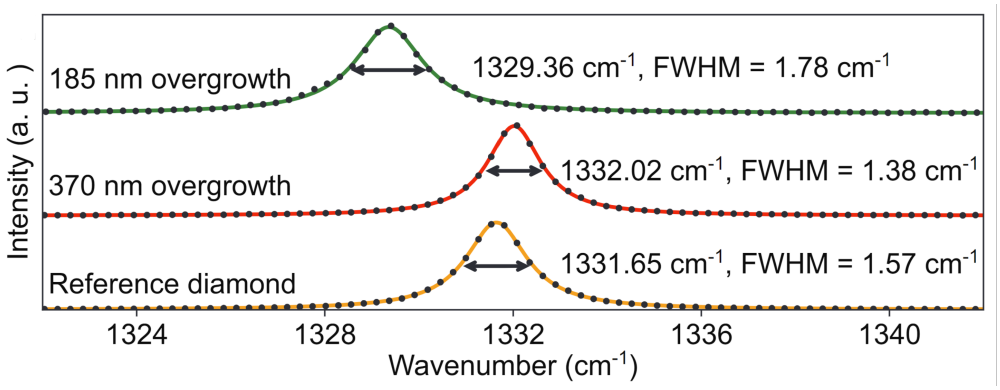

Figure 2.19: Room temperature Raman spectroscopy of diamond membranes and the reference diamond substrate. Green: The $\approx$185 nm (20 h) overgrowth membrane back-etched down to 100 nm. Red: The $\approx$370 nm (40 h) overgrowth, isotopically purified membrane back-etched down to 110 nm. Yellow: A surface strain-released, electronic grade single crystal diamond used as the reference.

roughness of diamond membranes, we apply atomic force microscopy (AFM) at every fabrication step. A summary of the roughness R_q is shown in Table 2.4, with the AFM images of the final diamond membrane shown in Figure 2.20.

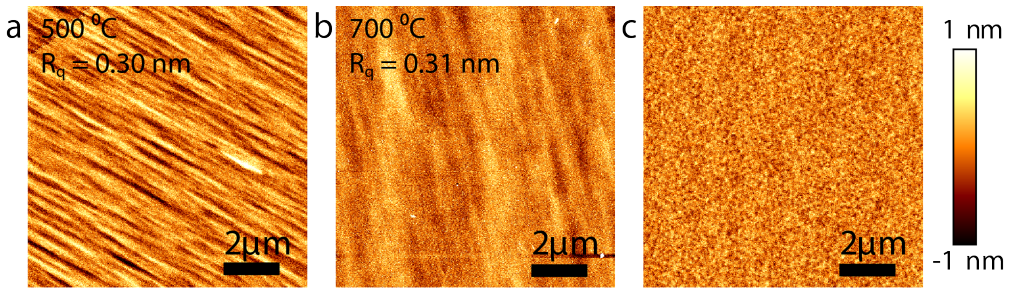

Figure 2.20: Surface morphology of diamond membranes. (a-b) AFM images of overgrowth patterns (as-grown side of membranes) at different heating plate temperatures. (c) An AFM image on the etched side of the membrane after multi-step etching.

To realize scalable and affordable membrane synthesis, we choose type 2a, optical grade single crystal diamonds as seed substrates, which has a surface roughness R_q of $\sim$30 nm with numerous polish defects. To minimize the growth defect concentration and improve the membrane surface morphology. we apply another fine-polish step to reduce the roughness to $Rq = 0.30$ nm. Additionally, this fine polish step ensures the final surface miscut (relative angle to the crystallographic (001) axis) is within $\leq 3^\circ$. Although this value is relatively consistent within a single substrate

Fabrication step/condition	AFM area	surface roughness R_q (nm)
As-purchased	10 µm x 10 µm	∼30 nm
Fine-polished	10 µm x 10 µm	0.2 nm
He^+ implanted and annealed	10 µm x 10 µm	0.27 nm
Overgrowth performed at 500 °C	10 µm x 10 µm	0.30 nm
Overgrowth performed at 700 °C	10 µm x 10 µm	0.31 nm
Overgrowth with excessive H etching	10 µm x 10 µm	0.69 nm
Overgrowth with surface contamination	10 µm x 10 µm	18.6 nm
Membrane post transfer	10 µm x 10 µm	1.17 nm
ICP etching with only Ar/Cl_2 step	200 nm x 200 nm	0.54 nm
Post complete ICP etching	10 µm x 10 µm	0.3 nm
ICP etching with only O_2 step	5 µm x 5 µm	6.78 nm
ICP-etched membrane with O_2 descum	200 nm x 200 nm	0.28 nm
ICP-etched membrane with strong O_2 ashing	200 nm x 200 nm	0.84 nm

Table 2.4: Surface roughness R_q of diamond membranes at different fabrication steps. The growth side is colored in blue, while the etched side is colored in red.

batch, it can vary between substrate batches, affecting the effective implantation angle and overgrowth characteristics [91]. The fine-polished substrates are subject to the He^+ implantation and annealing. Although the implantation creates a phase change of carbon covalent bonds from sp^3 to sp^2, the recovered diamond top layer preserves the surface roughness ($Rq \leq 0.30\,\mathrm{nm}$). This level of R_q is necessary for the diamond overgrowth step with minimal defect concentration.

The implanted and annealed diamond substrates serve as templates for subsequent overgrowth. Figure 2.20 (a) and (b) shows the overgrowth side AFM at different hotplate temperatures. Although this temperature modifies the growth condition and the growth rate, both $500\,^{\circ}\mathrm{C}$ (for $20\,\mathrm{h}$) and $700\,^{\circ}\mathrm{C}$ (for $40\,\mathrm{h}$) return smooth surfaces showing distinct step-flow growth striations [90] with a roughness R_q of $\leq 0.31\,\mathrm{nm}$. This number is less than the diamond lattice constant $0.357\,\mathrm{nm}$. Therefore, we claim the overgrowth side of the diamond membrane obtains an atomically smooth surface. We note that reaching such a smoothness with minimal growth defect concentration is not straightforward, as many other growth parameters could influence the surface morphology. For instance, the $40\,\mathrm{h}$ overgrown diamond surface with a pre-growth $60\,\mathrm{min}$ hydrogen plasma etch returns a R_q of $0.69\,\mathrm{nm}$. In addition, the residual surface strain from the fine polish may also

be a factor. An ICP-based surface strain release step [124] after the fine polish could release the strain and improve the surface morphology. Another example is a $40\,\mathrm{h}$ growth without proper surface preparation (acid cleaning). Residual contamination on the diamond surface generates growth defects (such as pits or pyramids) along the process and causes an increase of R_q to $18.6\,\mathrm{nm}$.

Unlike bulk diamond, membrane obtains two surfaces, and the etched side—the side defined via He^+ implantation—could also affect the color centers' coherence. When the membrane is freshly picked up from the diamond substrate, the Rq is $\approx 1.17\,\mathrm{nm}$, originating from the straggle of the He^+ implantation. This roughness can be reduced via Ar/Cl_2-based ICP etching. This physical-chemical etching has much faster etching rates for most materials than diamond, which could effectively remove the contamination and maintain or even improve the surface morphology during the process [163]. The R_q post Ar/Cl_2 etching is $0.54\,\mathrm{nm}$, indicating the presence of Cl-based contamination on the diamond surface discussed in previous studies [96]. Such contamination can be chemically removed by introducing O_2/Cl_2-O_2 ICP etching recipes, showing a R_q of $0.3\,\mathrm{nm}$ post complete etching. We note that the Ar/Cl_2 etching is critical to prevent roughness deterioration, as R_q increases noticeably if the O_2 etching is applied directly ($6.78\,\mathrm{nm}$) due to the preferential etching nature of an O_2-based plasma on crystallographic defects and polish-induced damage.

Another fabrication step affecting surface roughness is the downstream plasma ashing. We tested two plasma recipes, the O2 descum, and the high power recipe. No changes of R_q post O_2 descum treatment is observed ($0.28\,\mathrm{nm}$), but the high power recipe returns a worse surface morphology, with a R_q of $0.84\,\mathrm{nm}$. This is explained by the appearance of particle-like dust introduced from the chamber since the R_q of the contamination-free area remains to be $\leq 0.35\,\mathrm{nm}$. Such contamination can be reduced by switching to more specialized tooling. We currently use O2 descum for most diamond membrane bonding to minimize contamination and improve the bonding quality.

2.7.4 *Height and thickness variation detection*

There are three different approaches to measuring the height, thickness, and variation of the transferred membrane, including two-dimensional (2D) confocal laser scanning microscopy (CLSM), ellipsometry, and one-dimensional (1D) profilometry.

2D height mapping via CLSM The complete two-dimensional (2D) height map and surface topology of diamond membranes can be measured via CLSM (Olympus LEXT OLS4100 with a $405\,\mathrm{nm}$ laser). A microscope image of a diamond membrane directly bonded to a thermal oxide silicon substrate with the CLSM result is shown in Figure 2.21. Here the bonded membrane shows a uniform height of $309 \pm 8\,\mathrm{nm}$, with an equipment resolution of $\approx 10\,\mathrm{nm}$. Due to this relative coarse resolution, the CLSM is mainly used for detecting large-scale height inhomogeneity of diamond membranes' growth sides, including growth defects [164] and transfer process contamination.

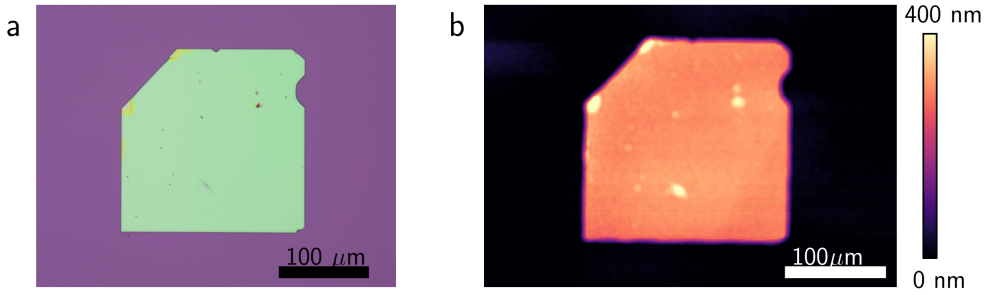

Figure 2.21: CLSM of a diamond membrane bonded to a thermal oxide silicon substrate. (a) The microscope image of the characterized device. In this image, several growth defects can be identified on the diamond membrane. (b) The 2D height map of the diamond membrane which shows an average height of $309 \pm 8\,\mathrm{nm}$. The raw data has received a plane-fit adjustment to remove substrate tilt aberrations. The X-Y resolution is quoted as $\leq 0.2\,\mu\mathrm{m}$, whereas the Z resolution is hardware defined to be $\leq 10\,\mathrm{nm}$.

Ellipsometry The ellipsometry method is able to provide accurate results for very thin transparent layers ($\leq 100\,\mathrm{nm}$). Therefore, we apply this method for $50\,\mathrm{nm}$-thick membranes used for photonic applications, which will be discussed in the next chapter. This technique was initially applied in nanophotonic integration studies [165]. Due to the size limitation of the membrane, the

scanning area is set to $85\,\mu\mathrm{m} \times 35\,\mu\mathrm{m}$ and is carefully aligned to the membrane surface. To fit the diamond layer, we use Cauchy's equation for transparent materials:

$$n(\lambda) = A + \frac{B \cdot 10^4}{\lambda^2} + \frac{C \cdot 10^9}{\lambda^4}, \tag{2.1}$$

where $A = 2.378$, $B = 1.300$ and $C = 0.000$, extracted from [166]. By using this model, we get a $\leq 4\,\mathrm{nm}$ height uncertainty for $\leq 50\,\mathrm{nm}$ membranes.

Profilometry The profilometry characterization can precisely measure the one-dimensional (1D) height profile of the membrane and is commonly used in the fabrication process for growth rate and global height variation characterizations. The measurement is mostly performed on diamond membrane devices post transfer. To improve the accuracy, the scanning trajectory covers the full length of the membrane.

The two diamond growth processes discussed in section 2.3.2 with substrate hotplate temperature set to $500\,^\circ\mathrm{C}$ and $700\,^\circ\mathrm{C}$, yields growth rates of $9.3(8)\,\mathrm{nm\,h^{-1}}$ and $6.2(4)\,\mathrm{nm\,h^{-1}}$, respectively. The uncertainty of the growth rate originates from multiple measurement trajectories. This growth rate reduction can be explained by increased surface mobility and desorption of precursor adatoms [167], and probably a non-linear reduction of nucleation sites.

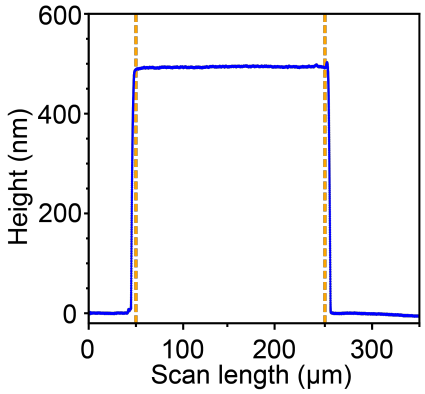

Figure 2.22: Profilometry of a membrane-silicon heterostructure. The membrane region is highlighted by two dashed orange lines. The thickness of the membrane is $493.7\,\mathrm{nm}$ with a standard deviation of $1.1\,\mathrm{nm}$.

For the global height variation characterization, we normally scan the final diamond membrane devices post cleaning. A typical direct-bonded diamond membrane on a silicon substrate is displayed in Figure 2.22, showing a height variation σ of $\approx 1\,\mathrm{nm}$. This value demonstrates the excellent flatness of the direct bonded devices. We note that this thickness variation σ is below the minimum detectable height of the equipment ($10\,\mathrm{nm}$) and the instrument resolution ($1.5\,\mathrm{nm}$) for large-scale scanning. As a comparison, the HSQ-bonded diamond membrane often obtains a flatness of $\approx 10\,\mathrm{nm}$. In general, uniform thickness across the entire membrane area is crucial for quantum photonics applications, which will be discussed in the next chapter.

2.7.5 Comparison of the two bonding methods

The two bonding methods, HSQ-based bonding and direct bonding, share a lot of similarities. Unlike other bonding methods that purely rely on Van der Waals forces [108], both methods offer strong bonds that remain effective against most nanofabrication processes (not HF) and cryogenic temperatures. In addition, they are both compatible with many carrier wafer choices and pre-patterned devices, which significantly improves the versatility of the platform. Furthermore, both bonding procedures obtain device yields above $90\,\%$ with room for further improvement, which is promising for scalable manufacturing. In a number of application scenarios, including group IV center measurements and thermal transport characterizations, both bonding methods are effective and thus interchangeable.

Comparably, the HSQ-based method has an even broader wafer choice —almost every substrate that can withstand the high-temperature annealing at $600\,^{\circ}\mathrm{C}$. Therefore, this method can be applied to the carriers that are relatively inert when receiving the surface plasma functionalization process. In addition, the method is compatible with most nanofabrication steps, including the well-known tri-acid cleaning [78], piranha clean, and even ultrasonication if no suspended diamond membrane is present. The HSQ method also provides a unique chance to perform strain engineering due to its special thermal properties at a certain annealing temperature range [168]. We will further discuss

the utilization of this unique property in Chapter 4. In contrast, the current direct-bonding method has slightly fewer carrier wafer choices due to the plasma activation efficiency, lower device yield due to incomplete control of the bonding approaching angle (which can be improved by switching to wafer bonder), and more strict post-nanofabrication methods. However, this method obtains much less fluorescence backgrounds, height variation and optical loss, which is ideal for NV^--based quantum sensing and quantum photonic applications.

2.8 Conclusion

In this chapter, we report a complete process flow to create diamond-based integrated material heterostructures based on the "smart-cut" technique. While this approach has been investigated before [120], this is the first demonstration to grow single crystal diamond on a damaged template with bulk-like crystal quality showing unprecedentedly narrow Raman linewidth and minimal growth defect concentration. The overgrown and ICP-etched diamond membrane obtains precise thickness control and atomically smooth surfaces on both sides. We further introduce isotopic purification during growth and δ-doping of ^{15}N for coherence protection and deterministic depth control of NV^- centers, which will be applied and characterized in the following chapters. In addition, we present two dry transfer and bonding methods to deterministically integrate pristine diamond membranes with various carrier wafers. Both methods obtain near-unity device yield, excellent nanofabrication compatibility, and allow for pre-structured substrates. In particular, the direct-bonded diamond membranes acquire nanometer-level height variation across the full membrane length $\approx 200\,\mu m$, with the HRTEM image revealing ordered, sub-nanometer bonding interfaces. While our current membrane size is $200\,\mu m$ by $200\,\mu m$, which is well motivated by scientific applications, larger membranes with millimeter size have been achieved [118]. Therefore, our technique has no technical barriers to realizing larger dimensions. Being compatible with standard semiconductor manufacturing processes, including wafer bonding, our method is promising for diamond-based quantum and electronic technologies. In the following few chapters, we will dis-

cuss our diamond membrane as a great platform for quantum photonics and an ideal host for spin defects such as NV^- and group IV centers for quantum sensing and networking applications.

CHAPTER 3

DIAMOND MEMBRANE FOR ON-CHIP NANOPHOTONIC INTEGRATION†

Abstract

Engineering photonic density of states near quantum emitters is critical to achieving efficient and tunable light-matter interactions. By modifying local optical environments and establishing coupling with emitters, we can manipulate their optical emission both spatially and spectrally. In the context of diamond and color centers, photonic state engineering is often realized via external microcavities or on-chip nanophotonic cavities. In this chapter, we will discuss the optical properties of the diamond membrane platform and its unique advantage in fabricating high-Q nanophotonic cavities. Following a general introduction to ring resonators, photonic crystal cavities, and their coupling to emitters, we will discuss three different types of nanoscale optical devices based on the diamond membrane platform: TiO_2-deposited fishbone cavities, fully-contact ring resonators, and suspended one- and two-dimensional photonic crystal cavities. These complementary cavity designs have great potential in efficient coupling with color centers for quantum photonics and networking applications.

3.1 Introduction

Most quantum objects used for qubits or qubit generation have atomic, microscopic, or mesoscopic length scales with relatively weak responses to control pulses and readouts. Therefore, engineering local density of states for improved interaction is crucial for qubit initialization, coherent control, and readout. Depending on the physical form of the information carriers and their energy scales, the device for density of state engineering can have many names and implementations. For in-

†. The work discussed in this section was reported in [94, 165, 169]

stance, microwave photon cavities often have the form of three-dimensional harmonic oscillators, coplanar waveguide resonators, or lumped LC element oscillators, which are commonly used in superconducting circuits [170–172], donors in silicon [173], and quantum dots [174]. Microwave phonons can live in high-overtone bulk acoustic resonators (HBAR), phononic cavities, or mechanical oscillators to couple with superconducting qubits or microwave and optical signals [175–177]. The spin waves inside ferromagnetic materials can be trapped inside the magnon cavity to realize novel couplings [178]. At optical frequency, photonic cavities can have many forms, including fine-polished mirror cavities for neutral atoms [179], photonic crystal (PhC) nanocavities, Febry-Perot microcavities to couple lights to quantum dots or other quantum emitters in solids state materials [17, 180, 181].

In the context of diamond, color centers (NV^-, group IVs) are promising qubit candidates. However, due to the relatively high refractive index of diamond ($n_{\text{diamond}} = 2.42$), most of the photons emitted by color centers are reflected from the diamond-air interface, with only up to $3\,\%$ being collected. To address this issue and improve the overall collection efficiency, some studies focus on reducing the internal reflection ratio using solid immersion lenses [43] or nanodiamonds [182]. These methods can improve the collection efficiency up to $30\,\%$ to $40\,\%$. Further improvement must include engineering the photon density of states using optical cavities. Besides, new forms of qubit can appear if strong light-emitter coupling can be achieved [68]. There are two major trends for the physical implementation of the optical cavities. One method uses microcavities made of flat or curved Fabry-Perot (FP) mirrors and engineered fiber tips [183]. This method is quite flexible when choosing emitter locations, and some cavities have exceptionally high finesse. However, they suffer from relatively low Purcell enhancement (a metric to define the emitter coupling, as discussed below) due to the large mode volume. Their scalability is also questionable, as quantum emitters require individual cavity setups. The other method is fabricating on-chip nanophotonic cavities (not necessarily made of diamond) and coupling color centers to the optical field maximum. This method usually obtains much higher Purcell enhancement and thus cooperativity C

[62], but it requires precise location control of the color center implantation, which is often realized via masked implantation or nano implantation [184, 185]. Moreover, this method lacks the selection step of color centers and cavities post fabrication, which reduces the device yield. Nevertheless, given the better and consistent performance of the nanophotonic devices and the continuously improving quality and yield, we will focus on the nanophotonic integration in this chapter and discuss the improvements introduced by the diamond membrane platform.

We will start by introducing two major types of on-chip designs: ring resonators and PhC cavities, followed by the metrics to evaluate their performances: finesse $\mathcal{F}$ and quality factor Q. We will then discuss the coupling between emitters and the cavity, with more related parameters involved: spontaneous emission rate, Purcell enhancements F_P in the weak coupling regime, and the cooperativity C in the strong coupling regime.

3.1.1 On-chip nanophotonic cavities

Ring resonator The design of the ring resonator originates from the optical waveguides, which are able to transmit optical signals (photons) through a long distance. These waveguides typically have a higher refractive index compared with the surrounding environment. From classical understanding, the refractive index discrepancy creates a total internal reflection condition that traps lights with large incident angles in the waveguide. When the cross section becomes smaller, the waveguides cannot host every spatial mode of the incident light. Instead, only several modes with significant spatial overlap with the transverse pattern of the waveguide are allowed to propagate.

Similar to electromagnetic fields in the vacuum, the field inside waveguides also gains phases during propagation. When a waveguide becomes a ring with a radius much larger than the wavelength of the light, the propagating light after the round trip will interfere with the incident light. Depending on the phase condition, this ring provides constructive interference and amplifies the incident field at certain wavelengths—a ring resonator. Typically, a ring resonator is coupled to other rings and waveguides to be fully functional. In this section, we will introduce only two simple cases:

a ring resonator coupled to one waveguide and two waveguides. More detailed derivation can be found in Ref [186]. All optical components here are considered to be reciprocal.

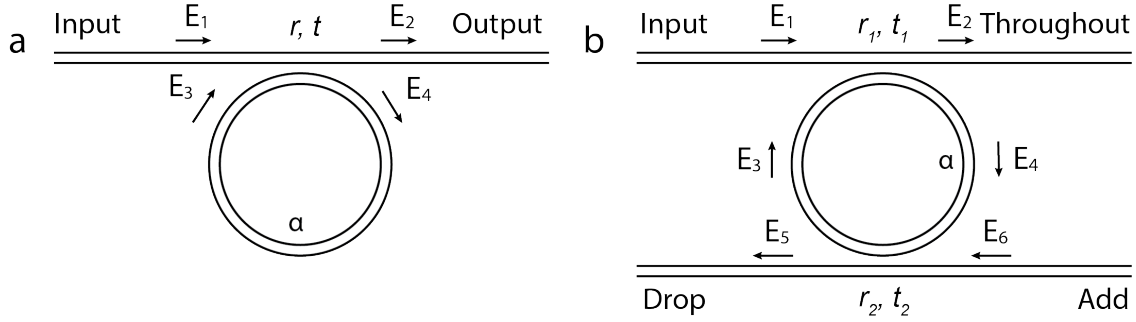

Figure 3.1: Schematics of the ring resonators. The single waveguide version is shown in (a), and the double waveguide version is shown in (b). The port definition is in accordance with Ref [187].

The schematic of the single waveguide ring resonator is shown in Figure 3.1 (a). We use a scatter matrix **S** to connect the fields of input-output elements:

$$\begin{bmatrix} E_2 \\ E_4 \end{bmatrix} = \mathbf{S} \begin{bmatrix} E_1 \\ E_3 \end{bmatrix} = \begin{bmatrix} S_{11} & S_{12} \\ S_{21} & S_{22} \end{bmatrix} \begin{bmatrix} E_1 \\ E_3 \end{bmatrix} \tag{3.1}$$

Here all elements in **S** are complex numbers. Since the coupling itself is reciprocal, we can reverse the input-output ports and write the equation as:

$$\begin{bmatrix} E_1 \\ E_3 \end{bmatrix} = \mathbf{S}^* \begin{bmatrix} E_2 \\ E_4 \end{bmatrix} \tag{3.2}$$

Therefore, we reach a simple equation for **S**: $\mathbf{S}\mathbf{S}^* = \mathbf{I}$. From this equation we can write S_{22} as $S_{22} = -\frac{S_{21}}{S_{21}^*} S_{11}^*$. Furthermore, we regard the coupler as a lossless element. According to the energy conservation law, we thus have

$$|E_2|^2 + |E_4|^2 = |E_1|^2 + |E_3|^2 \tag{3.3}$$

From this equation, we are able to extract two relations between **S** parameters: $S_{22} = -\frac{S_{12}}{S_{21}^*} S_{11}^*$,

and $|S_{11}|^2 + |S_{21}|^2 = 1$. Combining these equations, if we write S_{11} as r_c and S_{21} as t_c (two complex numbers), we then have an **S** matrix of:

$$\mathbf{S} = \begin{bmatrix} r_c & t_c \\ t_c & -r_c^* \frac{t_c}{t_c^*} \end{bmatrix} \tag{3.4}$$

For symmetric notation, we can write $r_c = r$ and $t_c = it$, where r and t are real numbers. The **S** matrix becomes:

$$\mathbf{S} = \begin{bmatrix} r & it \\ it & r \end{bmatrix} \tag{3.5}$$

For a ring resonator with a field loss parameter α, we can write the field coming out of the ring E_3 as $E_3 = ae^{i\phi}E_4$. By inserting this into the equation 3.1 with the use of 3.5, we then have a ratio between the field in the ring E_3 and the input field E_1:

$$\frac{E_3}{E_1} = \frac{itae^{i\phi}}{1 - rae^{i\phi}} \tag{3.6}$$

Where $a = e^{-\frac{\alpha}{2}2\pi R}$ is called single-pass amplitude transmission, and $\phi = k2\pi R$ is called single pass phase shift. Here, α is the optical loss (attenuation) of the ring resonator, k is the wavevector of the light and R is the radius of the ring. The intensity ratio between E_3 and E_1 is:

$$\frac{I_3}{I_1} = \left|\frac{E_3}{E_1}\right|^2 = \frac{(1 - r^2)a^2}{1 - 2ra\cos\phi + r^2a^2} \tag{3.7}$$

When $\cos\phi = 1$ ($k2\pi R = 1, R = m\lambda$), this ratio reaches maximum due to the constructive interference. For lossless rings ($a = 1$), this result can be further simplified as $\frac{1+r}{1-r}$ at maximum. Similarly, the power transmission can be written as:

$$\mathcal{T} = \frac{I_2}{I_1} = \left|\frac{E_2}{E_1}\right|^2 = \frac{a^2 - 2ra\cos\phi + r^2}{1 - 2ra\cos\phi + r^2a^2} \tag{3.8}$$

From these calculations, we can see that both transmission and reflection spectrum are periodic with respect to ϕ. We use finesse $\mathcal{F}$ to describe this spectral feature, which is defined as the free spectral range (FSR) between resonance peaks divided by the full width at half maximum (FWHM) of each peak. The half maximum point, where the power transmission $\mathcal{T}_{\phi_0}$ is a mean value of its maximum and minimum, is defined as

$$\mathcal{T}_{\phi_0} = \frac{1}{2}(\mathcal{T}_{\phi=2k\pi} + \mathcal{T}_{\phi=(2k+1)\pi}) \tag{3.9}$$

Where k is any integer. Solving the ϕ_0 from the above equation and inserting it to the finesse $\mathcal{F}$, we then have

$$\mathcal{F} = \frac{2\pi}{2\phi_0} = \frac{2\pi}{2\arccos\left(\frac{2ra}{1+r^2a^2}\right)} \tag{3.10}$$

From the above derivations, we find that if $a = r$ (the loss inside the ring equals the coupling), the minimum transmission $\mathcal{T}$ will be zero. This condition is called critical coupling, indicating the best light coupling from the waveguide to the ring. We also note that the finesse is not infinite, even for lossless ring resonators ($a = 1$). Therefore, an additional calculation to consider the coupling is often needed to derive the actual material loss from measured values.

Now, we turn to the double waveguide geometry (add-drop ring resonators). the schematic is shown in Figure 3.1 (b). Here, we only consider a simple case where the light is only provided by the input port ($E_6 = 0$), which can be transmitted to either the throughput port E_2 or drop port E_5. Followed by a similar derivation from above, we have the transmissions to two ports written as:

$$\mathcal{T}_1 = \frac{I_2}{I_1} = \left|\frac{r_1 - r_2 a e^{i\phi}}{1 - r_1 r_2 a e^{i\phi}}\right|^2 = \frac{a^2 r_2^2 - 2r_1 r_2 a\cos\phi + r_1^2}{1 - 2r_1 r_2 a\cos\phi + r_1^2 r_2^2 a^2} \tag{3.11}$$

$$\mathcal{T}_2 = \frac{I_5}{I_1} = \left|\frac{-t_1 t_2 \sqrt{a} e^{i\frac{\phi}{2}}}{1 - r_1 r_2 a e^{i\phi}}\right|^2 = \frac{(1 - r_1^2)(1 - r_2^2)a}{1 - 2r_1 r_2 a\cos\phi + r_1^2 r_2^2 a^2} \tag{3.12}$$

To compute the FWHM of the double ring, we turn to the transmission coefficient $\mathcal{T}_2$ and derive the value of ϕ_0 from $\mathcal{T}_{2,\phi_0} = \frac{1}{2}(\mathcal{T}_{2,\phi=2k\pi} + \mathcal{T}_{2,\phi=(2k+1)\pi})$. The result is quite similar to the single port value, with

$$\mathcal{F} = \frac{2\pi}{2\phi_0} = \frac{2\pi}{2\arccos\left(\frac{2r_1r_2a}{1+r_1^2r_2^2a^2}\right)} \tag{3.13}$$

If the cavity has a narrow FWHM (high finesse $\mathcal{F}$), we can apply the Taylor expansion to ϕ: $\cos\phi \approx 1 - \frac{1}{2}\phi^2$ and write the drop port as:

$$\mathcal{T}_2 \approx \frac{(1-r_1^2)(1-r_2^2)a}{(1-r_1r_2a)^2}\frac{1}{1+\frac{\phi^2}{\left(\frac{1-r_1r_2a}{\sqrt{r_1r_2a}}\right)^2}} \tag{3.14}$$

This equation shows that the transmission has a Lorentzian shape, which is in line with experimental observations. When the system has a large coupling with small loss ($1 - r_1r_2a \approx 0$), the above equation can be simplified as:

$$\mathcal{T}_2 \approx \frac{(1-r_1^2)(1-r_2^2)a}{(1-r_1r_2a)^2}\frac{1}{1+\left(\frac{\phi}{\pi/\mathcal{F}}\right)^2} \tag{3.15}$$

Therefore, the finesse can be directly deduced from the lineshape of the resonance spectrum. Compared with the single waveguide geometry, the drop ports are able to provide clean resonance peaks with a low signal background even if the ring resonator is not critically coupled. This relaxation of critical coupling simplifies the device design and is used later in our measurements.

Lastly, we discuss another commonly used metric for characterizing the cavity properties—quality factor Q. In high-quality cavity systems, it is defined as:

$$Q = \frac{\omega}{\Delta\omega} \approx \frac{\lambda}{\Delta\lambda} \tag{3.16}$$

This definition is quite similar to $\mathcal{F}$. We can write the relationship between finesse and quality

factor as $Q = \frac{n_{\text{eff}}L}{\lambda}\mathcal{F} = m\mathcal{F}$, where m is the ring resonator length counted by the effective wavelength of the incident light. From this equation, we find that the finesse $\mathcal{F}$ is a system property describing the material loss and the coupling, while the quality factor Q involves the length of the ring and can be modified by changing the ring size.

In reality, depending on the mode of the incident light, the effective refractive index n_{eff} can be different. Therefore, multiple resonance pairs (some transverse electric (TE) modes, some transverse magnetic (TM) modes) can be observed in a ring resonator spectrum.

PhC cavity Unlike the ring resonator, which uses the length of the ring to determine the resonance frequency, the PhC cavity approach dives into the local arrangements of dielectric constants. These arrangements can be 1D, 2D or 3D. Before introducing the nanophotonic cavity, which can be regarded as a photonic defect, we first discuss the "host" of this defect, which is the photonic crystal. Here, we only discuss a simple one-dimensional case, a periodic stack composed of two dielectric materials with permittivity ε_1 and ε_2. The schematic of such a material is shown in Figure 3.2 (a), with more derivation details listed in Ref [188]. This layered structure is often called distributed Bragg reflector (DBR) for high reflectivity purposes and has been utilized in many applications [189, 190].

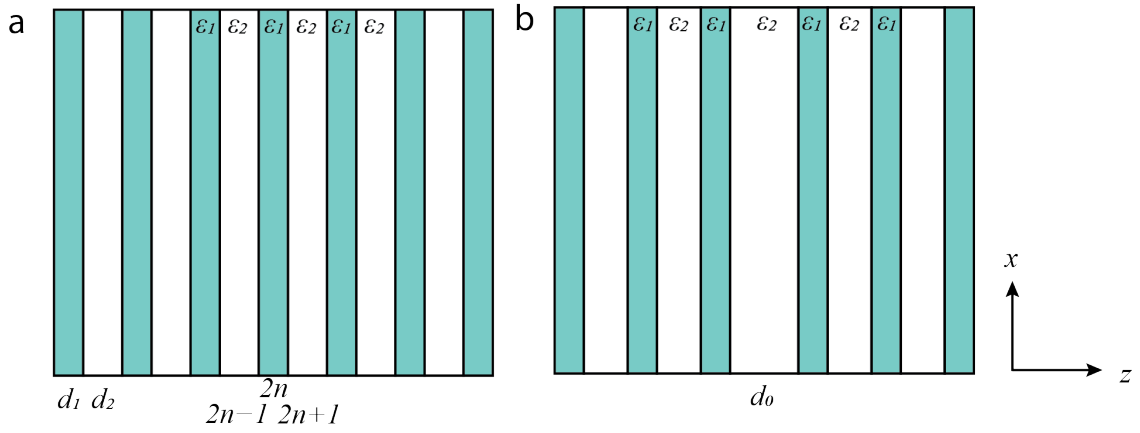

Figure 3.2: Schematics of a one-dimensional photonic crystal and a PhC cavity. In this example, the periodic structure comprises two materials with permittivity ε_1 and ε_2 and thickness d_1 and d_2, respectively. For the PhC cavity in (b), the photonic defect has a thickness of d_0.

We explore the TE and TM modes in this layered material. Specifically, we focus on the $2n-1$, $2n$, and $2n+1$ layers. For instance, in layer $2n$, the solution of E and H for TE and TM modes contains both forward and backward move solutions, which can be written as:

$$\text{TE: } E_{2n,j}(z) = a_{2n,j}e^{ik_j(z-n(d_1+d_2))} + b_{2n,j}e^{-ik_j(z-n(d_1+d_2))} \tag{3.17}$$

$$\text{TM: } H_{2n,j}(z) = a_{2n,j}e^{ik_j(z-n(d_1+d_2))} + b_{2n,j}e^{-ik_j(z-n(d_1+d_2))} \tag{3.18}$$

Where $a_{2n,j}$ and $b_{2n,j}$ are constant numbers that depend on the layer $2n$ and ε_j. The longitudinal wavevector is $\sqrt{\frac{\omega^2}{c^2}\varepsilon_j - k_\parallel^2}$, where $k_\parallel^2 = \sqrt{k_x^2 + k_y^2}$. By applying the boundary conditions at the interface $z = z_{2n} = n(d_1+d_2)$, we have:

$$a_{2n,1} + b_{2n,1} = a_{2n+1,2}e^{-ik_2d_2} + b_{2n+1,2}e^{ik_2d_2} \tag{3.19}$$

$$a_{2n,1} - b_{2n,1} = p_m\left(a_{2n+1,2}e^{-ik_2d_2} - b_{2n+1,2}e^{ik_2d_2}\right) \tag{3.20}$$

Here p_m is $\frac{k_2}{k_1}$ for Te modes and $\frac{k_2}{k_1}\frac{\varepsilon_1}{\varepsilon_2}$ for TM modes. Similarly, we can write the boundary conditions between $2n-1$ and $2n$ layers. To make sure the field inside a periodic potential with periodicity d_1+d_2 is physical, the field has to satisfy the *Floquet–Bloch theorem* [188]:

$$E(z+d_1+d_2) = e^{ik_B(d_1+d_2)}E(z) \tag{3.21}$$

This theorem is also used to analyze the behavior of electrons in a periodic potential from solids [31]. k_B is a wavevector called *Bloch wavevector*. Applying this function to the previous boundary conditions, we have:

$$a_{2n+1,2} = a_{2n-1,2}e^{ik_B(d_1+d_2)} \tag{3.22}$$

$$b_{2n+1,2} = b_{2n-1,2}e^{ik_B(d_1+d_2)} \tag{3.23}$$

To make sure the equations are solvable, the determinant of the matrix form of these equations, including $\{a_{2n,1}, b_{2n,1}, a_{2n+1,2}, b_{2n+1,2}\}$ must be zero. This implies a requirement of the k_B:

$$\cos k_B(d_1 + d_2) = \cos(k_1 d_1)\cos(k_2 d_2) - \frac{1}{2}\left(p_m + \frac{1}{p_m}\right)\sin(k_1 d_1)\sin(k_2 d_2) \tag{3.24}$$

Since the value of $\cos k_B(d_1 + d_2)$ is in the range $[-1, 1]$, there are certain conditions where no solution exists. We define the situation where no solution is available as the *photonic bandgap*. The incident light that falls into the bandgap will be reflected.

If we make some local arrangements that differ from the periodic layers at a certain depth z, we create a photonic defect inside the bandgap so that photons are hard to transmit from both directions. By doing that, we essentially create a PhC cavity. A schematic image is shown in Figure 3.2 (b). In practice, since periodic layers are not infinite, there is always a non-zero probability that the light can be leaked from the cavity. By optimizing the local arrangements via numerical simulations (for instance, Lumerical$^{@}$), the quality factor of the nanophotonic cavity design can easily reach 1×10^6 in many cases. This cavity creation method can also be expanded to 2D photonic crystal designs and even form directional photonic waveguides by modifying a connected line of defects [191].

3.1.2 Light-emitter coupling

For color center studies, an important goal of developing ring resonators and PhC cavities is to modify the emission properties of the centers. This goal does not only require the cavity to have high quality factor Q, but also (1) efficient coupling between the cavity and the emitter, and (2) efficient light out-coupling to external waveguides and other on-chip optical elements. The light out-coupling is often described as the critical coupling condition discussed above. Here, we focus on a few metrics commonly used to evaluate the coupling efficiency between the cavity and emitters.

Fermi's golden rule Fermi's golden rule is applied to understand and engineer the emission profile of quantum emitters. In quantum mechanics, the term *emission* is translated to an evolution of the quantum state $|\psi(t)\rangle$ according to the system Hamiltonian $\hat{H_{sys}} = \hat{H}_0 + \hat{H}_I$. Since the state $|\psi\rangle$ is normally defined in the basis of H_0 eigenstates $|n\rangle$ ($H_0 |n\rangle = E_n |n\rangle$), the only term responsible for the population evolution other than the phase gain is the interaction Hamiltonian H_I. This feature can be shown by inserting $|\psi(t)\rangle = \sum_n a_n(t) e^{-iE_n t/\hbar}$ into the Schrödinger equation $i\hbar \frac{d}{dt} |\psi(t)\rangle = \hat{H_{sys}} |\psi(t)\rangle$, which leads to [192]:

$$\frac{da_k(t)}{dt} = \frac{-i}{\hbar} \sum_n a_n(t) e^{-i\frac{E_n - E_k}{\hbar}t} \langle k|H_I|n\rangle \tag{3.25}$$

The derivation uses the orthogonal properties between states. The population evolution $a_k(t)$ is zero when there is no interaction Hamiltonian to link other states with $|k\rangle$. For optical emitters, this H_I is mainly provided by the incident optical field (electromagnetic field), which we treat as a perturbation (weak coupling regime). If we consider the spontaneous emission where the initial state is a particular eigenstate $|\psi(t=0)\rangle = |i\rangle$ and the final states are a continuum $|f\rangle$ which denotes the photons with different k vectors, the evolution of $|i\rangle$ and $|f\rangle$ is:

$$\frac{da_i(t)}{dt} = \frac{-i}{\hbar} \int d\varepsilon_f a_f(t) e^{-i\frac{E_f - E_i}{\hbar}t} \langle i|H_I|f\rangle \tag{3.26}$$

$$\frac{da_f(t)}{dt} = \frac{-i}{\hbar} a_i(t) e^{-i\frac{E_i - E_f}{\hbar}t} \langle f|H_I|i\rangle \tag{3.27}$$

Inserting the derivation of $a_f(t)$ into the $a_i(t)$ gives:

$$\frac{da_i(t)}{dt} = -\frac{1}{\hbar^2} \int d\varepsilon_f |\langle f|H_I|i\rangle|^2 \int_0^t dt' e^{-i\frac{E_f - E_i}{\hbar}(t-t')} a_i(t') \tag{3.28}$$

The process itself is non-Markovian. However, if the H_I is a perturbation term, we can apply Markov approximation and assume the system only depends on the present $a_i(t)$ and calculate the time integral directly. The integration $d\varepsilon_f$ is the sum over all $|f\rangle$ states that have the energy E_f,

which can be written as $\rho(E_f)dE_f$ By extending $t \to \infty$ and disregard the imaginary part of the time integral, we thus have:

$$\frac{da_i(t)}{dt} = -\frac{2\pi}{\hbar}\rho(E_f)|\left\langle f|H_I|i\right\rangle|^2 a_i(t) \tag{3.29}$$

By calculating the population $|a_i(t)|^2$ and its derivative, we then have a transition rate of:

$$\Gamma_{i\to f} = \frac{2\pi}{\hbar}|\left\langle f|H_I|i\right\rangle|^2 \rho(E_f) \tag{3.30}$$

This equation is Fermi's golden rule. It indicates that the emission rate is related to the (1) photon density of states $\rho(E_f)$, which can translate to $\rho(\omega)$, and (2) the physical property of the emitter $\left\langle f|H_I|i\right\rangle$. In our study, the emitter property is pre-defined, and the emission profile modification is realized through the photon density of state engineering.

Purcell enhancement In vacuum, the photon density of states in a finite volume V can be written as $\rho_0(\omega) = \frac{\omega^2 V}{\pi^2 c^3}$ [188]. The interaction Hamiltonian linking the two states can be regarded as the emitter dipole interacting with the electric field in the vacuum. By averaging the optical modes that actually interact with the dipole and inserting the zero point vacuum field $E_{\text{vac}} = \sqrt{\frac{\hbar\omega}{2V\varepsilon_0}}$, we have a free space spontaneous emission rate:

$$\Gamma_0 = \frac{\mu_{if}^2\omega_0^3}{3\pi\varepsilon_0\hbar c^3} = \frac{2\pi}{3}|g_0|^2\rho_0(\omega) \tag{3.31}$$

Where $g_0 = \frac{\mu_{if}}{\hbar}\sqrt{\frac{\hbar\omega}{2\varepsilon_0 V}}$ is the atom-field coupling strength if we treat the whole system quantum mechanically and write the Hamiltonian as the coupling between the atom and the photon states. From here, we can easily see that the local environment can indeed affect the emission rate. For instance, if the system is in a medium with refractive index n, then $\varepsilon_0 \to \varepsilon_n = n^2\varepsilon_0$ and $\rho_0(\omega) \to \rho_n(\omega) = n^3\rho_0(\omega)$, which returns a $\Gamma_n = n\Gamma_0$. In the case of the cavity, the field is not evenly distributed in all directions. If we align the cavity mode with the emitter dipole efficiently, we can

remove the pre-factor $\frac{1}{3}$ and write Γ in a more general case: $\Gamma = 2\pi|g|^2\rho(\omega)$.

For a relatively high Q single mode PhC cavity discussed in the previous section, the spectrum has a Lorentzian lineshape with a FWHM of $\Delta\omega$, and a single mode is spanned across the whole wavelength. Therefore, the density of states is also expressed in a Lorentzian lineshape:

$$D_c(\omega) = \frac{1}{\pi}\frac{\omega_c/2Q}{(\omega-\omega_c)^2 + (\omega_c/2Q)^2} \tag{3.32}$$

If the emitter dipole is on resonance and perfectly aligned with the electric field orientation, the emission rate is thus:

$$\Gamma = \frac{2\mu_{if}^2}{\hbar}\frac{Q}{\varepsilon_m V_m} \tag{3.33}$$

Here, the volume of the atom-photon coupling is written as V_m, and the permittivity of the material is ε_m. Compared with the same emitter in the vacuum, the ratio of the two is:

$$F = \frac{\Gamma}{\Gamma_0} = \frac{3}{4\pi}\frac{\lambda^3}{n^2}\frac{Q}{V_m} \tag{3.34}$$

For emitters that naturally live in a medium (such as color centers in diamond), we compare the spontaneous emission rate with the value inside the medium. This ratio $F_P = \frac{\Gamma}{\Gamma_n} = \frac{3}{4\pi}\frac{\lambda^3}{n^3}\frac{Q}{V_m}$ is called the Purcell factor. We note that this equation is only valid for the weak coupling regimes, and the strong coupling effect has to be considered if the Q is too high. Since the coupling g also introduces an imaginary term (damping) to the emitter frequency, the optical lifetime can be used to measure the Purcell factor in practice after adding the non-radiative decay and ZPL ratio (and branching for emitters with multiple ZPLs) into consideration.

Strong coupling regime When the coupling g exceeds the decay rate of the emitter γ (the spontaneous rate in a homogeneous medium) or the cavity decay rate κ (inversely related to the cavity Q), then the system behaves very differently compared to the weak coupling regime. For instance, if $g \sim \kappa \gg \gamma$, the resonances of the atom-cavity system deviate from the bare atom and cavity fre-

quencies, showing anti-crossing features in the spectrum with splitting dependent on the coupling g. In such a regime, a better system description would be the cooperativity, expressed as $C = \frac{4g^2}{\kappa\gamma}$. The strong coupling regime (often called cavity quantum electrodynamics, CQED) has very rich physics (see Ref [193]) and is beyond the scope of the discussion here.

3.1.3 An overview of diamond nanophotonic cavities

The previous efforts on diamond nanophotonic cavities largely overlapped with low-dimensional diamond fabrication and integration, as discussed in Chapter 2. Since we are interested in coupling color centers to these cavities, we only provide an overview of the results in visible wavelength and discuss their performances accordingly.

The least invasive way is to realize heterogeneous integration between bulk diamond and nanophotonic cavities made by other materials with even higher refractive indices. One example is the fabricated 1D gallium phosphide (GaP) cavities [80]. These cavities can have quality factors of up to 8900, with an observed Purcell factor of $\approx$30. The method does not involve any diamond fabrication, which helps protect the coherence of the color centers. The device's quality factor and performance are mainly limited by the fabrication of the GaP material, the stamping accuracy, and the yield of the cavity transfer process.

The second method is the well-known angular ICP etching. Originated from utilizing Faraday cages in the ICP chamber [99], the state-of-the-art etching utilizes focused ion beam (FIB) etching with angular control to achieve a cooperativity of over 100 [62], which is at the boundary of the strong coupling regime showing several unique quantum features [103]. The method can also be used for fabricating suspended microdisks and ring resonators with the highest quality factor to date (3×10^4 to 6×10^4 in visible wavelength) [194]. However, this method often requires special tooling, which is unavailable in many cleanroom configurations, limiting further promotion of this technique.

A more commonly accepted method is multi-step isotropic etching. This method shares the same

philosophy as the angular etching (undercut and suspend the diamond structure) but offers a more accessible recipe for regular cleanrooms. Since developed [195], this method has become widespreaded with many demonstrations from multiple research facilities [107, 108, 196, 197], with the performance comparable with the angular etching results.

Finally, we would like to mention that previous utilizations of direct-etched and "smart-cut" diamond membranes are also candidates for nanophotonic devices. However, due to the local height variation or imperfect crystal quality, the quality factor Q for fabricated ring resonators ranges from 1×10^3 to 2.4×10^4 [98, 118, 127, 198].

3.2 TiO2 cavities on diamond membranes

3.2.1 Device fabrication

For the three methods applied to diamond membrane heterostructures, the titanium oxide TiO_2 technique is the only one that does not involve diamond patterning and etching. The method has a similar philosophy to the GaP-diamond heterostructure realization [80], that a nanophotonic cavity with a high refractive index can be integrated with diamond to realize evanescent coupling with the color centers inside. Beyond diamond, this method is commonly used for other emitters hosted by materials with less straightforward fabrication processes [137]. In the case of integrated diamond membranes, the thickness of the diamond can be managed to be $\approx 50\,\mathrm{nm}$, which is much less than the operation wavelength of the nanophotonic cavities inside diamond ($250\,\mathrm{nm}$ to $350\,\mathrm{nm}$). By integrating membranes with low index substrates such as fused silica ($n = 1.46$), a cavity with confined mode volume can still be realized even using materials with a comparable index ($n \approx 2.4$), which is typically not realistic for bulk diamond substrates. This relaxed condition expands the choice of materials to fabricate nanophotonic cavities. In this work, we choose deposited TiO_2 ($n \geq 2.3$) using a standard atomic layer deposition (ALD) process.

The schematics of the TiO_2 cavity fabrication process are shown in Figure 3.2 (a)-(c). Although

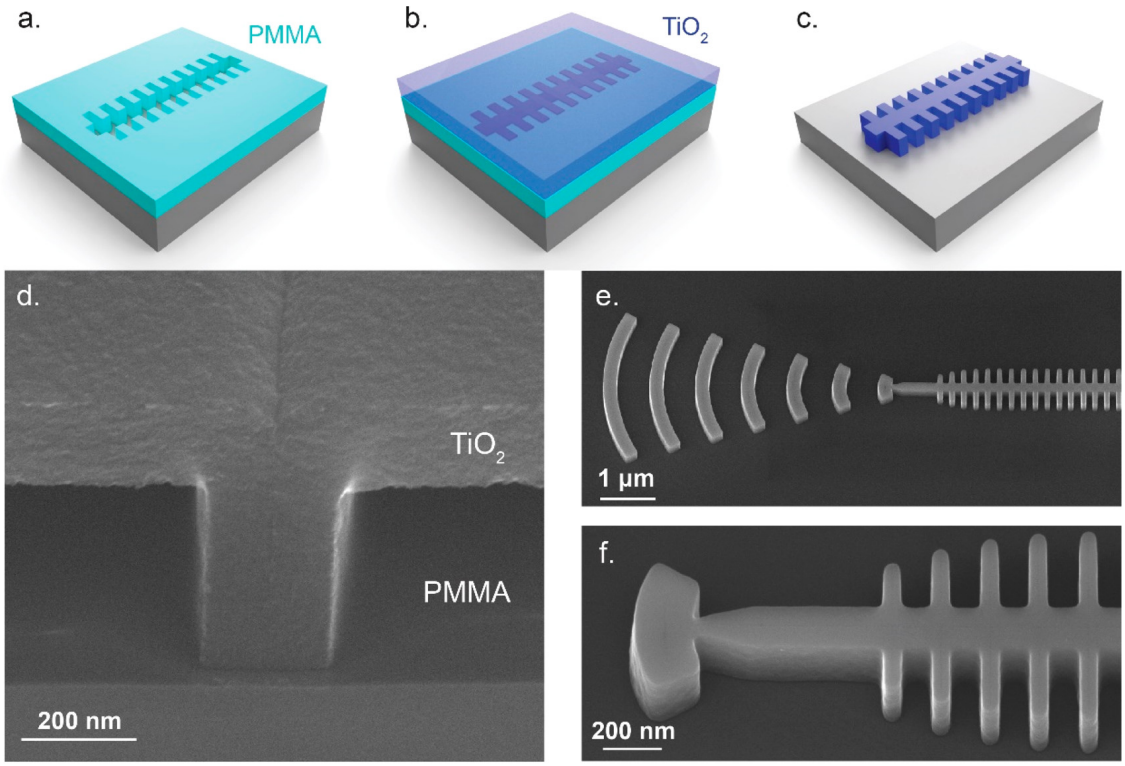

Figure 3.3: The fabrication process of TiO_2 nanophotonic cavities. (a)-(c) The schematics of the TiO_2 nanophotonic cavity fabrication using ALD process. (d)-(f) The SEM images of (d) deposited TiO_2 on the pre-patterned PMMA layer, (e) the completed photonic crystals with a grating coupler, and (f) a zoomed-in device showing vertical sidewalls with excellent smoothness. The figure is reproduced from [165].

TiO_2 is directly deposited onto the fused silica substrate in the schematics, the fabrication on the diamond membrane shares an almost identical recipe. The process starts with a cavity template definition via electron beam lithography, followed by a TiO_2 deposition of $\approx 300\,\mathrm{nm}$ ($\approx 250\,\mathrm{nm}$ for bare fused silica). This conformal layer overfills the Poly(methyl methacrylate) (PMMA) pattern. The temperature of the ALD step is kept low ($90\,^{\circ}\mathrm{C}$) to prevent PMMA from softening and TiO_2 from forming grain boundaries. Then, we etch the excessive TiO_2 on the top and remove the resist layer, leaving pristine nanostructures on the substrate. The device's local height variations can also be smoothed via the overfill and etching processes. The scanning electron microscope (SEM) images of the deposited TiO_2 and final devices are shown in Figure 3.3 (d)-(f). Unlike the template fabrication and transfer method [80], the TiO_2 cavities are defined at target locations

using electron beam lithography and thus obtain much higher location precision, which is crucial for aligning color centers with the field maximum to reach a stronger coupling. In addition, the deposited TiO_2 has better sidewall control over smoothness and angle compared with etched GaP or diamond cavities, which is important in terms of optical loss for nanophotonic cavities operating in visible wavelengths [199].

3.2.2 Cavities on HSQ-bonded diamond membranes

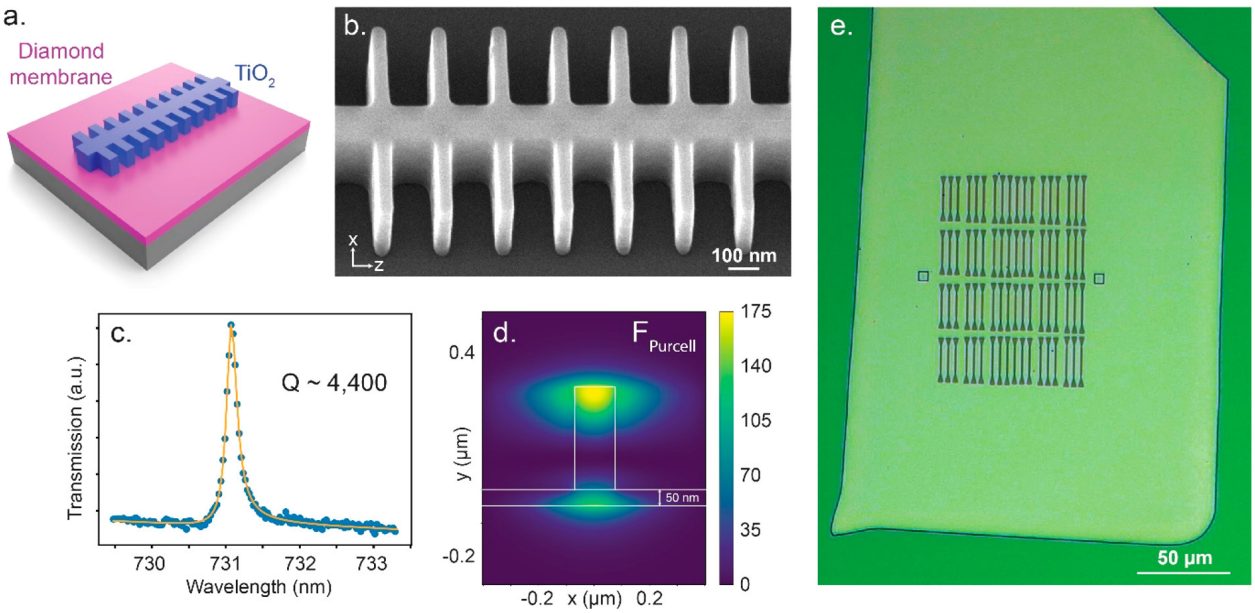

Figure 3.4: The characterization of TiO_2 cavities on a HSQ-bonded diamond membrane. (a) The schematic of the TiO_2 devices fabricated on the diamond membrane. The membrane is transferred and bonded to the fused silica substrate before the cavity patterning. (b) The SEM image of a TiO_2 PhC cavity on the membrane, showing less filling factors of TiO_2 compared with bare fused silica results. (c) A typical quality factor Q for a fishbone cavity on the diamond membrane. (d) Simulated Purcell enhancement in the cavity and the diamond membrane, showing a maximum value of 175 inside the cavity and 115 in the membrane. (e) A microscope image of the fabricated device. The figure is reproduced from [165].

The schematic of TiO_2 nanophotonic cavities deposited on a HSQ-bonded diamond membrane is shown in Figure 3.4 (a), with the microscope image of the cavities shown in Figure 3.4 (e). Compared with ring resonators, PhC cavities have much less mode volume, which can induce a higher Purcell enhancement with the same quality factor. Since the PhC cavities are deposited

instead of etched, we choose the pattern as fishbones instead of regular punched-hole designs [99]. This design can also be applied to realized phononic crystals due to better handling of strain distribution and phonon transmission [101]. The photonic crystal design (filling factor of the TiO_2 compared with air gaps), displayed as the SEM image from Figure 3.4 (b), is slightly different from that on bare fused silica substrates (Figure 3.3 (f)) to accommodate the presence of the high-index diamond membrane.

To design a PhC cavity, normally a photonic crystal is simulated and optimized first to ensure a photonic bandgap around the operation wavelength is present. In reality, the number of fins for the photonic crystal cannot be infinite, and this finite fin number determines the amount of light that can be transmitted into the cavity. Although a higher number of fins usually indicates a higher quality factor of the cavity using the same material, it also limits the coupling between the cavity and the incident light and reduces the signal in the transmission spectrum. Therefore, a balance between the quality factor and the transmission signal strength has to be implemented. In this work, many cavities are fabricated using the 25-fin design. Secondly, some local variations are introduced in the middle by playing with the filling ratio or the distance (pitch) between fins. In this case, the pinch of the fin is gradually decreased by $10\,\%$ in the middle of the cavity [165]. The measured quality factor of a cavity at $731\,\mathrm{nm}$ wavelength is ≈ 4400, shown in Figure 3.4 (c). The interpretation of the result is related to the designed field profile with the local maximum concentrated on the top and the bottom of the TiO_2 layer instead of the cavity center [80]. Although shifting the mode from the cavity center introduces more surface participation in the loss mechanism, this design can generate a significant evanescent field inside the diamond membrane. The simulated Purcell enhancement induced by the strong evanescent field is displayed in Figure 3.4 (d), showing a maximum value of 175 inside the cavity and 115 in the membrane. For SiV^- centers, this value could translate to a cooperativity of 1 to 10 [196].

Compared with TiO_2 cavities directly fabricated on fused silica substrates, there is a factor of 2 reduction over the average quality factor. The optical loss of the system could come from (1)

internal loss from ALD-deposited instead of single crystal TiO_2, (2) imperfect diamond membrane crystal quality (Raman linewidth $\approx 1.7\,\mathrm{cm}^{-1}$ compared with the bulk diamond value $\approx 1.55\,\mathrm{cm}^{-1}$), and (3) optical loss from the HSQ. The porous HSQ resist transforms into a dense SiO_x layer after annealing [98], which introduces optical scattering and absorption (as verified by measuring the fluorescence background). Therefore, in the next round of optimization, we deposit cavities onto direct-bonded membranes with bulk-like crystal quality to reduce the optical loss.

3.2.3 Cavities on direct-bonded diamond membranes

In this section, we reproduced the fabrication process of TiO_2 nanophotonic cavities by replacing the HSQ-bonded diamond membranes with direct-bonded ones that have improved crystal quality. To quantitatively characterize the loss mechanism, we keep the thickness of the membrane and the cavity design the same. We also fabricate ring resonators with coupling waveguides to provide an additional metric to analyze the optical loss. The schematic of the TiO_2 cavities and ring resonators is shown in Figure 3.5 (a). Excitation and collection ports (grating couplers) are highlighted in red and blue. Microscope images of deposited PhC cavities and ring resonators are shown in Figure 3.5 (b). We note that these cavities are fabricated on the same diamond membrane but with different rounds of fabrication thanks to the straightforward cavity removal process [165]. This feature highlights the robustness of the membranes to cleanroom processing and the recyclability of photonic integration. SEM images of fishbone cavities and ring resonators on the diamond membrane are shown in Figure 3.5 (d)-(e), featuring planarized top surfaces and smooth sidewalls.

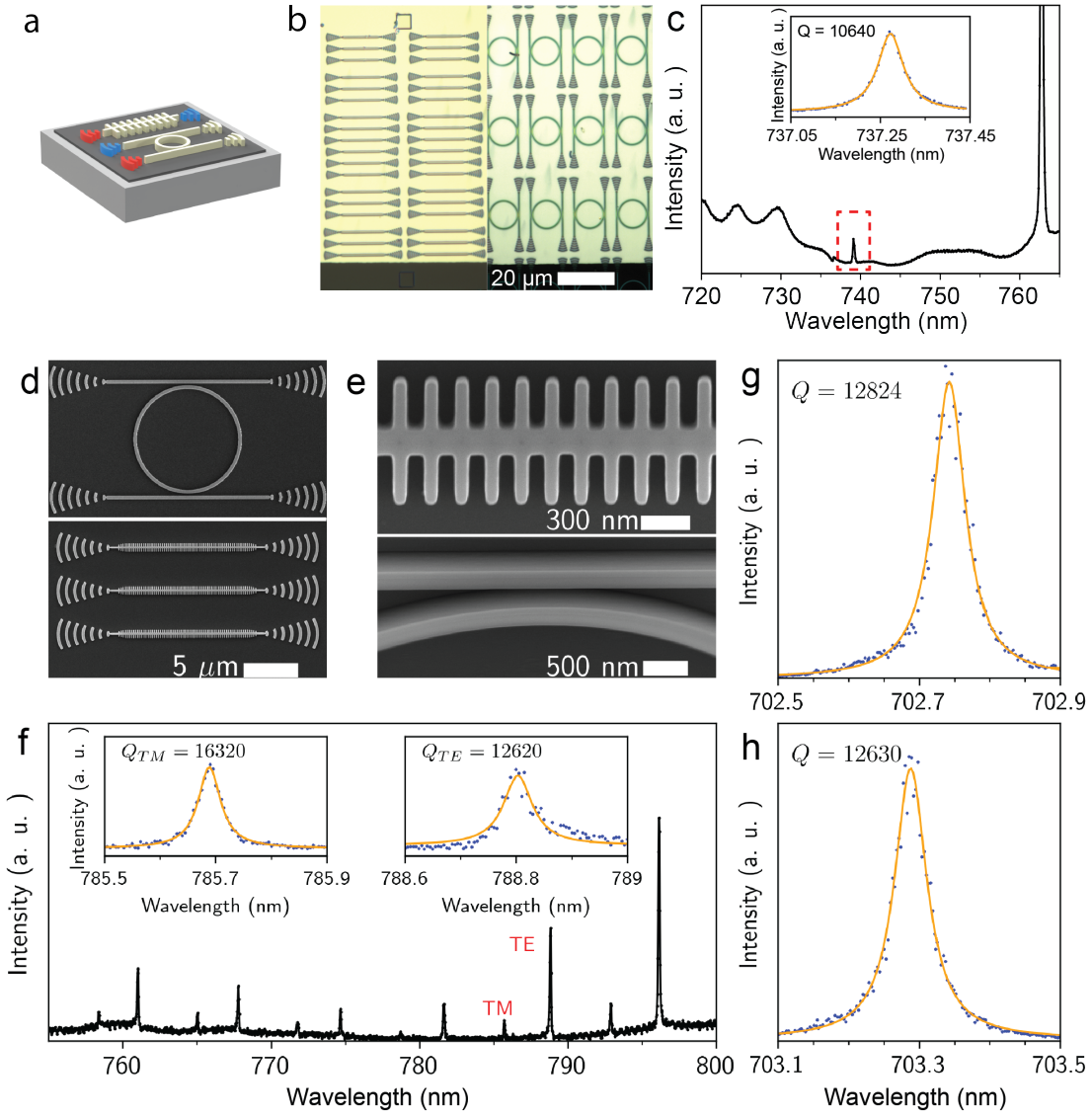

Figure 3.5: The characterization of TiO_2 cavities on direct-bonded diamond membranes. (a) The schematic of TiO_2-based nanophotonics on diamond membrane heterostructures. (b) Microscope images of TiO_2 fishbone cavities and ring resonators on a $50\,\mathrm{nm}$-thick diamond membrane. Images are taken at the same location but in different fabrication rounds. (c) The transmission spectrum of a fishbone cavity with the resonant frequency at $737.26\,\mathrm{nm}$. Inset: the transmission of the cavity measured with a tunable laser excitation, showing a quality factor Q of 10640 ± 118. (d)-(e) Zoomed-out (zoomed-in) SEM images of fishbone cavities and ring resonators on the diamond membrane, featuring flat top surfaces and smooth sidewalls. (f) The transmission spectrum of a TiO_2 ring resonator measured at the drop port. Insets: the TE and TM cavity resonances measured using a tunable laser. (g-h) Quality factors Q_{TiO_2} of the best two TiO_2 fishbone cavities fabricated on bare fused silica substrates.

The transmission measurement result of a fishbone PhC cavity is shown in Figure 3.5 (c). This cavity has a target wavelength of $737\,\mathrm{nm}$ — the wavelength of SiV emission. The measured quality factor Q is as high as $10\,640$, with a three-device average of 10150 ± 350. These values are about 2.5 times higher than the same cavities on the HSQ-bonded membrane, indicating significant optical losses from the HSQ bonding layer and the imperfect crystal quality of diamond. With the updated Q factors, we predict a maximum Purcell enhancement factor of 270 in the diamond, which is suitable for state-of-the-art experiments in cavity quantum electrodynamics [200]. Similarly, the ring resonator fabrication using the same recipe is measured through the drop port. The quality factors for TE and TM modes are $Q_{TE} = 12620$ and $Q_{TM} = 16319$, as shown in Figure 3.5 (f). The mode profile is identified via separate polarization measurements. With the same finesse, these quality factor values can be further improved via geometry optimization, such as larger rings [201].

Lastly, we estimate the optical loss from the diamond membrane by repeating the process on a bare fused silica substrate in the same fabrication round. The average of the best two measured cavities returns a value of $Q_{\mathrm{TiO_2}} = 12727$. Spectra of these cavities are displayed in Figure 3.5 (g)-(h). This $Q_{\mathrm{TiO_2}}$ is affected by the optical scattering within the deposited TiO_2 and the surfaces of the cavity (top surface, interface between TiO_2 and fused silica, sidewalls). Subtracting the average Q obtained from the diamond membrane results returns an approximate optical loss of the bonded diamond-fused silica system to be $Q_{sys} \approx 50000$, which is dominated by the optical losses at diamond/fused silica and diamond/TiO_2 interfaces.

3.3 Contact diamond ring resonators on fused silica

3.3.1 Device fabrication

In addition to the TiO_2 deposition method, we also explore the application of diamond membranes for on-chip quantum photonics by fabricating fully contact diamond ring resonators and waveg-

uides on thermal oxide substrates. These waveguides enable direct photonic integration with other on-chip devices. The schematic of the device is shown in Figure 3.6 (a). Without the need for diamond undercut, which is commonly used to create suspended diamond photonics from monolithic bulk diamond [99, 195], our fabrication features a single patterning and etching step using Al_2O_3 hard masks. The bright and dark microscope images of the final devices are shown in Figure 3.6 (b). With minimal fluorescence other than the device layout, the dark field image demonstrates the high quality and uniformity of the fabrication process.

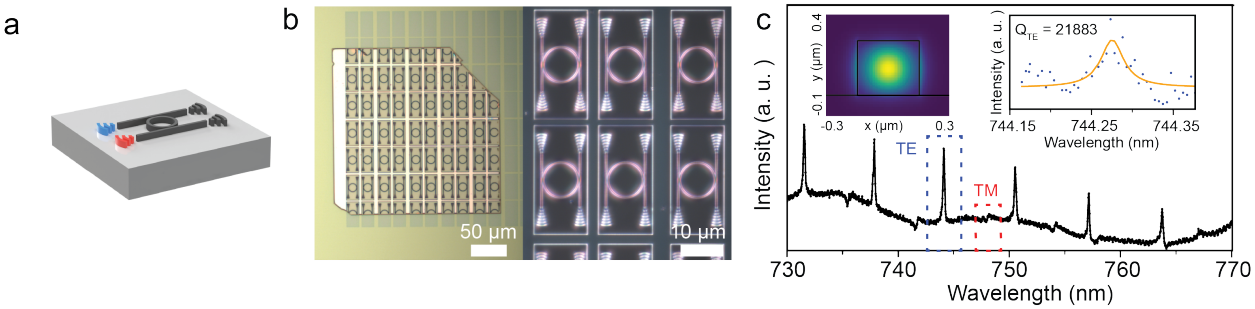

Figure 3.6: Fully contact diamond ring resonators fabricated using direct-bonded membranes. (a) The schematic of a fully contact diamond ring resonator on a carrier wafer. (b) The bright and dark field microscope images of the ICP-etched diamond ring resonators on a thermal oxide silicon substrate, showing great uniformity with minimal process contamination. (c) The transmission spectrum of the diamond ring resonator measured at the drop port. Insets: the TE mode profile inside the ring and the TE cavity resonance with a quality factor Q_{TE} of 21883 ± 6284. The signal fluctuation is caused by the instability of the optical setup.

3.3.2 Optical characterization

We performed the exact transmission measurement as the TiO_2 ring resonators. The measurement result is plotted in Figure 3.6 (c). An etched ring resonator exhibits quality factors Q of $21\,883$ at visible wavelength with excellent field confinement within the diamond. Although the values are slightly lower than the best-reported visible-wavelength suspended diamond ring resonators (3×10^4 to 6×10^4) [194], we note that the actual finesse might be comparable, given the reported value is measured on a larger ring. In addition, fully contact ring resonators offer direct integration with other visible-frequency photonic platforms, including lithium niobate, silicon nitride, titanium

dioxide, and on-chip light sources and detectors, paving the path for hybrid quantum photonic technologies.

3.4 Suspended diamond nanophotonic cavities

3.4.1 Device fabrication

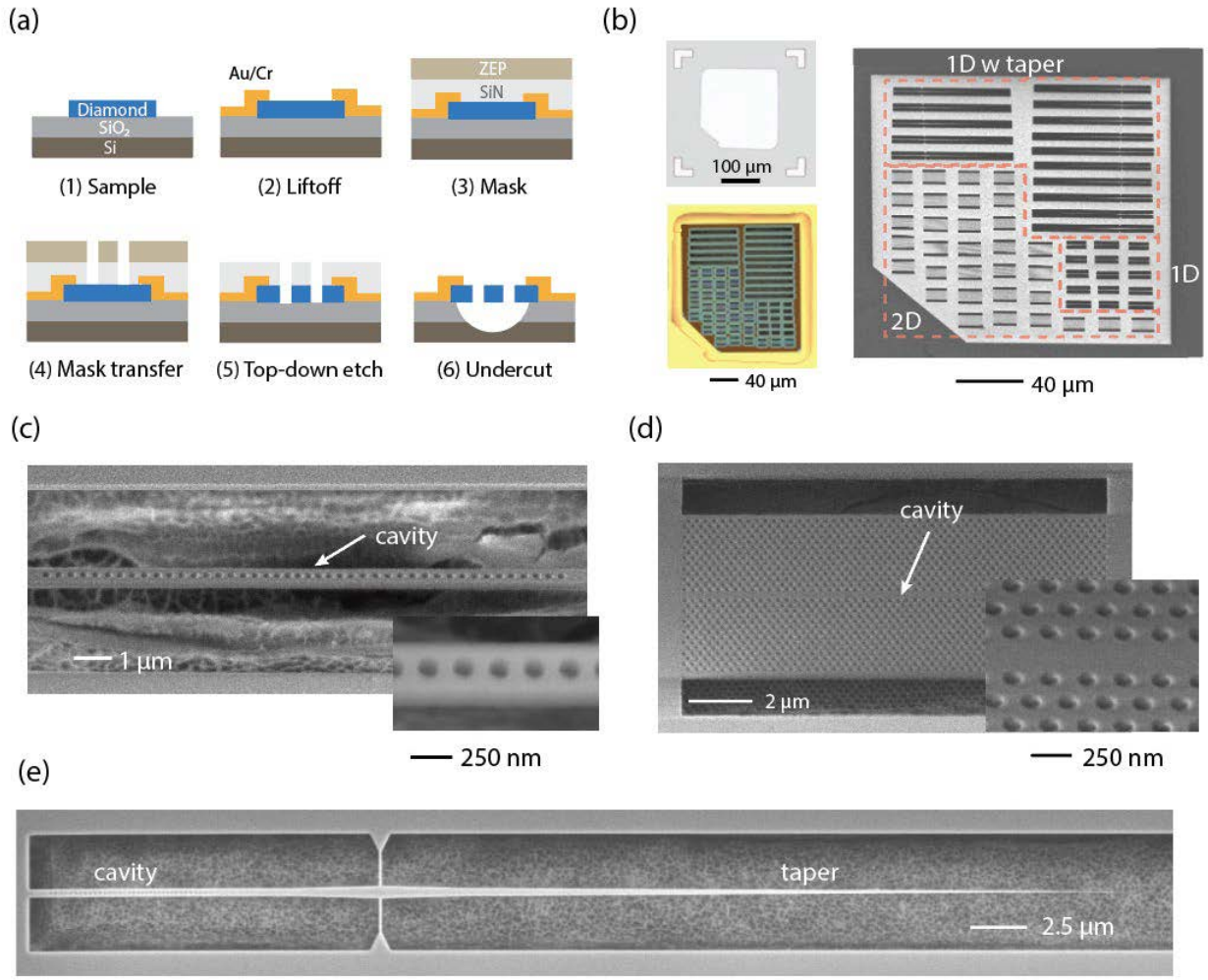

Figure 3.7: Fabrication of suspended PhC cavities using a direct-bonded diamond membrane. (a) The schematic of the PhC cavity fabrication flow. (b) Left: microscope images of the diamond membrane before and after cavity fabrication. Right: the SEM image of the fabricated sample. (c)-(d) The SEM images of 1D and 2D PhC cavities. The inset is the zoomed-in image showing the details of the holes. Images are taken at a 45° angle. (e) The SEM image of the 1D PhC cavity with the fiber taper. The figure is reproduced from [169].

Lastly, we explore the potential of the diamond membrane platform for fabricating suspended nanophotonic cavities. The dielectric environment of the suspended cavity only contains the diamond and surfaces, with optical modes hosted in the center of the device, which is simpler than fully contact TiO_2 cavities. In addition, PhC cavities can have high quality factors Q with small mode volumes and deterministic emitter placement, which greatly enhances light-matter interactions and allows for efficient control and readout of the emitter spin state. Therefore, many landmark demonstrations involving diamond nanophotonic cavities are realized via the suspended approach [73]. However, due to the imperfect sidewall control during ICP etching (especially the undercut step), many cavities fabricated using angle etching or isotropic etching have Q factors in the low $\sim 1 \times 10^4$ range, which is much lower than the simulated value ($\geq 1 \times 10^6$). By utilizing pristine and homogeneous diamond membranes that are directly bonded onto oxide substrates, we can tremendously simplify the fabrication procedure by replacing the sophisticated undercut step with a simple oxide wet etch. This highly selective chemical process maintains the surface morphology of the back side, leaving only two sidewalls subject to top-down ICP etching roughness control.

In this demonstration, a diamond membrane with $160\,\mathrm{nm}$ thickness is used to fabricate PhC cavities. The membrane has a surface roughness of $\leq 0.3\,\mathrm{nm}$ with a global height variation of $\approx 1\,\mathrm{nm}$, which are essential for minimizing optical loss and maintaining the device uniformity. Figure 3.7 (a) shows the schematic of the overall fabrication process. Starting from direct-bonded membranes with implanted SiV^-, a layer of Au/Cr is deposited and lift-off to define a "frame" around the membrane and secure it from subsequent chemical etching. Then, the hard mask for etching (silicon nitride, Si_3N_4) and the electron beam resist (ZEP) are prepared. The cavity pattern is written by electron beam lithography, which is then transferred to the hard mask using ICP etching. After resist removal, the cavity pattern is transferred to the diamond membrane via oxygen-based ICP etching. Finally, hydrofluoric acid (HF) is used to remove the hard mask and the oxide layer underneath it. To prevent optical mode leakage and coupling loss from the silicon wafer, another

XeF_2 etch is applied to remove some of the silicon and increase the separation between the substrate and the cavity. The microscope image of the original membrane and the same one fabricated with devices are shown on the left of Figure 3.7 (b), with the SEM image on the right. The layout includes multiple designs, including 1D PhC cavities, 2D PhC cavities, and 1D cavities with taper for fiber coupling. We adapt the design from previous demonstrations described in Ref [197, 202], where PhCs are created by introducing air holes with uniform spacing. From photonic crystals, the 1D cavities are formed by introducing a quadratic hole shift near the waveguide center, and the 2D cavities are formed by shifting the center holes outwards in the PhC line-defect waveguide. Both designs maintain the hole size, which is robust against design drifts or exposure offset during lithography. The typical simulated Q and mode volume V for our 1D (2D) cavities are $\approx 1 \times 10^6$ ($\approx 7.6 \times 10^5$) and ≈ 0.5 (≈ 2.9) $(\lambda/n)^3$. The SEM images of the 1D and 2D PhC cavities are shown in Figure 3.7 (c)-(d). For practical applications, it is also important to enable the light out-coupling with waveguides and eventually fibers to effectively initialize and readout the spin states to generate entanglements. Therefore, we include a third design, a 1D PhC cavity coupled to a feeding waveguide with a taper region to allow efficient coupling to a tapered fiber [102, 203]. The SEM image is shown in Figure 3.7 (e). The improved preferential coupling is achieved by reducing the number of holes in the photonic crystal mirror on the side of the waveguide while keeping the other side the same. This device structure has a simulated cavity Q of $\approx 1.9 \times 10^5$.

3.4.2 Optical measurements

We first perform PL measurements on PhC cavities at room temperature using off-resonant green excitation ($523\,\mathrm{nm}$) and measure the fluorescence using a spectrometer system. The measured 1D and 2D PhC cavity resonances with respect to the distance between holes match the simulation value well, showing wavelength deviations of less than $1.1\,\%$. In addition, we observe that $100\,\%$ (30 out of 30) of 1D cavities and $85\,\%$ (23 out of 27) of 2D cavities characterized have spectrometer-limited quality factors ($Q \geq 2 \times 10^4$). To accurately obtain the cavity reso-

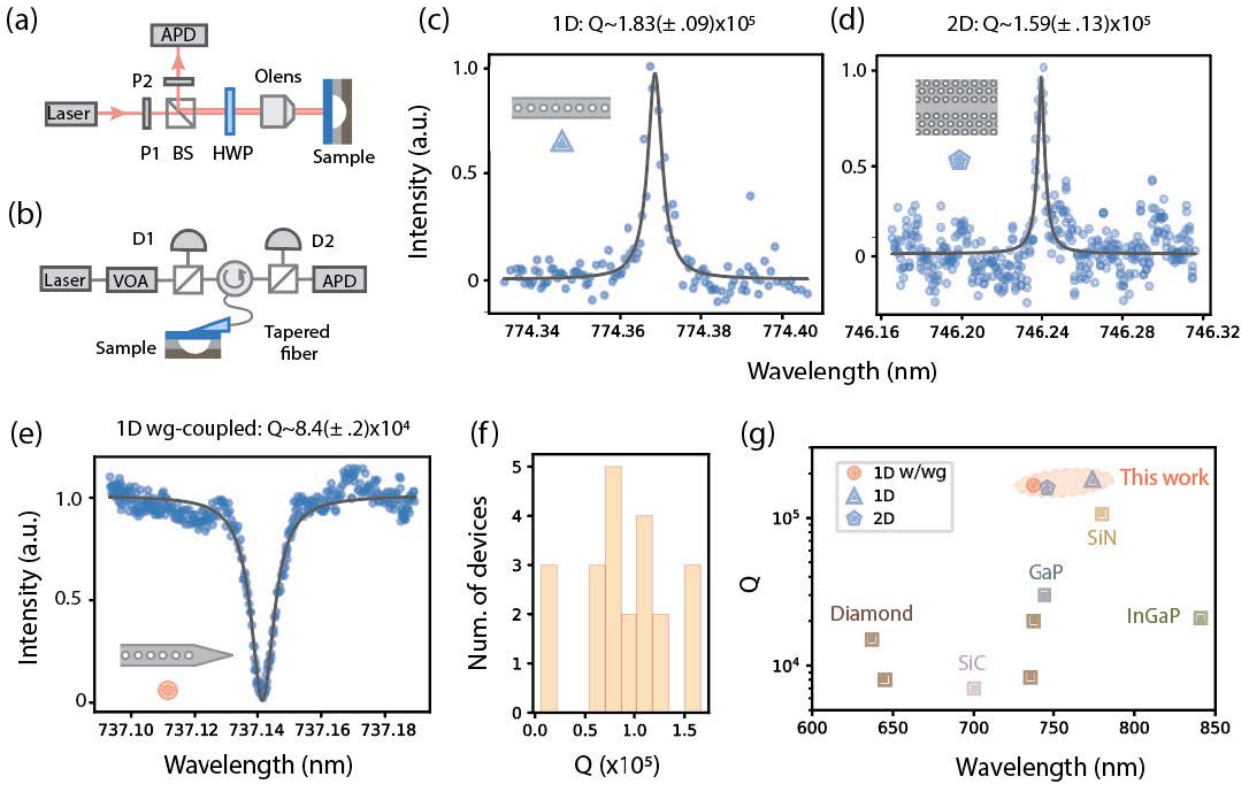

Figure 3.8: Quality factor measurement of 1D and 2D PhC cavities. (a) The schematic of the cross-polarization measurement. Olens: objective lens. P1 and P2 are orthogonal to filter out the incident light. (b) The schematic of the fiber-coupling setup for measuring the cavity reflection signals. We use the same laser for the cross-polarization measurement. The variable optical attenuator is applied to stabilize the input power, which is measured via photodiodes (D1, D2). A fiber-based circulator is applied to extract the reflected signal from the fiber. (c)-(d) On-resonance scan of the 1D and 2D PhC cavities using the cross-polarization setup. (e) On-resonance scan of the 1D PhD cavity preferentially coupled to a waveguide. The cavity is shown to be nearly critically coupled as the signal contrast is $\approx 95\,\%$ in reflection. (f) The histogram of all the cavities that are measured and resolved in the wavelength range between $710\,\mathrm{nm}$ and $770\,\mathrm{nm}$. (g) The comparison of our work with previous demonstrations as referenced in the text. The figure is reproduced from [169].

nance and quality factors, we perform cross-polarization measurements using a tunable laser, two polarizers (P1, P2), a beam splitter (BS), and a half-wave plate (HWP). The schematic of the cross-polarization measurement is shown in Figure 3.8 (a). Compared with PL measurement, the cross-polarization measurement does not require strong fluorescence on the cavity (which is normally detrimental) and is thus more suitable for measuring high quality, low optical background resonators. Figure 3.8 (c)-(d) shows the reflection spectra of the fundamental modes measured from the best 1D and 2D PhC cavities. The peaks are fitted to the Lorentzian function with Q factors of $1.83(9) \times 10^5$ and $1.59(13) \times 10^5$, respectively. The figure for the Q factor comparison versus wavelength is shown in Figure 3.8 (g). We emphasize that the Q factor of the 1D PhC cavity is about one order of magnitude higher than previously reported diamond cavities operating in visible wavelengths and is the new record for visible PhC cavities in any materials, including diamond [62, 105, 198, 204], silicon nitride [205], aluminum nitride [206], silicon carbide [207], GaP [80], and InGaP [208]. Similarly, our method to fabricate 2D PhC cavities produces Q factors that are 20 to 100 times higher than the state-of-the-art studies realized in diamond [98, 202]. This improvement is mainly because our fabrication approach has suspended 2D structures with flat surfaces and uniform height by nature, which is typically hard to achieve using quasi-isotropic etching or direct etching from diamond thin films. Lastly, we demonstrate the high device yield by collecting the histogram of the Q factors from all cavities we have measured. As shown in Figure 3.8 (f), most 1D and 2D PhC cavities exhibit Q factors of over 5×10^4, which further showcases the uniformity and yield of this platform.

We also characterize the 1D PhC cavities coupled to the waveguides. The measurement setup is an optical fiber coupling system shown in Figure 3.8 (b). The light from the tunable laser is power stabilized by the attenuator (VOA) before sending into the device, and the reflected light is detected by an avalanche photon detector (APD). Here, only pW power excitation is used to detect the reflection signal to reduce the heating effect. Figure 3.8 (e) shows the reflection spectrum from the highest Q cavity. The loaded Q is measured to be 8.4×10^4. The minimum cavity reflection is

$\leq 5\,\%$ with $95.3(3)\,\%$ of signal contrast, indicating that the cavity is nearly critically coupled. By measuring the system's transmission loss and comparing that with the total optical loss measured by D1 and D2, we estimate the coupling efficiency between the fiber and the waveguide to be $\approx 65\,\%$.

3.4.3 SiV⁻ center coupled to the cavity

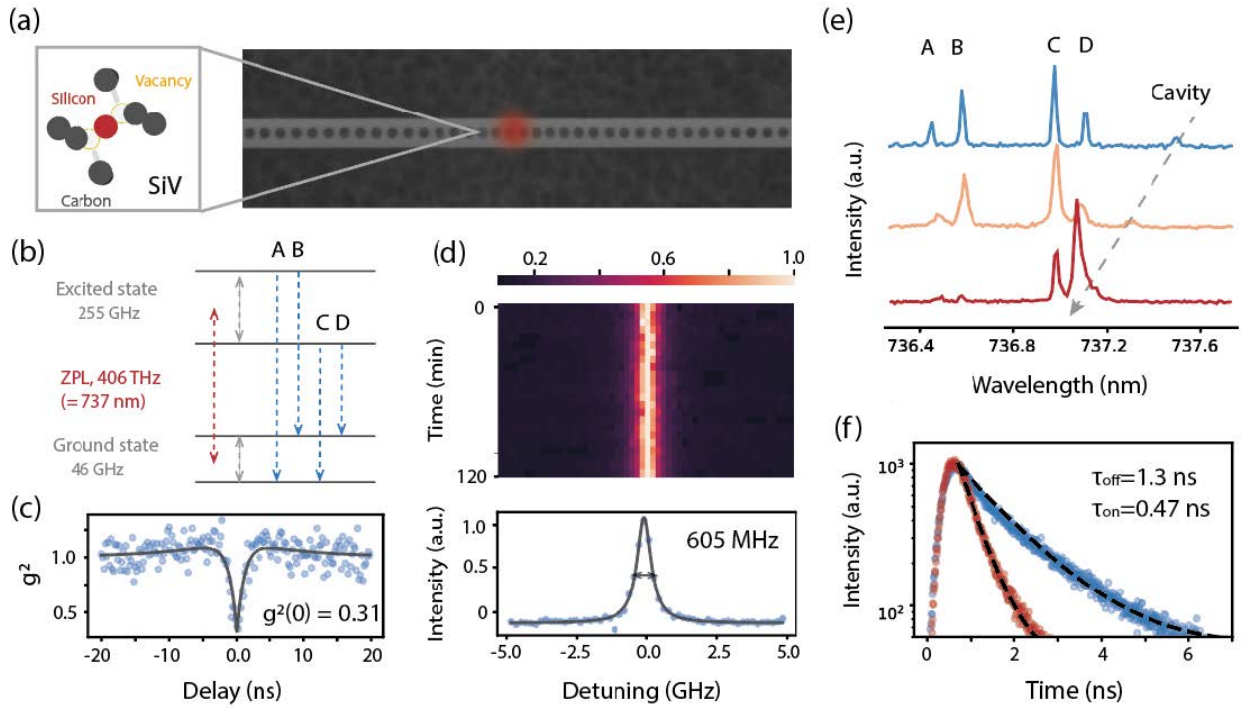

Figure 3.9: Characterization of a SiV⁻ center embedded in an 1D PhC cavity measured at $4\,\mathrm{K}$. (a) An illustration of a SiV⁻ placed close to the center of a 1D PhC cavity. (b) The energy diagram of SiV⁻, featuring four ZPL transitions near $737\,\mathrm{nm}$. (c) Second-order correlation measurement of the C line using resonant excitation. The excitation power is kept low to avoid Rabi-like features in the $g^2(t)$ plot. (d) The ZPL emission profile for a $2\,\mathrm{h}$ scan (upper panel) and a single scan (lower panel). (e) The PL spectra of the cavity-SiV⁻ system. Each spectrum is normalized to the highest peak. (f) Time-resolved PL measurement of the SiV⁻ showing a lifetime reduction with a factor of 3 when the SiV⁻ is on-resonance (red) with the cavity compared to the off-resonance condition (blue). The figure is reproduced from [169].

In this section, we characterize the emitter properties of SiV⁻ inside the nanophotonic cavities. Stable and bright emitters strongly coupled with cavities are required for cavity quantum electro-

dynamics (QED) experiments. To measure the optical coherence of the SiV^-, the measurement is performed at a cryogenic temperature ($4\,\mathrm{K}$). The SiV^-s are formed prior to the cavity fabrication without location control, resulting in randomly distributed centers. In this work, we characterize two SiV^- centers embedded in high-Q cavities. The illustration is shown in Figure 3.9 (a). The energy diagram of SiV^- is plotted in Figure 3.9 (b), showing four ZPL transitions (A to D) near $737\,\mathrm{nm}$ wavelength at $4\,\mathrm{K}$. First, we measure the C transition of the SiV^- at $737.09\,\mathrm{nm}$. The ZPL profile shown in the upper panel of Figure 3.9 (d) has an optical linewidth of $605\,\mathrm{MHz}$ with minimal spectral diffusion in 2 hours (lower panel). This ZPL linewidth is slightly broader than the typical value of ion-implanted SiV^- centers [209], which could possibly caused by the laser broadening, membrane synthesis, cavity fabrication, and measurement temperature [94]. We also measure the second-order correlation ($g^2(t)$) of the SiV using resonant excitation. The measured intensity histogram shown in Figure 3.9 (c) exhibits a clear anti-bunching feature with $g^2(0) = 0.31 \pm 0.12$, confirming the single-photon nature of the SiV^-. The non-zero value of $g^2(0)$ is mostly due to the dark counts of the APD and the spatial drift of the SiV^-.

Lastly, we investigate the coupling between another single SiV^- to a cavity. We choose a cavity with a resonant wavelength of $737.5\,\mathrm{nm}$ and a measured Q factor of 1.2×10^5. The fluorescence of the cavity-SiV^- system is shown in Figure 3.9 (e), including four ZPL peaks and the cavity resonance. We gradually tune the cavity resonance via gas condensation and laser annealing [197], and observe a blue shift of the cavity resonance when applying the annealing laser. When the cavity is on-resonance with the D-peak (red curve in Figure 3.9 (e)), we observe a $\approx$20-fold intensity enhancement of the D line emission compared with the far-detuned conditions ($\Delta \approx 0.4\,\mathrm{nm}$, blue curve in Figure 3.9 (e)). This change of rate suggests that the emission of the SiV^- is improved by the Purcell enhancement.

We conduct a time-resolved PL measurement to quantitatively measure the coupling between the SiV^- and the cavity. The measured PL intensities versus time for on-resonance (red) and off-resonance conditions are plotted in Figure 3.9 (f). By fitting the curves with a single exponential

decay and a constant offset, we obtain the optical lifetime of SiV^- to be $0.470(6)\,\mathrm{ns}$ ($1.30(1)\,\mathrm{ns}$) in on- (off-) resonance conditions. The Purcell factor of the zero-phonon line F_{ZPL} can be estimated by comparing the two lifetimes and taking the fraction of emission ε_{ZPL} into consideration: $F_{ZPL} = \frac{\tau_{off}/\tau_{on}-1}{\varepsilon_{ZPL}}$ [196]. Here ε_{ZPL} is the fraction of the total emission into the D line, which is estimated by the product of the SiV^- Debye-Waller factor ($70\,\%$) [32] and the branching ratio of $19.3\,\%$ at $4\,\mathrm{K}$ [196]. The Purcell factor F_P is estimated by a similar equation: $F_P = \frac{\tau_{off}/\tau_{on}-1}{\varepsilon}$, where $\varepsilon = \frac{\gamma_D}{\gamma_D+\gamma_{rad,other}+\gamma_{nr}}$. Here γ_D, $\gamma_{rad,other}$, and γ_{nr} are the radiative emission of the D line, radiative emission of other ZPL lines, and the phonon sideband, and the non-radiative decay. Using the quantum efficiency $QE = \frac{\gamma_{rad}}{\gamma_{rad}+\gamma_{nr}} = 51\%$ [196], we estimate a Purcell factor F_P of $\approx$18, which is in good agreement with the spectral intensity enhancement. This number is much smaller than the value purely calculated from the cavity performance using $F_P = \frac{3}{4\pi^2}\frac{\lambda^3}{n^3}\frac{Q}{V} = 1.8 \times 10^4$. This large deviation is mainly caused by the large displacement of the SiV^- position with respect to the cavity field maximum due to random bulk implantation and the imperfect alignment between the cavity mode and the emission profile of SiV^-. In the future, mask implantation can be introduced to enable precise location control and improve the coupling with the cavities [62, 68]. Furthermore, we estimate the cooperativity C if the masked implantation is applied. Our system could reach a C of $\geq$440 for critically coupled 1D PhC cavities using experimental values. This number is four times higher than the highest value reported previously [62] and could enable a real strong coupling regime where the coupling strength is comparable or even higher than the cavity and emitter decays.

3.5 Conclusion

In this chapter, we discuss three methods to fabricate nanophotonic cavities based on the diamond membrane platform. The TiO_2 deposition method has minimum requirements for diamond material processing and offers strong evanescent coupling. The fully contact diamond waveguides and ring resonators are compatible with other on-chip photonic devices and are ideal for integrated

photonic applications. The suspended 1D and 2D PhC cavities have record-high quality factors in the visible wavelength. In addition, they can be efficiently coupled to waveguides that can be integrated with fiber optics for quantum networking applications. In the future, nanophotonic fabrication can be integrated with masked implantation to achieve the strong coupling regime between cavities and emitters and unlock novel pathways for efficient spin-photon interface and practical quantum networking systems. Efficient light out-coupling methods that preserve the spin properties of color centers can also be applied for NV^- based quantum sensing applications. Ideally, the diamond membrane platform can enable truly heterogeneous integration of color centers with existing and emerging photonic circuits and act as a functional layer in future photonic systems, which also include thin-film lithium niobate [210], aluminum nitride [211], and CMOS-compatible devices [212].

CHAPTER 4

STRAINED SNV$^-$ CENTERS FOR QUANTUM NETWORKING[†]

Abstract

Group IV centers in diamond are promising candidates for quantum networking applications. However, although they have shown impressive progress recently, their performance and future potential are negatively impacted by millikelvin operation temperature or inconvenient microwave spin manipulation. Here, by applying the HSQ-based transfer method discussed in Chapter 2, we are able to deterministically generate large a strain profile for tin vacancy centers (SnV$^-$) in diamond membranes. This external, in-plane strain profile reduces the phonon population that causes spin depolarization magnitude, improves the SnV$^-$ spin coherence, and elevates the operation temperature. The anisotropic strain also enables efficient coherent spin manipulation between the two qubit states via microwave, greatly improving the gate fidelity. Compared with the all-optical method, this microwave-based manipulation offers straightforward, high-fidelity qubit operations and integration possibilities with on-chip nanophotonics and nuclear spins. Combined with transform-limited optical linewidth in a wide range of temperatures, the strained SnV$^-$ is a prime candidate for practical quantum nodes in quantum networking systems.

4.1 Introduction

In the quantum networking field, group IV centers have shown much greater potential than its predecessor—NV$^-$ centers and have been utilized in a number of landmark demonstrations [62, 108]. Compared with NV$^-$, the group IV centers' D_{3d} symmetry leads to insensitive optical transitions against first-order electric field (charge) noise [60], which significantly suppresses the spectral diffusion against surface spins and nanofabrication processes. Additionally, their inversion symmetry leads to a small displacement of electrons between optical ground and excited states, which

†. The work discussed in this section was reported in [64]

results in a favorable Debye-Waller factor with the majority of photons emitted at the zero phonon line (ZPL) wavelength, which is critical for improving the spin-photon entanglement generation rate [213]. Despite impressive, we have to realize some fundamental differences between group IVs and NV^- centers. The main difference comes from their electronic configurations. The energy levels of NV^- mainly depend on the spin-spin interaction between electrons. Therefore, the spin coherence tends to have a weak coupling with the electron orbits. Even at room temperature, the coherence time of NV^- is often not limited by the spin-phonon interactions which determine the spin lifetime T_1. Furthermore, the spin-spin interaction leads to zero-field splitting. Thus, a small magnetic field would be sufficient to define a spin qubit. In contrast, the electronic structure of group IV centers is mainly determined by the spin-orbit coupling, which splits the ground state into two orbital branches, each with two states belonging to different spin ($S = \pm 1/2$) and orbital configurations. The two quantum states in the lowest branch form a natural qubit choice. However, this qubit does not have zero filed splitting and thus requires a sufficiently large magnetic field to operate (see Figure 1.1 and Figure 1.2). Moreover, the qubit states can interact with energy levels in the upper branch with different orbital states but the same spin. This coupling, which can be easily realized via phonon-driven transitions [76], provides a decoherence channel outside of the qubit subspace. Due to the strong temperature dependence of phonon density, all group IV centers can only be operated at cryogenic temperatures. Specifically, with small spin-orbit coupling ($48\,\mathrm{GHz}$) and thus considerable phonon interaction, SiV^- centers can only be operated at millikelvin temperatures [67, 214] unless local phonon density of states can be engineered through nanostructuring [101]. An alternative approach is to work with group IV centers with larger spin-orbit couplings. These centers typically contain heavier group IV elements, such as SnV^- or PbV^- [89, 215]. Another issue of group IV qubits is the coherent spin manipulation. Unlike NV^- which does not involve orbit change when driving the spin states, group IV centers have different orbits for qubit levels, which naturally prohibits the coherent spin manipulation via microwave (MW). Luckily, with spin-orbit coupling-defined qubit levels, group IV centers tend to have large strain

susceptibility, which enables orbit mixing between qubit states and thus MW spin manipulations. The added strain also offers extra coherence protection via strain engineering [216]. The state-of-the-art strain magnitude can only reach $0.01\,\%$ to $0.02\,\%$ due to the exceptional hardness of diamond [216]. Therefore, they have been mainly use for light group IVs such as SiV^-. Further improvement of the coherence and operation temperature while avoiding operating at a high qubit frequency due to the strong-strain effect requires a combination of large spin-orbit coupling (such as SnV^-, $850\,\mathrm{GHz}$) and moderately large strain profile. These numbers are challenging to reach via current methods, and a controlled process to generate considerable strain is desired to promote heavy group IVs such as SnV^- as coherent and cost-effective quantum networking nodes.

In this chapter, we introduce our approach to generate strained SnV^- centers using our integrated diamond membrane material platform. By bonding diamond membranes containing SnV^- centers to fused silica substrates, we leverage the very different thermal expansion coefficients between diamond and fused silica carriers. Due to the much thinner diamond membrane ($\approx 160\,\mathrm{nm}$) compared with the carrier wafer ($\approx 500\,\mu\mathrm{m}$), the thermal expansion coefficient mismatch generates a large in-plane strain profile on diamond (approaching $0.1\,\%$), which remains uniform across the membrane thickness due to its exceptional rigidness. The strain profile at this level enables the MW manipulation of the SnV^- electron spin and improves the coherence time and operation temperature. We first discuss the physics of SnV^-, including energy levels, related Hamiltonians, and the implication of strain engineering to the center. We will then discuss the device layout and numerical calculation of the strain profile, followed by the spin manipulation and coherence characterizations. Both all-optical and MW-based methods are presented to form a complete basis regarding various spin manipulation protocols.

4.2 Electronic configuration of strained SnV^- centers

In this section, we first introduce the basis of the SnV^- center in the optical ground and excited states based on its group symmetry. We then discuss several Hamiltonian terms of SnV^- that are

important to understanding its physical properties. Depending on the strain profile, the SnV^- can behave differently. Due to the relatively complicated form of eigenvalues and eigenstates when the strain is present, we only calculate the solution with zero strain and provide qualitative discussions regarding the classification of three regimes: low-strain limit, intermediate regime, and high-strain limit. In the following sections, the numerical calculations, physical model of the spin coherence, and microwave manipulation efficiency estimation will be discussed, along with the experimental results.

4.2.1 Hamiltonian of the strained SnV^-

Negatively-charged group IV centers are spin-$1/2$ systems. They share the same D_{3d} point defect symmetry and numbers of electrons. There are a total of seven electrons that matter to the optical and spin properties occupying the $|e_x\rangle$ and $|e_y\rangle$ orbits for ground and excited states, which include eight sites. $|e_x\rangle$ and $|e_y\rangle$ orbits are essentially superpositions of covalent bonds. For the optical ground state, four electrons occupy the $|e_u\rangle$ states, leaving one freedom in the $|e_g\rangle$ states, while one $|e_u\rangle$ state has an unfulfilled hole for the excited state. To keep the consistency with other group IV center studies, we use the same notation as SiV^- to describe the basis of the SnV^- in the ground and excited states [60]:

$$\begin{aligned} {}^2E_g \text{ Ground states:} &\{|e_{gx}\uparrow\rangle, |e_{gx}\downarrow\rangle, |e_{gy}\uparrow\rangle, |e_{gy}\downarrow\rangle\} \\ {}^2E_u \text{ Excited states:} &\{|e_{ux}\uparrow\rangle, |e_{ux}\downarrow\rangle, |e_{uy}\uparrow\rangle, |e_{uy}\downarrow\rangle\} \end{aligned} \tag{4.1}$$

Both ground and excited states are doubly degenerate in terms of orbits and spins. These degeneracies can be lifted by interaction terms, including spin-orbit coupling, external magnetic field (Zeeman effect), and crystal effects (strain). Here we write those interaction terms in the basis we choose: the spin-orbit coupling $\hat{H}_{\text{SO}}$, electron-phonon interaction (Jahn-Teller effect), the strain effect $\hat{H}_{\text{strain}}$ which includes the strain profile and susceptibility, and the Zeeman effect due to static magnetic field $\hat{H}_Z$. Following Ref [60], we combine the Jahn-Teller term with the strain

term since they share the same form. Therefore, the system Hamiltonian including all interaction terms is written as follows:

$$\hat{H}_{\text{sys}} = \hat{H}_{\text{SO}} + \hat{H}_{\text{strain}} + \hat{H}_Z. \tag{4.2}$$

Before diving deeply into the physical properties of the strained SnV^-, we first briefly discuss each term in the Hamiltonian in the next few paragraphs.

Spin-orbit coupling The physics behind the spin-orbit term can be interpreted as an energy shift induced by the interaction between a magnetic dipole and a magnetic field. In this case, the magnetic dipole is the qubit spin, and the magnetic field is generated from the "movement" of an electric field, which is the qubit in certain orbits. Therefore, the spin states are coupled to the orbital states that lift the degeneracy. In general cases, the spin-orbit coupling can be written as $H_{SO} = \frac{\lambda}{2}\hat{\mathbf{L}}\hat{\mathbf{S}}$, where λ is the interaction strength, $\hat{\mathbf{L}}$ is the orbital angular momentum operator, and $\hat{\mathbf{S}}$ is the spin operator. For group IV centers, the orbital angular momentum operators $\hat{L}_x, \hat{L}_y$ vanish due to the group symmetry for the Hamiltonian expressed in the $\{|e_x\rangle, |e_y\rangle\}$ basis [60]. Therefore, only the following $\hat{L}_z$ term is non-zero:

$$\hat{L}_z = \begin{bmatrix} 0 & -i \\ i & 0 \end{bmatrix} \tag{4.3}$$

Here we have set $\hbar$ to 1. In the $\{|e_x\uparrow\rangle, |e_x\downarrow\rangle, |e_y\uparrow\rangle, |e_y\downarrow\rangle\}$ basis, only $\hat{S}_z$ term is coupled to $\hat{L}_z$, and the spin-orbit coupling Hamiltonian can be written as follows:

$$\hat{H}_{SO} = \frac{\lambda}{2}\hat{L}_z\hat{S}_z = \frac{\lambda}{2}\begin{bmatrix} 0 & -i \\ i & 0 \end{bmatrix} \otimes \begin{bmatrix} 1 & 0 \\ 0 & -1 \end{bmatrix} = \begin{bmatrix} 0 & 0 & -i\lambda/2 & 0 \\ 0 & 0 & 0 & i\lambda/2 \\ i\lambda/2 & 0 & 0 & 0 \\ 0 & -i\lambda/2 & 0 & 0 \end{bmatrix}. \tag{4.4}$$

Depending on the specific states, the value of λ varies. For instance, $\lambda_g = 850\,\text{GHz}$ for optical

ground states, while λ_u(or λ_e)$\approx$3000 GHz for excited states.

Strain The strain in the crystal stands for the relative spatial change of atoms from their reference points. Depending on the types of collective spatial shifts, the strain can be categorized into normal strains and shear strains. A common method to analyze strain is to write the strain as a 3×3 tensor $\overleftrightarrow{\epsilon}$. The diagonal elements $\{\epsilon_{xx}, \epsilon_{yy}, \epsilon_{zz}\}$ are normal strains which refer to purely distance change. In contrast, non-diagonal elements $\{\epsilon_{xy}, \epsilon_{xz}, \epsilon_{yz}\}$ are shear strains indicating an angular change of the lattice structure. Here we use the fact that in diamond $\epsilon_{xy} = \epsilon_{yx}$, $\epsilon_{xz} = \epsilon_{zx}$ and $\epsilon_{yz} = \epsilon_{zy}$. We note that the values of strain elements are subject to basis transformations. A strain profile containing only diagonal elements in the lab frame may show non-zero shear strains in the local frame. The strain influences the system via distortion of electron wavefunctions, which is purely an orbital effect. The Hamiltonian can be written as follows:

$$\hat{H}_{\text{strain}} = \begin{bmatrix} \varepsilon_{A_1} - \varepsilon_{E_x} & \varepsilon_{E_y} \\ \varepsilon_{E_y} & \varepsilon_{A_1} + \varepsilon_{E_x} \end{bmatrix} \otimes \mathbb{I}_2. \tag{4.5}$$

Here we group the strain effect elements as $\{\varepsilon_{A_1}, \varepsilon_{E_x}, \varepsilon_{E_y}\}$ according to the irreducible representations $\{A_1, E_x, E_y\}$ of the D_{3d} point group which forms the basis of the group IV defects. Unless specified, the A_1 group is usually not included in most discussions throughout the chapter since it only generates global energy shifts (optical transition frequency) instead of relative shifts within the ground or excited states. It is shown as an identity matrix. We also note that the strain effect elements are expressed in the SnV^-'s local frame, where the z-axis corresponds to the high symmetry axis of the SnV^- along the direction of two split vacancies. The high symmetry axis is also called the quantization axis. The emergence of the quantization axis is another important difference between point defects and free atoms whose quantization can be arbitrarily defined by the external magnetic field. Due to the symmetries of the molecular structures, spin states are

well-quantized only along certain directions, and spin-mixing will appear if the external magnetic field is misaligned with the quantization axis. The spin-mixing feature can be observed via optical cyclicity measurements [67], which will be covered later in this chapter. The terms $\{\varepsilon_{A_1}$, ε_{E_x}, $\varepsilon_{E_y}\}$ can be written as a linear combination of the diagonal $(\epsilon_{xx}, \epsilon_{yy}, \epsilon_{zz})$ and off-diagonal $(\epsilon_{xy}, \epsilon_{yz}, \epsilon_{zx})$ elements in the strain tensor $\overleftrightarrow{\epsilon}$ [63]:

$$\begin{aligned}
\varepsilon_{A_1} &= t_\perp \left(\epsilon_{xx} + \epsilon_{yy}\right) + t_\parallel \epsilon_{zz}, \\
\varepsilon_{E_x} &= d \left(\epsilon_{xx} - \epsilon_{yy}\right) + f\epsilon_{zx}, \\
\varepsilon_{E_y} &= -2d\epsilon_{xy} + f\epsilon_{yz},
\end{aligned} \tag{4.6}$$

Here $\overleftrightarrow{\epsilon}$ is expressed in the local basis of SnV$^-$, where z-direction is along the high symmetry axis and x, y plane is orthogonal to the axis described by Ref [60]. $t_\perp, t_\parallel, d$ and f are four strain-susceptibility parameters describing the strain-response of the ground and excited electronic states categorized by point groups and strain types. Specifically, they are partial derivatives written as $\frac{\partial \varepsilon_{A_1}}{\partial(\epsilon_{xx}+\epsilon_{yy})}, \frac{\partial \varepsilon_{A_1}}{\partial \epsilon_{zz}}, \frac{\partial \varepsilon_{E_x}}{\partial(\epsilon_{xx}-\epsilon_{yy})}, \frac{\partial \varepsilon_{E_x}}{\partial \epsilon_{zx}}$, respectively. In the following texts, we ignore the diagonal term ϵ_{A_1}, which only causes a global emission profile shift. The simplified Hamiltonian can be thus written in the following form:

$$\hat{H}_{\text{strain}} = \begin{bmatrix} -\varepsilon_{E_x} & \varepsilon_{E_y} \\ \varepsilon_{E_y} & \varepsilon_{E_x} \end{bmatrix} \otimes \mathbb{I}_2 = \begin{bmatrix} -\varepsilon_{E_x} & 0 & \varepsilon_{E_y} & 0 \\ 0 & -\varepsilon_{E_x} & 0 & \varepsilon_{E_y} \\ \varepsilon_{E_y} & 0 & \varepsilon_{E_x} & 0 \\ 0 & \varepsilon_{E_y} & 0 & \varepsilon_{E_x} \end{bmatrix}. \tag{4.7}$$

Zeeman The Zeeman effect of spin defects in solids usually includes both orbital and spin terms. Due to the D_{3d} symmetry of the SnV$^-$, the orbital component $H_{Z,L}$ of the Hamiltonian H_Z only includes one single term $\hat{L}_z B_z$ [60]. Unlike the spin term, the orbital term includes a pre-factor q

[85] called *effective reduction factor*. This pre-factor is less than 1, which accounts for (1) electron-phonon interaction (Ham term) and (2) the symmetry of the defect being lower than $O(3)$ (Steven's factor). Both terms have different values for the ground and excited states, leading to different q parameters, which affect the emission wavelength between optical transitions.

The total H_Z Hamiltonian is the sum of an orbital $H_{Z,L}$ and spin component $H_{Z,S}$:

$$\hat{H}_Z = \hat{H}_{Z,L} + \hat{H}_{Z,S} = q\mu_B\gamma_L\hat{L}_z B_z + g\mu_B\hat{\mathbf{S}}\cdot\mathbf{B} - 2\mu_B\delta_f\hat{S}_z B_z \tag{4.8}$$

This expression can be explicitly written as:

$$q\gamma_L\begin{bmatrix} 0 & 0 & -iB_z & 0 \\ 0 & 0 & 0 & -iB_z \\ iB_z & 0 & 0 & 0 \\ 0 & iB_z & 0 & 0 \end{bmatrix} + \frac{\gamma_S}{2}\begin{bmatrix} (1-2\delta_f)B_z & B_x - iB_y & 0 & 0 \\ B_x + iB_y & -(1-2\delta_f)B_z & 0 & 0 \\ 0 & 0 & (1-2\delta_f)B_z & B_x - iB_y \\ 0 & 0 & B_x + iB_y & -(1-2\delta_f)B_z \end{bmatrix} \tag{4.9}$$

where μ_B is the Bohr magneton and B_x, B_y, B_z are the components of the external, static magnetic field along the x, y, z directions in the local SnV^- frame, respectively. The last term $2\mu_B\delta_f\hat{S}_z B_z$ originates from correcting with a factor δ_f the electronic Landé g factor to account for spin-phonon interaction mediated by spin-orbit coupling [85]. In the following discussions, we will only use the Ham factor and set Steven's factor as 1 ($\delta_f = 0$) except for the experimental interpretation of optical splitting with external magnetic field in section 4.4, where we give estimates on the possible values of Steven's factor.

Stark effect SnV^- belongs to the D_{3d} point group, which indicates an inversion symmetry of its electronic wavefunction (no permanent dipole). Therefore, the ZPL emission wavelength is first-order insensitive to the external electric field (no first-order Stark shift). Although this feature reduces the spectral drift of the ZPL wavelength which is beneficial for consistent entanglement generation [73], the insensitivity leads to challenging ZPL wavelength tuning via second or higher order Stark effect which is necessary for spectral alignment and indistinguishable photon gener-

ation [217, 218]. Therefore, some recent demonstrations studied an alternative method utilizing electro-optic modulators (EOMs) for external spectral alignment [23]. Since the work discussed here does not involve any active spectral tuning method, we will omit the Stark effect Hamiltonian term in this chapter. In Chapter 6, we will come back to the Stark effect induced by nearby charge fluctuations.

4.2.2 SnV^- in different strain regime

Zero strain When zero strain is present, the system Hamiltonian can be expressed as

$$\hat{H}_{sys} = \hat{H}_{SO} + \hat{H}_Z \tag{4.10}$$

If we use $B_+ = B_x + iB_y$ to express the misaligned magnetic field, The eigenvalues and corresponding eigenstates of H_{sys} are:

$$\begin{aligned}
\lambda_1 &= q\mu B_z - \tfrac{1}{2}\sqrt{4\mu^2 B_+^2 + (2\mu B_z + \lambda_{SO})^2} \\
\lambda_2 &= q\mu B_z + \tfrac{1}{2}\sqrt{4\mu^2 B_+^2 + (2\mu B_z + \lambda_{SO})^2} \\
\lambda_3 &= -q\mu B_z - \tfrac{1}{2}\sqrt{4\mu^2 B_+^2 + (2\mu B_z - \lambda_{SO})^2} \\
\lambda_4 &= -q\mu B_z + \tfrac{1}{2}\sqrt{4\mu^2 B_+^2 + (2\mu B_z - \lambda_{SO})^2}
\end{aligned} \tag{4.11}$$

$$\begin{aligned}
|1\rangle &= |e_+\rangle \otimes \left[|\downarrow\rangle - \frac{2\mu B_+}{\lambda_{SO}+2\mu B_z+\sqrt{4\mu^2 B_+^2+(2\mu B_z+\lambda_{SO})^2}} |\uparrow\rangle \right] \\
|2\rangle &= |e_+\rangle \otimes \left[|\uparrow\rangle + \frac{2\mu B_+}{\lambda_{SO}+2\mu B_z+\sqrt{4\mu^2 B_+^2+(2\mu B_z+\lambda_{SO})^2}} |\downarrow\rangle \right] \\
|3\rangle &= |e_-\rangle \otimes \left[|\uparrow\rangle - \frac{2\mu B_+}{\lambda_{SO}-2\mu B_z+\sqrt{4\mu^2 B_+^2+(2\mu B_z-\lambda_{SO})^2}} |\downarrow\rangle \right] \\
|4\rangle &= |e_-\rangle \otimes \left[|\downarrow\rangle + \frac{2\mu B_+}{\lambda_{SO}-2\mu B_z+\sqrt{4\mu^2 B_+^2+(2\mu B_z-\lambda_{SO})^2}} |\uparrow\rangle \right]
\end{aligned} \tag{4.12}$$

Due to the relatively small Zeeman effect ($g\mu_B\hat{\mathbf{S}}\cdot\mathbf{B}$) compared with the spin-orbit coupling λ_{SO}, the eigenvalues λ_1 and λ_3 are the qubit states of the SnV^-, with eigenvalues belonging to two orthogonal orbits ($|e_+\rangle$ and $|e_-\rangle$). Since MW spin manipulation efficiency is correlated with the Zeeman effect of the oscillating magnetic field ($H_{MW} = H_Z^{ac}$), MW drive is not viable for strain-free SnV^- spin control and all-optical Raman-based method should be used instead [71]. The parameter $\frac{2\mu B_+}{\lambda_{SO}\pm 2\mu B_z+\sqrt{4\mu^2 B_+^2+(2\mu B_z+\lambda_{SO})^2}} \approx \frac{\mu B_+}{\lambda_{SO}}$ is the β factor indicating the misalignment of the spin quantization axis with respect to the high symmetry axis (usually very small) and can be used to estimate the optical cyclicity, which is the ratio of spin conserving and flipping transition intensities between ground and excited states.

Non-zero strain With the strain Hamiltonian added to H_{sys}, the exact solution of eigenvalues and eigenstates becomes complicated and hard to interpret, and numerical calculations must be implemented. However, we can first take a look at a simpler case, a strained SnV^- at zero magnetic field:

$$\hat{H}_{sys} = \hat{H}_{SO} + \hat{H}_{strain} \tag{4.13}$$

The exact solution of this Hamiltonian can be written as:

$$\begin{aligned}
-\sqrt{\varepsilon_{E_{gx}}^2+\varepsilon_{E_{gy}}^2+(\tfrac{\lambda_{SO}}{2})^2}\begin{cases} |e_A\uparrow\rangle &= \frac{1}{\sqrt{\alpha^2+|\beta|^2}}\left(\alpha|e_x\uparrow\rangle+\beta|e_y\uparrow\rangle\right)\\ |e_B\downarrow\rangle &= \frac{1}{\sqrt{\alpha^2+|\beta|^2}}\left(\alpha|e_x\downarrow\rangle+\beta^*|e_y\downarrow\rangle\right)\end{cases}\\
+\sqrt{\varepsilon_{E_{gx}}^2+\varepsilon_{E_{gy}}^2+(\tfrac{\lambda_{SO}}{2})^2}\begin{cases} |e_C\uparrow\rangle &= \frac{1}{\sqrt{\gamma^2+|\beta|^2}}\left(\gamma|e_x\uparrow\rangle+\beta|e_y\uparrow\rangle\right)\\ |e_D\downarrow\rangle &= \frac{1}{\sqrt{\gamma^2+|\beta|^2}}\left(\gamma|e_x\downarrow\rangle+\beta^*|e_y\downarrow\rangle\right)\end{cases}
\end{aligned} \tag{4.14}$$

where $\alpha = -\sqrt{\varepsilon_{E_{gx}}^2+\varepsilon_{E_{gy}}^2+(\frac{\lambda_{SO}}{2})^2}-\varepsilon_{E_{gx}}$, $\beta = \varepsilon_{E_{gy}}+i\lambda_{SO}/2$, and $\gamma = \sqrt{\varepsilon_{E_{gx}}^2+\varepsilon_{E_{gy}}^2+(\frac{\lambda_{SO}}{2})^2}-\varepsilon_{E_{gx}}$. Since the strain Hamiltonian only affects the orbital part of the SnV^-, it cannot lift the full degeneracy of ground or excited states, leading to two branches. The

lowest energy branch with eigenvalue $-\sqrt{\varepsilon_{E_{gx}}^2+\varepsilon_{E_{gy}}^2+(\frac{\lambda_{SO}}{2})^2}$ is the qubit subspace, still with no zero-field splitting and requires an external magnetic field to remove the degeneracy. Looking at the orbital part of the eigenstates, we can immediately observe the difference compared with the strain-free case. First, the presence of strain effectively increases the energy splitting between branches (from λ_{SO} to $2\sqrt{\varepsilon_{E_{gx}}^2+\varepsilon_{E_{gy}}^2+(\frac{\lambda_{SO}}{2})^2}$), which is beneficial to coherence protection against phonon decay as discussed in subsequent sections. Second, the orbital states in the qubit subspace are $|e_A\rangle = \frac{1}{\sqrt{\alpha^2+|\beta|^2}}\left(\alpha\,|e_x\rangle + \beta\,\left|e_y\right\rangle\right)$ and $|e_B\rangle = \frac{1}{\sqrt{\alpha^2+|\beta|^2}}\left(\alpha\,|e_x\rangle + \beta^*\,\left|e_y\right\rangle\right)$, with non-zero orbit overlap:

$$\langle e_A|e_B\rangle = 1 - \frac{\frac{\lambda_{SO}}{2}(\frac{\lambda_{SO}}{2} - i\varepsilon_{E_{gy}})}{\sqrt{\varepsilon_{E_{gx}}^2+\varepsilon_{E_{gy}}^2+(\frac{\lambda_{SO}}{2})^2}(\varepsilon_{E_{gx}}+\sqrt{\varepsilon_{E_{gx}}^2+\varepsilon_{E_{gy}}^2+(\frac{\lambda_{SO}}{2})^2})} \tag{4.15}$$

This deviation from orthogonal orbitals enables MW transitions between qubit states, with the efficiency depending on the overlap magnitude regardless of the strain magnitude. Therefore, implantation-induced local strain can enable the MW manipulation of some centers [70].

Technically, there is no clear definition of the boundary of the strain regimes. Qualitatively speaking, the low-strain limit indicates a regime dominated by the spin-orbit coupling ($\varepsilon_{E_{gx}}^2+\varepsilon_{E_{gy}}^2 \ll (\frac{\lambda_{SO}}{2})^2$), while high-strain limit indicates much stronger strain magnitude compared with spin-orbit coupling ($\varepsilon_{E_{gx}}^2+\varepsilon_{E_{gy}}^2 \gg (\frac{\lambda_{SO}}{2})^2$). For instance, in the low strain limit, the overlap between $|e_A\rangle$ and $|e_B\rangle$ states can be simplified as: $|\langle e_A|e_B\rangle| \approx \sqrt{(\varepsilon_{E_{gx}}^2+\varepsilon_{E_{gy}}^2)/(\frac{\lambda_{SO}}{2})^2}$. In the high strain limit, however, $|\langle e_A|e_B\rangle| \approx 1$, indicating almost identical orbits for both qubit states with maximum MW drive efficiency.

4.3 System parameters and device realization

4.3.1 Strain susceptibility

SnV^- has four strain susceptibility parameters: $t_\perp, t_\parallel, d$, and f. Here we focus on ε_{E_x} and ε_{E_y} strain which only involves two parameters d and f. If we look at the strain Hamiltonian in Eq. 4.7 and diagonalize it, we can find the energy difference $\triangle_{\text{gs(es)}}$ that lifts the degeneracy of the ground (gs) and excited (es) states:

$$\triangle_{\text{gs(es)}} = 2\sqrt{[d_{\text{gs(es)}}(\epsilon_{xx} - \epsilon_{yy}) + f_{\text{gs(es)}}\epsilon_{zx}]^2 + [-2d_{\text{gs(es)}}\epsilon_{xy} + f_{\text{gs(es)}}\epsilon_{yz}]^2}, \tag{4.16}$$

Here, the d and f parameters for ground and excited states are computed from density functional theory (DFT) calculations. The functionals for this calculation include PBE [219] and SCAN [220]. The supercell consists of 511 atoms with a [0.5, 0.5] occupation number for the $|e_x \downarrow\rangle, |e_y \downarrow\rangle$ orbitals. The splittings $\triangle_{\text{gs(es)}}$ are approximated by the energy difference of the corresponding Kohn-Sham (KS) orbitals, and the strain susceptibilities $d_{\text{gs}}, d_{\text{es}}, f_{\text{gs}}, f_{\text{es}}$ are obtained from Eq. 4.16 by artificially modifying the lattice parameters of the supercell to generate $(\epsilon_{xx} - \epsilon_{yy})$, ϵ_{zx}, ϵ_{xy}, and ϵ_{yz} strains. The results from both functionals are summarized in Table 4.1, showing similar values. Combined with the strain profile simulation, these numbers are used for estimating the strain response of SnV^- in the following sections.

Functional	d_{gs}	d_{es}	f_{gs}	f_{es}
PBE	0.787	0.956	-0.562	-2.555
SCAN	0.834	0.921	-0.563	-2.592

Table 4.1: Computed strain susceptibilities (see text) of the SnV^- in diamond, numbers are in units of PHz/strain, which are obtained with the PBE and SCAN functionals.

4.3.2 Strain magnitude simulation

Simulation model We use COMSOL Multiphysics$^{@}$ to simulate the strain profile of the diamond membrane bonded to the fused silica substrates via HSQ. Specifically, we choose to bond the membrane onto a pre-patterned substrate with an etched trench to reduce the fluorescence background of HSQ and introduce some strain variation across the diamond. Since the strain effect ε in Eq. 4.5 is defined in local SnV frame while the simulation result $\tilde{\epsilon}$ belongs to the lab frame, a series of rotation operations are applied. In the lab frame, the edges of the diamond belong to the $\langle 100 \rangle$ set, which is in parallel with the lab axes $\{x, y, z\}$, while in the local frame, one direction in the $\langle 111 \rangle$ set is the z' direction. From $\langle 100 \rangle$ to $\langle 110 \rangle$ to $\langle 111 \rangle$, the rotation operators are thus a combination of $\hat{R}_z(45^\circ)$ and $\hat{R}_y(54.7^\circ)$:

$$\epsilon = \hat{R}_y^\dagger(54.7^\circ)\, \hat{R}_z^\dagger(45^\circ)\, \tilde{\epsilon}\, \hat{R}_z(45^\circ)\, \hat{R}_y(54.7^\circ) \tag{4.17}$$

Here $\hat{R}_y(\theta)$ and $\hat{R}_z(\theta)$ refer to:

$$\hat{R}_y(\theta) = \begin{bmatrix} \cos(\theta) & 0 & \sin(\theta) \\ 0 & 1 & 0 \\ -\sin(\theta) & 0 & \cos(\theta) \end{bmatrix}, \qquad \hat{R}_z(\theta) = \begin{bmatrix} \cos(\theta) & -\sin(\theta) & 0 \\ \sin(\theta) & \cos(\theta) & 0 \\ 0 & 0 & 1 \end{bmatrix} \tag{4.18}$$

In the actual simulation, we use a three-dimensional (3D) geometry for the device layout, as shown in Figure 4.1 (a). Except for the length of the carrier wafer ($350\,\mu\mathrm{m}$ instead of $7\,\mathrm{mm}$), all other parameters match the experimental values. The temperature-dependent thermal expansion coefficient of diamond and fused silica are obtained from Ref [221–224]. According to Ref [168], HSQ is healed with a condensed molecular structure at a temperature of $\approx 450\,^\circ\mathrm{C}$. Therefore, we choose $450\,^\circ\mathrm{C}$ as the initial strain-free temperature and $4\,\mathrm{K}$ as the final temperature, which is the cryo-

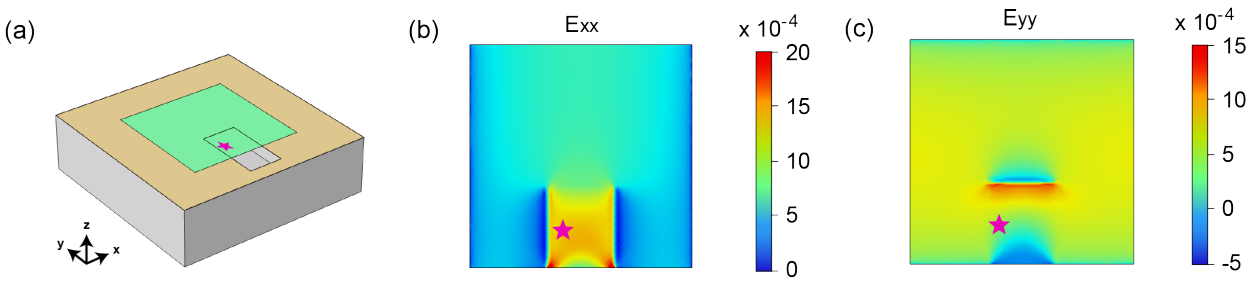

Figure 4.1: Simulated strain profile of the diamond membrane. (a) The 3D structure of the simulated device. The green membrane is the diamond, the brown layer is the HSQ, and the grey substrate is the fused silica substrate. The total length of the carrier wafer is limited to $350\,\mu\mathrm{m}$. (b-c) The $\tilde{\epsilon}_{xx}$ (E_{xx}) and $\tilde{\epsilon}_{yy}$ (E_{yy}) strain profile of the membrane. The region of the SnV^- centers characterized experimentally is labeled as a red star.

genic temperature of our setup. We note that thermal expansion coefficients of both fused silica and diamond become negligible below $30\,\mathrm{K}$; thus, this simulated strain profile is valid within the temperature range of interest ($1.7\,\mathrm{K}$ to $7\,\mathrm{K}$) in this study.

Simulation result The simulated strain $\tilde{\epsilon}_{xx}$ and $\tilde{\epsilon}_{yy}$ are shown in Figure 4.1 (b)-(c). We note that in the lab frame, the thermal-induced positive tensile strain is confined in the xy plane, which only induces a non-zero negative strain along z (Poisson's ratio), and the off-diagonal shear strain is 2-3 orders of magnitude smaller than the diagonal ones. Therefore, we neglect the off-diagonal strain values in the lab frame and use the following matrix to represent the simulated strain profile:

$$\tilde{\epsilon} = \begin{bmatrix} 1.3e^{-3} & 0 & 0 \\ 0 & 6.8e^{-4} & 0 \\ 0 & 0 & -2.5e^{-4} \end{bmatrix}, \qquad \epsilon = \begin{bmatrix} 1.6e^{-4} & -1.8e^{-4} & 5.8e^{-4} \\ -1.8e^{-4} & 9.9e^{-4} & -2.5e^{-4} \\ 5.8e^{-4} & -2.5e^{-4} & 5.8e^{-4} \end{bmatrix} \tag{4.19}$$

Although $\tilde{\epsilon}$ only includes diagonal elements, the transformed strain tensor ϵ in SnV^-'s local frame contains non-negligible off-diagonal elements which also affect the properties of the center through d and f parameters. Later in the chapter, we will compare the experimental data with the simulated

strain profile and susceptibilities.

4.3.3 Microwave signal delivery

System design We use the fabrication technique discussed in Chapter 2 to generate highly strained diamond membranes on fused silica substrates. The diamond membrane sits on top of a pre-patterned substrate with a $5\,\mu\mathrm{m}$-deep etched trench to reduce the HSQ fluorescence background. When the diamond membrane device is ready for measurement post transfer and etching, we fabricate an on-chip coplanar waveguide (CPW) to deliver microwave signals to target SnV^- centers. Compared with wire-bonded metal striplines [225], the lithography-defined CPW offers more deterministic and reproducible microwave signal delivery at the target location. In this work, most of the CPW waveguides are designed to have 50 Ω impedance to match the rest of the electronics in the setup. Based on the permittivity of the fused silica (≈ 3.7), the width of the center and the gap is set to $60\,\mu\mathrm{m}$ and $6\,\mu\mathrm{m}$ to be compatible with the resolution of the photo-lithography. To enhance the local field strength near the SnV^- region, the center of the CPW is reduced to $6\,\mu\mathrm{m}$ around the fused silica trench. The ground lines of the CPW waveguide are designed to go around the membrane to be compatible with the trench design while offering a balanced microwave delivery mode. Although this design could be further optimized based on the permittivity of diamond and the membrane thickness, the special design near the diamond membrane area has a much smaller footprint compared with the MW wavelength and introduces small signal reflection. In addition, we use a two-port microwave transmission design, which has the potential to drive centers in multiple on-chip devices in the future. The two-port design also allows the microwave signal to be transmitted and dissipated/measured outside of the chamber, relaxing the requirements for reflected signal management (such as circulator) and allowing for more accurate MW signal strength estimation. The microscope image of the CPW on the chip is shown in Figure 4.2 (a), with the transmission data of an identical device shown in Figure 4.2 (b). The transmission loss is relatively low from DC to $15\,\mathrm{GHz}$, with microwave loss $P_{\text{in}} - P_{\text{out}} - P_{\text{reflected}}$ (mostly thermal dissipation) to be 1.5

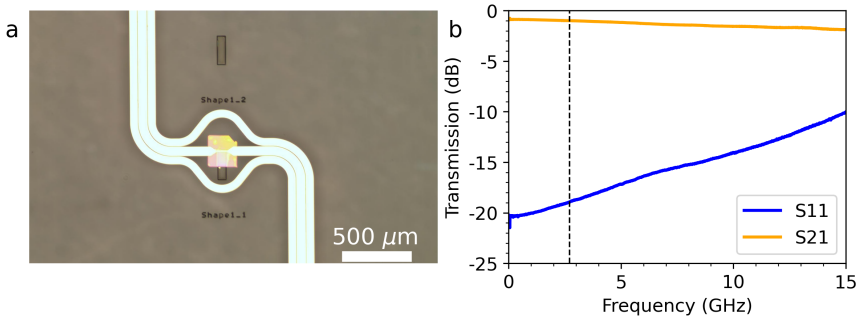

Figure 4.2: Microwave signal delivery via CPW. (a) Microscope image of the CPW. The bonding pad for wire bonding is not included. The middle region is the bonded diamond membrane with a pre-defined trench. (b) The transmission of the CPW measured via a probe station using a vector network analyzer (VNA). The S11 is the reflection spectrum, while the S21 is the transmission. The operation frequency used in this work (2.75 GHz) is labeled as a black dashed line.

dB around the operation point of this work (2.75 GHz).

MW field simulation The electromagnetic field simulation is also performed via COMSOL Multiphysics$^{@}$. The simulation model is shown in Figure 4.3 (a). In the simulation, we set the MW drive power to 24 dBm at frequency 2.75 GHz. The characteristic impedance of the CPW (the yellow rectangle in Figure 4.3 (a)) is set to 50Ω. The width of the signal line is 6 µm, consistent with the device layout. The magnetic field distribution is presented in Figure 4.3 (b). Based on the simulation results, we expect the effective magnetic field that is applied to the color centers 3 µm to 10 µm away ranges from 5 mT to 1 mT, corresponding to a transverse B field of 3 mT to 0.6 mT in the local SnV^- frame.

4.4 Properties of strained SnV^- centers

4.4.1 Device layout

In previous sections, we have discussed the device design and fabrication process. This section will focus on the optical and spin properties of SnV^- centers in the strain diamond membrane at cryogenic temperatures. This strain is generated through heterogeneous thermal expansion dispar-

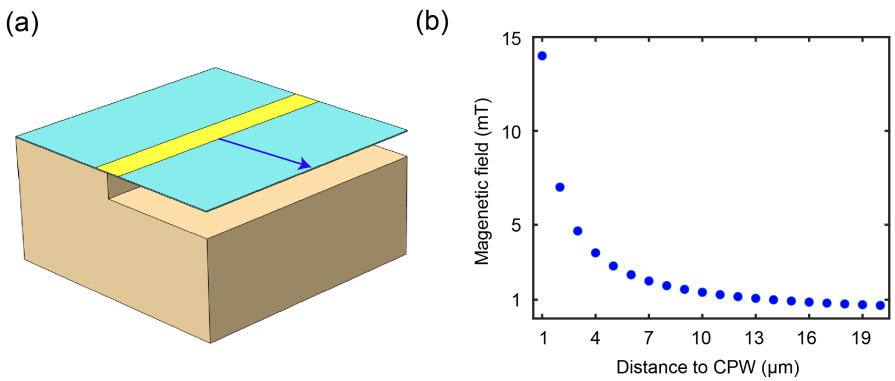

Figure 4.3: Simulation of the microwave field in diamond membrane. (a) The 3D structure of the simulated device. The length (width) of the suspended diamond membrane is set to $50\,\mu\mathrm{m}$ ($25\,\mu\mathrm{m}$). The MW signal has a width of $6\,\mu\mathrm{m}$. The sample is half-suspended to imitate the real device layout. (b) The magnetic field distribution in the diamond membrane as a function of distance to the CPW. The simulated depth is $40\,\mathrm{nm}$ from the top surface of the diamond, and the simulated position is labeled as a blue arrow in (a).

ities between diamond and fused silica and affects the SnV^- via strain susceptibility parameters d and f. Fused silica's much smaller thermal expansion coefficient results in a positive, tensile strain to the SnV^-. The schematic of this strain generation process is shown in Figure 4.4 (a). This uniform thermal strain is passive, which is complimentary to some recent demonstrations utilizing electromechanically-induced strain [79, 216]. Figure 4.4 (b) is the detailed microscope image of the diamond-membrane heterostructure device from Figure 4.2 (a).

4.4.2 PL spectra of SnV^-

We apply a widely-used optical method called confocal microscopy to directly measure the PL properties of SnV^- centers [226]. This method has a sub-micrometer ($\approx 300\,\mathrm{nm}$) lateral resolution and is ideal for characterizing spatially apart individual emitters. As discussed in section 4.2.2, the crystal strain monotonically increases the orbital splitting of SnV^- centers, and this effect can be captured by their PL spectra at cryogenic temperature, which is $1.7\,\mathrm{K}$ in this work. The energy level diagram is shown in Figure 4.4 (c), which highlights the ground and excited state orbital splitting (Δ_{gs}, Δ_{es}) and the corresponding contributions of spin-orbit coupling, strain, and

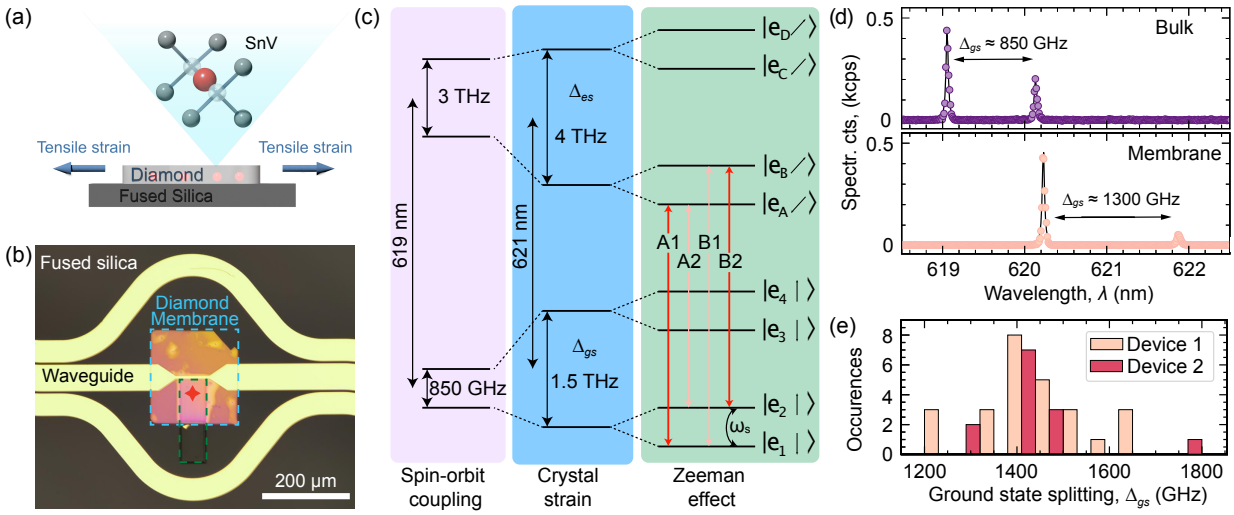

Figure 4.4: Strained SnV^- in diamond membrane heterostructures. (a) The schematic of the diamond-fused silica heterostructure. The static tensile strain inside the membrane is generated from the disparity of thermal expansion coefficients between diamond and fused silica. (b) The microscope image of the diamond membrane (dashed cyan region) bonded to the fused silica substrate. A trench (dashed green region) was fabricated before bonding. The gold coplanar waveguide is fabricated post bonding to introduce microwave signals. A red star highlights the location of the SnV^- center used in this study. (c) The energy level of strained SnVs. Unstrained, strained, and strained centers in the presence of a magnetic field are colored purple, blue, and green, respectively. (d) The PL spectrum of a strained SnV^- center (orange), showing a red-shifted zero-phonon line (ZPL) wavelength with a much larger ground-state splitting compared with the values in bulk diamond (purple). (e) The statistics of the SnV^- ground-state splitting. Two different devices with identical layouts are measured. Device 1 (pink) is used for all-optical spin control (discussed in the SI), and device 2 (red) is used for microwave spin control.

magnetic Zeeman interaction in purple, blue, and green boxes. When the magnetic field is absent, two main ZPL lines are observable under off-resonant excitation (green laser, $532\,\mathrm{nm}$): C line between lower branches of optical ground and excited states, and D line between the upper branch of optical ground state and the lower branch of optical excited state. A and B lines connecting the upper branch of the excited state are normally missing for SnV^- due to much faster phonon decay processes to the lower branch instead of optical transition at such a high energy ($3\,\mathrm{GHz}$ to $4\,\mathrm{GHz}$). The ZPL peaks are named according to Ref [60]. The C and D lines of typical SnV^- spectra in strained membrane and bulk diamond are shown in Figure 4.4 (d), with a stark contrast of energy differences between the two ZPL lines (ground state splitting between two branches) showing $\Delta_{gs} = \approx 1300(850)\,\mathrm{GHz}$, respectively.

We emphasize that the strain generation is a deterministic process, and all SnV^- centers in the membrane are comparably strained. As shown in Figure 4.4 (e), we observed a distribution of the orbital branches splitting Δ_{gs} centered around $1500\,\mathrm{GHz}$ across different devices with a minimum (maximum) value of $1200(1800)\,\mathrm{GHz}$. Using the DFT strain susceptibility results, we estimate a diamond membrane strain magnitude of $0.075\,\%$ according to the simulated strain profile. This number is about 0.55 times of the simulated value, as shown in Figure 4.5. This magnitude mismatch could come from the inaccurate approximation of energy splittings from KS orbitals, the mismatch of the thermal expansion ratios between COMSOL$^{@}$ simulation and reality, or a lower softening temperature of HSQ rather than the reported healing temperature [168]. In the following discussions, we add this 0.55 pre-factor to the strain profile to best capture the system properties. Nonetheless, the magnitude of the strain ϵ is 5 to 10 times larger than the previous reported values [63, 68].

The SnV^- strain regime As mentioned in previous sections, there is no exact description to categorize the strain magnitude to different regimes. In this work, we qualitatively make the judgment via the ground state energy splitting Δ_{gs}. In the low-strain regime, the energy splitting is close to the spin-orbit coupling strength, which is nearly constant, while in the high-strain regime, the

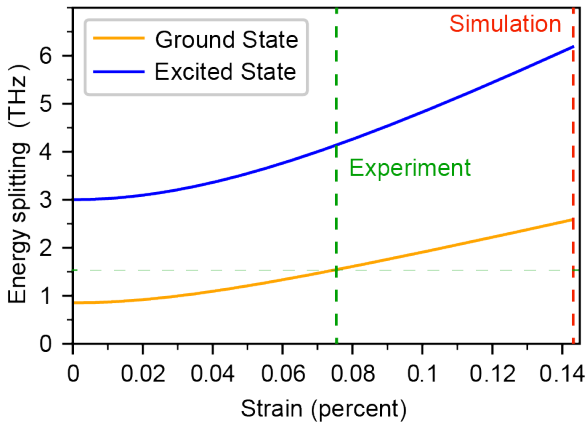

Figure 4.5: Strain profile comparison between simulated and experimentally measured results using the energy splitting between two orbital branches in ground and excited states. The simulated and experimentally observed strain magnitudes are labeled in dashed red and green lines, respectively. The DFT-simulated strain susceptibility parameters are used. The real strain profile is considered to be the COMSOL$^{@}$ simulated strain profile times a scalar pre-factor, which is 0.55 in this case.

splitting scales linearly with the strain magnitude. Guided by that, we use $\Delta_{gs} = 1200\,\mathrm{GHz}$ as the boundary between low-strain and intermediate regimes, and $\Delta_{gs} = 2600\,\mathrm{GHz}$ between intermediate and high-strain regimes. For our strain profile, these values translate to strain magnitudes of $0.055\,\%$ and $0.143\,\%$. Therefore, most of SnV^- centers in diamond membranes fall into the intermediate strain regime where spin-orbit coupling and crystal strain have comparable effects, and numerical calculations has to be applied to estimate the system properties.

4.4.3 Emission properties of strained SnV^-

Polarization One concern of the strained SnV^- centers is the potential change of the polarization profile. At zero strain, the polarization of SnV^- ZPL photons depends on their molecular orientations and can be categorized as two groups if $\langle 100 \rangle$ diamond is used. We probe the polarization of the strained SnV^- centers via a motor-mounted half-wave plate and a linear polarizer in the detection path. The photon emission intensity of the C and D lines with respect to the polarizer angle in the lab frame is shown in Fig 4.6 (no external magnetic field). Both figures indicate the same

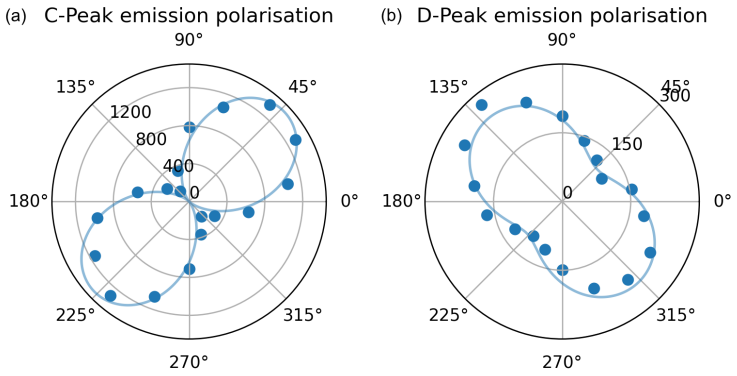

Figure 4.6: Intensity of the (a) C line and (b) D line PL emission of SnV^- over linear polarization in the lab-frame, showing negligible difference from strain-free group IV centers. The solid lines are fitting curves of the expected polarization, which is linear for the C line and circular for the D line. They are projected to the lab frame according to the model in Ref [60].

polarization profile as bulk group IV color centers, indicating that the polarization does not change when a strain of this magnitude is introduced.

Optical lifetime Another concern of the strained SnV^- is their optical lifetime when living in strained thin film diamond, a very different dielectric environment from bulk diamond. In this work, we perform the optical lifetime measurement by resonantly driving the C line at the zero magnetic field with an EOM, followed by an abrupt turning off while observing the emission intensity decay. The fall time of the EOM is $\approx 200\,\mathrm{ps}$. As shown in Figure 4.7, the decay time of a typical strained SnV^- is $4.93(19)\,\mathrm{ns}$ with a single exponential decay profile, which is similar to the bulk value [215]. Typically, the lifetime is expected to extend for shallow-doped centers due to the refractive index variation. This is observed at another SnV^- measured in the next section. However, we note that the dielectric environment is not the only factor that affects the optical lifetime, as additional non-radiative decay channels on the diamond surface could also reduce the lifetime [227], which seems to be the case for this particular center.

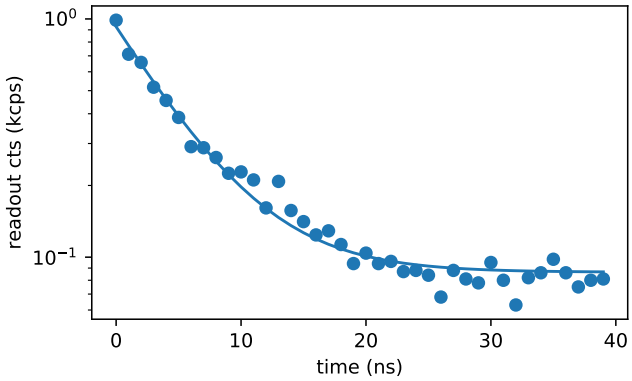

Figure 4.7: Optical lifetime measurement of the C line. The solid line is the fitting curve with a single-exponential, showing a decay time of $4.93(19)$ ns.

4.4.4 Optical properties with magnetic field

After obtaining the optical properties of the SnV^- at the zero magnetic field, we first measure the optical transitions of SnV^- as a function of the magnetic B field orientation and verify that the symmetry of the defect is still preserved even under considerable strain. Here we use the $\langle 111 \rangle$ crystal axis, the high symmetry axis of SnV^- as the z direction, and rotate the B field in both polar (θ) and azimuthal (ϕ) angles while keeping its magnitude the same ($0.2\,\mathrm{T}$). We focus on two specific optical transitions, the spin-conserving transitions in the C line group with labels A1 and B2 shown in Figure 4.4 (c). The optical cyclicity and energy splitting of the two transitions are critical for the later SnV^- spin initialization, all-optical spin manipulation, and spin readout. The absolute energy splitting between the two spin-conserving transitions (A1-B2) with respect to the angles θ and ϕ is shown in Figure 4.8. First, we find from this observation that large splittings at moderate B field angles are achievable ($6\,\mathrm{GHz\,T^{-1}}$), which is ideal for high-fidelity spin initialization and control. Second, there is little correlation between energy splittings and ϕ angles, indicating a ϕ rotational symmetry of the splitting with respect to $\langle 111 \rangle$—the intrinsic spin quantization axis of SnV^-—which is similar to the zero strain case.

Optical splitting with external B field Although there are quite some similarities between the result in Figure 4.8 and the strain-free SnV^-'s, we have to note that besides the normal A1-B2

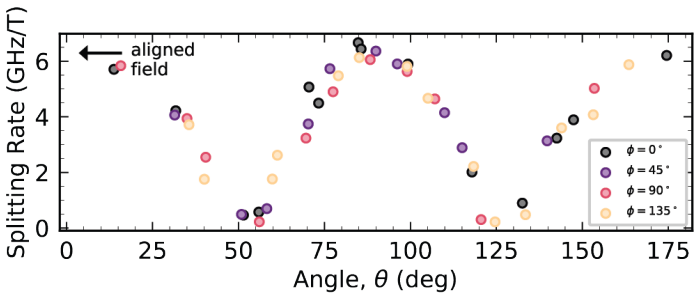

Figure 4.8: The energy splitting rate between the A1-B2 spin conserving transitions with respect to the polar angle θ of the applied magnetic field at different azimuthal angle ϕ. The aligned field is highlighted with a black arrow. The measurement is performed at $1.7\,\mathrm{K}$.

splitting maximum along the quantization axis, an additional local maximum at $\theta = 90°$—the equator plane perpendicular to the quantization axis—is observed, where no splitting is expected at the zero strain case.

To quantitatively understand this phenomenon, we perform a full 3D scan of the B field orientation with approximately equal θ and ϕ spacings, with the (flattened) measurement result shown in Figure 4.9 (a). We also numerically calculate the energy of the $A1, B2$ optical transitions with varying B field orientations by diagonalizing the system Hamiltonian H_{sys} of Eq. 4.2, with results displayed in Figure 4.9 (b)-(c). When constructing the Hamiltonian H_{sys}, we regard Steven's terms g_L (in ground and excited states) in the reduction factor q as free parameters and determine the range of it to match the experimental values. The difference of the splitting magnitude when the B field is aligned with the quantization axis ($\theta = 0$) and aligned along the equator ($\theta = \pi/2$) is plotted in Figure 4.9 (c) with varying $g_L \in [0, 1]$ in ground and excited states. The white region refers to the $g_{L,gs}$ and $g_{L,es}$ pairs that match the experimental values when taking into the system Hamiltonian. In short, this novel feature arises from the moderate crystal strain regime, which is mainly visible for a magnetic field orthogonal to the spin-orbit-dictated quantization axis.

Spin-conserving transitions in different strain regimes Based on the simulation and experiment values, we numerically explore the spin-conserving transition splittings in different strain regimes. To plot the optical transitions, the magnetic field B is set to $80\,\mathrm{mT}$ along the quantiza-

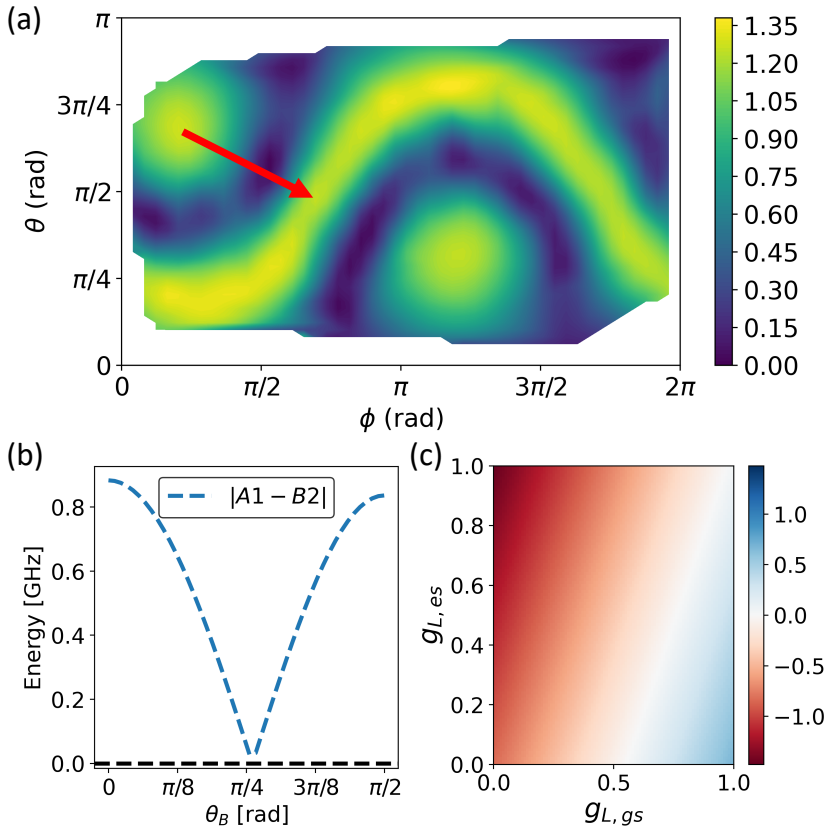

Figure 4.9: Experimentally measured and simulated spin-conserving optical transitions $A1, B2$ with varying external magnetic field B. (a) Scanning of the splittings between $A1, B2$ transitions with varying B field orientations. The magnitude of B is set to $0.2\,\mathrm{T}$. The x, y axis represents the azimuthal (ϕ) and polar angle (θ) of the B field in the lab frame (not SnV^- local frame). The two poles on the plot represent directions along the quantization axis of the SnV^-, and the belt represents the equator. The heatmap is colored by the energy splitting in terms of GHz. (b) Simulated splittings of the $A1, B2$ transitions by diagonalizing the system Hamiltonian along a chosen path of varying B field orientations. This path in the lab frame is depicted as a red arrow in (a). The x axis represents the polar angle of the B field in the SnV^- local frame. The simulation agrees qualitatively with experiments with the magnitude of splitting underestimated by $0.4\,\mathrm{GHz}$. (c) The differences between the $A1, B2$ splittings at $\theta = 0$ and $\theta = \pi/2$ with varying Steven's reduction factor in the ground and excited states. The white region corresponds to pairs of Steven's reduction factor for ground and excited states that match the experimental observations when taken into the diagonalized Hamiltonian.

tion axis ($\langle 111 \rangle$ direction), with the strain set to be the simulated profile with an additional scaling factor. The total strain magnitude is used as the x axis to simplify the demonstration. A total of four transitions $\{A1, A2, B1, B2\}$ are plotted in Figure 4.10. Compared with the low-strain "spin-orbit" regime and the high-strain regime, our experimentally observed result sits in between, which belongs to a non-trivial intermediate region where neither spin-orbit coupling nor strain can be treated as perturbation terms. Unlike SiV^- centers [63], SnV^- obtains larger quenching factor q in the ground state (0.471) than the excited state (0.125) [85], leading to a significant splitting even at zero strain. In addition, by calculating the same splitting curve with B field set to the equator orientation, we observed an inverted A1-B2 sequence, which indicates that the relative energy between A1 and B2 changes the sign when the θ angle increases from 0° to 90°. Identifying the A1 and B2 transitions is necessary for the spin initialization and readout in the following experiments.

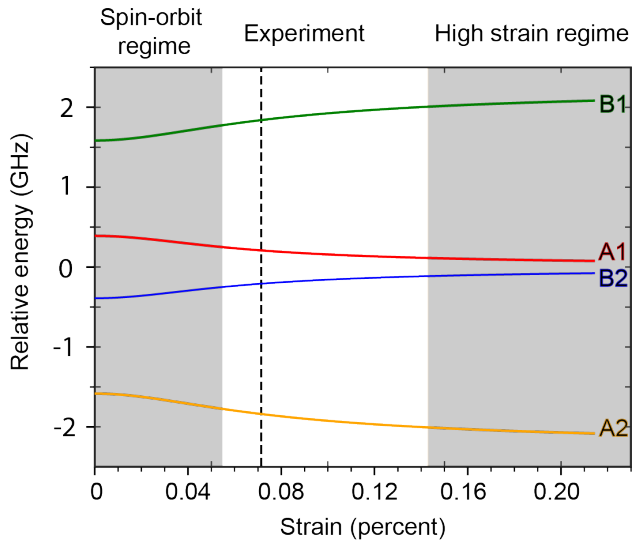

Figure 4.10: Spin-conserving transition frequencies in different strain regimes. The relative strain profile stays the same with only the scaling factor sweeping. The magnitude of the strain is defined by the norm of the tensor. The B field is set to be $80\,\mathrm{mT}$ along the quantization axis $\langle 111 \rangle$.

Optical cyclicity and operation points for all-optical and MW spin control The optical cyclicity is defined as the branching ratio between spin-conserving and spin-flipping transitions. This value depends on the spin and optical properties of SnV^- and the external optical field. Theoreti-

cally, we can calculate an analogous problem that only connects the intrinsic properties of SnV^-, which is the spontaneous emission rate ratio between spin-conserving and spin-flipping transitions. That refers to the optical cyclicity with the absence of external optical excitation. According to Ref [60], we use optical dipole matrices to calculate the emission rates of the two transitions. These rates (probability) can be expressed using Fermi's Golden Rule:

$$P = 2\pi\rho|\left\langle\psi_f\right| e\cdot\hat{\mathbf{r}}\left|\psi_i\right\rangle|^2 = 2\pi\rho|\left\langle\psi_f\right|\hat{\mathbf{p}}\left|\psi_i\right\rangle|^2 \tag{4.20}$$

Where ρ is the density of states that we set to 1 here. The $|\psi_i\rangle$ and $|\psi_f\rangle$ are the initial and final states of the SnV^- which we assign to the excited state minimum $|e_A\downarrow\rangle$ and ground states $|e_1\downarrow\rangle$ ($|e_2\uparrow\rangle$) for spin conserving (flipping) transitions. The optical dipole $\hat{\mathbf{p}}$ is defined as:

$$\hat{p_x} = e\begin{bmatrix}1&0&0&0\\0&1&0&0\\0&0&-1&0\\0&0&0&-1\end{bmatrix}, \hat{p_y} = e\begin{bmatrix}0&0&-1&0\\0&0&0&-1\\-1&0&0&0\\0&-1&0&0\end{bmatrix}, \hat{p_z} = e\begin{bmatrix}1&0&0&0\\0&1&0&0\\0&0&1&0\\0&0&0&1\end{bmatrix} \tag{4.21}$$

Using this definition, we can calculate the spin-flip possibility, which is the inverse of the spontaneous cyclicity $\frac{1}{\eta} = \frac{P_{\text{flipping}}}{P_{\text{conserving}}}$ with respect to the strain magnitude and the B field polar angle θ. This result is shown in Figure 4.11. Depending on the specific spin manipulation mechanism, the ideal operation points for MW and all-optical spin manipulation differ. In principle, the MW spin manipulation method only uses optical excitation for initialization and readout purposes. Therefore, a higher cyclicity is preferred to improve the overall signal counts. In contrast, the all-optical manipulation method requires a lower optical cyclicity to drive the spin state efficiently via small laser power and reduce the optical dephasing. The operation points of the MW and all-optical spin control used in this work are highlighted in white (black) stars, showing a cyclicity of $\geq$2000 if $\theta < 4^\circ$ and a cyclicity of $\approx$20 if $\theta > 85^\circ$. Although the MW operation point has a lower cyclic-

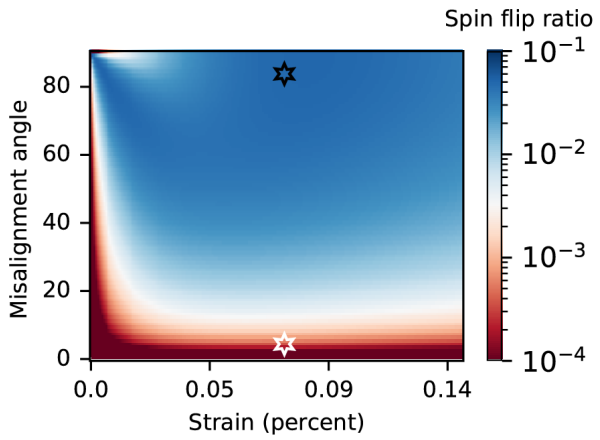

Figure 4.11: The calculated cyclicity of the SnV^- with respect to the B field polar angle θ and the strain magnitude. The operation point of the MW (all-optical) spin control of the SnV^- is highlighted in white (black) stars.

ity compared with low strain SiV^-s [67], this value is still compatible with single shot readout requirements if the signal count can be improved by device design or setup optimization. In the following two sections, we will discuss both MW and all-optical spin manipulation methods using these operation points.

Optical coherence and temperature dependence As a potential quantum networking node candidate, the optical coherence (averaged ZPL linewidth) is crucial for establishing stable remote entanglements at an appreciable rate. In this work, our measurement reveals near-transform limited optical linewidths for the strained SnV^- centers, showing that the presence of strain does not alter the excellent coherence properties of the optical transitions, which have been previously demonstrated with unstrained centers [215, 228]. The optical linewidths of the $\{A1, B2\}$ transitions are shown in Figure 4.12 (a). This $20\,\mathrm{s}$ average scan returns a mean linewidth of $47.4(16)\,\mathrm{MHz}$, only $40\,\%$ more than the lifetime-limited value of $32.26(19)\,\mathrm{MHz}$ (calculated from the $4.933(190)\,\mathrm{ns}$ optical lifetime). To further demonstrate the potential of the strained SnV^- center as a promising spin-photon interface at low-cost cryogenic systems with elevated operation temperature, we also investigate the temperature dependence of the SnV^- optical coherence. The linewidth statistics are

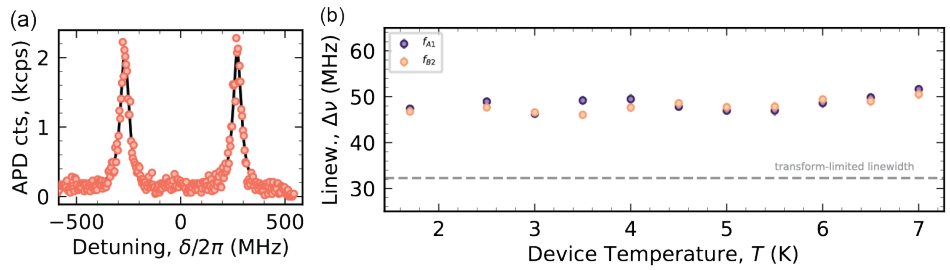

Figure 4.12: Optical coherence of SnV^- with external magnetic field present. (a) PLE scan of A1 and B2 transitions averaged over $20\,\mathrm{s}$ taken with a roughly aligned B-field with a magnitude of $81.5\,\mathrm{mT}$. The average linewidth for both transitions is below $48\,\mathrm{MHz}$, which is less than 1.5 times the lifetime limited value ($32.26(19)\,\mathrm{MHz}$). (b) ZPL linewidths of the A1 and B2 transitions with respect to the temperature, showing negligible broadening with the maximum linewidth below $52.0(8)\,\mathrm{MHz}$. The transform-limited linewidth is shown as a dashed line.

shown in Figure 4.12 (b). The ZPL linewidth remains unchanged for both A1 and B2 transitions up to $7\,\mathrm{K}$, with the maximum linewidth below $52.0(8)\,\mathrm{MHz}$—only $60\,\%$ higher than the transform-limited value. With excellent optical coherence, even modest Purcell enhancement of SnV^- ZPL can generate lifetime-limited photons suitable for efficient entanglement generation.

In addition, we characterize the long-term spectral stability of the $\{A1, B2\}$ transitions by acquiring the PLE spectra for more than 11 hours. The data is displayed in Figure 4.13, showing excellent stability with only slight spectral diffusion. By fitting each acquired PLE trace [229], we extract the common mode and difference mode shifts of the spin-conserving transition using Gaussian fitting. As a result, the center frequency $f_{A1} + f_{B2}$ has a standard deviation of σ =$23.8(1)\,\mathrm{MHz}$, while the splitting $f_{A1} - f_{B2}$ has a standard deviation of σ_s =$13.28(6)\,\mathrm{MHz}$. The linewidth and peak stability are comparable to other group IV center results in nanostructures and confirm the excellent potential of these defects for quantum photonic applications [68, 107, 108].

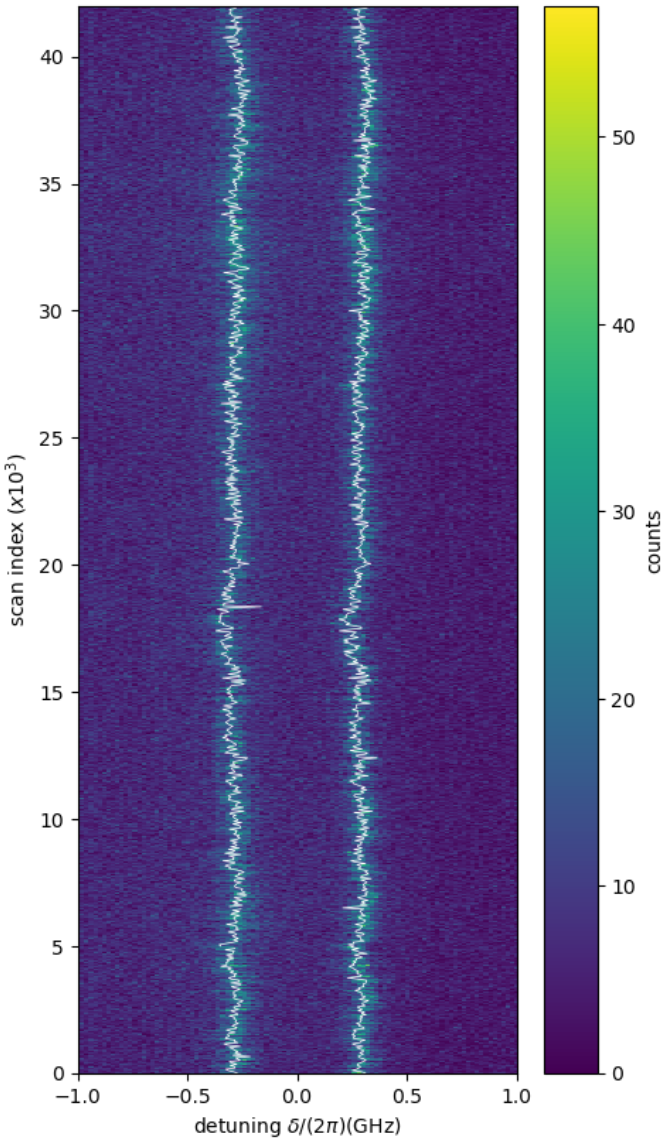

Figure 4.13: Time evolution of the PLE line shape. Each vertical cut is the average of fast PLE scans over $1\,\mathrm{s}$, with each shot of the measurement containing both green and red excitation. The solid white line is the fitted emitter resonance frequency.

4.5 MW spin control of SnV^-

4.5.1 B field alignment and optical initialization

As discussed in the previous section, the operation point of MW-based spin manipulation favors high optical cyclicity with the magnetic field roughly aligned to the SnV^-'s high symmetry axis. Therefore, we first measure the power saturation curve and use the optical cyclicity information to optimize the magnetic field orientation before initializing the SnV^- spin.

Power saturation With prior knowledge of the optical lifetime, the power-dependent decay rate is an important characterization step to extract the spin initialization rate, optical cyclicity, and saturation power [71]. The power saturation curve for a typical SnV^- is shown in Figure 4.14. Here the decay rate (initialization rate) is fit by $\frac{1}{\eta}\frac{\Gamma}{2}\frac{p/p_{\text{sat}}}{1+p/p_{\text{sat}}}$, where η is the optical cyclicity, Γ is the optical decay rate, and p_{sat} is the saturation power. For this specific characterization, the magnetic field is roughly aligned to the quantization axis, and we find a saturation power of $7.96\,\text{nW}$ with an optical cyclicity $\eta \approx 2018$ when the excitation polarization is roughly optimized. For microwave spin control measurements, we operate at a saturation parameter of $s = p/p_{\text{sat}} \approx 10$ for the initialization and readout pulses.

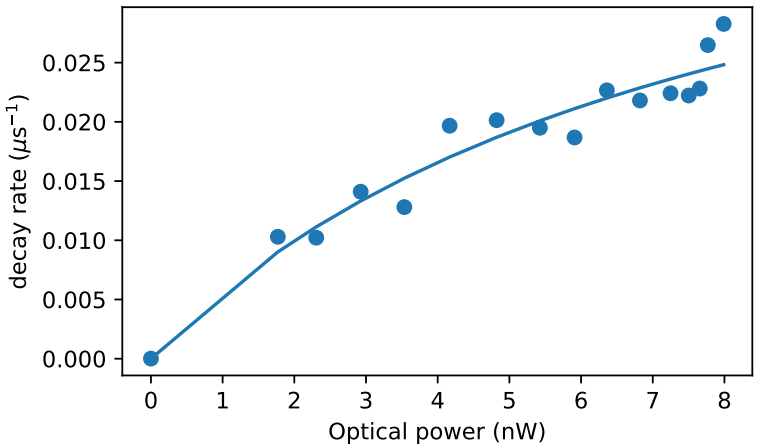

Figure 4.14: Decay rates of SnV^- at different laser powers with a fit by $\frac{1}{\eta}\frac{\Gamma}{2}\frac{p/p_{\text{sat}}}{1+p/p_{\text{sat}}}$

Optical cyclicity optimization Since the optical cyclicity has a single local maximum close to the pole of the emitter axis, we can further optimize it by sweeping two of the three magnet axes independently once the B field is roughly aligned. The cyclicity data by varying the B_x or B_y is shown in Figure 4.15, extracted by measuring the decay rate curve mentioned in the power saturation measurements. Only a moderate increase in cyclicity is observed, indicating a strain-limited maximum achievable cyclicity that aligns with the previous analysis. Therefore, we roughly optimize the B field orientation so that the cyclicity reaches $\eta \approx 2500$, similar to previous strained SiV^- measurements [67].

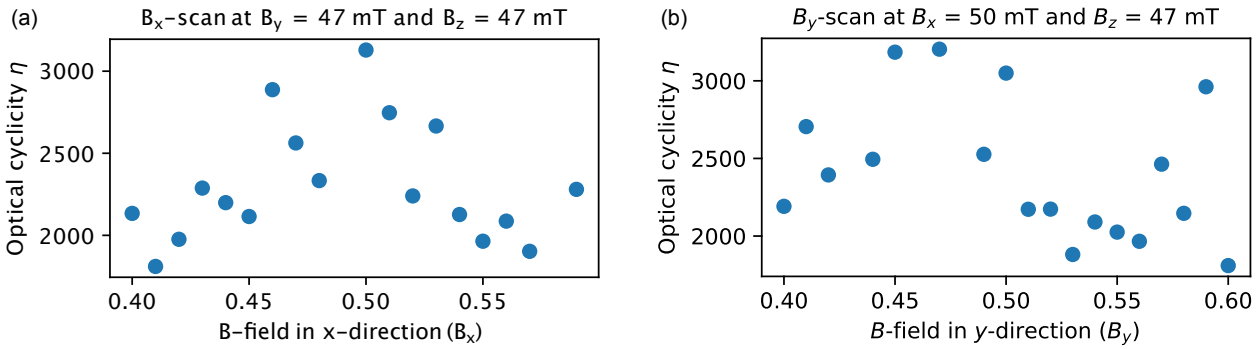

Figure 4.15: Optical cyclicity optimization at (a) fixed B_y and B_z, with swept B_x and (b) fixed B_x and B_z, with swept B_y.

Spin initialization With optical cyclicity optimized, we can proceed to the SnV^- spin initialization. High-fidelity spin initialization and readout highly depend on not only narrow optical linewidths of $A1, B2$ but also resolvable splitting between the two, which is related to the B field magnitude. The spin initialization curve of the SnV^- with subtracted background is shown in Figure 4.16, indicating an exponential decay constant of $24.2(3)\,\mu s$. We set the initialization pulse duration to $200\,\mu s$, which translates to an initialization fidelity of $98.8\,\%$. Although a cyclicity of 2500 is still not sufficient for single shot readout threshold in our setup, such a technique can be enabled via on-chip structures (nanophotonics, fiber couplers or grating couplers, solid immersion lenses) [62, 106, 107, 197, 230, 231] or external methods such as microcavities [190, 232, 233].

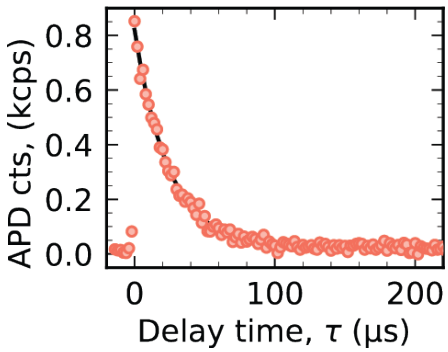

Figure 4.16: The spin initialization curve of the $A1$ transition with background subtracted, showing a time constant of $24.2(3)\,\mu\mathrm{s}$ and an initialization fidelity of $98.82\,\%$. The measurement is performed at $1.7\,\mathrm{K}$.

4.5.2 MW driving efficiency

The MW spin manipulation with frequency matching the qubit frequency ω_s can only be efficient if some crystal strain is present, as discussed in Ref [63, 234] and previous sections. We numerically calculate the electronic g factor to characterize the efficiency of the MW field—essentially oscillating (AC) B field—that drives the spin state of the SnV^-. The SnV^- response includes both spin and orbital Zeeman effects:

$$g = \frac{2}{\mu_B} \langle e_1 \downarrow | \left(\hat{H}^{ac}_{Z,L} + \hat{H}^{ac}_{Z,S} \right) | e_2 \uparrow \rangle \tag{4.22}$$

$$\hat{H}^{ac}_{Z,L} + \hat{H}^{ac}_{Z,S} = \begin{bmatrix} B^{ac}_z & B^{ac}_x - iB^{ac}_y & -iqB^{ac}_z & 0 \\ B^{ac}_x + iB^{ac}_y & -B^{ac}_z & 0 & -iqB^{ac}_z \\ iqB^{ac}_z & 0 & B^{ac}_z & B^{ac}_x - iB^{ac}_y \\ 0 & iqB^{ac}_z & B^{ac}_x + iB^{ac}_y & -B^{ac}_z \end{bmatrix} \tag{4.23}$$

Here, the $\mathbf{B}^{ac}$ is a normalized vector indicating the direction of the oscillating B field of the microwave. The actual driving field should be multiplied by an additional scalar. The $|e_1 \downarrow\rangle$ and

$|e_2 \uparrow\rangle$ are the two spin states of the SnV^- used as qubit states, as shown in Figure 4.4 (c). In numerical calculations, the Ham reduction factor q of the ground state is set to 0.471 according to [85].

First, we investigate the effect of strain on the transverse and longitudinal g factor, with the result shown in Figure 4.17 (a). In this simulation, the static **B** field is set to be $80\,\mathrm{mT}$ along the SnV^- high symmetry axis (quantization axis), which is in line with our experimental configuration. The calculated result indicates a transverse g factor of 1.64 for our device. This value is relatively high compared with the spin-orbit regime for low-strain centers (≤ 0.3) and is close to the free electron value ($g = 2$). The longitudinal g remains a minimum value which is expected. Second, we explore the angular dependence of the transverse g factor with different static field orientations using our experimentally observed strain profile. We observe a weak angular dependence of g, indicating a consistently efficient MW driving efficiency regardless of the static B field orientation.

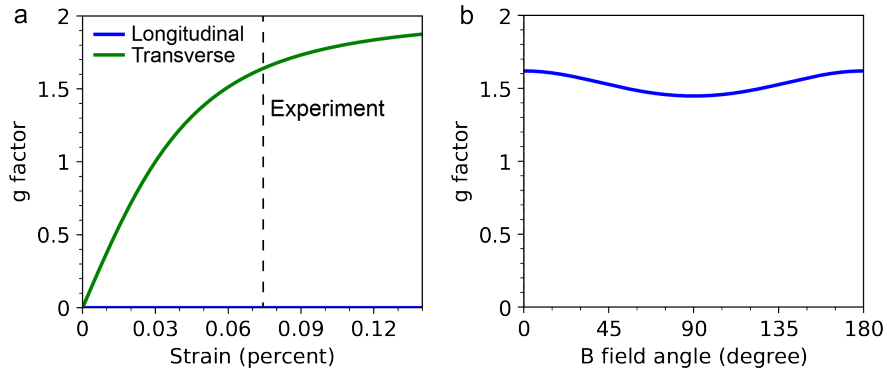

Figure 4.17: MW g factor calculation. (a) The transverse and longitudinal g factor with respect to the strain magnitude. The static B field is set to be $80\,\mathrm{mT}$ along the quantization axis $\langle 111\rangle$. (b) The angular dependence of the g factor with respect to different static field orientations (polar angle).

4.5.3 MW manipulation of SnV^-

High-fidelity spin control is a critical component of a spin-photon interface for quantum networking. To realize efficient MW spin driving, we generate a large crystal strain in the diamond membrane, which leads to an effective Landé factor g of 1.62 for the transverse microwave field. In

addition, the MW waveguide around the measurement area is tapered to a width of $6\,\mu\mathrm{m}$ to enhance the microwave field amplitude, as shown in Figure 4.4 (b). The target SnV^- center is $\approx 4\,\mu\mathrm{m}$ away from the waveguide, which ensures an efficient exposure to the MW driving field.

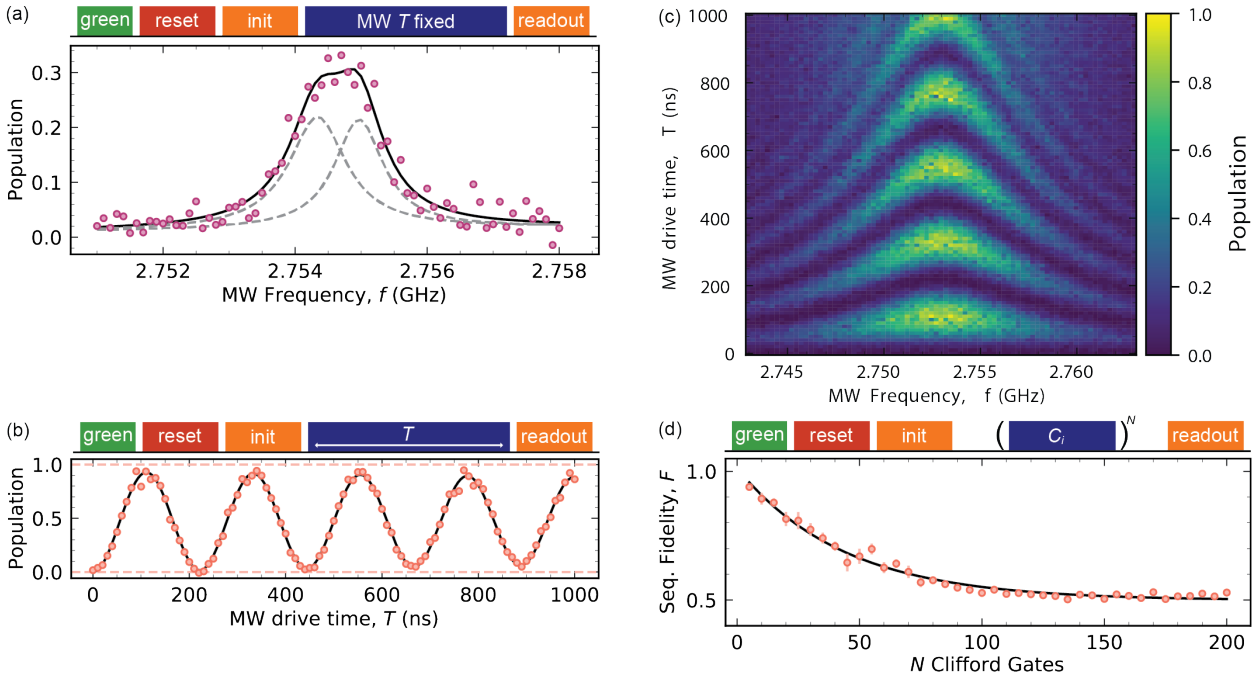

Figure 4.18: MW control of the strained SnV^- center at $1.7\,\mathrm{K}$. (a) Pulsed ODMR spectrum with scanned MW frequency. The data (purple dots) is fitted with two Lorentzian functions (dashed line) split by $628(182)\,\mathrm{kHz}$, each with a linewidth of $1047(208)\,\mathrm{kHz}$ and $891(197)\,\mathrm{kHz}$, respectively. (b) On-resonance Rabi oscillation of the SnV^- at zero detuning, showing a Rabi frequency $\Omega/2\pi$ of $4.50(2)\,\mathrm{MHz}$ with a fidelity of $99.36(9)\,\%$. (c) Rabi chevron oscillations as a function of the MW driving frequency. (d) Randomized benchmarking of SnV^- shows an average gate fidelity of $97.7(1)\,\%$. The Rabi frequency is set to $2.8\,\mathrm{MHz}$ in this experiment to avoid excess heating effects.

ODMR With the device and setup ready, we first initialize the spin via optical pumping and scan the MW frequency across the expected spin resonance while monitoring the fluorescence intensity of the spin readout at $1.7\,\mathrm{K}$. We show in Figure 4.18 (a) a clear signature of optically detected magnetic resonance (ODMR) for the target SnV^- center at the frequency $2.755\,\mathrm{GHz}$. This qubit frequency is slightly higher than the anticipated value ($2.1\,\mathrm{GHz}$) at an applied static magnetic field of $81.5\,\mathrm{mT}$. The mismatch could originate from the slight difference between the displayed and the actual magnetic field due to hysteresis and the deviation of the effective reduction factors

under strain from the values shown in Ref [85]. In addition, the ODMR shows a profile with two overlapping peaks separated by $628(182)\,\mathrm{kHz}$. This feature indicates an interaction between the electronic spin of the SnV^- with other spin systems in the vicinity, which might be a [^{13}C] nuclear spin or an electron spin from a P1 center.

Rabi oscillation After obtaining the two power-broadened ODMR transitions, we can resonantly drive the SnV^- spin state with a Rabi frequency $\Omega/2\pi$ of up to $4.50(2)\,\mathrm{MHz}$. The simple Rabi oscillation and chevrons (Rabi oscillations with different detuned driving frequencies) are displayed in Figure 4.18 (b)-(c). From the figures, we observe a long-time averaged Rabi π-gate fidelity of $99.36(9)\,\%$, which shows a significant improvement from the all-optical Raman-based spin control results [71]. The MW power delivered to the device is approximately 24 dBm ($250\,\mathrm{mW}$), which is comparable with the previous strained SnV^- demonstration [68] and is significantly lower than SnV^- centers working in a lower strain regime [70].

Randomized benchmarking The single qubit gate fidelity of the MW-controlled SnV^- is characterized via randomized benchmarking. In this case, we use the following Clifford gate set: $\{I$, π_x, π_y, $\pi_x/2$, $-\pi_x/2$, $\pi_y/2$, $-\pi_y/2\}$. For a measurement including N gates, we randomly choose the first $(N-1)$-gates, use the last gate to undo the sequence, and then perform a z-basis measurement. The π-gate duration t_π is acquired from the Rabi measurement, whereas $\pi/2$-gates have a duration of $t_{\pi/2}$. The identity operation I is implemented as wait-time for t_π. No buffer times are added as they would make the qubit prone to dephasing errors. However, the Rabi rate is slower ($2.8\,\mathrm{MHz}$, 18 dBm) to prevent excessive heating effect, which would lead to undesired/unnatural spin decoherence and decay. The benchmarking result is shown in Figure 4.18 (d). With a fidelity fitting of $A \cdot F^N + B$, we can get the error per Clifford gate which is $97.7(1)\,\%$ [235], an excellent number for group IV centers.

Power dependence of the Rabi frequency To investigate the power dependence of the Rabi frequency, we sweep the MW drive at different power levels. At low power regime below 24 dBm, we observe the expected $\sqrt{p}$-behavior. However, once the power reaches 24 dBm, there is an apparent deviation of this $\sqrt{p}$ dependence, as shown in Figure 4.19. Here, all power and voltages are referred to the estimated value on the device, which can be extracted by separate calibration measurements through the transmission waveguide. Although we do not observe any cryostat temperature change during the Rabi measurement, this deviation still strongly indicates some local heating effect from the heated gold stripline. The heating effect could be managed by replacing gold with some B-field compatible superconducting metals (such as niobium) to deliver the MW signal [236].

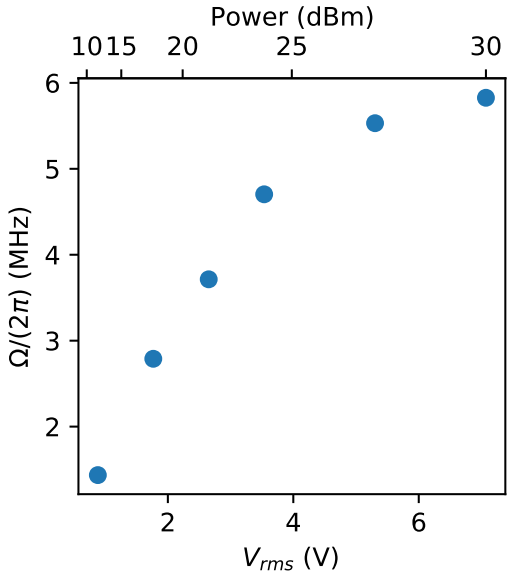

Figure 4.19: Fitted Rabi-frequency $\Omega/2\pi$ over MW power level, showing the expected $\sqrt{p}$-behaviour for low drive powers $p < 24$ dBm and a clear deviation beyond 24 dBm.

4.5.4 SnV⁻ spin coherence at 1.7 K

In this section, we focus on the coherence time T_2^* and T_2 measurements at $1.7\,\mathrm{K}$. At this temperature, the spin coherence is not limited by the spin lifetime T_1^{spin}, which is verified later in the section. Equipped with high-fidelity MW control, we first perform a Ramsey measurement. The

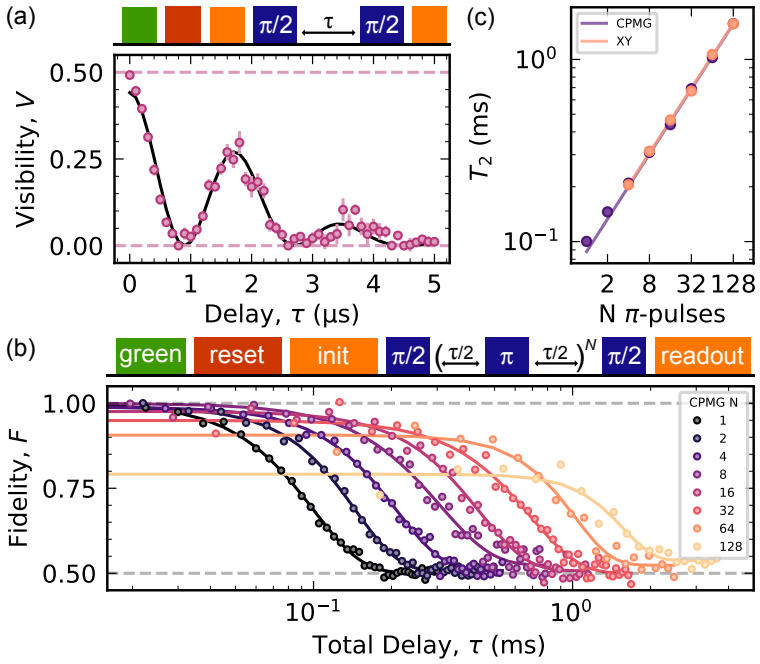

Figure 4.20: Spin coherence of the strained SnV^- at 1.7 K. (a) T_2^* of the SnV^-, showing a dephasing time of $2.5(1)\,\mu s$. The extra beating pattern of $554(5)\,kHz$ is estimated to be an interaction with the electron or nuclear spin in the vicinity. (b) Dynamical decoupling of the SnV^- via CPMG pulses. The CPMG-1 (spin-echo) returns a $T_{2,\text{echo}}$ of $100(1)\,\mu s$, while the CPMG-128 reaches a $T_{2,\text{CPMG128}}$ of $1.57(8)\,ms$. (c) The scaling of T_2 with the number of CPMG and XY pulses, which shows a sub-linear dependence.

pulse sequence and the result are shown in Figure 4.20 (a). The Gaussian envelope of the Ramsey oscillation returns a spin dephasing time T_2^* of $2.5(1)\,\mu s$. In addition, we observe another indication of a proximal spin showing as a beating pattern in the Ramsey measurement. This echoes our finding in the ODMR, which can be understood as a qubit with its frequency ω_s detuned from the driving frequency ω, leading to a slow oscillation pattern. By doing phase-dependent readout separately, we verify that this beating pattern remains, indicating that artificial MW signal detuning is not the cause. This number is comparable to the SiV^- result [67], with possible decoherence sources including crystal vacancies and defects in the diamond and surface spins from both sides of the membrane [78]. We also perform another measurement with a larger B field value ($117\,mT$, $3.694\,GHz$ qubit frequency) which returns a comparable T_2^* value of $2.63(14)\,\mu s$, indicating that g-factor fluctuations as reported in Ref [67] are not the limiting factor of our T_2^*.

In addition to the T_2^* characterizations, we also apply advanced pulse sequences, such as dynamical decoupling via CPMG (Carr-Purcell-Meiboom-Gill) and XY sequences [237, 238] to filter the noise spectrum and extend the spin coherence. The CPMG results are shown in Figure 4.20 (b). The $T_{2,\text{echo}}$, which is $T_{2,\text{CPMG1}}$, returns a value of $100(1)$ µs that is much longer than the T_2^* value, indicating substantial low-frequency magnetic noise which could potentially come from surface or bulk electronic spins since the nuclear spin bath is hugely suppressed by the isotopic engineering. Remarkably, the $T_{2,\text{CPMG128}}$ prolongs the SnV^- spin coherence to $1.57(8)\,\text{ms}$. We note that even with no signal normalization being applied, the CPMG figure remains a high signal fidelity of $\approx 80\,\%$ for up to 128 pulses, which can be further improved by using XY pulses. Future implementations of faster Rabi pulses with superconducting metal waveguides could further improve the signal fidelity to higher numbers of pulses. With a separate XY pulses experiment, we plot the relationship between T_2 time constants and the number of CPMG or XY pulses N in Figure 4.20 (c) and fit it with the scaling $T_2 \sim N^\beta$. The fitting curve shows a sub-linear dependence with a β factor of $0.593(8)$, indicating that the T_1 limit is well above $1.5\,\text{ms}$. In addition, we observe minimal T_2 differences between CPMG and XY sequences. Since XY sequences are more resilient to control pulse errors (rotation or offset errors) compared to CPMG [238, 239], this finding verifies that our control setup does not limit coherence.

4.5.5 SnV^- operation at elevated temperature

For Group IV centers, the dominant decoherence source of the electronic spin qubit is the electron-phonon interaction (phonon-mediated decay) between orbital branches [76, 234]. The interaction rate depends on the thermal phonon population, which relates to the energy splitting Δ_{gs} between orbital branches. In addition to using heavier group IV elements (Sn), the qubit coherence of our work also benefits from the presence of the crystal strain, which increases the effective branch splitting to $2\sqrt{\varepsilon_{E_{gx}}^2 + \varepsilon_{E_{gy}}^2 + (\frac{\lambda_{SO}}{2})^2}$ between optical ground and excited states. The reduced phonon population in the upper branch leads to a higher operation temperature for SnV^-.

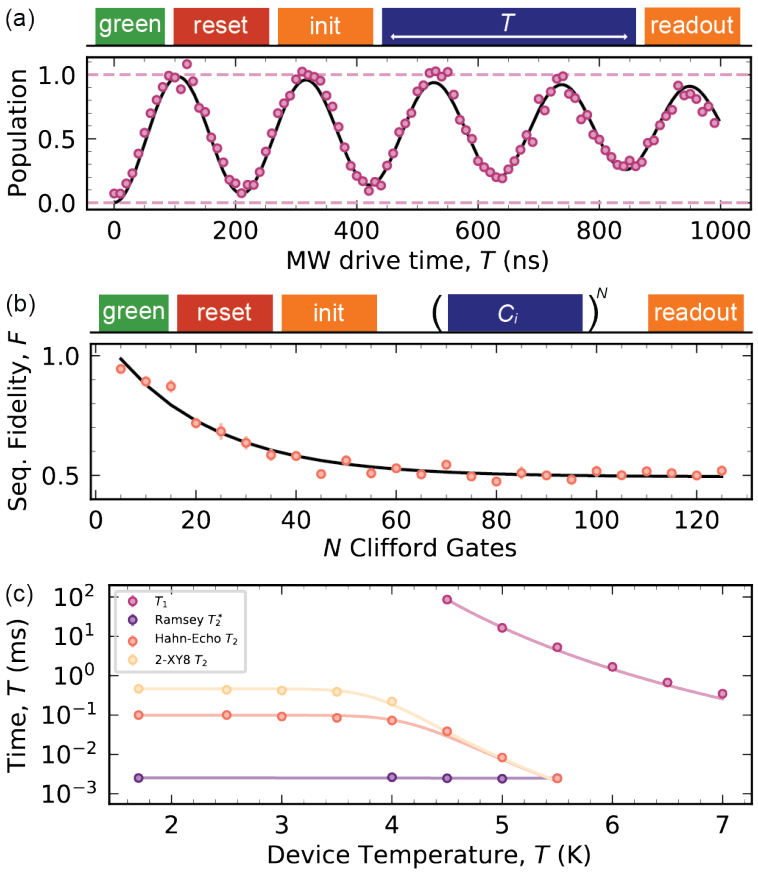

Figure 4.21: Performance of the strained SnV^- at $4\,K$. (a) Rabi oscillation of the SnV^- center, showing a gate fidelity of $97.7(5)\,\%$ (b) Randomized benchmarking at $4\,K$, showing an average gate fidelity of $95.7(3)\,\%$. (c) Temperature dependence of the spin decay time T_1^{spin}, dephasing times T_2^*, $T_{2,\text{echo}}$, and $T_{2,\,2XY8}$.

First we characterize the MW manipulation performance at $4\,K$. The Rabi oscillation of the SnV^- at $4\,K$ is shown in Figure 4.21 (a). The π gate fidelity is characterized to be $97.7(5)\,\%$, only slightly lower than the value at $1.7\,K$ due to background heating limitations. The randomized benchmarking result returns an average gate fidelity of $95.7(3)\,\%$, confirming the preserved high fidelity spin manipulation at $4\,K$. Again, this randomized benchmarking uses the same $2.8\,MHz$ Rabi rate.

Equipped with high fidelity gate operations, we then investigate the spin coherence of SnV^- at $4\,K$. Due to the much larger branch splitting Δ_{gs} of the strained SnV^- ($\approx$1300 GHz) compared with bulk SnV^- ($\approx$850 GHz), we expect a much weaker electron-phonon interaction. This is confirmed

by our temperature dependence data of T_1^{spin}, T_2^*, $T_{2,\text{echo}}$ and $T_{2,2\text{XY8}}$ shown in Figure 4.21 (c). Fitting the same β factor in $T_2 \sim N^\beta$ curve using Hahn-echo and XY4 coherence time data returns a value of $0.391(8)$ at $4\,\text{K}$ and 0.014 at $4.5\,\text{K}$, indicating that the dominant decoherence mechanism becomes phonon-induced spin decay instead of the spin bath (no coherence improvement vs pulses).

From Figure 4.21 (c) we observe another interesting feature, a much lower T_1-limited dephasing time compared with the measured decay time T_1^{spin}. This feature originates from the fact that only spin-flipping transitions between the lower and upper orbital branches drive T_1^{spin}. In contrast, any phonon-induced transitions, including spin-conserving ones between orbital branches, lead to spin decoherence (see the next section for more details). For instance, the spin depolarization path $|e_1\downarrow\rangle \rightarrow |e_3\downarrow\rangle \rightarrow |e_1\downarrow\rangle$ does not change the $|e_1\downarrow\rangle$ state population (and thus would not be captured by T_1^{spin}), but the phase information is lost due to different precession frequencies in the orbital branches [63]. In our case, the MW-operation point has highly cycling photon and phonon transitions due to the well-aligned magnetic field, which leads to he huge ratio between T_1^{spin} and T_1-limited dephasing ($\approx$2000). Nevertheless, T_2^* at $4\,\text{K}$ remains at $2.7(1)\,\mu\text{s}$, which is comparable to the $1.7\,\text{K}$ value. $T_{2,echo}$ only decreases slightly to $74(2)\,\mu\text{s}$, with $T_{2,2XY8}$ reaching the depolarization-limited T_2—$223(10)\,\mu\text{s}$. We emphasize that all these numbers are the record high values for all group IV qubits at $4\,\text{K}$ to date.

4.6 All-optical spin control of SnV$^-$

Measurement configuration We have shown in the MW manipulation that strained SnV$^-$ have excellent spin manipulation fidelity and spin coherence. Now we revisit the previous operation mechanism [71], all-optical spin control of SnV$^-$ and investigate additional system properties. As discussed earlier, the magnetic field B is aligned roughly on the equator plane of SnV$^-$, perpendicular to the quantization axis, to ensure sufficient spin-conserving transition splitting and low optical cyclicity η.

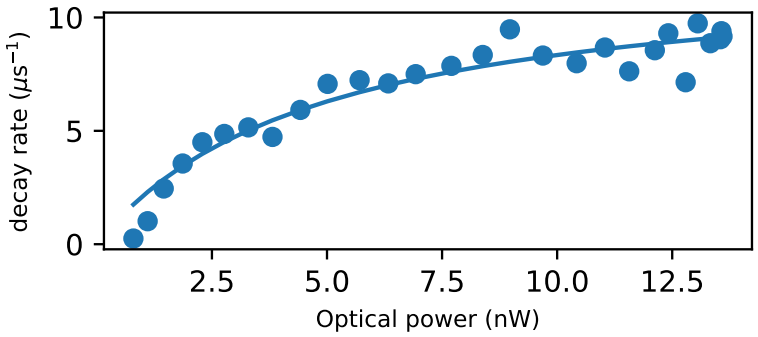

Figure 4.22: Initialization rates of strained SnV$^-$ at different laser powers with a fit by $\frac{1}{\eta}\frac{\Gamma}{2}\frac{p/p_{\text{sat}}}{1+p/p_{\text{sat}}}$.

Here we use another strained SnV$^-$ with a ground state splitting of Δ_{gs} =1384 GHz. The measurement is performed at 1.7 K. First, we extract an optical lifetime of 7.04(10) ns, which is compatible with an SnV$^-$ in the proximity of a surface [227]. By applying a magnetic field of $|B| = 100\,\text{mT}$ perpendicular to the emitter axis, we measure the power saturation curve shown in Figure 4.22. Using the fitting function $\frac{1}{\eta}\frac{\Gamma}{2}\frac{p/p_{\text{sat}}}{1+p/p_{\text{sat}}}$, we extract a saturation power of p_{sat} =4.82(81) nW and a cyclicity of $\eta = 5.78(36)$. Such a cyclicity is ideal for the Raman-based all-optical control method.

Coherent population trapping (CPT) CPT is a commonly used method to characterize group IV spin qubits with short coherence times [65]. In our implementation, the CPT feature is observed by creating an optical lambda system and simultaneously driving the spin-conserving transition $A1$ and the spin-flipping transition $A2$. By changing the detuning frequency of the spin-flipping transition, a dip in the spectrum is present. This optical response indicates a population change of the qubit state, which can be explained by electromagnetically induced transparency (EIT) [240]. The linewidth of the CPT is affected by multiple factors, including laser power and linewidth, spin coherence, and optical coherence. The CPT data is shown in Figure 4.23. Fitting the data with the model in Ref [71] by assuming a very long qubit coherence, we get an excited state decay rate of $\Gamma/2\pi$ =26.52(91) MHz, which is only 17 % larger than the transform-limited linewidth $\Gamma_0/(2\pi)$ = 22.60(5) MHz.

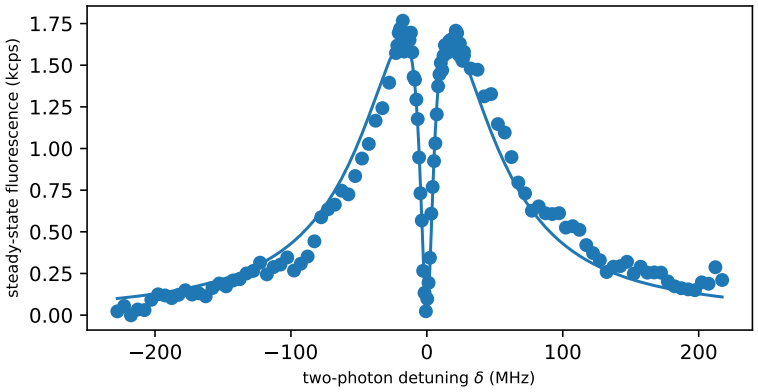

Figure 4.23: Coherent population trapping measured on an SnV^- at perpendicular magnetic fields.

All-optical spin manipulation The all-optical spin manipulation relies on a Raman drive, which consists of laser excitation pairs forming a Λ structure detuned from the actual excited states. In this work, we operate at a single-photon detuning of $\Delta = 1.5\,\mathrm{GHz}$. By limiting the laser sideband power to $p = 455\,\mathrm{nW}$, we observe an intrinsic ODMR linewidth of $\delta f = 1/T_{2^*} = 899(54)\,\mathrm{kHz}$, which is shown in Figure 4.24 (a). The observed qubit frequency is $f_{\mathrm{qubit}} = 2.321\,\mathrm{GHz}$, yielding a g factor of 1.66, verifying that perpendicular B fields can couple to the strained SnV^- efficiently. By sweeping the Raman drive time T at the laser sideband power $P = 1012\,\mathrm{nW}$, we are able to get a Rabi frequency of $\Omega/2\pi$ = $450(47)\,\mathrm{kHz}$, as shown in Figure 4.24 (b). The π-gate fidelity F_π = is $83(2)\,\%$, which is similar to Ref [71]. The limited gate fidelity can be explained by the non-zero excited state excitation from the virtual Raman transition and optically induced dephasing.

Spin decay time We additionally measure the temperature dependence of the spin decay time T_1^{spin} as shown in Figure 4.25. We note that the lifetime here is much shorter than the T_1^{spin} measured in the MW-based protocol due to the spin and orbital mixing between orbitals discussed later in the section.

Spin coherence time For the coherence time of SnV^- at $1.7\,\mathrm{K}$, we observe a Ramsey coherence T_2^* of $1.13(7)\,\mu\mathrm{s}$ as shown in Figure 4.26 (a), and a Hahn-Echo coherence T_2 of $35.45(296)\,\mu\mathrm{s}$ as shown in Figure 4.26 (b). These values are relatively short compared to the measurements

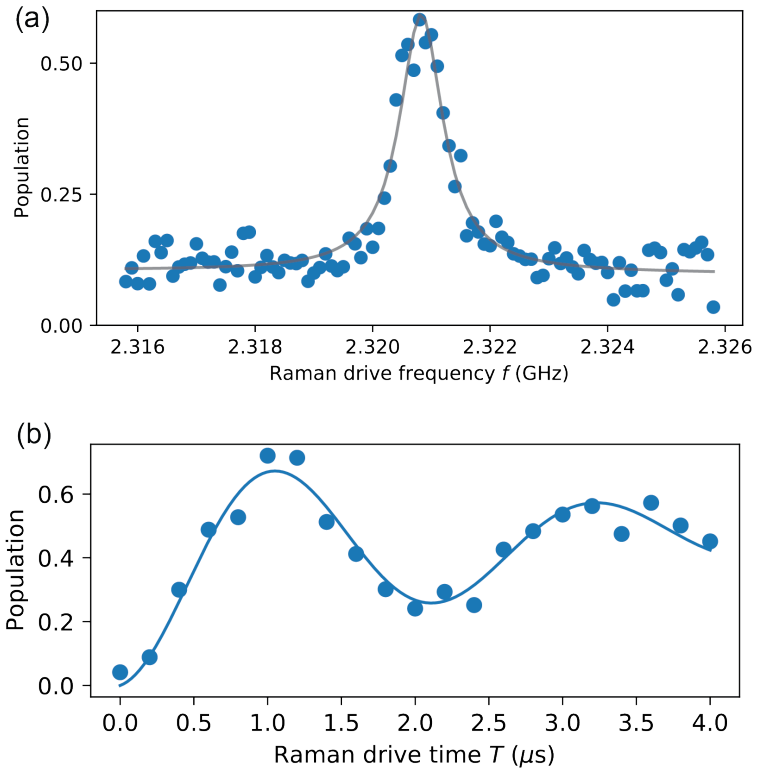

Figure 4.24: All-optical spin control of SnV^-. (a) Pulsed ODMR at perpendicular B-field directions. (b) Spin control at perpendicular B-field directions with a sideband power of $p = 1012\,\mathrm{nW}$.

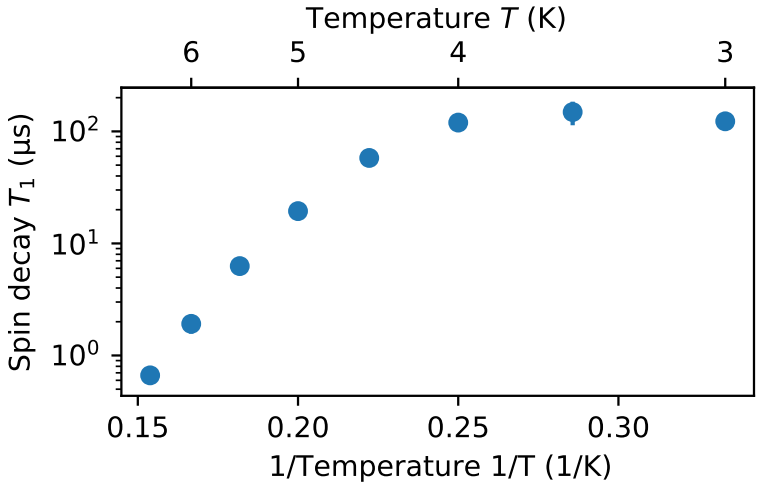

Figure 4.25: Temperature dependence of the all-optical T_1^{spin}.

performed by the MW spin manipulation, indicating a moderate optical dephasing mechanism.

Spin depolarization: orbital and spin T_1 Due to the degenerate spin-$1/2$ system, the qubit subspace only occupies the lower branch of the optical ground state. Therefore, spin depolarization could have multiple possibilities. Typically, we consider two types of spin decay channels, namely orbit (T_1^{orbit}) and spin (T_1^{spin}) [65]. The T_1^{orbit} refers to the spin depolarization between orbital branches in the ground state but with the same spin projection outside of the qubit subspace. In contrast, the T_1^{spin} refers to a more natural definition, the spin depolarization between the qubit states. Both processes are induced by the spin-phonon interaction in the diamond crystal, which is the dominant decoherence source of SnV$^-$. Since T_1^{spin} directly relates to the coherence of the SnV$^-$, we focus on the discussion to T_1^{spin} in this work.

There are three main phonon-induced T_1^{spin} decay paths at low temperature [63]: direct single phonon, resonant two phonons (Orbach process) [241], and off-resonant two phonons (Raman process). Similar to SiV$^-$, we found much slower single phonon and Raman spin decay rates for SnV$^-$ at temperatures below $30\,\text{K}$. Therefore, we only discuss the Orbach process here and study its intensity dependence with the B field orientation (θ) and the strain magnitude. Adapted from Ref [241], we write the Orbach decay rate γ_{spin}^2 as follows:

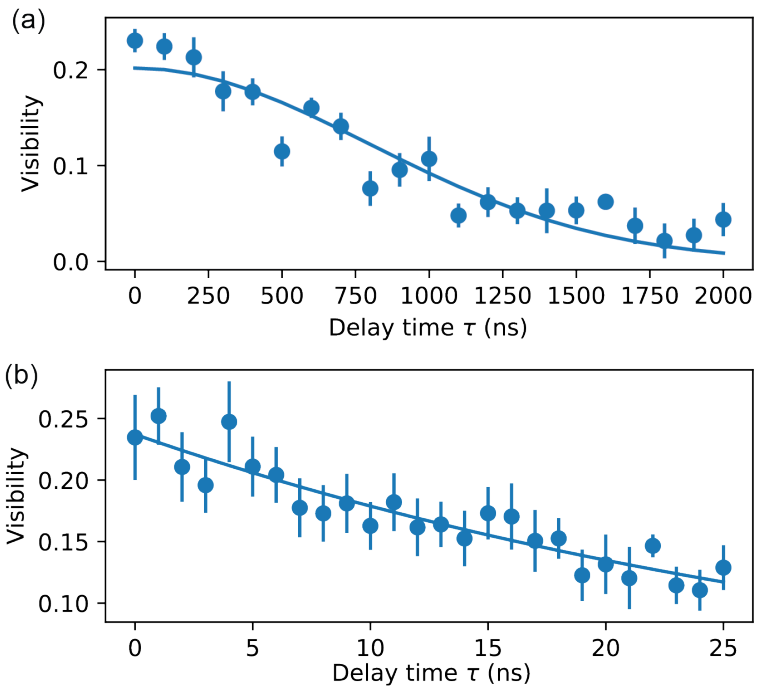

Figure 4.26: Coherence time T_2 of SnV^- from the all-optical control method. (a) Ramsey measurement showing an inhomogeneous dephasing time of $T_2^* = 1.13(7)$ µs. (b) Hahn-Echo measurement showing a dephasing time of $T_2 = 35.45(296)$ µs

$$\gamma_{spin}^2 \propto \frac{\Delta_{gs}^3}{\exp\left(h\Delta_{gs}/k_BT\right) - 1} \frac{\left|\sum_j \langle e_1 \downarrow| H_\varepsilon^{AC} |e_j\rangle \langle e_j| H_\varepsilon^{AC} |e_2 \uparrow\rangle\right|^2}{\sum_{ij} \left|\langle e_i| H_\varepsilon^{ac} |e_j\rangle\right|^2} \tag{4.24}$$

Here i represent the states in the lower orbital branch ($|e_1 \downarrow\rangle$, $|e_2 \uparrow\rangle$) and j represent the states belonging to the upper orbital branch ($|e_3 \downarrow\rangle$, $|e_4 \uparrow\rangle$). The H_ε^{AC} denotes an AC strain field, which refers to the phonon interaction in the crystal. Without any detailed discussion of the phonon modes, we only use a balanced magnitude for the $H_{\varepsilon_{Ex}}^{AC}$ and $H_{\varepsilon_{Ey}}^{AC}$ and calculate the average effect, with H_ε^{AC} written as follows:

$$H_{\varepsilon}^{AC} = e \begin{bmatrix} -1 & 0 & 1 & 0 \\ 0 & -1 & 0 & 1 \\ 1 & 0 & 1 & 0 \\ 0 & 1 & 0 & 1 \end{bmatrix}, \tag{4.25}$$

Figure 4.27 shows the relative spin decay rate at temperature $4\,\mathrm{K}$ with the maximum number normalized to 1. At the strain level of our device, we choose the operation points for MW-based and all-optical methods based on spectral separation and optical cyclicity. These operation points are highlighted as black and white stars in the figure. From the calculation we deduce a ratio of 500 to 1200 between the two T_1^{spin}, which is roughly aligned with our experimental values measured at $6\,\mathrm{K}$ (MW-based control T_1^{spin} $=2.5\,\mathrm{ms}$, all-optical control T_1^{spin} $=1.65\,\mu\mathrm{s}$). We note that as a pre-factor, the temperature would not change the decay rate ratio between the two configurations, thus this ratio can be measured at any temperature. The match between calculated and measured values reiterates that the Orbach process is the dominant factor for the T_1^{spin} decay.

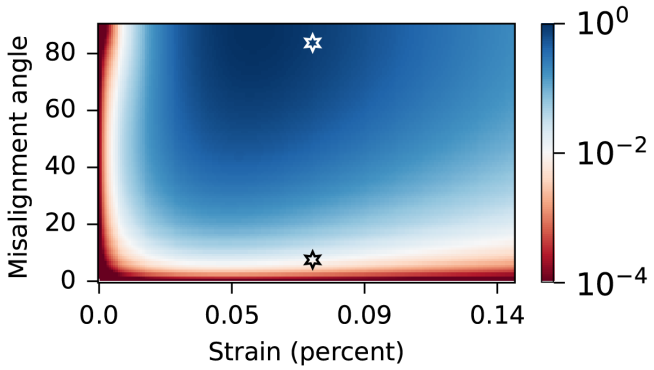

Figure 4.27: The calculated Orbach decay rate of the SnV^- with respect to the B field polar angle θ and the strain magnitude. The operation points for the MW-based and all-optical control of the SnV^- spin qubit are highlighted as black and white stars, respectively.

4.7 Conclusion

In this chapter, we introduce one application of the diamond membrane for quantum technologies—strain tuning of group IV quantum emitters. By creating a simple diamond membrane-fused silica heterostructure, we generate a significant passive strain of $0.05\,\%$ to $0.1\,\%$ in diamond by leveraging the differences in thermal expansion coefficients. The presence of strain enables efficient, high-fidelity microwave control of the SnV^- spin. In addition, the strain profile greatly increases the energy splitting between the two orbital levels of the SnV^-, suppresses the phonon-mediated spin decay, and improves the spin coherence and operation temperature at up to $4\,\mathrm{K}$. In combination with near lifetime-limited optical linewidths up to $7\,\mathrm{K}$, these improvements reduce the technological barrier towards practical, cost-efficient quantum networking nodes. Notebly, we reach a Rabi π gate fidelity of $99.36(9)\,\%$ ($97.7(5)\,\%$) with a randomized single qubit gate fidelity of $97.7(1)\,\%$ ($95.7(3)\,\%$) at $1.7\,\mathrm{K}$ ($4\,\mathrm{K}$). The spin coherence can be extended to $1.57(8)\,\mathrm{ms}$ at $1.7\,\mathrm{K}$ and $223(10)\,\mu\mathrm{s}$ at $4\,\mathrm{K}$ by applying dynamical decoupling pulses. These numbers can be further improved by generating higher strain through heterostructure optimization and additional active tuning. Moreover, derived from scalable diamond membrane generation, our platform is compatible with additional on-chip integration, such as integrated photonics discussed in Chapter 3 [94, 169] and MEMS structures, unleashing more exciting opportunities for solid-state quantum technologies.

CHAPTER 5

NV$^-$ CENTERS FOR QUANTUM SENSING APPLICATIONS[†]

Abstract

NV$^-$ center in diamond is one of the most widely used spin defects in quantum technology. Although NV$^-$ has been utilized to demonstrate quantum computing and networking, quantum sensing is the most common and widespread application. The NV$^-$ center's C_{3v} point group symmetry is both a gift and a challenge. These centers are sensitive to the target signal but are also prone to various types of environmental noises. Such a unique combination often reduces NV$^-$ coherence if they are close to poorly prepared surfaces, lattice damage, or distortion. In this chapter, we focus on the quantum sensing application and investigate the coherence of NV$^-$ inside our diamond membranes. As a sensitive probe, the electronic and optical properties of NV$^-$ can also be used for characterizing the diamond membrane itself. At last, we will introduce an application of NV$^-$ centers in diamond membranes for quantum bio-sensing. The preserved qubit coherence and successful real-world implementation will unlock more sensing opportunities in future practice.

5.1 Introduction

NV$^-$ center is the most famous point defect in diamond and has had significant progress in the past few decades. We have discussed the basic properties, operation mechanisms, and applications of NV$^-$ center in Chapter 1. In this chapter, we will focus on the main application of the NV$^-$ center—quantum sensing. Unlike quantum networking [43], quantum sensing does not require exceptional optical coherence and cryogenic temperature operation. Most NV$^-$ quantum sensors are measured at room temperature. In addition, except for some far-field sensing such as general magnetic field sensing for navigation [242], most nanoscale sensing regime requires NV$^-$ centers

†. The work discussed in this section was reported in [40, 94]

to be closer to the diamond surface, where many sensing targets can be around [243]. Although NV^- can have well-preserved coherence when living deeply inside the crystal [82], the coherence of near-surface centers is heavily influenced by the surface spins [78], including improper surface treatments, contamination, and excess surface roughness. In addition, when the density of NV^- increases, the coherence is also impacted by the large density of nitrogen impurity, which are present as P1 centers with non-zero electron spin. The nuclear spins, especially ^{13}C with $1.1\,\%$ in natural isotope, can also affect the NV^- coherence. Since the magnetic field sensitivity is inversely related to the coherence [244], the nanoscale quantum sensing research must balance the relationship between the qubit coherence, NV^- density, and sensing distance to optimize the overall sensitivity. Another implication of NV^-'s extreme sensitivity to surface spins is that the coherence can be easily impacted by device nanofabrication, which prevents people from many device designs (especially collection efficiency improvements) except for μm-size solid immersion lenses [43], general diamond etching [96], and the use of oil objectives.

One of the major aims of our sub-μm-thick diamond membranes discussed in Chapter 2 is NV^- quantum sensing. Before applying them to real-world applications, we have to characterize the NV^-'s coherence property to ensure their sensitivity is comparable with bulk centers. As mentioned in Chapter 2, the membrane fabrication is carefully designed to minimize the spin environment. Some techniques include atomically smooth surface polish, crystal quality optimization to reach a bulk-like Raman feature, and ^{12}C isotopic purification during growth to minimize the background nuclear spin density. In this section, we will characterize NV^- centers in the membrane, compare their spin coherence with the bulk values, and gain insights into the magnetic noise levels in the crystal [78, 245–247]. In addition, the NV^- optical characterizations provide invaluable information on the diamond membranes' material properties, such as strain distribution, surface termination, and impurity background. Furthermore, we will present a proof-of-concept device using diamond membranes and microfluid channels for quantum bio-sensing. The successful implementation of the diamond membrane will unleash the potential of this versatile platform for

more exciting applications.

5.2 Spin coherence of NV⁻ in membrane

5.2.1 Measurement protocol

Standard free induction decay (FID) and spin echo (SE) sequences are used to measure T_2^* and T_2 of NV⁻. The measurement sequences are displayed in Figure 5.1, which contains two branches to measure both the $|m = 0\rangle$ and $|m = -1\rangle$ projections. After spin initialization and a $\pi/2$-pulse on the NV⁻, the spin evolves for a time τ (a π_y pulse at $\tau/2$ is applied for the SE) before another $+\pi/2$-pulse or $-\pi/2$-pulse is applied to for readout. The green laser is used for both spin readout and initialization. The readout windows at the beginning of each laser pulse are binned as the readout signals, $S_{0,-1}$, and the readout window at the end is binned as a reference, R, which serves to correct for slow drifts after each measurement cycle [248].

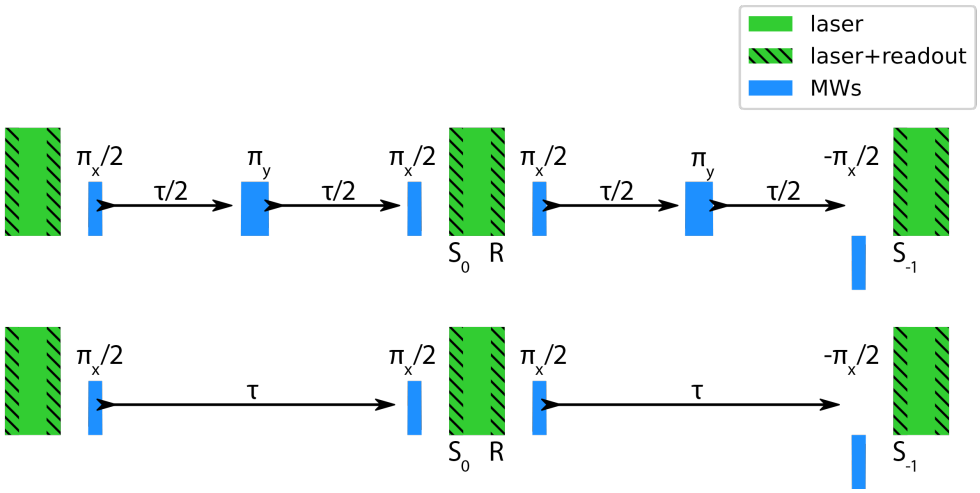

Figure 5.1: NV⁻ Coherence measurement sequences. Both the spin echo (a) and free induction decay (b) sequences have readout, initialization, state preparation, and state projection pulses. The spin echo sequence has an additional π-pulse to refocus the spin.

We fit T_2^* measurement data to the following function [249]:

$$B + \exp\left[-(t/T_2^*)^2\right] \cdot \sum_{i=1}^{2I+1} a_i \cos\left(2\pi f_i(t+\phi_i)\right), \tag{5.1}$$

Here B is the background offset since both $|m=0\rangle$ and $|m=-1\rangle$ states are "bright" with different count rates. a_i, f_i, and ϕ_i are the amplitude, frequency (detuning), and phase of each sinusoid corresponding to each nitrogen hyperfine peak. I is the nitrogen nuclear spin ($1/2$ for ^{15}N, 1 for ^{14}N). For SE measurements, the T_2 data are fit to:

$$B + A\exp\left[-(t/T_2)^n\right], \tag{5.2}$$

Where B is the offset, A is the amplitude, and n is either a free parameter or fixed at 3 [249], when the former does not fit. Physically, this number n connects to the spin bath properties, such as P1 centers [83].

5.2.2 Coherence time of NV⁻ in HSQ-bonded membranes

NV$^-$ centers is a spin-1 system with a zero field splitting of $2.87\,\mathrm{GHz}$. To effectively measure the spin coherence, a static magnetic field of $15\,\mathrm{gauss}$ is applied at approximately 35° to the $[100]$ sample surface to split the spin levels $|m=1\rangle$ and $|m=-1\rangle$. Given the orientation of the sample, this magnetic field is 10° misaligned to the [111] crystal axis. All NV$^-$ center measurements are performed at room temperature with atmosphere pressure. NV$^-$ centers along all four possible crystal orientations are measured. Their orientations are determined by distinguishable transition frequencies due to different Zeeman splittings. The MW signal is delivered via a standalone metal wire bonded across the diamond membrane.

Figure 5.2 (a)-(b) show the representative free induction decay (T_2^*) and spin echo (T_2) curves of a single long-lived NV$^-$. The oscillations in the first $100\,\mu\mathrm{s}$ of Figure 5.2 (a) arise from the aliasing of the electron spin echo envelope modulation. These measurements indicate that the diamond membrane fabrication does not preclude the formation of highly coherent spin qubits, even

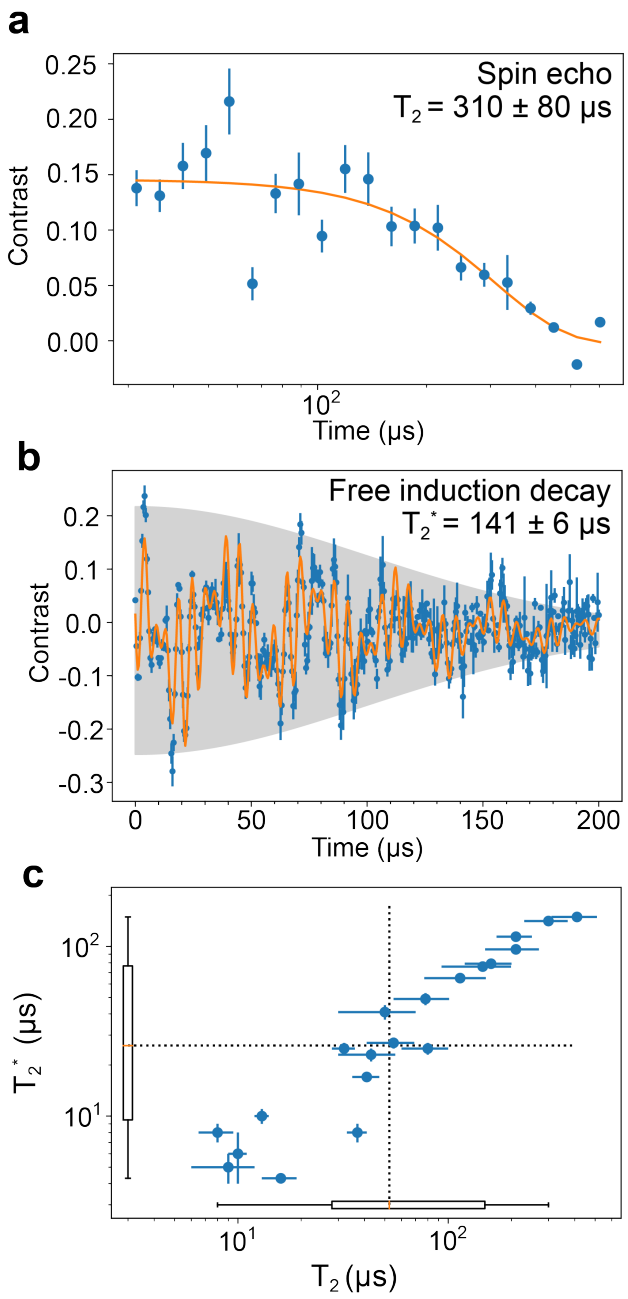

Figure 5.2: Coherence of NV$^-$ in HSQ-bonded membranes at room temperature. (a-b) Representative spin echo and free induction decay curves of a single long-lived NV$^-$, accompanied by fitted T_2 and T_2^* coherence time constants. The oscillations in the first $100\,\mu s$ of (a) arise from the aliasing of the electron spin echo envelope modulation. (c) A scatter plot of T_2^* and T_2 times for the 20 measured NV$^-$ centers. Inset box plots denote median values of $26\,\mu s$ and $52.5\,\mu s$ (dashed lines) and lower-quartile values of $9.5\,\mu s$ and $28\,\mu s$. Error bars are fit errors.

with a total membrane thickness of $\approx 130\,\mathrm{nm}$. A scatter plot of coherence times from all 20 NV^- centers we measured is shown in Figure 5.2 (c), showing a spread of $4.3(3)\,\mu s$ to $149(7)\,\mu s$ and $8(2)\,\mu s$ to $400(100)\,\mu s$ of T_2^* and T_2, respectively. The large span of coherence times indicates that NV^- centers are evenly distributed over the thickness of the membrane, with some residing within $\leq 15\,\mathrm{nm}$ from both surfaces ($T_2 \approx 10\,\mu s$) where previous work demonstrated decoherence from surface noise [78, 246]. Some others are more likely to be away from both surfaces ($T_2 \geq 300\,\mu s$). This is also inline with the observation in Ref [90], where T_2 times for deep δ-doped NV^- centers ($\geq 52\,\mathrm{nm}$) are on the order of $\approx 700\,\mu s$, while the measured values drops drastically as the δ-doped layer was brought closer to the diamond surface ($\leq 35\,\mathrm{nm}$). Based on these observations, we conclude that many of the centers we measured should come from naturally incorporated nitrogen in the diamond membrane, as implanted ^{14}N have a predefined depth—$40\,\mathrm{nm}$. However, statistically, the surface proximity distribution of the NV^- alone cannot fully account for a large number of NV^- centers with $T_2 \leq 100\,\mu s$. Another decoherence source might be the ion implantation of other species (Si^+, Ge^+, Sn^+) in the same device, which is known to introduce crystal damage throughout the ion path and create spin-full vacancy complexes that are not mobilized nor annihilated during the annealing process [247]. Nonetheless, the spin echo coherence time (T_2 up to $400\,\mu s$) is comparable with near bulk-like properties for centers of this depth, and the free induction decay (T_2^* up to $150\,\mu s$) outperforms commercially available bulk material due to the ^{12}C purification. The coherence times presented here are fully compatible with applications in quantum sensing and hybrid quantum systems [245, 250, 251].

Spin decay time T_1 To confirm that the coherence T_2 of NV^- centers is not limited by the spin population decay time T_1, We compare T_1 for two NV^- centers with an order of magnitude separation in T_2. The differential T_1 measurement for NVX ($T_2 = 13(1)\,\mu s$) and NVY ($T_2 = 146(53)\,\mu s$) is shown in Figure 5.3. Over $5\,\mathrm{ms}$ of measurement duration, there is no observable increased decay for NVX compared with NVY, indicating that T_1 plays no role in limiting the coherence.

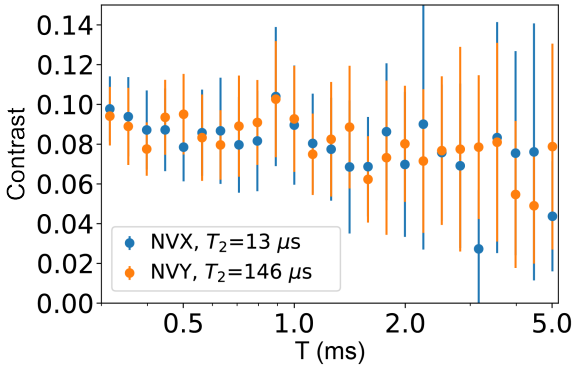

Figure 5.3: NV$^-$ spin lifetime at room temperature. A total of two NV$^-$ centers are measured; they have an order of magnitude spread in T_2 times but show similar T_1 decay curves.

5.2.3 Coherence time of NV$^-$ in direct-bonded membranes

We know that the diamond membrane synthesis maintains the spin coherence properties of NV$^-$. Here, we examine the compatibility of the direct-bonding methods for quantum technologies by measuring a direct-bonded membrane at room temperature. The membrane we use is similar to the HSQ-bonded ones, which is $\approx 150\,\mathrm{nm}$ thick and bonded to a thermal oxide substrate. In addition to implanted and naturally formed ^{14}NV$^-$ centers, this membrane contains naturally formed ^{15}NV$^-$, which originates from the diamond growth chamber that is regularly used for δ-doping of [^{15}N] [40]. The measurement results of two NV$^-$ centers are shown in Figure 5.4, including ODMR spectra, Ramsey measurements (T_2^*), Fourier transformation of T_2^*, and Hahn echo measurements (T_2). The isotope of nitrogens is identified by the ODMR features shown in Figure 5.4 (a)-(b). Ramsey measurements displayed in Figure 5.4 (c)-(d) shows T_2^* of $92(16)$ µs and $66(9)$ µs, respectively. These notably long T_2^* directly imply a high-performance ^{12}C isotopic purification during diamond membrane growth. To better understand the interaction picture, we reproduce the two T_2^* measurements with a much finer scan and perform the Fourier transform to the measurement results (to avoid undersampling), as shown in Figure 5.4 (e)-(f). From the Fourier transform, we can easily tell that the ^{15}NV$^-$ (Figure 5.4 (e)) is coupled to a nearby ^{13}C nuclear spin. This results in an interesting oscillation pattern in its spin echo measurement shown in Figure 5.4 (g). Never-

theless, this NV$^-$ center shows remarkably long Hahn-echo T_2 of $632(21)$ µs, which is comparable to the 600 µs to 2000 µs coherence time range reported in isotopically-purified bulk diamond [131], showing that the direct-bonding method does not bring excess decoherence sources.

Now, we analyze the oscillation pattern in the spin echo measurement. We first write down the interaction term from the weakly coupled ^{13}C. In the rotational frame of the NV$^-$ electron spin, the Hamiltonian is given by:

$$H = \omega_n I_z + S_z(AI_z + BI_x) = (Am_s - \omega_n)I_z + Bm_s I_x \tag{5.3}$$

Where $m_s \in \{0, 1\}$ is determined by the electron spin state. The I_z and I_x are the nuclear spin operators. Diagonalizing the Hamiltonian gives the resonance frequency $K = \sqrt{(Am_s - \omega_n)^2 + (Bm_s)^2}$, such that $K_+ = \sqrt{(A - \omega_n)^2 + (B)^2}$ and $K_- = \omega_n$ for the two NV$^-$ spin states. Therefore, the fitting function of spin echo can be simplified to the following form:

$$\begin{aligned} f(\tau) &= Ae^{(-\frac{\tau}{T_2})^n}\left[1 + 2\left(\frac{B\omega_n}{K_+K_-}\right)^2 \sin^2\left(\frac{2\pi K_+\tau}{4} + \phi_0\right)\sin^2\left(\frac{2\pi K_-\tau}{4} + \phi_1\right)\right] \\ &= Ae^{(-\frac{\tau}{T_2})^n}\left[1 + 2\left(\frac{B}{K_+}\right)^2 \sin^2\left(\frac{2\pi K_+\tau}{4} + \phi_0\right)\sin^2\left(\frac{2\pi K_-\tau}{4} + \phi_1\right)\right] \end{aligned} \tag{5.4}$$

Here τ is defined as the total wait time of the spin echo measurement, which lasts from the beginning of the $\frac{\pi}{2}$ pulse to the end of the second $\frac{\pi}{2}$ pulse. It has a factor of 2 difference from the original reference [252]. From this fitting curve, we can easily find two oscillating frequencies, $\frac{2\pi K_+}{4}$ and $\frac{2\pi K_-}{4}$, that is in line with the T_2 oscillation curve. The modulation frequencies—$97.32(5)$ kHz and $14.82(5)$ kHz—correspond to the free precession of ^{13}C at ≈ 91 gauss (the magnetic field used for spin measurements) and the combination of free precession and coherent coupling strength of the ^{13}C to the ^{15}NV$^-$.

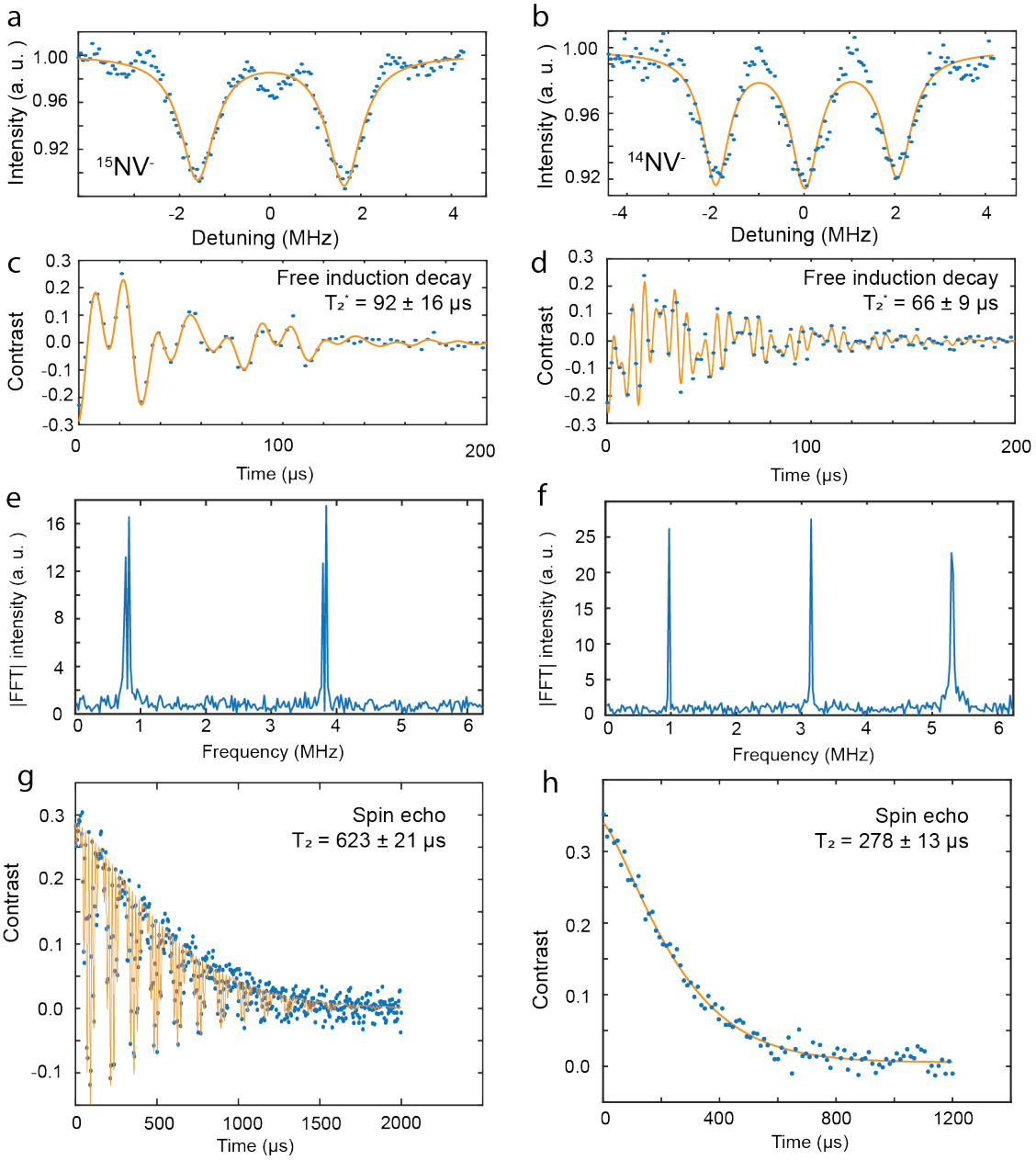

Figure 5.4: Spin coherence of NV$^-$ centers in direct-bonded membranes at room temperature. (a), (c), (e), (g) are measured from a single ^{15}NV$^-$ while (b), (d), (f), (h) are measured from a single ^{14}NV$^-$. (a)-(b): the ODMR spectra. We simplified the fitting using multi-peak Lorentzian to retrieve the ODMR frequency and linewidth. (c)-(d): Free induction decay (Ramsey measurement) of the NV$^-$ centers. Both NV$^-$s show notably long T_2^* times due to the isotopic purification during overgrowth. (e)-(f): Fourier transformations of finely sampled Ramsey measurements show the Larmor precession frequencies coming from in e) the intrinsic ^{15}N with additional splitting from a distant ^{13}C and in (f) only the intrinsic ^{14}N. (g)-(h): Hahn echo measurements of the ^{15}NV$^-$ and ^{14}NV$^-$ showing long T_2 values.

Using the fitted frequency parameters, we obtain $A = \omega_n \pm \sqrt{K_+^2 - B^2}$, which is either $90.493\,\mathrm{kHz}$ or $104.176\,\mathrm{kHz}$. We can then use this value to make a rough estimate of the separation between the ^{13}C and our NV$^-$ center. By ignoring the Fermi contact interaction, the interaction terms can be written as:

$$\begin{aligned} A &= \frac{\mu_0 \gamma_e \gamma_n \hbar}{4\pi r^3}(3\cos^2\theta - 1) \\ B &= \frac{\mu_0 \gamma_e \gamma_n \hbar}{4\pi r^3} 3\cos\theta \sin\theta \end{aligned} \tag{5.5}$$

Solving these equations for θ and r gives [253]:

$$\begin{aligned} \theta &= \arctan\left(\frac{1}{2}\left(-3\frac{A}{B} + \sqrt{9\frac{A^2}{B^2} + 8}\right)\right) \\ r &= \left(\frac{\mu_0 \gamma_e \gamma_n \hbar (3\cos^2\theta - 1)}{4\pi A}\right)^{1/3} \end{aligned} \tag{5.6}$$

Inserting the numbers we have returns an $r = 1.40\,\mathrm{nm}$ with $\theta = 5.5^\circ$ or $r = 1.33\,\mathrm{nm}$ with $\theta = 4.8^\circ$ for $A = 90.493$ or $104.176\,\mathrm{kHz}$. We note that this effect is not apparent for ^{14}NV$^-$, as its large quadrupole interaction at low magnetic fields suppresses the spin echo modulation regardless of the magnetic field alignment [249]. As a result, it returns a simple decay without modulation, as shown in Figure 5.4 (h).

5.3 Characterizing membrane properties using NV$^-$

5.3.1 NV$^-$ strain measurements

In addition to the magnetic field, the NV$^-$ center is also sensitive to both strain and electric field ($\mathbf{\Pi}$) through spin state coupling, as shown in the Hamiltonian:

$$H = (D + \Pi_z)S_z^2 + \Pi_x \left(S_y^2 - S_x^2\right) + \Pi_y(S_xS_y + S_yS_x). \tag{5.7}$$

In practice, parallel strain/electric field (Π_z) shifts the effective zero-field splitting, while the perpendicular components ($\Pi_{x,y}$) split the upper and lower spin transitions [254]. Therefore, the spin state transitions of NV$^-$ is a good indicator of the local electric and strain fields, which can thus be used for membrane strain characterizations when no external E field is present. From Ref [255], the strain susceptibilities are $d_{\sigma:\parallel,\perp} = 13.3\,\mathrm{GHz}$ and $21.5\,\mathrm{GHz}$, thus we expect parallel and perpendicular effects to be of similar magnitudes.

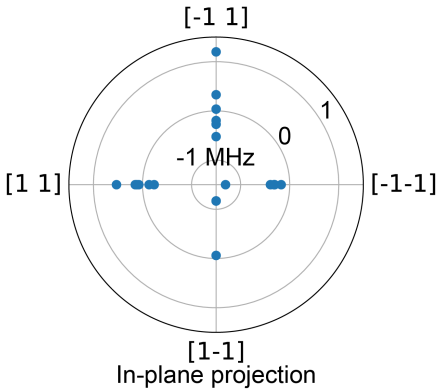

Figure 5.5: Zero-field splitting of measured NV$^-$ centers in different orientations.

For the diamond membrane bonded to the silicon substrate using HSQ, We measure the ODMR of the NV centers versus their orientations as shown in Figure 5.5. The shifts of the zero-field splitting can be used to extract an upper bound on the strain in the membrane. If we assume the larger shifts of $\approx 1\,\mathrm{MHz}$ arise entirely from crystal strain (no implantation damage)—an over-estimate given the above discussion—we arrive at a strain of $< 10^{-4}$ which is relatively small for such a device heterostructure. Multiple factors of the membrane transfer process can contribute to the built-in strain. For instance, the dry transfer might introduce in-plane strain due to non-zero approaching angle and speed. Additionally, some on-chip structures (such as trenches) can modify the strain distribution across the membrane.

5.3.2 *Background [N] and [NV$^-$] estimation*

Unlike group IV centers, NV$^-$ centers are widely present in natural and artificial diamonds. There are three primary sources of nitrogen in diamond, including ion implantation, δ-doping [90], and natural incorporation. They can all form NV$^-$ centers at certain conditions. The naturally incorporated nitrogen impurities mostly come from the presence of the nitrogen element during the formation of diamond (either naturally or artificially). They always have a non-negligible density inside diamond with a lack of deterministic location control. Therefore, they are often called "background [N]" and become a metric for diamond grade classification. For instance, most optical grade single crystal diamonds have parts-per-million (ppm) level [N], while the electronic grade only has parts-per-billion (ppb) concentration.

The diamond membrane synthesis shows a very low natural [N] abundance concentration which is lower than the upper bound of the SIMS equipment resolution ($4.5(2) \times 10^{15}\,\mathrm{cm}^{-3}$, $\leq 26(1)\,\mathrm{ppb}$). Fortunately, the synthesis process is highly amenable to *in-situ* δ-doping of ^{15}N during overgrowth [90]. These δ-doped nitrogen is isotopically engineered to be ^{15}N which shows different ODMR features from the ^{14}N overgrowth background ($99.64\,\%$ natural abundance). Therefore, by limiting the density of ^{15}NV$^-$ and ^{14}NV$^-$, the ^{14}N concentration can be estimated by categorizing and counting the fluorescent color centers via ODMR features in the PL map. The membrane we use here has a δ-doped layer with $2\,\mathrm{nm}$ thickness inside a $110\,\mathrm{nm}$-thick diamond membrane. The PL map of the membrane is shown in Figure 5.6. The ^{15}NV$^-$ centers are labeled in teal circles, while background ^{14}NV$^-$ are in white rectangles, with representative hyperfine-resolved ODMR spectra presented to the right, showing 2 or 3 peaks depending on the nuclear spin. By counting the number of NV$^-$ features, we observe a $7:11$ ratio of $[^{15}\mathrm{NV}^-]:[^{14}\mathrm{NV}^-]$. Combined with our knowledge of ^{15}NV$^-$ concentration which is $30.8(57)\,\mathrm{ppb}$ via SIMS, we can work out an approximate density of the [^{14}N] if we assume a same conversion efficiency for both the δ-doped [^{15}N] and background in-grown natural abundance [N]. Once effective layer thicknesses are considered, i.e., $2\,\mathrm{nm}$ thick portion of [^{15}N] versus a $110\,\mathrm{nm}$ thick $\approx$ [^{14}N] membrane, we end up with a normalized observed

$[^{15}\mathrm{NV}^-] : [^{14}\mathrm{NV}^-]_{\mathrm{normalized}}$ of $7 : 0.2$, resulting in a background $[^{14}\mathrm{N}]$ of $0.124(5) \times 10^{15}\,\mathrm{cm}^{-3}$ $(0.70(3)\,\mathrm{ppb})$. This concentration is comparable with electronic grade diamonds, and at this level, P_1 centers should not contribute heavily to the decoherence [256].

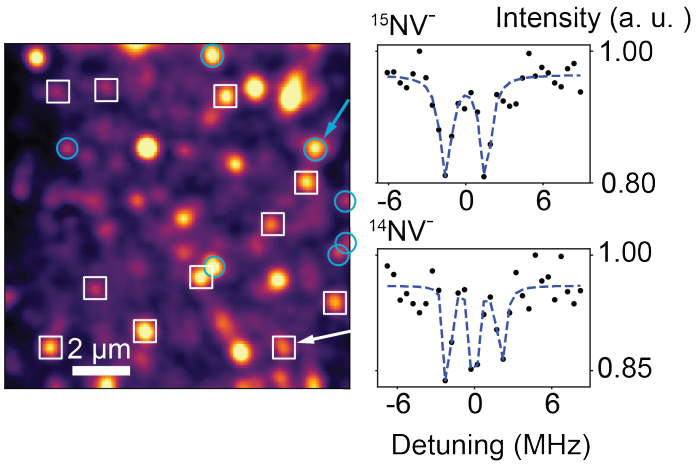

Figure 5.6: NV^- PL map of a δ-doped membrane with $^{15}\mathrm{NV}^-$ centers (teal circles) and $^{14}\mathrm{NV}^-$ centers (white squares) labeled. The pulsed-ODMR spectra of the NV^- centers are at right.

5.3.3 NV^- centers at $4\,\mathrm{K}$

One major issue of the HSQ-bonded membrane for NV^--based quantum sensing is its excessive background fluorescence, which leads to sophisticated trench design on the carrier wafer and vapor HF process to remove the deposited HSQ [40]. Thanks to the low optical background of the direct bonding method, we are able to resolve individual NV^- centers in the diamond membrane directly. To obtain NV^- center's charge stability information—a good indicator of membrane's surface termination at the bonding interface that depends on the plasma treatments —we cool down the membrane sample to $4\,\mathrm{K}$ and measure the NV^- optical properties. The PL map of individual NV^- centers is displayed in Figure 5.7 (a), showing a signal-to-background ratio of over 1.4. The charge stability information is deduced from the spectra of NV^- in three separately prepared direct-bonded membranes. Three membranes are from a single mother substrate doped *in-situ* with $^{15}\mathrm{N}$ and thus contain the same NV^- density. They are bonded to thermal oxide substrates with (1) no

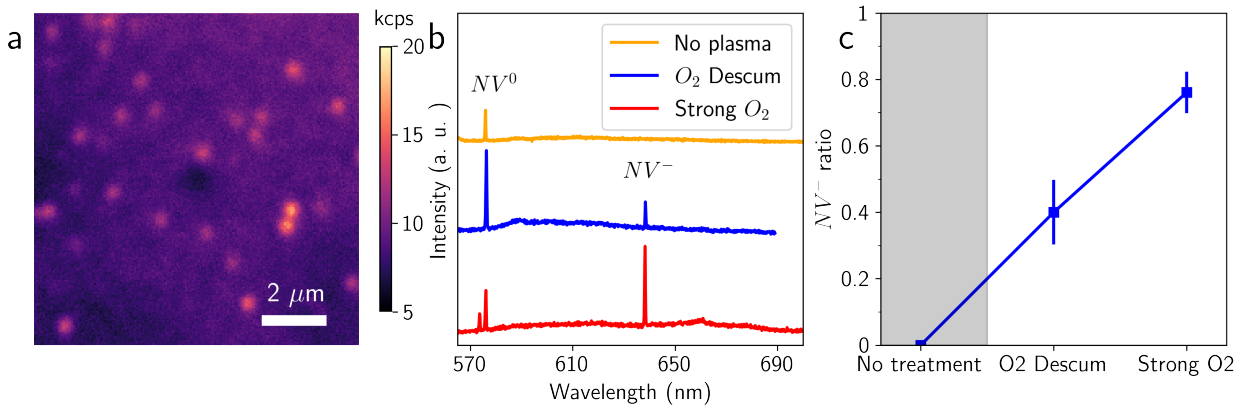

Figure 5.7: Optical characterization of NV^- centers in direct-bonded diamond membrane measured at $4\,K$. (a) A PL map of NV^- centers in a diamond membrane. The excitation source is a green laser with $325\,\mu W$ power. Signals are collected using a $561\,nm$ longpass filter. The signal-to-background ratio is ≈ 1.4. (b) The spectra of NV centers with no plasma (orange), O_2 descum (blue), or high power O_2 plasma treatment (red) before bonding. The dominant NV^0 originates from the Ar/H_2 annealing. The appearance of NV^- indicates the surface oxygen termination of the diamond bonding interface. The small peak on the left side of the red curve is the Raman response of the diamond due to a different excitation laser wavelength used for that specific measurement ($532\,nm$ instead of $519\,nm$). (c) The ratio of NV in its negatively charged state with respect to different plasma conditions on the diamond bonding interface. The NV^- ratio increased from 0 to $76(6)\,\%$ using high-power plasma treatment. Calculation of this ratio takes the Huang-Rhys factor of NV^0 (3.3) and NV^- (4.0) into account. [257]

plasma treatment, (2) O_2 descum, and (3) high-power plasma ashing on the diamond bonding side. The NV^- spectra from these membranes are shown in Figure 5.7 (b). With no plasma treatment, NV^- centers almost entirely remain at the neutral charge state due to the hydrogen termination effect from the Ar/H_2 annealing process [258]. In contrast, membranes treated with oxygen plasma have considerably higher NV^-/NV^0 ratio. This ratio is positively correlated with the strength of the O_2 ashing plasma, indicating a proper oxygen termination which helps keep NV center in its negatively charged state [259]. The calculated ratio of NV^- in both charge states ($NV^-/(NV^- + NV^0)$) is shown in Figure 5.7 (c), indicating that this dry oxygen termination method can be used to desirably engineer the diamond near-surface Fermi level for NV^- based applications [153, 260].

5.4 NV^- centers in bonded membranes for bio sensing applications

For most NV^--related quantum sensing applications, a diamond sensor is typically brought close to sensing targets. To leverage the proximity of the sensing target and the coherence of NV^-, most sensitive NV^- sensors rely on high-purity single-crystals with the sensing target bound on the diamond's top surface [42]. Except for scanning NV^- tips [261], many experiments still rely on bulk diamond with large thickness and refractive index, which typically requires optical initialization and readout of the sensing qubits from the top surface. Consequently, the target systems need to possess optical transparency, low auto-fluorescence, and high photostability, which are significant restrictions for many studies, especially biological systems. With only $\approx 200\,\mathrm{nm}$-thickness, the direct-bonded membranes are able to address these issues by enabling optical addressability through the back of the membrane without the need for passing through the top surface and the sensing target.

5.4.1 NV^- center imaging and verification

Before implementing direct-bonded membranes with bio-sensing device components (surface functionalizations, microfluidic channels, etc.), we first study the photostability and addressability of individual NV^- centers in bonded diamond membranes, as well as the compatibility of NV^- identification with the state-of-the-art bio-sensing and imaging methods. The diamond membranes used here include individual δ-doped NV^- centers and have been studied in a previous work [40]. These membranes are bonded to fused silica coverslips, which are sufficiently large to host microfluidic channels. Unlike previous NV^- studies, the illumination is provided from the back of the membrane through the fused silica coverslip, with the oil objective applied to improve the signal collection. In addition, we use widefield imaging instead of a confocal microscope to identify the NV^- locations. The $532\,\mathrm{nm}$ laser with $\approx 35\,\mathrm{mW}$ power covers an effective field-of-view of $73\,\mu\mathrm{m}$ by $73\,\mu\mathrm{m}$, indicating a 1-2 orders of magnitude lower power density compared with typical confocal setups.

Figure 5.8 (a) is a widefield fluorescence micrograph of a direct-bonded diamond membrane. The fluorescence background of the diamond membrane region is very low, which is comparable to or even darker than the coverslip due to the large refractive index of diamond. There are also many bright, diffraction-limit spots in the diamond membrane, which are later verified as predominately NV^- centers. These centers show excellent photostability (negligible photobleaching) under continuous excitation.

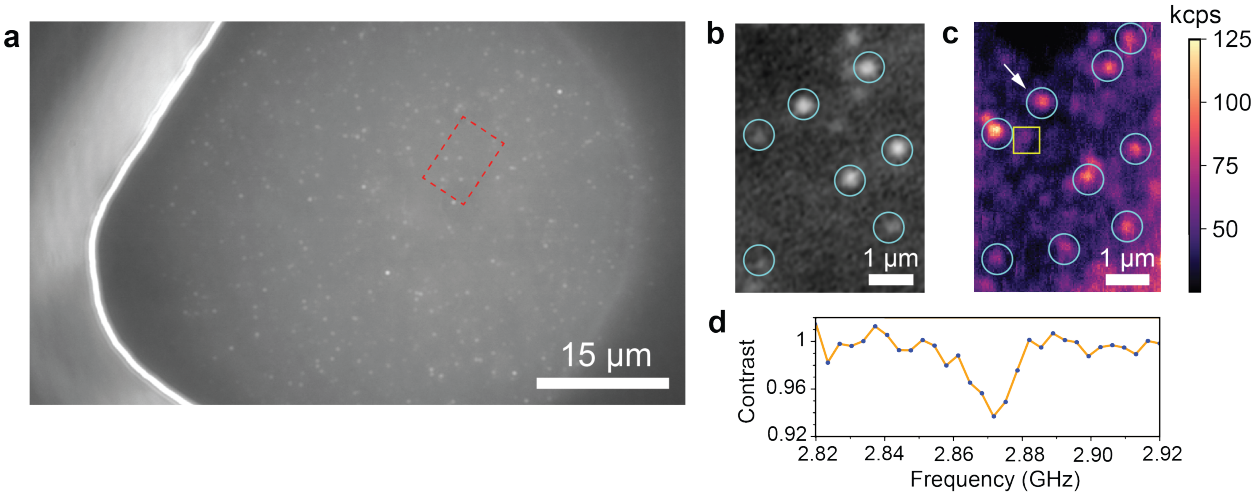

Figure 5.8: Imaging and confirmation of NV^- centers. (a) Widefield fluorescence microscope image of a diamond membrane corner containing individual NV^- centers at room temperature. Only a small round area in the center is under illumination to avoid reflection signals from membrane edges. (b) The zoomed-in image of the boxed region shown in (a) post rotation. (c) A PL image of the same region as (b) using a separate confocal setup at room temperature. Emitters confirmed to be (not) NV^- centers are highlighted in cyan circles (yellow boxes). The same symbols are used in (b). (d) A representative CW-ODMR spectrum from the NV^- center highlighted with a white arrow in (c).

The verification of NV^- centers is performed at a separate room temperature confocal setup with external microwave signal delivery through a gold wire. After locating the same region imaged by the widefield camera, we perform ODMR measurements to the bright spots in the confocal PL map. The camera image and the PL map from the exact location are plotted in Figure 5.8 (b)-(c). The emitters are confirmed to be NV^- centers through the presence of their characteristic 2.87 GHz zero-field splitting by ODMR spectroscopy, shown as cyan circles. Emitters without such a feature are labeled as yellow boxes. We note that most of the bright emitters (12 out of

14) are NV^- centers, reiterating the excellent photostability of the centers and the relatively low fluorescence background. The signal contrast is slightly lower with a broader ODMR linewidth due to the power broadening of the measurement. According to the coherence measurements in the previous section, these NV^- centers have excellent spin coherence, which is ideal for sensing purposes.

5.4.2 Device design and sensing target incorporation

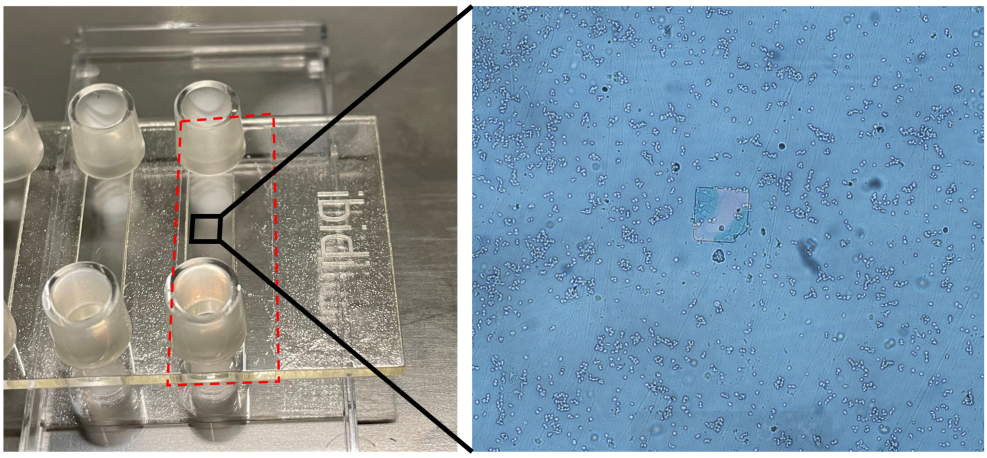

Figure 5.9: The assembled flow channel device for bio-imaging and sensing. A fused silica coverslip (red dashed box) with a diamond membrane bonded to the center is attached to a flow channel slide. RAW cells are incubated, fixed, and stained inside the flow channel, as shown in the right microscopic image.

In addition to the direct-bonded membrane and coverslip, two other components are introduced to form a complete bio-imaging system: surface functionalization of the diamond membrane (target molecule immobilization) and flow channel assembly. The bio-compatible surface functionalization is achieved following the strategy introduced in Ref [125]: atomic layer deposition (ALD) of an oxide layer to prepare the surface for subsequent biochemical modifications while protecting the near-surface NV^- coherence. After surface functionalization, a flow channel is assembled on top of the coverslip for microfluidic characterizations. An image of the assembled device is shown in Figure 5.9, with the diamond membrane and immobilized cells shown in the microscope image

on the right.

5.4.3 Simultaneous imaging of NV⁻ and sensing targets

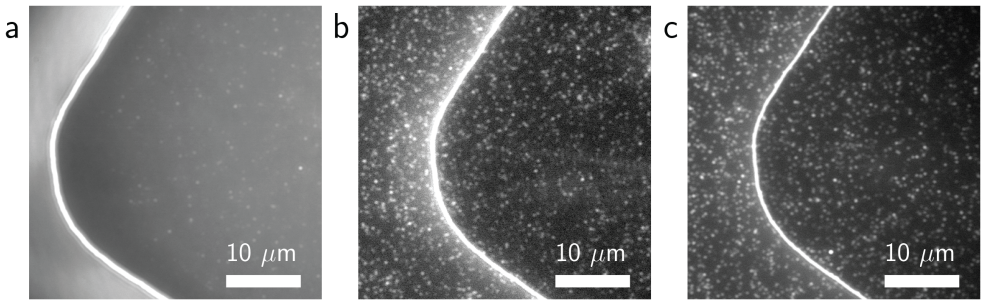

Figure 5.10: Widefield images of NV^- and two sensing targets. (a) A widefield image of NV^-. (b)-(c) Widefield fluorescence microscope images of (b) Alexa-488-labeled streptavidin protein and (c) streptavidin-conjugated Qdot-525 quantum dots that are immobilized at the same region shown in (a) via biotinylated surface functionalization.

When the flow channel has been assembled, attachment of target molecules is achieved using either streptavidin labeled with Alexa-488 dye or streptavidin-conjugated Qdot-525 quantum dots. These molecules are introduced to the flow channel sequentially (not simultaneously), each with several minutes of incubation and phosphate-buffered saline (PBS) wash before being imaged by the widefield camera. After imaging, these molecules are photobleached using intense illumination to allow for the next incubation process. The fluorescence of individual Alexa488-labeled streptavidin molecules and streptavidin-conjugated Qdot-525 quantum dots are shown in Figure 5.10. This imaging method enables detecting the positions of not only NV^- centers but also target proteins on the membrane's surface, which is important for NV^--based single-molecule nuclear magnetic resonance (NMR) [262] and electron paramagnetic resonance [263] spectroscopy. This method also allows for the efficient identification of NV^- centers that have a desired molecular target within the sensing range.

The sensing targets are chosen to have a spectral separation ($488\,\mathrm{nm}$ laser excitation, 525/50 or 510/20 nm band-pass imaging filter for signal collection) from the NV^- excitation and signal collection wavelength. Specifically, Qdot-525 uses a narrow filter of 510/20 nm for signal collection,

which forms a complete spectral separation from the NV^- excitation. This enables simultaneous imaging of both NV^- and sensing targets using a dual-imaging system. The schematic of the dual imaging system is shown in Figure 5.11 (b), and the dual-color images simultaneously displaying NV^- centers and Qdot-525 are shown in Figure 5.11 (a). Image pairs from the same field of view are spectrally separated using a dichroic beam splitter, with a 510/20 nm filter in the short wavelength path and a $594\,\mathrm{nm}$ long-pass filter in the long wavelength path. This method enables the selection of NV^--target molecule pairs that are spatially closed to each other for subsequent quantum sensing experiments.

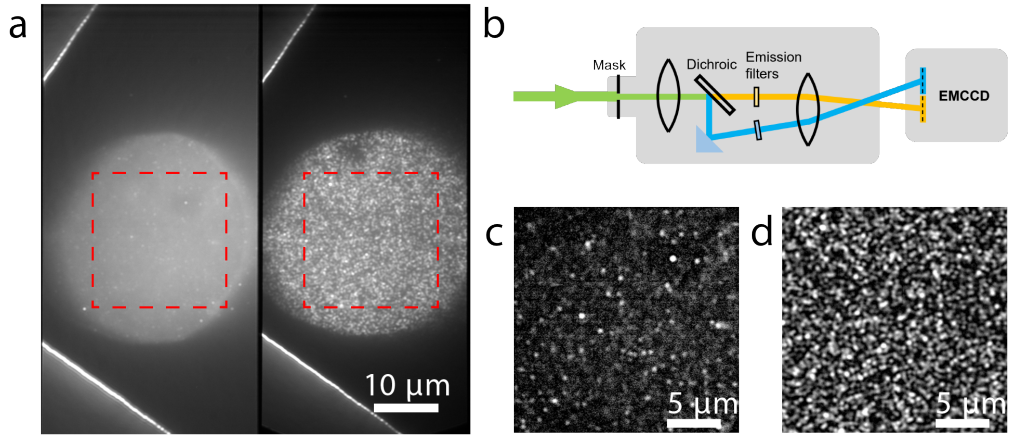

Figure 5.11: Simultaneous detection of both NV^- and Qdot-525. (a) A single-exposure image acquired on an EMCCD, showing two sub-images of the same area differentiated by emission wavelengths. The left sub-image is the NV^- map, and the right is the Qd-525. (b) Schematic illustration of the Hamamatsu W-VIEW GEMINI system used in this experiment. (c)-(d) The zoomed-in view of the regions in (a) indicated by red boxes, respectively. During a single exposure which lasted $100\,\mathrm{s}$, $488\,\mathrm{nm}$ laser was switched on only for the first $10\,\mathrm{s}$ while the $532\,\mathrm{nm}$ laser was on for the entire duration to help balance the overall intensities of the two sub-images.

5.4.4 Total internal reflection fluorescence (TIRF)-microscopy

TIRF condition and evanescent field profile By utilizing the refractive index difference between diamond ($n_{\mathrm{diamond}} = 2.42$), fused silica ($n_{\mathrm{glass}} = 1.46$) and water ($n_{\mathrm{water}} = 1.33$), we integrate the TIRF-microscopy to our diamond membrane devices to demonstrate bio-imaging at a reduced level of background luminescence. In principle, the depth resolution of TIRF-microscopy

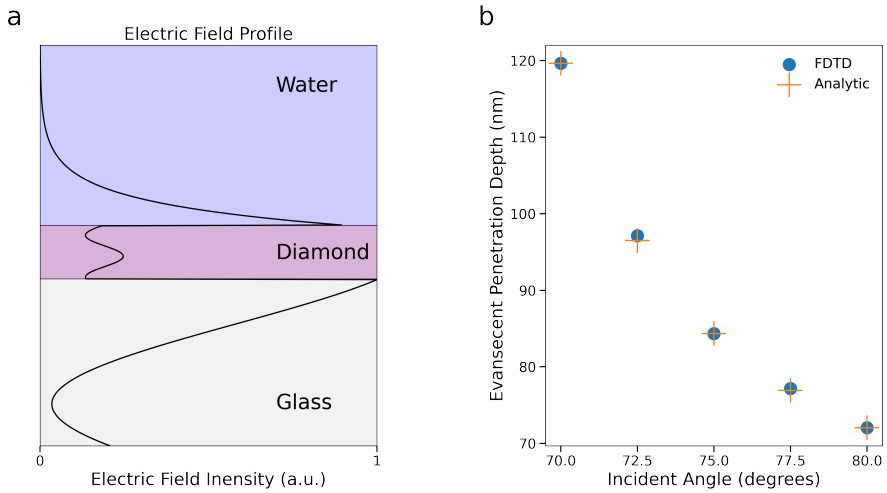

Figure 5.12: Calculated intensity profile in diamond-membrane-TIRF microscopy. (a) Simulated electric field intensity profile across a $160\,\mathrm{nm}$-thick diamond membrane between a glass substrate and water. The light is p-polarized with an incident angle 70°, as referenced in the glass substrate. (b) Intensity decay constant in the water layer calculated using FDTD (blue circle) and analytically (orange cross) for angles greater than the critical angle.

originates from the rapid evanescent field decay of light incident at angles greater than the critical angle. For our system, this critical angle is $\theta_c = \sin^{-1}(n_{\text{water}}/n_{\text{glass}}) \approx 66^\circ$. We use Lumerical$^{@}$ simulation to calculate the electric intensity profile across the diamond membrane. A typical simulation result for p-polarized light with an incident angle of 70° is shown in Figure 5.12 (a), showing an exponential decay of electric field intensity in the water. By simulating the field intensity at different incident angles displayed in Figure 5.12 (b), we can extract the decay constant in wafer which matches the analytic expression $\frac{\lambda_o}{4\pi}(n_1^2\sin^2(\theta) - n_2^2)^{-1/2}$ for incident angles greater than θ_c [188]. Such large incident angles are accessible in our setup thanks to the 1.5 numerical aperture (NA) of the oil objective. From the figure, we expect our diamond membrane TIRF configuration to have a depth resolution of $\leq 100\,\mathrm{nm}$.

Guided by the simulation results, we integrate a diamond membrane with a flow channel with macrophage-like RAW cells grown on the diamond surface. The cells are fixed by incubating with paraformaldehyde and labeled with Alexa-488. The schematic illustration of our TIRF-microscopy is shown in Figure 5.13 (a). Staining the toll-like receptor 2 (TLR2) with Alexa-488-labeled anti-

TLR2 antibody reveals in TIRF imaging the location of individual proteins distributed across the back surface of the cell that is close to the diamond surface (Figure 5.13 (c)). The imaging result is in stark contrast with the epi-luminescence mode, where background fluorescence reduces the signal-to-noise ratio and prevents the imaging of individual molecules on the back surface (Figure 5.13 (b)). We note that the larger index of refraction ($n = 2.42$) of diamond results in an evanescent field that falls 1.6-times faster off compared with a bare glass microscope coverslip ($n = 1.46$) and thus provides even higher contrast images. In short, experiments enabled by the flow channel demonstrate remarkable flexibility to interface target samples with quantum diamond sensors, which is challenging through conventional approaches [264].

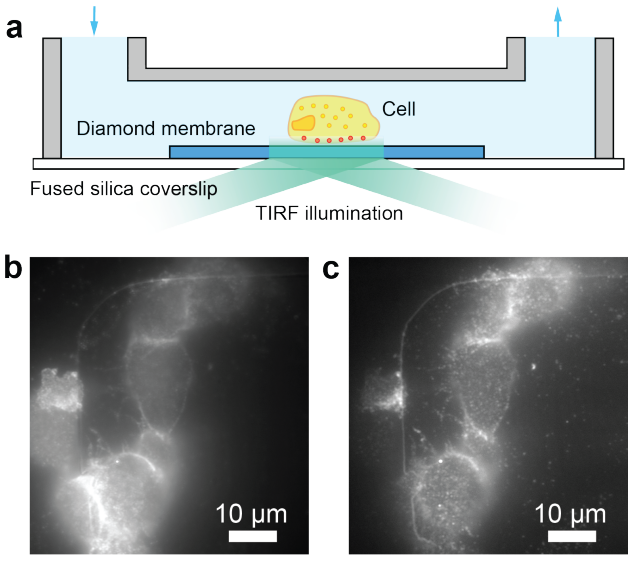

Figure 5.13: TIRF-microscopy using a diamond membrane device. (a) The schematic illustration of the flow channel structure and a cell illuminated by total internal reflection light through the diamond membrane. (b)-(c) Fluorescence microscope images of Alexa-488-labeled TLR2 receptors on RAW cell surfaces under (b) episcopic and (c) objective-based TIRF illumination. Edges of the diamond membrane are also visible in these images.

CHAPTER 6

GEV$^-$ CENTER AS A SOLID-STATE ATOMIC ANTENNA[†]

Abstract

In previous chapters, we discussed two types of color centers—optically active spin qubits—and studied their spin properties and manipulation methods. In this section, we focus on the near-field emission properties of a specific color center, GeV$^-$ from the group IV center family. Near-field emissions are usually captured by other objects within a short distance. Here, we use nearby carbon vacancies that are only a few nanometers away as probes to monitor the emission profile. The changes of carbon vacancies' charge states can be screened by the ZPL wavelength shift of GeV$^-$ due to the second-order Stark effect. We also correlate the ZPL shift to the carbon vacancies' PL emission to further conclude the nature of this interaction. Furthermore, we regard the GeV$^-$ as an optical antenna and investigate the near-field amplification of the center by driving carbon vacancies' charge states using lasers that are either on- or off-resonance with GeV$^-$'s ZPL wavelength. The amplification can be directly calculated by comparing the threshold laser power. With the maximum amplification reaching a million, the GeV$^-$ shows its great potential as a powerful near-field, narrow-bandwidth optical antenna that inspires interesting new applications in spectroscopy, sensing, and quantum science as a complement to conventional nanoantennas.

6.1 Theoretical background

6.1.1 Optical antenna

The term optical antenna originates from its traditional counterparts, microwave (MW) or radio frequency (RF) antennas. These antennas usually consist of metal wires with a total footprint that is less or comparable to the operation wavelength to minimize destructive interference. Based

†. The work discussed in this section was reported in [265]

on the functionality of a general antenna, the optical antenna is defined as *a device designed to convert free propagating optical radiation to localized energy efficiently, and vice versa* [266]. A typical optical antenna that generates an electromagnetic field can be simplified as a dipole with its characteristic size (sometimes significantly) smaller than the wavelength. Although, in principle, any optical dipole can be used as an antenna, there are several metrics to evaluate if an antenna is suitable for specific applications, including gain, directivity, tunability, operation wavelength, and bandwidth. Unlike traditional antennae, optical antennae usually do not have feeding waveguides and are often used via remote excitation. To date, the most commonly applied optical antennae are various forms of plasmonic nanostructures [267]. The optical antenna can generate huge field confinement that can be used to guide light and amplify local light-matter interactions for a broad range of classical and quantum applications, including communications, sensing, imaging, photodetection enhancement, heat transfer, and spectroscopy [268–276].

6.1.2 Radiation field of a GeV⁻ center

Here, we introduce the radiation field of a GeV^- center in diamond by treating it as an atomic dipole with an additional damping term Γ' in addition to its spontaneous lifetime Γ_0 [188]. This treatment is valid as long as the distance of the radiation field R we calculate is beyond the characteristic length of the dipole: $R \gg d_c \approx 0.2\,\mathrm{nm}$.

General expression For a group of charges close to each other (distance much smaller than the wavelength), the electromagnetic field they generate cannot be accurately described by the macroscopic parameters such as the electric displacement D and the magnetic field H in Maxwell's equations. Instead, every charge needs to be treated individually in this microscopic system:

$$\rho(\boldsymbol{r}) = \sum_n q_n \delta(\boldsymbol{r} - \boldsymbol{r}_n) \tag{6.1}$$

$$\boldsymbol{j}(\boldsymbol{r}) = \sum_n q_n \dot{\boldsymbol{r}_n} \delta(\boldsymbol{r} - \boldsymbol{r}_n) \tag{6.2}$$

If we expand the expression of $\boldsymbol{j}(\boldsymbol{r})$ in a Taylor series with respect to the origin $\boldsymbol{r}_0$, the center of the charge distribution, then we have

$$\boldsymbol{j}(\boldsymbol{r}, t) = \frac{d}{dt}\boldsymbol{p}(t)\delta(\boldsymbol{r} - \boldsymbol{r}_0) \tag{6.3}$$

Where $\boldsymbol{p}(t) = \sum_n q_n(\boldsymbol{r}_n(t) - \boldsymbol{r}_0)$ is the usual definition of a system's electric dipole. In our case, the GeV^- has a very narrow characteristic emission profile at the ZPL wavelength $\approx 602\,\mathrm{nm}$. Therefore, we treat the oscillating dipole with a harmonic time dependence $\boldsymbol{j}(\boldsymbol{r}, t) = \mathrm{Re}\,[\boldsymbol{j}(\boldsymbol{r})\exp(-i\omega t)]$ and $\boldsymbol{p}(t) = \mathrm{Re}\,[\boldsymbol{p}\exp(-i\omega t)]$ and write the current density in a simple form as $\boldsymbol{j}(\boldsymbol{r}) = -i\omega\boldsymbol{p}\delta(\boldsymbol{r} - \boldsymbol{r}_0)$. It can be interpreted that to the lowest order, the current density of a microscopic system can be regarded as an oscillating dipole around the charge center.

Now, we turn to the electromagnetic field generated by this current density. We use a Green function $\overleftrightarrow{G}$ as the bridge to link the current density $\boldsymbol{j}(\boldsymbol{r})$ and the electric field $\boldsymbol{E}(\boldsymbol{r})$. This function is a tensor with each column referring to the effect of a current density with unit strength flowing to a specific axis of the coordinate $\{x, y, z\}$. For a homogeneous medium (in this case, diamond), the electric field can be written as [188]:

$$\boldsymbol{E}(\boldsymbol{r}) = \boldsymbol{E}_0(\boldsymbol{r}) + i\omega\mu\mu_0 \int_V \overleftrightarrow{G}(\boldsymbol{r}, \boldsymbol{r}')\boldsymbol{j}(\boldsymbol{r}')dV' \tag{6.4}$$

By inserting the expression of $\boldsymbol{j}(\boldsymbol{r})$ we find:

$$\boldsymbol{E}(\boldsymbol{r}) = \boldsymbol{E}_0(\boldsymbol{r}) + \omega^2\mu\mu_0 \overleftrightarrow{G}(\boldsymbol{r}, \boldsymbol{r}_0)\boldsymbol{p} \tag{6.5}$$

We note that there are two parameters that affect the system behavior: the Green function $\overleftrightarrow{G}$ that depends on the distance and orientation between the source of dipole and the observation point, and the time-dependent dipole $\boldsymbol{p}$ which is related to the emission properties of GeV^{-}. The term $\boldsymbol{E}_0$ refers to the external driving field that is used to compare the field amplification.

Green function For a homogeneous space, the Green function $\overleftrightarrow{G}$ can be written as:

$$\overleftrightarrow{G}(\boldsymbol{r}, \boldsymbol{r}_0) = \left(\overleftrightarrow{I} + \frac{1}{k^2}\nabla\nabla\right) G(\boldsymbol{r}, \boldsymbol{r}_0) = \left(\overleftrightarrow{I} + \frac{1}{k^2}\nabla\nabla\right) \frac{\exp(ik|\boldsymbol{r} - \boldsymbol{r}_0|)}{4\pi|\boldsymbol{r} - \boldsymbol{r}_0|} \tag{6.6}$$

Expanding the expression in a Cartesian coordinate, we have:

$$\overleftrightarrow{G}(\boldsymbol{r}, \boldsymbol{r}_0) = \frac{\exp(ikR)}{4\pi R}\left[\left(1 + \frac{ikR - 1}{k^2R^2}\right)\overleftrightarrow{I} + \frac{3 - 3ikR - k^2R^2}{k^2R^2}\frac{\boldsymbol{RR}}{R^2}\right] \tag{6.7}$$

In this study, we are interested in the near-field term since the distance is much smaller than the wavelength. Therefore, we ignore the $(kR)^{-1}$ and the $(kR)^{-2}$ terms, leaving only the $(kR)^{-3}$ term behind:

$$\overleftrightarrow{G}(\boldsymbol{r}, \boldsymbol{r}_0) = \overleftrightarrow{G}(\boldsymbol{r}, \boldsymbol{r}_0)_{NF} = \frac{\exp(ikR)}{4\pi R}\frac{1}{k^2R^2}\left[-\overleftrightarrow{I} + 3\frac{\boldsymbol{RR}}{R^2}\right] \tag{6.8}$$

Here R is the distance of the observation point $R = |\boldsymbol{r} - \boldsymbol{r}_0|$, $\boldsymbol{RR}$ is the outer product of the $\boldsymbol{R}$ with itself.

Dipole moment Although the dipole moment is written as a simple notation $\boldsymbol{p}$, it contains all the information of how the GeV^{-} responds to the incident electric field and should be treated carefully. In general, the Hamiltonian of the GeV^{-} system with an external electric field can be written as:

$$\hat{H} = \hat{H}_0 + \hat{H}'(t) \tag{6.9}$$

Since the GeV^- is an atomic scale system, the electric field is spatially invariant. Therefore, we write the field as $\boldsymbol{E}(\boldsymbol{r},t) \approx \boldsymbol{E}_0 \cos(\omega t)$. At the first order, if we only consider dipole interactions (no higher order terms), the interaction Hamiltonian is then $\hat{H}'(t) = -\hat{\boldsymbol{p}}(\boldsymbol{r}) \cdot \boldsymbol{E}_0 \cos(\omega t)$, where $\boldsymbol{p}$ is the total dipole of the GeV^- system. We must emphasize that although GeV^- does not have a permanent dipole in the ground state, its optical dipole is non-zero.

For simplicity, we only consider the two energy levels we are interested in: optical ground and excited states of GeV^-, written as Ψ_g and Ψ_e. As an approximation, we assume that the population of GeV^- is entirely in these two states (no dark, metastable state). We thus write the quantum state as:

$$\Psi(\boldsymbol{r},t) = c_g(t)\Psi_g(\boldsymbol{r},t) + c_e(t)\Psi_e(\boldsymbol{r},t) \tag{6.10}$$

Where two population parameters $|c_g|^2 + |c_e|^2 = 1$. If we introduce the transition frequency $\omega_0 = (E_e - E_g)/\hbar$, then the equations for c_g and c_e can then be written as:

$$\dot{c}_g(t) = c_e(t)\frac{i}{\hbar}\boldsymbol{p}_{ge} \cdot \boldsymbol{E}_0 \cos(\omega t)\mathrm{e}^{-i\omega_0 t} \tag{6.11}$$

$$\dot{c}_e(t) + \frac{\Gamma}{2}c_e(t) = c_g(t)\frac{i}{\hbar}\boldsymbol{p}_{eg} \cdot \boldsymbol{E}_0 \cos(\omega t)\mathrm{e}^{+i\omega_0 t} \tag{6.12}$$

Where $\boldsymbol{p}_{ge}$ and $\boldsymbol{p}_{eg}$ are transition dipoles connection the two energy levels defined as $\boldsymbol{p}_{ij} = \langle i|\boldsymbol{p}|j\rangle$ which are time independent system parameters. The transition dipoles satisfy $\boldsymbol{p}_{ge} = \boldsymbol{p}_{eg}^*$. The time dependence of c_g, c_e, and thus $\boldsymbol{p}$ are related to the explicit form of the external driving. For our laser excitation, which is almost on-resonance with ω_0, we can apply the rotation wave approximation to the system and only extract the term that oscillates slowly. In addition, the damping term $\Gamma = \Gamma_0 + \Gamma'$ includes both spontaneous emission and other decay channels. In our case we choose $\Gamma' = 3\Gamma_0$ which is commonly observed in other GeV^- studies [40, 100, 213]. With the damping term present, the steady state of the dipole moment can be calculated using the

equation $\boldsymbol{p}(t) = \langle \Psi_e | \boldsymbol{p} | \Psi_g \rangle = c_g^* c_e \boldsymbol{p}_{ge} \mathrm{e}^{-i\omega_0 t} + c_e^* c_g \boldsymbol{p}_{eg} \mathrm{e}^{+i\omega_0 t}$, which can be written as:

$$\boldsymbol{p} = \overleftrightarrow{\alpha} \boldsymbol{E} = \frac{\boldsymbol{p}_{ge}\boldsymbol{p}_{eg}}{\hbar} \frac{\omega_0 - \omega + i\Gamma/2}{(\omega_0 - \omega)^2 + \Gamma^2/4 + \omega_R^2/2} \boldsymbol{E}_0 \tag{6.13}$$

Where $\omega_R = \frac{|\boldsymbol{p}_{eg} \cdot \boldsymbol{E}_0|}{\hbar}$ is the Rabi frequency when the drive is on-resonance. The usual Rabi frequency for off-resonance drive is $\Omega = \sqrt{(\omega_0 - \omega)^2 + \omega_R^2}$. Obviously, the dipole moment $\boldsymbol{p}$ does not have a simple linear relationship with the incident field $\boldsymbol{E}$. For our study, the on-resonance driving field is at a moderate power (less than the saturation power of GeV$^-$ to prevent linewidth broadening in many cases). Therefore, we can simplify the equation as:

$$\boldsymbol{p} = \overleftrightarrow{\alpha} \boldsymbol{E} = \frac{\boldsymbol{p}_{ge}\boldsymbol{p}_{eg}}{\hbar} \frac{1}{\omega_0 - \omega - i\Gamma/2} \boldsymbol{E}_0 \tag{6.14}$$

Field intensity amplification Combining the result from the Green function, we can thus write down the amplification ratio $\frac{\boldsymbol{E}(\boldsymbol{r})}{E_0(\boldsymbol{r}_0)}$:

$$\frac{\boldsymbol{E}(\boldsymbol{r})}{E_0(\boldsymbol{r}_0)} = \hat{\boldsymbol{E}}_0(\boldsymbol{r}_0) + \frac{3\exp(ikR)}{4k^3R^3} \left[-\overleftrightarrow{I} + 3\frac{\boldsymbol{R}\boldsymbol{R}}{R^2} \right] \frac{\hat{\boldsymbol{p}}_{ge}\hat{\boldsymbol{p}}_{eg}}{-\Delta/\Gamma_0 - i(1 + \Gamma'/\Gamma_0)/2} \hat{\boldsymbol{E}}_0(\boldsymbol{r}_0) \tag{6.15}$$

Where $\hat{\boldsymbol{E}}_0(\boldsymbol{r}_0)$ is the unit vector with the direction of the incident electric field, and $\{\hat{\boldsymbol{p}}_{ge}, \hat{\boldsymbol{p}}_{eg}\}$ are the unit vectors of the transition dipole. We use the fact that at optical frequency $\mu_r = 1$ and the spontaneous emission rate in solid we derived in Chapter 3: $\Gamma_0 = \frac{n|\boldsymbol{p}_{ge}|^2\omega_0^3}{3\pi\varepsilon_0\hbar c^3}$. If we ignore the orientation factor and only look at the scaling of this equation for the electric field intensity when the laser is on resonance ($\Delta \to 0$), we have:

$$\frac{I(\boldsymbol{r})}{I_0} = \left| \frac{\boldsymbol{E}(\boldsymbol{r})}{E_0(\boldsymbol{r}_0)} \right|^2 \sim \left(\frac{1}{1 + \Gamma'/\Gamma_0} \right)^2 \frac{1}{(kR)^6} \tag{6.16}$$

Therefore, the field intensity amplification can be massive at a very small detection distance $\boldsymbol{R}$. Figure 6.1 (a) shows the schematic of the GeV$^-$ used as a near-field optical antenna under resonant

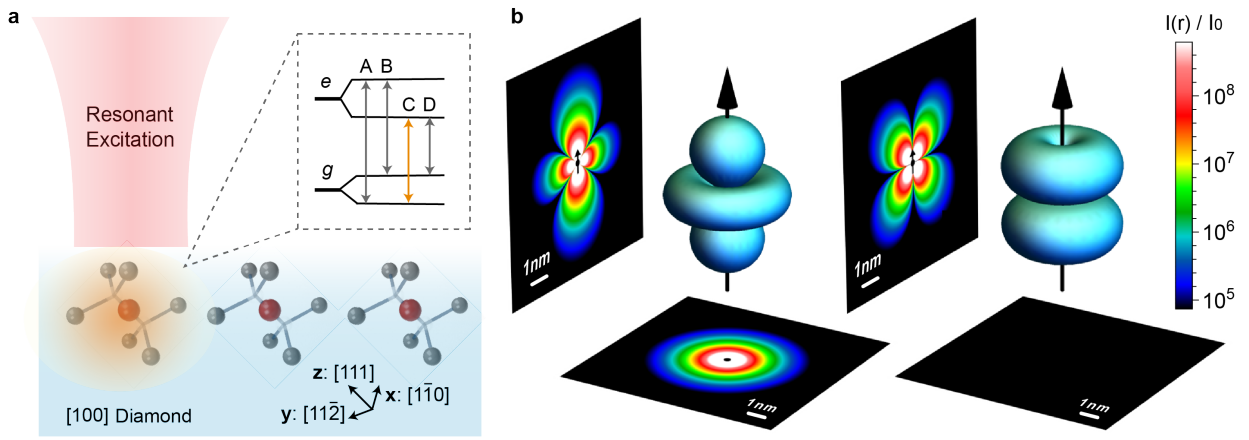

Figure 6.1: GeV^- center as a near-field antenna. (a) The schematic of the GeV^- center as a near-field optical antenna. Inset: the energy diagram of the GeV^-. The C transition is used for resonant excitation. (b) The calculation result of the electromagnetic field enhancement using GeV^-. In this calculation, the incident field (resonant excitation) is polarized along the symmetry axis of GeV^- (z direction in (a)). The 3D contours represent an intensity amplification $\frac{I(\boldsymbol{r})}{I_0}$ of 5×10^5. The left (right) plot corresponds to the near field polarized along (perpendicular to) the GeV^- dipole orientation. Two intensity plots on the left and bottom are the intensity amplification as a function of distance and polar or azimuthal angles. The figure is reproduced from Ref [265].

excitation. We use the C line in the ZPL transitions to drive the GeV^- resonantly. Figure 6.1 (b) shows the calculated scattered optical field intensity of GeV^- as a function of distance and angle when the resonant excitation is aligned with the GeV^- dipole (along the symmetry axis). We note that the scattered field can become significantly more intense than the excitation field, with the intensity enhancement exceeding 1×10^8 as a distance $\leq 1\,\mathrm{nm}$ (dipole approximation may breakdown if the distance is less than this value).

Although, in principle, every emitter can be regarded as a near-field antenna, the ratio of the total decay rate and the transform-limited radiative decay rate determines the amplification magnitude. This effect is represented by the other term in the amplification $\left(\frac{1}{1+\Gamma'/\Gamma_0}\right)^2$, which is related to the optical properties of the emitter. As an emitter with excellent optical coherence, the GeV^- at $4\,\mathrm{K}$ only have $\Gamma' \approx 3\Gamma_0$ which yields a pre-factor of $\frac{1}{10}$. For many emitters, $\frac{\Gamma'}{\Gamma_0}$ can be over a thousand, leading to a pre-factor of 1×10^{-6} which compromises the near-field amplification value. These additional decays include charge fluctuations, electromagnetic noise, dark states, and more. In

practice, another branching ratio needs to be considered: the ratio of the emission (usually ZPL) compared with the total radiative decay (spectral density of emission). This branching ratio is often calculated via the Debye-Waller factor, which is also far from ideal for many emitters except for group IV centers in diamond.

6.1.3 Field enhancement of a plasmonic nanosphere

To evaluate the GeV$^-$'s field intensity amplification, we analyze another commonly used object for near-field optical enhancements: a plasmonic nanosphere. In short, the plasmonic effect only happens on certain types of metals. If we write the dielectric constant of metal as $\varepsilon_m = \varepsilon' + i\varepsilon''$ where both ε' and ε'' are real numbers, then ε' has to be sufficiently negative to allow the plasmonic mode to exist [188] This requirement leads to noble metals such as gold and silver.

A nanosphere can be regarded as a small spherical particle with a radius r_0. We can analyze its electric field distribution inside and outside the nanosphere. Since r_0 is much smaller than the metal's skin depth $d = \lambda/(4\pi\sqrt{\varepsilon_m})$ which is the field decay constant of the metal, the electric potential (and thus the electric field) exists both inside and outside of the nanosphere. We can write the two potentials as Φ_1 and Φ_2. With r_0 much smaller than the emission wavelength, the nanosphere can be treated as a quasi-static model which satisfies $\boldsymbol{E} = -\nabla\Phi$, with the charge-free Laplace equation $\nabla^2\Phi = 0$. Using the spherical coordinate expression (r, θ, φ) for the nanosphere, we can write and solve Φ_1 and Φ_2 by utilizing boundary conditions at $r = r_0$ (assuming the incident field yields $\Psi_0 = -E_0 x$) [188]:

$$\Phi_1 = -E_0 \frac{3\varepsilon_r}{\varepsilon_m + 2\varepsilon_r} r\cos\theta \tag{6.17}$$

$$\Phi_2 = -E_0 r\cos\theta + E_0 \frac{\varepsilon_m - \varepsilon_r}{\varepsilon_m + 2\varepsilon_r} r_0^3 \frac{\cos\theta}{r^2} \tag{6.18}$$

Where ε_m and ε_r are the dielectric constants of the metal and the medium. Here, we are only interested in the range that is out of the nanosphere, so we calculate the electric field based on Φ_2

and get:

$$\boldsymbol{E}_2 = -\nabla\Phi_2 = E_0(\cos\theta\boldsymbol{n}_r - \sin\theta\boldsymbol{n}_\theta) + \frac{\varepsilon_m - \varepsilon_r}{\varepsilon_m + 2\varepsilon_r}\frac{r_0^3}{r^3}E_0(2\cos\theta\boldsymbol{n}_r + \sin\theta\boldsymbol{n}_\theta) \tag{6.19}$$

The first term is the incident field, and the second term is the scattered field that can be regarded as the field of a dipole $\boldsymbol{p}$ located at the center of the sphere. This dipole can be written as $\boldsymbol{p} = \varepsilon_r\alpha(\omega)\boldsymbol{E}_0$, where $\alpha(\omega)$ is the polarizability (a scalar, not a tensor as GeV$^-$ since the metal nanosphere is isotropic) written as:

$$\alpha(\omega) = 4\pi\varepsilon_0 r_0^3\frac{\varepsilon_m(\omega) - \varepsilon_r}{\varepsilon_m(\omega) + 2\varepsilon_r} \tag{6.20}$$

Note that what we have now is the polarizability of the external field. However, what we need is the effective polarizability which includes the self-generated electric field, which is related to the radiation reaction force $\boldsymbol{F}_r = q\boldsymbol{E}_{\text{self}} = \frac{q^2\frac{d^3}{dt^3}\boldsymbol{r}}{6\pi\varepsilon_0 c^3}$. Adding this into the effective polarizability equation $\boldsymbol{p} = \alpha_{\text{eff}}(\omega)\boldsymbol{E}_0(\boldsymbol{r}_0)$ and calculate the result in vacuum we thus have:

$$\alpha_{\text{eff}}(\omega) = \frac{\alpha(\omega)}{1 - i\frac{k^3}{6\pi\varepsilon_0}\alpha(\omega)} \tag{6.21}$$

We insert the result into the expression of the field amplification in vacuum (which is normally true for plasmonic systems to have resonance) and use the same form of the expression (and also notation) for GeV$^-$:

$$\frac{\boldsymbol{E}(\boldsymbol{r})}{E_0(\boldsymbol{r}_0)} = \hat{\boldsymbol{E}}_0(\boldsymbol{r}_0) + \frac{3\text{exp}(ikR)}{2k^3R^3}\frac{i}{1 + \frac{6\pi\varepsilon_0 i}{\alpha(\omega)k^3}}\left[-\overleftrightarrow{I} + 3\frac{\boldsymbol{RR}}{R^2}\right]\hat{\boldsymbol{E}}_0(\boldsymbol{r}_0) \tag{6.22}$$

Now we consider the "near-resonance" case, where the denominator of the $\alpha(\omega)$ is (almost) zero. This requires that the real part of $\varepsilon_m(\omega)$ equals $-2\varepsilon_r$, and only a small imaginary value is left behind. It is a pretty accurate approximation for silver in the resonant condition. We use the scattering and absorption cross-section to describe the near-resonant condition. The scattering

cross-section is defined as the total scattered power divided by the intensity of the incident wave, which can be written as $\sigma_{\text{scatt}} = \frac{k^4}{6\pi\varepsilon_0^2}|\alpha(\omega)|^2$ [188]. The absorption cross-section is the power dissipation divided by the intensity of the incident wave, which is $\sigma_{\text{abs}} = \frac{k}{\varepsilon_0}\text{Im}\left[\alpha(\omega)\right]$. In the near-resonant case, the $\alpha(\omega)$ is a very large imaginary number since the denominator is imaginary and small. Therefore, we can insert $\frac{\sigma_{\text{abs}}}{\sigma_{\text{scatt}}}$ into the electric field equation and have:

$$\frac{\boldsymbol{E}(\boldsymbol{r})}{E_0(\boldsymbol{r}_0)} = \hat{\boldsymbol{E}}_0(\boldsymbol{r}_0) + \frac{3\text{exp}(ikR)}{2k^3R^3}\frac{i}{1+\frac{\sigma_{\text{abs}}}{\sigma_{\text{scatt}}}}\left[-\overleftrightarrow{I} + 3\frac{\boldsymbol{RR}}{R^2}\right]\hat{\boldsymbol{E}}_0(\boldsymbol{r}_0) \tag{6.23}$$

For atomic dipoles, the ratio of the absorption and scattering cross sections is related to its intrinsic and extrinsic linewidths: $\frac{\sigma_{\text{abs}}}{\sigma_{\text{scatt}}} = \frac{\Gamma'}{\Gamma_0}$. Therefore, both GeV$^-$ and the plasmonic nanosphere use the same parameter $\frac{\sigma_{\text{abs}}}{\sigma_{\text{scatt}}}$ to determine the maximum enhancement value.

6.1.4 Comparison of the GeV$^-$ and the plasmonic nanosphere

In practice, the $\frac{\sigma_{\text{abs}}}{\sigma_{\text{scatt}}}$ value for GeV$^-$ can be as small as 3 as discussed before, but this value cannot be too small for plasmonic structures since the material properties are not engineerable ($\varepsilon_m(\omega) + 2\varepsilon_r$ is not tunable and cannot be sufficiently small). In addition, the distance $\boldsymbol{R}$ has to be larger than the radius of the nanosphere r_0, which limits the minimum distance for the near-field effect. The distance also needs to be not too close to the metallic scatterers to reduce the Ohmic losses [284, 285]. All these effect eventually limits the field enhancement to $|\frac{\boldsymbol{E}(\boldsymbol{r})}{E_0(\boldsymbol{r}_0)}|^2_{\text{max}} \approx 500$ for the nanosphere (given the best-case scenario of silver). Therefore, the plasmonic structures generally exhibit a lower near-field amplification when on-resonance.

In addition to the analytical calculation, we also numerically calculate the field enhancement and the cross-section ratio of the GeV$^-$ and the nanosphere as shown in Figure 6.2 (a)-(b). Here, the subwavelength $k_0R \ll 1$ prediction is shown as the dashed line, which saturates when the nanosphere radius is small. For larger radius ($k_0R \lesssim 1$), a full Mie theory has to be applied to get the accurate numbers [286, 287]. We note that the GeV$^-$ outperforms the nanosphere when the

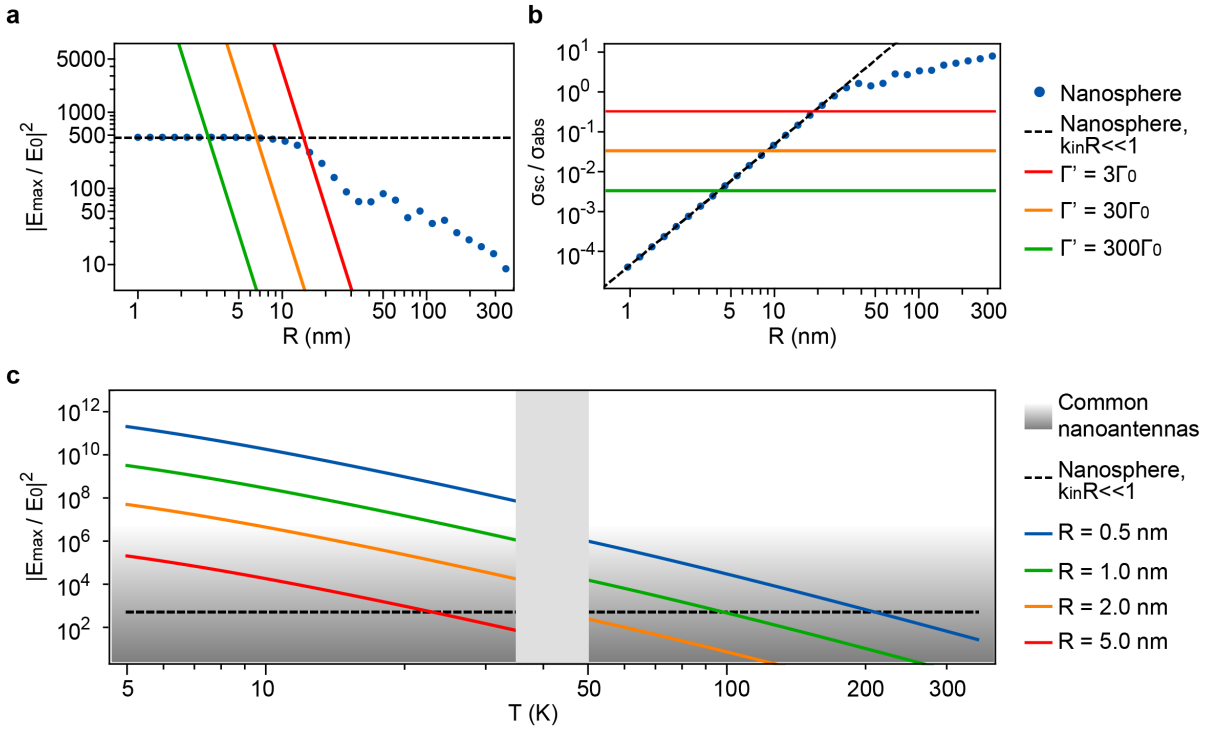

Figure 6.2: Comparison of the intensity amplification between GeV^- and the metallic nanosphere. (a-b) The field intensity enhancement and cross-section ratio calculation for the GeV^- and metallic nanospheres. The solid, colored lines refer to GeV^- with different decay constants, with the incident field aligned with the transition dipole. The dashed line is the quasi-static limit of the nanosphere as calculated before, which is valid for a subwavelength radius $k_0 R \ll 1$ [188]. The blue dots are a more careful treatment for the nanospheres with a larger radius. They are calculated by a full Mie expansion up to the first 15 multipole orders [277]. All nanosphere results are derived at the plasma resonance frequency of the silver, which is $354\,\mathrm{nm}$ [278]. (c) Calculated temperature dependence of the GeV^- intensity enhancement at different distances R. The gray-to-white shaded region depicts the usual range of field enhancements by common plasmonic nanoantennae [279–283]. The figure is reproduced from Ref [265].

distance is less than $5\,\mathrm{nm}$ to $20\,\mathrm{nm}$ even for very large extrinsic decay $\Gamma' = 300\Gamma_0$.

At last, we consider the temperature dependence of GeV$^-$'s non-radiative losses Γ', which sharply increases at temperatures higher than those of our experimental setup $(4\,\mathrm{K})$ due to electron-phonon interactions. The calculated curves are plotted in Figure 6.2 (c). The temperature dependence of Γ' is extracted from Ref [100, 288]. We calculate the maximum amplification ar distances $R = 0.5,\ 1,\ 2,\ 5$ from the GeV (solid, colored lines) and the silver nanosphere (dashed line). Again, we show that for a wide range of cryogenic temperatures $T < 50\,\mathrm{K}$, the GeV$^-$ exhibits remarkable amplification performance, emphasizing its potential in low temperature near-field applications.

6.2 Carbon monovacancy as an optical field detector

So far, we have theoretically calculated the performance of the GeV$^-$ as an optical antenna. To experimentally verify its optical enhancement, we need another object in the vicinity that can have an observable response when detecting the optical field. In this work, we choose carbon vacancies in diamond, a commonly present point defect with a moderate density in diamond membranes. These defects can be only a few nanometers from the GeV$^-$, and their optical response includes charge state manipulation ($V^0 \leftrightarrow V^-$) and PL feature from the GR1 center (V^0) [289].

6.2.1 Stark shift of the GeV$^-$ center

Due to their D_{3d} point group symmetry, group IV centers have zero first-order Stark shift due to the lack of permanent dipole. Therefore, only quadruple and higher order effects have been observed [217, 218]. Although this second-order Stark effect is not friendly for ZPL tuning, it provides a unique chance to detect local charge fluctuations within only a few nanometers. We write the spectral change of the ZPL using the polarizability tensor $\overleftrightarrow{\alpha}$ (Note: this is the polarizability for

DC fields, not for optical frequency discussed in the last section):

$$\Delta E_{\text{ZPL}} = \frac{1}{2}\boldsymbol{E}\overleftrightarrow{\alpha}\boldsymbol{E} = \frac{1}{2}\left(E_x, E_y, E_z\right)\begin{pmatrix}\alpha_{xx} & \alpha_{xy} & \alpha_{xz}\\ \alpha_{yx} & \alpha_{yy} & \alpha_{yz}\\ \alpha_{zx} & \alpha_{zy} & \alpha_{zz}\end{pmatrix}\begin{pmatrix}E_x\\ E_y\\ E_z\end{pmatrix} \tag{6.24}$$

For simplicity, we calculate the tensor in the local GeV$^-$ coordinate. Each element in $\overleftrightarrow{\alpha}$ is calculated using density functional theory (DFT) by applying homogeneous electric fields along various directions. Using the $[111]$ direction as z, $[1\bar{1}0]$ as y and $[11\bar{2}]$ as x, the calculated total polarizability (including both ground state and excited state changes) is:

$$\overleftrightarrow{\alpha} = \begin{pmatrix}2.589 & 0.028 & -0.402\\ 0.028 & 2.688 & -0.216\\ -0.402 & -0.216 & 13.90\end{pmatrix}(\text{Å}^3) \tag{6.25}$$

With $\overleftrightarrow{\alpha}$, we are able to calculate the ZPL emission shift for any charges that are nearby. Since our optical measurement for GeV$^-$ is based on many averages, the charge fluctuation has to be observable and reproducible. Therefore, it requires the charge traps—atomic defects—that are only a few nanometers away from the GeV$^-$, which posts a challenging requirement for the minimum defect density. For all atomic defects in diamond, carbon vacancy center is an ideal candidate since (1) they enable charge cycling between the neutral (GR1) and negative (ND1) states, (2) their formation is a side-effect of the GeV$^-$ formation, which requires no additional treatments, and (3) they are formed using ion implantation, so the density of the defect is only high *locally*, which does not affect the general crystal quality and the GeV coherence.

In this work, we choose to use carbon vacancies (V_C) as the detector of the GeV$^-$ antenna. The additional electron that determines the charge state of V_C can generate a considerable second-order Stark shift that can be observed by the GeV$^-$ ZPL shift at $4\,\text{K}$ if the vacancy is within a few

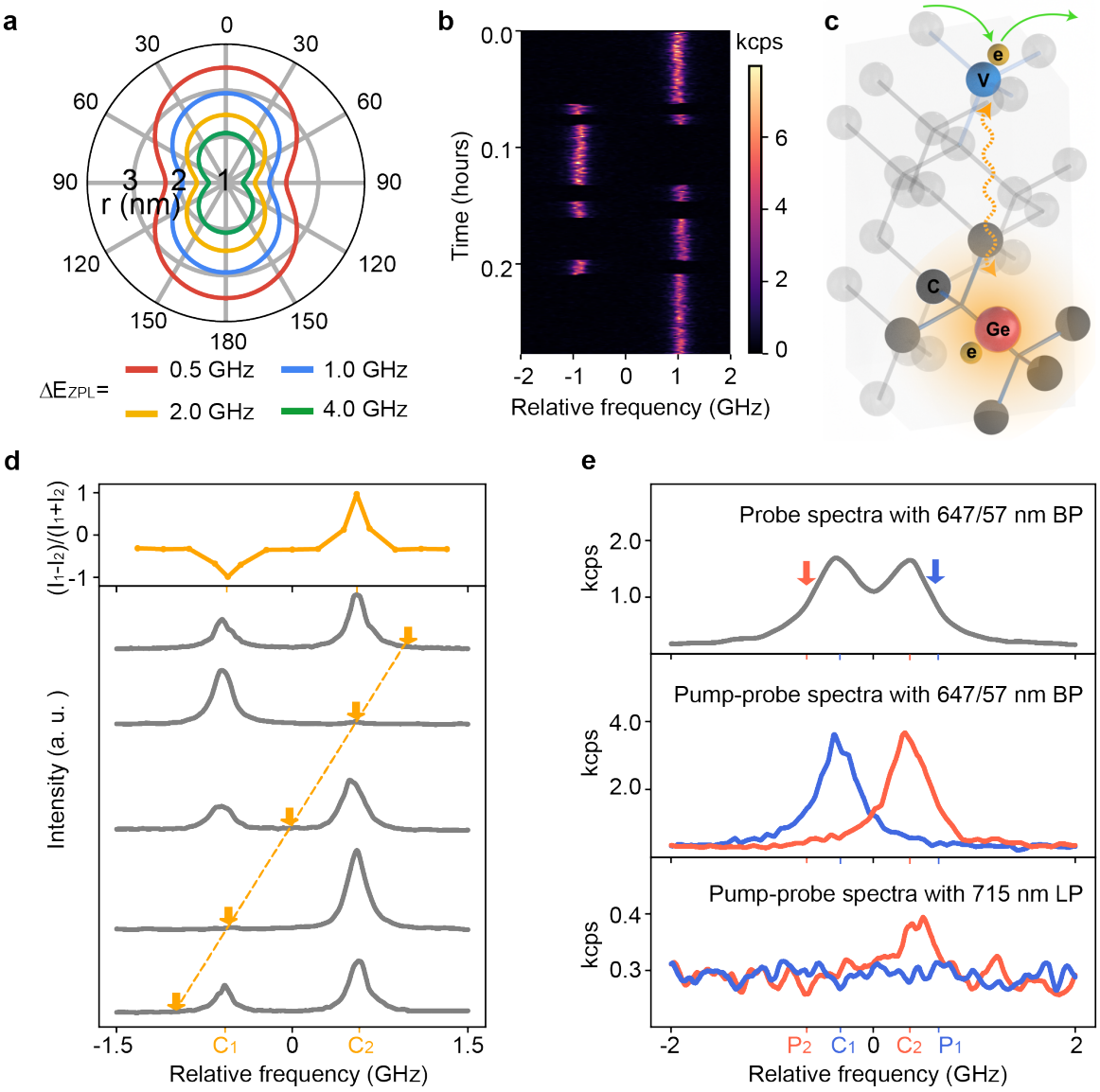

Figure 6.3: Detection and manipulation of a vacancy charge state using GeV. (a) The DFT calculation of the Stark shift of GeV^-'s ZPL if a charge is added to or removed from the vicinity. The angle refers to the polar angle with respect to the high symmetry axis of GeV^-. (b) PLE spectrum of a GeV^- showing spectral hopping over time. The measurement is performed for 17 min. (c) The schematic of the experiment, showing that the GeV^- behaves like an atomic scale optical antenna and manipulates the charge state of V_C when being resonantly excited. (d) Average PLE spectra obtained by different laser pumping frequencies, which are indicated by the orange arrow in the figure. The upper figure shows the signal contrast of the two peaks as a function of the excitation frequency. (e) FRET between a GeV^- and a V_C. The upper figure is obtained without pumping, while the middle figure contains the GeV^- spectra with different pumping frequencies showing an effective V_C charge state initialization. The lower figure is obtained by the same excitation but using a 715 nm long-pass filter to collect the signal from GR1 only. The figure is reproduced from Ref [265].

nanometers away. The simulation of the ZPL emission shift with respect to the charge cycling of a nearby V_C is shown in Figure 6.3 (a). We find that at some specific distances and orientations, the ZPL shift can be as large as a few GHz, which is much larger than the linewidth of the ZPL C line ($\approx$100 MHz) and can be spectrally determined. For this simulation, we limit the minimum distance between the GeV^- and the V_C to be in good agreement with the dipole approximation and avoid $GeV-V_x$ formation discussion [290].

6.2.2 Observation of the V_C charge state

Experimentally, the detection of V_C's charge state is achieved by measuring the wavelength of GeV's ZPL via the photoluminescence excitation (PLE) method: scanning the laser around the C-line of GeV's ZPL and collecting the phonon sideband signals with respect to the frequency. As discussed in the last section, charge state cycling of nearby V_Cs should induce a corresponding hopping of GeV's ZPL between discrete, energetically split transitions. This prediction is in agreement with our observation of a number of GeV^- centers measured in the diamond membrane and group IV centers mentioned in previous reports [40, 291]. A typical spectral hopping feature measured using a weak ($\sim$10 nW) laser excitation is shown in Figure 6.3 (b), showing a hopping distance of $\approx$2 GHz. Normally, the observed hopping distance ranges from $0.3\,\mathrm{GHz}$ to $17\,\mathrm{GHz}$. A notable feature of the hopping phenomenon is the relatively slow rate, indicating a stable electronic environment of the V_C when the laser excitation is low.

In parallel with the V_C charge state cycling theory, some other possibilities that could lead to such a hopping phenomenon have been theoretically and experimentally investigated [265]. These hypotheses include (1) breaking of the Jahn-Teller configurations of the GeV^- in the presence of the external strain, (2) hydrogen reorientation of the vacancy-hydrogen (VH) complex near the GeV^-, (3) hopping of the helium atom between two vacancy sites of a divacancy center near the GeV^-, and (4) charge state change of other defect centers near the GeV^-, such as nitrogen substitution and divacancy. They are ruled out due to extremely high hopping distance, unnaturally quick hop-

ping rate, unstable configuration under room temperature, stable configuration at low-temperature annealing, or large charge cycling energy threshold, which requires lower wavelength lasers to manipulate. To confirm the V_C charge state cycling hypothesis, we performed an additional test by observing the photoluminescence signal from the GR1 center (V_C^0) directly, as discussed below.

6.2.3 Manipulation of the V_C charge state

The V_C serves as the detector of the GeV^- antenna. Therefore, its charge state cycling should be able to be manipulated by the GeV^- emission. In addition, the V_C can also have charge state cycling under far-field optical illumination [289, 292, 293], which is commonly observed in other defects [294, 295]. The experiment schematic is shown in Figure 6.3 (c). To observe the charge state manipulation effect, we use a continuous wave (CW) laser to pump the system at various frequencies: on-resonance, partially on-resonance, and off-resonance, followed by a weak laser to detect the ZPL position. The two ZPL peaks are labeled as C_1 and C_2, respectively. The measurement results are plotted in Figure 6.3 (d), showing that resonantly pumping one of the ZPL peaks will change the charge state of V_C and thus initialize the ZPL to the other peak position. This finding has a direct implication for group IV centers used in quantum applications. Specifically, one can resonantly pump the undesired ZPL peak (or peaks if multiple vacancies are around) to eliminate hopping-induced spectral instability. In addition, this finding indicates that local charge defect concentration causes spectral instability. Therefore, the spectral properties of color centers can be improved by minimizing the local vacancy concentration via *in-situ* doping, shallow implantation followed by overgrowth, or high-pressure high-temperature (HPHT) annealing [90, 184, 228]. Moreover, the GeV^- hopping statistics can provide valuable information on the local vacancy concentration, which is a helpful metric for improving the material quality.

6.2.4 *Förster resonance energy transfer (FRET)*

To confidently confirm the origin of the GeV^- spectral hopping, we performed another experiment involving direct observation of the fluorescence signal from V_C. For the two charge states of V_C, the negative state V_C^- (ND1) is optically active at wavelengths from $390\,\mathrm{nm}$ to $700\,\mathrm{nm}$, while the neutral charge state V_C^0 (GR1) is optically active at wavelengths from $730\,\mathrm{nm}$ to $850\,\mathrm{nm}$. In this experiment, we seek to determine the charge state of the V_C by observing the PL from individual V_C through resonant excitation of the GeV^-. This local, non-radiative, dipole-dipole interaction-induced energy transfer is called FRET. This phenomenon has been investigated using NV^-, where off-resonant excitation with low driving efficiency has been applied [296, 297]. In this work, we use atomic-resonance-enhanced FRET to significantly improve the driving efficiency of the process, which leads to high signal-to-noise even for weakly radiative systems like GR1. To verify that, we investigate a GeV^- center with two hopping peaks. The operation mechanism and results are shown in Figure 6.3 (e). Due to the close distance between the two peaks, we initialize the system using a frequency that is slightly detuned from the peak position to reach the optimal fidelity, labeled as P_1 and P_2. We note that adding an additional electron generates a red shift to the ZPL wavelength. Therefore, the lower energy peak C_1 refers to the negative charge state ND1, and the higher energy peak C_2 indicates the neutral charge state GR1. This estimation is confirmed by the lower graph in Figure 6.3 (e), that the C_2 photoluminescence corresponds to a simultaneous fluorescence from ND1. In contrast, the C_2 photoluminescence corresponds to no signals within the filter range ($\geq 710\,\mathrm{nm}$). This experiment marks the first experimental observation of fluorescence from individual GR1 centers, which are typically challenging to achieve due to their poor quantum efficiency and the presence of metastable shelving states [289]. Furthermore, the experiment confirming the FRET relies on a probe power of only $3\,\mathrm{nW}$ for a confocal setup, which is several orders of magnitude lower than the typical $10\,\mu\mathrm{W}$ to $100\,\mu\mathrm{W}$ excitation power used in single-molecule FRET studies [298, 299]. The high FRET efficiency and the ability to observe single GR1 centers demonstrate the unique advantage of the GeV^- antenna, including

excellent optical coherence and nanometer scale detection distance.

6.3 GeV⁻ antenna characterization

6.3.1 Power dependence of the resonant driving through GeV

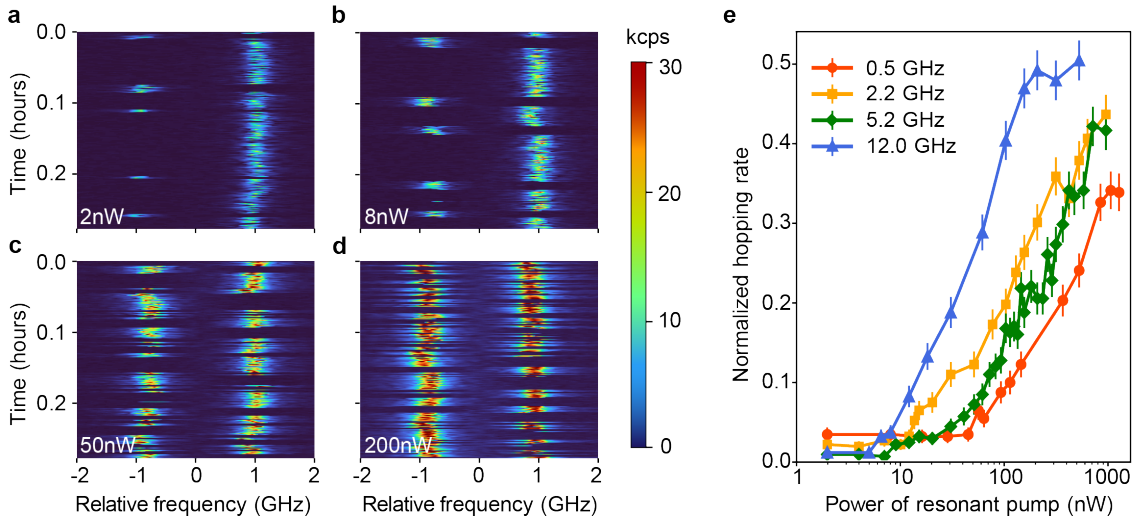

Figure 6.4: Power dependence of the charge cycling rate when driving the GeV⁻ antenna. (a)-(d) Time-dependent PLE spectra of a hopping GeV⁻ measured at different powers: 2 nW, 8 nW, 50 nW, and 200 nW. (e) The normalized hopping rate versus resonant laser power for GeV⁻ centers with different ZPL hopping separation. The excitation power threshold decreases as the ZPL separation increases. The figure is reproduced from Ref [265].

After confirming the nature of the GeV⁻ hopping and verifying the capability of manipulating the V_C charge state, in this section, we examine the correlation between the hopping separation, GeV⁻-V_C separation, and field intensity enhancements. As calculated in Figure 6.1 (b) and 6.3 (a), both field intensity amplification and hopping separation are negatively correlated with the distance between the GeV⁻ and the V_C. To quantitatively understand the correlations, we perform power dependence measurements to the system by continuously scanning the laser across the two GeV⁻ hopping peaks using a triangular pulse shape. At different power levels, this scanning laser acts both as a pump to manipulate the V_C charge states and a probe to detect the state. Figure 6.4

(a)-(d) shows a power dependence measurement of a GeV^- with $2\,\mathrm{GHz}$ hopping separation using the time-dependent PLE method. We note that the hopping rate remains unchanged (only brighter signals) when the laser power increases from $2\,\mathrm{nW}$ to $8\,\mathrm{nW}$ as shown in 6.4 (a) to (b). However, we observe a significant hopping rate increase when the laser power reaches $50\,\mathrm{nW}$ (Figure 6.4 (c)), indicating a threshold intensity of the optical field to drive the V_C charge transition. To quantitatively investigate the hopping phenomenon, we define a normalized hopping rate, the ratio between the number of incidences ZPL switches to the other peak and the total number of scans, which is 400 in all cases. This rate cannot exceed 0.5 since 0.5 indicates a purely random ZPL location, and a rate of 1 means a deterministic spectral switching (Rabi drive), which is impractical. We plot the normalized rates for GeV^- centers with different hopping separations in Figure 6.4 (e). This figure shows that GeV^- centers with larger ZPL separations (closer V_C) tend to have lower laser power to initiate the spectral hopping, which is in good agreement with the near-field nature of the GeV^- atomic antenna. We also observe some GeV^-s with ZPL separation exceeding $15\,\mathrm{GHz}$. With that separation, the dipole approximation may break, and the system has to be understood as a hybridization between the GeV^- and the V_C, which is beyond the scope of this work.

6.3.2 Off-resonance driving and field amplification estimation

To quantify the degree of near-field amplification, we compare the hopping rate of GeV^- with the off-resonance pumping result. The presence of the atomic antenna can improve the effective cross-section of the light-matter interaction, which results in a reduction of the threshold laser power at on-resonance conditions. The off-resonance laser used for the comparison is a $633\,\mathrm{nm}$ red laser, which is red detuned from the GeV^- ZPL and thus does not interact with it. The optical setup and the laser sequence for off-resonance pumping and detection are detailed in Figure 6.5 (a). The power dependence of a GeV^-'s hopping rate using on- and off-resonance lasers are shown in Figure 6.5 (b). This specific GeV^- has a ZPL separation of $12\,\mathrm{GHz}$, indicating a very close V_C. We observe a nW level of the threshold power for the on-resonance drive, while this value is dozens of

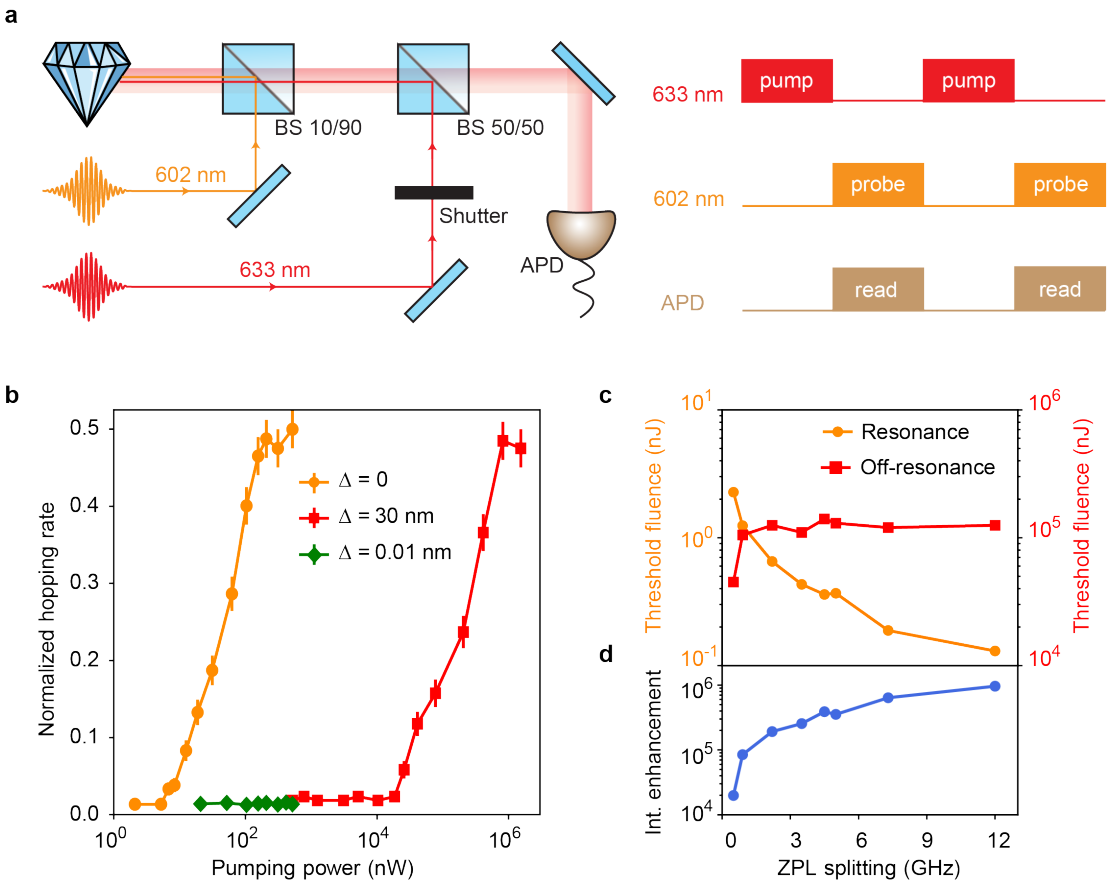

Figure 6.5: Field enhancement of the GeV$^-$. (a) The optical setup and the laser sequence for off-resonance pumping measurements. The on-resonance probe power is kept at $3\,\mathrm{nW}$ to avoid introducing additional hopping. (b) Normalized hopping rates of a GeV$^-$ with $12\,\mathrm{GHz}$ of ZPL separation. The laser power is in an on-resonance (orange) or off-resonance (green, red) regime. (c) The on-resonance and off-resonance laser threshold power with respect to the ZPL separation (splitting). The fluence here is calculated by the laser power times a constant pumping time. The threshold power is defined as the power at which the hopping rate is increased by $50\,\%$ compared with the low power value. (d) The optical field intensity amplification is calculated after considering the effective excitation ratio (branching ratio). The figure is reproduced from Ref [265].

μW for the off-resonance drive, which is $3 \sim 4$ orders of magnitude higher than the on-resonance value. We also study the hopping rate with a slightly off-resonance laser ($0.01\,\mathrm{nm}$ red detuned) and find no hopping rate until $1\,\mu\mathrm{W}$, reiterating the inefficiency of the off-resonant excitation.

We note that the on-resonance drive is a laser scanning across the resonance frequency, with the scanning range ($5\,\mathrm{GHz}$ to $20\,\mathrm{GHz}$, depending on the ZPL separation) much larger than the linewidth of the ZPL ($\approx 100\,\mathrm{MHz}$). Therefore, we include a branching ratio and calculate the effective resonant driving power, which is approximately two orders of magnitude lower than the measured scanning laser power. Adding this branching ratio into the comparison, we find that the optical field intensity enhancement is typically at a range of 1×10^4 to 1×10^6, as shown in Figure 6.5 (d). We also note in Figure 6.5 (c) that the on-resonance threshold power (the fluence divided by a constant pump time) is inversely related to the ZPL separation, while the off-resonance driving has a constant threshold power, which is in line with our model. The intensity enhancement values are slightly lower than the theoretical calculations shown in Figure 6.1 (b), primarily due to the poor laser polarization control of the setup. Nonetheless, the intensity enhancement result supports GeV^- as an excellent optical antenna.

6.4 Conclusion

In this work, we show the remarkable capability of GeV^- centers in diamond membrane to generate localized field intensity as an atomic scale optical antenna. We introduce the carbon monovcacancy centers V_C in diamond to detect and characterize the field amplification via second-order Stark effect to the GeV^- center. Upon resonant excitation, GeV^- centers are able to sense and manipulate the proximal charge environment, which can be used to improve their optical coherence for quantum networking applications. Our study also shows that the field intensity amplification can exceed a million, which is remarkable for an optical antenna in solid-state platforms. The correlation between GeV^--V_C spatial separation and intensity amplification can be used to further identify the location of the vacancies in subsequent studies. This technique can be extended to study electrons

on the diamond surface in the future to enable more exciting sensing opportunities. The discovery here can impact various scientific disciplines, including nanoscale Raman spectroscopy, FRET-based detection, photochemistry, and more. It also inspires works from other coherent solid state emitters, such as molecules, defects in hexagonal boron nitride and silicon carbide, and rare-earth dopants [17, 300–303].

CHAPTER 7

SUMMARY AND OUTLOOK

The heart of the work presented in this dissertation is the diamond membrane as an integrated material platform for quantum technologies. As the introduction mentions, color centers in diamond, such as NV^- centers and group IV centers, are promising candidates for quantum technologies, including quantum networking and sensing. Future development of this platform requires material and device innovation to unleash color centers from the bulky substrate. In Chapter 2, we reviewed the state-of-the-art nanofabrication progress in fabricating the low-dimensional diamond and introduced our methods originated from the "smart-cut" technique. After countless process optimizations and innovations, our diamond membrane platform acquires pristine material properties that are fully compatible with quantum applications. In addition, we developed deterministic methods to bond diamond membranes with other materials, which enables integrated diamond-based substrate manufacturing. From there, we started to discuss the applications of such a material platform.

In Chapter 3, we focused on on-chip nanophotonic devices for quantum photonic and networking applications. Both applications require efficient on-chip photon transmission and spin-photon interaction, which is traditionally challenging for bulk diamonds. Utilizating integrated diamond membranes greatly reduces the fabrication complexity and limitations, which improves the devices' flexibility and performance. We showed record high quality factors for nanophotonic cavities in visible wavelengths fabricated from diamond membranes. In Chapter 4, we presented one unique application of the diamond membrane when its aspect ratio becomes significantly large. By integrating the diamond membrane with fused silica, a material with a very different thermal expansion ratio, we are able to generate a considerable tensile strain profile inside the diamond, which has a profound impact on the spin and optical properties of the hosted SnV^- centers. We showed that strain significantly improves the coherence of SnV^- by reducing the electron-phonon interaction strength and enabling efficient microwave spin control. Thus, strain engineering makes

SnV^- a prime candidate for next-generation quantum networking nodes. We discussed in Chapter 5 the excellent coherence properties of NV^- centers inside diamond membranes with only one hundred nanometer thickness. This coherence time performance is typically hard to achieve for most diamond nanostructures. We demonstrated the potential of these hosted NV^- centers for quantum bio-sensing applications. Chapter 6 is a story about the optical properties of GeV^- centers in the diamond membrane. The excellent optical coherence of group IV centers are ideal candidates as near-field optical antennae due to their exceptionally high field intensity amplification on a nanometer scale.

As a material platform, integrated diamond membranes have numerous applications in the quantum world. Once practical issues regarding the membrane size and process scalability can be solved via larger seed substrates and wafer bonders, this precious and popular material (at this moment) should soon become available as a common choice for the research society. We believe that more novel applications covering quantum technology, semiconductor industry, optics, and photonics will emerge as integrated diamond membranes become widely available.

REFERENCES

[1] McCullouch, B. G.; Lueprasert, K. 2D Bar-Code Applications in Construction. *Journal of Construction Engineering and Management* **1994**, *120*, 739–752.

[2] Pittler, M. S.; Powers, D. M.; Schnabel, D. L. System Development and Technology Aspects of the IBM 3081 Processor Complex. *IBM Journal of Research and Development* **1982**, *26*, 2–11.

[3] Dennard, R. H. Field Effect Transistor Memory. U.S. Patent 3 387 286, June 1968.

[4] William A. Goddard, J. J. L. Direct Access Magnetic Disc Storage Device. U.S. Patent 3 503 060, March 1970.

[5] Bhagyaveni, M. A.; Kalidoss, R.; Vishvaksenan, K. S. *Introduction to Analog and Digital Communication*; 2016; pp 41–82.

[6] Nielsen, M. A.; Chuang, I. L. *Quantum Computation and Quantum Information: 10th Anniversary Edition*; Cambridge University Press, 2010.

[7] DiVincenzo, D. P. The Physical Implementation of Quantum Computation. *Fortschritte der Physik* **2000**, *48*, 771–783.

[8] Arute, F. et al. Quantum supremacy using a programmable superconducting processor. *Nature* **2019**, *574*, 505–510.

[9] Bernien, H.; Schwartz, S.; Keesling, A.; Levine, H.; Omran, A.; Pichler, H.; Choi, S.; Zibrov, A. S.; Endres, M.; Greiner, M.; Vuletic, V.; Lukin, M. D. Probing many-body dynamics on a 51-atom quantum simulator. *Nature* **2017**, *551*, 579–584.

[10] Bao, Y.; Yu, S. S.; Anderegg, L.; Chae, E.; Ketterle, W.; Ni, K.-K.; Doyle, J. M. Dipolar spin-exchange and entanglement between molecules in an optical tweezer array. *Science* **2023**, *382*, 1138–1143.

[11] Monroe, C.; Campbell, W. C.; Duan, L. M.; Gong, Z. X.; Gorshkov, A. V.; Hess, P. W.; Islam, R.; Kim, K.; Linke, N. M.; Pagano, G.; Richerme, P.; Senko, C.; Yao, N. Y. Programmable quantum simulations of spin systems with trapped ions. *Rev. Mod. Phys.* **2021**, *93*, 025001.

[12] Postler, L.; Heußen, S.; Pogorelov, I.; Rispler, M.; Feldker, T.; Meth, M.; Marciniak, C. D.; Stricker, R.; Ringbauer, M.; Blatt, R.; Schindler, P.; Müller, M.; Monz, T. Demonstration of fault-tolerant universal quantum gate operations. *Nature* **2022**, *605*, 675–680.

[13] Zhou, X.; Koolstra, G.; Zhang, X.; Yang, G.; Han, X.; Dizdar, B.; Li, X.; Divan, R.; Guo, W.; Murch, K. W.; Schuster, D. I.; Jin, D. Single electrons on solid neon as a solid-state qubit platform. *Nature* **2022**, *605*, 46–50.

[14] He, Y.; Gorman, S. K.; Keith, D.; Kranz, L.; Keizer, J. G.; Simmons, M. Y. A two-qubit gate between phosphorus donor electrons in silicon. *Nature* **2019**, *571*, 371–375.

[15] O'Brien, J. L. Optical Quantum Computing. *Science* **2007**, *318*, 1567–1570.

[16] Dutt, M. V. G.; Childress, L.; Jiang, L.; Togan, E.; Maze, J.; Jelezko, F.; Zibrov, A. S.; Hemmer, P. R.; Lukin, M. D. Quantum Register Based on Individual Electronic and Nuclear Spin Qubits in Diamond. *Science* **2007**, *316*, 1312–1316.

[17] Zhong, T.; Kindem, J. M.; Bartholomew, J. G.; Rochman, J.; Craiciu, I.; Miyazono, E.; Bettinelli, M.; Cavalli, E.; Verma, V.; Nam, S. W.; Marsili, F.; Shaw, M. D.; Beyer, A. D.; Faraon, A. Nanophotonic rare-earth quantum memory with optically controlled retrieval. *Science* **2017**, *357*, 1392–1395.

[18] Hosseini, M.; Campbell, G.; Sparkes, B. M.; Lam, P. K.; Buchler, B. C. Unconditional room-temperature quantum memory. *Nature Physics* **2011**, *7*, 794–798.

[19] Liao, S. K. et al. Satellite-to-ground quantum key distribution. *Nature* **2017**, *549*, 43–47.

[20] Stevenson, P.; Phenicie, C. M.; Gray, I.; Horvath, S. P.; Welinski, S.; Ferrenti, A. M.; Ferrier, A.; Goldner, P.; Das, S.; Ramesh, R.; Cava, R. J.; de Leon, N. P.; Thompson, J. D. Erbium-implanted materials for quantum communication applications. *Phys. Rev. B* **2022**, *105*, 224106.

[21] Lettner, T.; Gyger, S.; Zeuner, K. D.; Schweickert, L.; Steinhauer, S.; Reuterskiöld Hedlund, C.; Stroj, S.; Rastelli, A.; Hammar, M.; Trotta, R.; Jöns, K. D.; Zwiller, V. Strain-Controlled Quantum Dot Fine Structure for Entangled Photon Generation at 1550 nm. *Nano Letters* **2021**, *21*, 10501–10506.

[22] van Leent, T.; Bock, M.; Garthoff, R.; Redeker, K.; Zhang, W.; Bauer, T.; Rosenfeld, W.; Becher, C.; Weinfurter, H. Long-Distance Distribution of Atom-Photon Entanglement at Telecom Wavelength. *Phys. Rev. Lett.* **2020**, *124*, 010510.

[23] Bersin, E. et al. Telecom Networking with a Diamond Quantum Memory. *PRX Quantum* **2024**, *5*, 010303.

[24] Jiang, W.; Sarabalis, C. J.; Dahmani, Y. D.; Patel, R. N.; Mayor, F. M.; McKenna, T. P.; Laer, R. V.; Safavi-Naeini, A. H. Efficient bidirectional piezo-optomechanical transduction between microwave and optical frequency. *Nature Communications* **2020**, *11*, 1166.

[25] Delaney, R. D.; Urmey, M. D.; Mittal, S.; Brubaker, B. M.; Kindem, J. M.; Burns, P. S.; Regal, C. A.; Lehnert, K. W. Superconducting-qubit readout via low-backaction electro-optic transduction. *Nature* **2022**, *606*, 489–493.

[26] Degen, C. L.; Reinhard, F.; Cappellaro, P. Quantum sensing. *Rev. Mod. Phys.* **2017**, *89*, 035002.

[27] Aslam, N.; Zhou, H.; Urbach, E. K.; Turner, M. J.; Walsworth, R. L.; Lukin, M. D.; Park, H. Quantum sensors for biomedical applications. *Nature Reviews Physics* **2023**, *5*, 157–169.

[28] Sedlacek, J. A.; Schwettmann, A.; Kübler, H.; Löw, R.; Pfau, T.; Shaffer, J. P. Microwave electrometry with Rydberg atoms in a vapour cell using bright atomic resonances. *Nature Physics* **2012**, *8*, 819–824.

[29] Dixit, A. V.; Chakram, S.; He, K.; Agrawal, A.; Naik, R. K.; Schuster, D. I.; Chou, A. Searching for Dark Matter with a Superconducting Qubit. *Phys. Rev. Lett.* **2021**, *126*, 141302.

[30] Bothwell, T.; Kennedy, C. J.; Aeppli, A.; Kedar, D.; Robinson, J. M.; Oelker, E.; Staron, A.; Ye, J. Resolving the gravitational redshift across a millimetre-scale atomic sample. *Nature* **2022**, *602*, 420–424.

[31] Ashcroft, N.; Mermin, N. *Solid State Physics*; Cengage Learning, 2011.

[32] Aharonovich, I.; Castelletto, S.; Simpson, D. A.; Su, C.-H.; Greentree, A. D.; Prawer, S. Diamond-based single-photon emitters. *Reports on Progress in Physics* **2011**, *74*, 076501.

[33] Hill, C. D.; Peretz, E.; Hile, S. J.; House, M. G.; Fuechsle, M.; Rogge, S.; Simmons, M. Y.; Hollenberg, L. C. L. A surface code quantum computer in silicon. *Science Advances* **2015**, *1*, e1500707.

[34] Shigley, J. E.; Breeding, C. M. Optical defects in diamond: A quick reference chart. *Gems and Gemology* **2013**, *49*, 107–111.

[35] Doherty, M. W.; Manson, N. B.; Delaney, P.; Jelezko, F.; Wrachtrup, J.; Hollenberg, L. C. The nitrogen-vacancy colour centre in diamond. *Physics Reports* **2013**, *528*, 1–45.

[36] Du Preez, L. Electron paramagnetic resonance and optical invesitgations of defect centres in diamond. *PhD Thesis, University of the Witwatersrand* **1965**,

[37] Mita, Y. Change of absorption spectra in type-Ib diamond with heavy neutron irradiation. *Phys. Rev. B* **1996**, *53*, 11360–11364.

[38] Haque, A.; Sumaiya, S. An Overview on the Formation and Processing of Nitrogen-Vacancy Photonic Centers in Diamond by Ion Implantation. *Journal of Manufacturing and Materials Processing* **2017**, *1*, 6.

[39] Hong, C. K.; Ou, Z. Y.; Mandel, L. Measurement of subpicosecond time intervals between two photons by interference. *Phys. Rev. Lett.* **1987**, *59*, 2044–2046.

[40] Guo, X.; Delegan, N.; Karsch, J.; Li, Z.; Liu, T.; Shreiner, R.; Butcher, A.; Awschalom, D.; Heremans, F.; High, A. Tunable and Transferable Diamond Membranes for Integrated Quantum Technologies. *Nano Letters* **2021**, *21*, 10392–10399.

[41] Goldman, M. L.; Doherty, M. W.; Sipahigil, A.; Yao, N. Y.; Bennett, S. D.; Manson, N. B.; Kubanek, A.; Lukin, M. D. State-selective intersystem crossing in nitrogen-vacancy centers. *Phys. Rev. B* **2015**, *91*, 165201.

[42] Schirhagl, R.; Chang, K.; Loretz, M.; Degen, C. L. Nitrogen-vacancy centers in diamond: Nanoscale sensors for physics and biology. *Annual Review of Physical Chemistry* **2014**, *65*, 83–105.

[43] Bernien, H.; Hensen, B.; Pfaff, W.; Koolstra, G.; Blok, M. S.; Robledo, L.; Taminiau, T. H.; Markham, M.; Twitchen, D. J.; Childress, L.; Hanson, R. Heralded entanglement between solid-state qubits separated by three metres. *Nature* **2013**, *497*, 86–90.

[44] Taminiau, T. H.; Cramer, J.; Van Der Sar, T.; Dobrovitski, V. V.; Hanson, R. Universal control and error correction in multi-qubit spin registers in diamond. *Nature Nanotechnology* **2014**, *9*, 171–176.

[45] Abobeih, M. H.; Wang, Y.; Randall, J.; Loenen, S. J.; Bradley, C. E.; Markham, M.; Twitchen, D. J.; Terhal, B. M.; Taminiau, T. H. Fault-tolerant operation of a logical qubit in a diamond quantum processor. *Nature* **2022**, *606*, 884–889.

[46] Bluvstein, D. et al. Logical quantum processor based on reconfigurable atom arrays. *Nature* **2024**, *626*, 58–65.

[47] Pompili, M.; Hermans, S. L. N.; Baier, S.; Beukers, H. K. C.; Humphreys, P. C.; Schouten, R. N.; Vermeulen, R. F. L.; Tiggelman, M. J.; dos Santos Martins, L.; Dirkse, B.; Wehner, S.; Hanson, R. Realization of a multinode quantum network of remote solid-state qubits. *Science* **2021**, *372*, 259–264.

[48] Kucsko, G.; Maurer, P. C.; Yao, N. Y.; Kubo, M.; Noh, H. J.; Lo, P. K.; Park, H.; Lukin, M. D. Nanometre-scale thermometry in a living cell. *Nature* **2013**, *500*, 54–58.

[49] Thiel, L.; Wang, Z.; Tschudin, M. A.; Rohner, D.; Gutiérrez-Lezama, I.; Ubrig, N.; Gibertini, M.; Giannini, E.; Morpurgo, A. F.; Maletinsky, P. Probing magnetism in 2D materials at the nanoscale with single-spin microscopy. *Science* **2019**, *364*, 973–976.

[50] Devience, S. J.; Pham, L. M.; Lovchinsky, I.; Sushkov, A. O.; Bar-Gill, N.; Belthangady, C.; Casola, F.; Corbett, M.; Zhang, H.; Lukin, M.; Park, H.; Yacoby, A.; Walsworth, R. L. Nanoscale NMR spectroscopy and imaging of multiple nuclear species. *Nature Nanotechnology* **2015**, *10*, 129–134.

[51] Yip, K. Y.; Ho, K. O.; Yu, K. Y.; Chen, Y.; Zhang, W.; Kasahara, S.; Mizukami, Y.; Shibauchi, T.; Matsuda, Y.; Goh, S. K.; Yang, S. Measuring magnetic field texture in correlated electron systems under extreme conditions. *Science* **2019**, *366*, 1355 – 1359.

[52] Vavilov, V.; Gippius, A. Investigation of the cathodoluminescence of epitaxial diamond films. *Sov. Phys. Semicond.* **1980**, *14*, 1078–1079.

[53] Clark, C. D.; Kanda, H.; Kiflawi, I.; Sittas, G. Silicon defects in diamond. *Phys. Rev. B* **1995**, *51*, 16681–16688.

[54] Wang, C.; Kurtsiefer, C.; Weinfurter, H.; Burchard, B. Single photon emission from SiV centres in diamond produced by ion implantation. *Journal of Physics B: Atomic, Molecular and Optical Physics* **2005**, *39*, 37.

[55] Iwasaki, T. et al. Germanium-Vacancy Single Color Centers in Diamond. *Scientific Reports* **2015**, *5*, 12882.

[56] Iwasaki, T.; Miyamoto, Y.; Taniguchi, T.; Siyushev, P.; Metsch, M. H.; Jelezko, F.; Hatano, M. Tin-Vacancy Quantum Emitters in Diamond. *Phys. Rev. Lett.* **2017**, *119*, 253601.

[57] Ditalia Tchernij, S. et al. Single-Photon Emitters in Lead-Implanted Single-Crystal Diamond. *ACS Photonics* **2018**, *5*, 4864–4871.

[58] Gali, A.; Maze, J. R. Ab initio study of the split silicon-vacancy defect in diamond: Electronic structure and related properties. *Phys. Rev. B* **2013**, *88*, 235205.

[59] Goss, J. P.; Briddon, P. R.; Shaw, M. J. Density functional simulations of silicon-containing point defects in diamond. *Phys. Rev. B* **2007**, *76*, 075204.

[60] Hepp, C.; Müller, T.; Waselowski, V.; Becker, J. N.; Pingault, B.; Sternschulte, H.; Steinmüller-Nethl, D.; Gali, A.; Maze, J. R.; Atatüre, M.; Becher, C. Electronic Structure of the Silicon Vacancy Color Center in Diamond. *Phys. Rev. Lett.* **2014**, *112*, 036405.

[61] Neu, E.; Steinmetz, D.; Riedrich-Möller, J.; Gsell, S.; Fischer, M.; Schreck, M.; Becher, C. Single photon emission from silicon-vacancy colour centres in chemical vapour deposition nano-diamonds on iridium. *New Journal of Physics* **2011**, *13*, 025012.

[62] Bhaskar, M. K.; Riedinger, R.; Machielse, B.; Levonian, D. S.; Nguyen, C. T.; Knall, E. N.; Park, H.; Englund, D.; Lončar, M.; Sukachev, D. D.; Lukin, M. D. Experimental demonstration of memory-enhanced quantum communication. *Nature* **2020**, *580*, 60–64.

[63] Meesala, S. et al. Strain engineering of the silicon-vacancy center in diamond. *Phys. Rev. B* **2018**, *97*, 1–13.

[64] Guo, X. et al. Microwave-Based Quantum Control and Coherence Protection of Tin-Vacancy Spin Qubits in a Strain-Tuned Diamond-Membrane Heterostructure. *Phys. Rev. X* **2023**, *13*, 041037.

[65] Rogers, L. J.; Jahnke, K. D.; Metsch, M. H.; Sipahigil, A.; Binder, J. M.; Teraji, T.; Sumiya, H.; Isoya, J.; Lukin, M. D.; Hemmer, P.; Jelezko, F. All-Optical Initialization, Readout, and Coherent Preparation of Single Silicon-Vacancy Spins in Diamond. *Phys. Rev. Lett.* **2014**, *113*, 263602.

[66] Pingault, B.; Becker, J. N.; Schulte, C. H. H.; Arend, C.; Hepp, C.; Godde, T.; Tartakovskii, A. I.; Markham, M.; Becher, C.; Atatüre, M. All-Optical Formation of Coherent Dark States of Silicon-Vacancy Spins in Diamond. *Phys. Rev. Lett.* **2014**, *113*, 263601.

[67] Sukachev, D. D.; Sipahigil, A.; Nguyen, C. T.; Bhaskar, M. K.; Evans, R. E.; Jelezko, F.; Lukin, M. D. Silicon-Vacancy Spin Qubit in Diamond: A Quantum Memory Exceeding 10 ms with Single-Shot State Readout. *Phys. Rev. Lett.* **2017**, *119*, 223602.

[68] Stas, P.-J. et al. Robust multi-qubit quantum network node with integrated error detection. *Science* **2022**, *378*, 557–560.

[69] Senkalla, K.; Genov, G.; Metsch, M. H.; Siyushev, P.; Jelezko, F. Germanium Vacancy in Diamond Quantum Memory Exceeding 20 ms. *Phys. Rev. Lett.* **2024**, *132*, 026901.

[70] Rosenthal, E. I.; Anderson, C. P.; Kleidermacher, H. C.; Stein, A. J.; Lee, H.; Grzesik, J.; Scuri, G.; Rugar, A. E.; Riedel, D.; Aghaeimeibodi, S.; Ahn, G. H.; Van Gasse, K.; Vučković, J. Microwave Spin Control of a Tin-Vacancy Qubit in Diamond. *Phys. Rev. X* **2023**, *13*, 031022.

[71] Debroux, R.; Michaels, C. P.; Purser, C. M.; Wan, N.; Trusheim, M. E.; Arjona Martínez, J.; Parker, R. A.; Stramma, A. M.; Chen, K. C.; de Santis, L.; Alexeev, E. M.; Ferrari, A. C.; Englund, D.; Gangloff, D. A.; Atatüre, M. Quantum Control of the Tin-Vacancy Spin Qubit in Diamond. *Phys. Rev. X* **2021**, *11*, 041041.

[72] Bersin, E. et al. Development of a Boston-area 50-km fiber quantum network testbed. *Phys. Rev. Appl.* **2024**, *21*, 014024.

[73] Knaut, C. M. et al. Entanglement of Nanophotonic Quantum Memory Nodes in a Telecommunication Network. *arXiv preprint* **2023**, 2310.01316.

[74] Lukin, D. M.; Guidry, M. A.; Vučković, J. Integrated Quantum Photonics with Silicon Carbide: Challenges and Prospects. *PRX Quantum* **2020**, *1*, 1–19.

[75] Higginbottom, D. B. et al. Optical observation of single spins in silicon. *Nature* **2022**, *607*, 266–270.

[76] Jahnke, K. D.; Sipahigil, A.; Binder, J. M.; Doherty, M. W.; Metsch, M.; Rogers, L. J.; Manson, N. B.; Lukin, M. D.; Jelezko, F. Electron–phonon processes of the silicon-vacancy centre in diamond. *New Journal of Physics* **2015**, *17*, 043011.

[77] Fan, J.-W.; Cojocaru, I.; Becker, J.; Fedotov, I. V.; Alkahtani, M. H. A.; Alajlan, A.; Blakley, S.; Rezaee, M.; Lyamkina, A.; Palyanov, Y. N.; Borzdov, Y. M.; Yang, Y.-P.; Zheltikov, A.; Hemmer, P.; Akimov, A. V. Germanium-Vacancy Color Center in Diamond as a Temperature Sensor. *ACS Photonics* **2018**, *5*, 765–770.

[78] Sangtawesin, S. et al. Origins of Diamond Surface Noise Probed by Correlating Single-Spin Measurements with Surface Spectroscopy. *Phys. Rev. X* **2019**, *9*, 1–17.

[79] Dang, C.; Chou, J.-P.; Dai, B.; Chou, C.-T.; Yang, Y.; Fan, R.; Lin, W.; Meng, F.; Hu, A.; Zhu, J.; Han, J.; Minor, A. M.; Li, J.; Lu, Y. Achieving large uniform tensile elasticity in microfabricated diamond. *Science* **2021**, *371*, 76–78.

[80] Chakravarthi, S.; Yama, N. S.; Abulnaga, A.; Huang, D.; Pederson, C.; Hestroffer, K.; Hatami, F.; de Leon, N. P.; Fu, K.-M. C. Hybrid Integration of GaP Photonic Crystal Cavities with Silicon-Vacancy Centers in Diamond by Stamp-Transfer. *Nano Letters* **2023**, *23*, 3708–3715.

[81] Libby, W. *Radiocarbon Dating*; Phoenix science series; University of Chicago Press, 1965.

[82] Bar-Gill, N.; Pham, L. M.; Jarmola, A.; Budker, D.; Walsworth, R. L. Solid-state electronic spin coherence time approaching one second. *Nature Communications* **2013**, *4*, 1743.

[83] Park, H.; Lee, J.; Han, S.; Oh, S.; Seo, H. Decoherence of nitrogen-vacancy spin ensembles in a nitrogen electron-nuclear spin bath in diamond. *npj Quantum Information* **2022**, *8*, 95.

[84] Arunkumar, N.; Olsson, K. S.; Oon, J. T.; Hart, C. A.; Bucher, D. B.; Glenn, D. R.; Lukin, M. D.; Park, H.; Ham, D.; Walsworth, R. L. Quantum Logic Enhanced Sensing in Solid-State Spin Ensembles. *Phys. Rev. Lett.* **2023**, *131*, 100801.

[85] Thiering, G. m. H.; Gali, A. Ab Initio Magneto-Optical Spectrum of Group-IV Vacancy Color Centers in Diamond. *Phys. Rev. X* **2018**, *8*, 021063.

[86] Koizumi, S. *Power electronics device applications of diamond semiconductors*; Woodhead Publishing series in electronic and optical materials; Woodhead Publishing, an imprint of Elsevier: Duxford, United Kingdom, 2018.

[87] Sang, L. Diamond as the heat spreader for the thermal dissipation of GaN-based electronic devices. *Functional Diamond* **2021**, *1*, 174–188.

[88] Bovenkerk, B. D. H. P.; Bundy, F. P.; Hall, H. T.; Strong, H. M. Preperation of Diamond. *Nature* **1959**, *184*, 1094–1098.

[89] Wang, P.; Kazak, L.; Senkalla, K.; Siyushev, P.; Abe, R.; Taniguchi, T.; Onoda, S.; Kato, H.; Makino, T.; Hatano, M.; Jelezko, F.; Iwasaki, T. Transform-Limited Photon Emission from a Lead-Vacancy Center in Diamond above 10 K. *Phys. Rev. Lett.* **2024**, *132*, 073601.

[90] Ohno, K.; Joseph Heremans, F.; Bassett, L. C.; Myers, B. A.; Toyli, D. M.; Bleszynski Jayich, A. C.; Palmstrøm, C. J.; Awschalom, D. D. Engineering shallow spins in diamond with nitrogen delta-doping. *Applied Physics Letters* **2012**, *101*, 082413.

[91] Meynell, S. A.; McLellan, C. A.; Hughes, L. B.; Wang, W.; Mates, T. E.; Mukherjee, K.; Bleszynski Jayich, A. C. Engineering quantum-coherent defects: The role of substrate miscut in chemical vapor deposition diamond growth. *Applied Physics Letters* **2020**, *117*, 194001.

[92] Schreck, M.; Gsell, S.; Brescia, R.; Fischer, M. Ion bombardment induced buried lateral growth: the key mechanism for the synthesis of single crystal diamond wafers. *Scientific Reports* **2017**, *7*, 44462.

[93] Sedov, V.; Martyanov, A.; Savin, S.; Bolshakov, A.; Bushuev, E.; Khomich, A.; Kudryavtsev, O.; Krivobok, V.; Nikolaev, S.; Ralchenko, V. Growth of polycrystalline and single-crystal CVD diamonds with bright photoluminescence of Ge-V color centers using germane GeH4 as the dopant source. *Diamond and Related Materials* **2018**, *90*, 47–53.

[94] Guo, X. et al. Direct-bonded diamond membranes for heterogeneous quantum and electronic technologies. *arXiv preprint* **2023**, 2306.04408.

[95] Smits, J.; Damron, J. T.; Kehayias, P.; McDowell, A. F.; Mosavian, N.; Fescenko, I.; Ristoff, N.; Laraoui, A.; Jarmola, A.; Acosta, V. M. Two-dimensional nuclear magnetic resonance spectroscopy with a microfluidic diamond quantum sensor. *Science Advances* **2019**, *5*, 1–8.

[96] Ruf, M.; Ijspeert, M.; Van Dam, S.; De Jong, N.; Van Den Berg, H.; Evers, G.; Hanson, R. Optically Coherent Nitrogen-Vacancy Centers in Micrometer-Thin Etched Diamond Membranes. *Nano Letters* **2019**, *19*, 3987–3992.

[97] Høy Jensen, R.; Janitz, E.; Fontana, Y.; He, Y.; Gobron, O.; Radko, I. P.; Bhaskar, M.; Evans, R.; Rodríguez Rosenblueth, C. D.; Childress, L.; Huck, A.; Lund Andersen, U. Cavity-Enhanced Photon Emission from a Single Germanium-Vacancy Center in a Diamond Membrane. *Phys. Rev. Applied* **2020**, *13*, 1–8.

[98] Jung, T.; Kreiner, L.; Pauly, C.; Mücklich, F.; Edmonds, A. M.; Markham, M.; Becher, C. Reproducible fabrication and characterization of diamond membranes for photonic crystal cavities. *Physica Status Solidi (A) Applications and Materials Science* **2016**, *213*, 3254–3264.

[99] Burek, M. J.; De Leon, N. P.; Shields, B. J.; Hausmann, B. J.; Chu, Y.; Quan, Q.; Zibrov, A. S.; Park, H.; Lukin, M. D.; Lončar, M. Free-standing mechanical and photonic nanostructures in single-crystal diamond. *Nano Letters* **2012**, *12*, 6084–6089.

[100] Bhaskar, M. K.; Sukachev, D. D.; Sipahigil, A.; Evans, R. E.; Burek, M. J.; Nguyen, C. T.; Rogers, L. J.; Siyushev, P.; Metsch, M. H.; Park, H., et al. Quantum nonlinear optics with a germanium-vacancy color center in a nanoscale diamond waveguide. *Phys. Rev. Lett.* **2017**, *118*, 223603.

[101] Kuruma, K.; Pingault, B.; Chia, C.; Haas, M.; Joe, G. D.; Assumpcao, D. R.; Ding, S. W.; Jin, C.; Xin, C.; Yeh, M.; Sinclair, N.; Lončar, M. Engineering Phonon-Qubit Interactions using Phononic Crystals. *arXiv preprint* **2023**, 2310.06236.

[102] Zeng, B.; De-Eknamkul, C.; Assumpcao, D.; Renaud, D.; Wang, Z.; Riedel, D.; Ha, J.; Robens, C.; Levonian, D.; Lukin, M.; Riedinger, R.; Bhaskar, M.; Sukachev, D.; Loncar, M.; Machielse, B. Cryogenic packaging of nanophotonic devices with a low coupling loss < 1 dB. *Applied Physics Letters* **2023**, *123*, 161106.

[103] Evans, R. E.; Bhaskar, M. K.; Sukachev, D. D.; Nguyen, C. T.; Sipahigil, A.; Burek, M. J.; Machielse, B.; Zhang, G. H.; Zibrov, A. S.; Bielejec, E.; Park, H.; Lončar, M.; Lukin, M. D. Photon-mediated interactions between quantum emitters in a diamond nanocavity. *Science* **2018**, *362*, 662–665.

[104] Chia, C.; Machielse, B.; Shams-Ansari, A.; Lončar, M. Development of hard masks for reactive ion beam angled etching of diamond. *Opt. Express* **2022**, *30*, 14189–14201.

[105] Mouradian, S.; Wan, N. H.; Schröder, T.; Englund, D. Rectangular photonic crystal nanobeam cavities in bulk diamond. *Applied Physics Letters* **2017**, *111*, 021103.

[106] Parker, R. A.; Arjona Martínez, J.; Chen, K. C.; Stramma, A. M.; Harris, I. B.; Michaels, C. P.; Trusheim, M. E.; Hayhurst Appel, M.; Purser, C. M.; Roth, W. G.; Englund, D.; Atatüre, M. A diamond nanophotonic interface with an optically accessible deterministic electronuclear spin register. *Nature Photonics* **2024**, *18*, 156–161.

[107] Rugar, A. E.; Aghaeimeibodi, S.; Riedel, D.; Dory, C.; Lu, H.; McQuade, P. J.; Shen, Z. X.; Melosh, N. A.; Vučković, J. Quantum Photonic Interface for Tin-Vacancy Centers in Diamond. *Phys. Rev. X* **2021**, *11*, 031021.

[108] Wan, N. H.; Lu, T. J.; Chen, K. C.; Walsh, M. P.; Trusheim, M. E.; De Santis, L.; Bersin, E. A.; Harris, I. B.; Mouradian, S. L.; Christen, I. R.; Bielejec, E. S.; Englund, D. Large-scale integration of artificial atoms in hybrid photonic circuits. *Nature* **2020**, *583*, 226–231.

[109] Palm, K. J.; Dong, M.; Golter, D. A.; Clark, G.; Zimmermann, M.; Chen, K. C.; Li, L.; Menssen, A.; Leenheer, A. J.; Dominguez, D.; Gilbert, G.; Eichenfield, M.; Englund, D. Modular chip-integrated photonic control of artificial atoms in diamond waveguides. *Optica* **2023**, *10*, 634.

[110] Maletinsky, P.; Hong, S.; Grinolds, M. S.; Hausmann, B.; Lukin, M. D.; Walsworth, R. L.; Loncar, M.; Yacoby, A. A robust scanning diamond sensor for nanoscale imaging with single nitrogen-vacancy centres. *Nature Nanotechnology* **2012**, *7*, 320–324.

[111] Celler, G. K.; Cristoloveanu, S. Frontiers of silicon-on-insulator. *Journal of Applied Physics* **2003**, *93*, 4955–4978.

[112] Di Cioccio, L.; Letertre, F.; Le Tiec, Y.; Papon, A.; Jaussaud, C.; Bruel, M. Silicon carbide on insulator formation by the Smart-Cut® process. *Materials Science and Engineering: B* **1997**, *46*, 349–356.

[113] Lu, H.; Sadani, B.; Courjal, N.; Ulliac, G.; Smith, N.; Stenger, V.; Collet, M.; Baida, F. I.; Bernal, M.-P. Enhanced electro-optical lithium niobate photonic crystal wire waveguide on a smart-cut thin film. *Opt. Express* **2012**, *20*, 2974–2981.

[114] Magyar, A. P.; Lee, J. C.; Limarga, A. M.; Aharonovich, I.; Rol, F.; Clarke, D. R.; Huang, M.; Hu, E. L. Fabrication of thin, luminescent, single-crystal diamond membranes. *Applied Physics Letters* **2011**, *99*, 1–4.

[115] Aharonovich, I.; Lee, J. C.; Magyar, A. P.; Buckley, B. B.; Yale, C. G.; Awschalom, D. D.; Hu, E. L. Homoepitaxial Growth of Single Crystal Diamond Membranes for Quantum Information Processing. *Advanced Materials* **2012**, *24*, 54–59.

[116] Trycz, A.; Regan, B.; Kianinia, M.; Bray, K.; Toth, M.; Aharonovich, I. Bottom up engineering of single crystal diamond membranes with germanium vacancy color centers. *Opt. Mater. Express* **2019**, *9*, 4708–4715.

[117] Westerhausen, M. T.; Trycz, A. T.; Stewart, C.; Nonahal, M.; Regan, B.; Kianinia, M.; Aharonovich, I. Controlled Doping of GeV and SnV Color Centers in Diamond Using Chemical Vapor Deposition. *ACS Applied Materials and Interfaces* **2020**, *12*, 29700–29705.

[118] Piracha, A. H.; Rath, P.; Ganesan, K.; Kühn, S.; Pernice, W. H.; Prawer, S. Scalable Fabrication of Integrated Nanophotonic Circuits on Arrays of Thin Single Crystal Diamond Membrane Windows. *Nano Letters* **2016**, *16*, 3341–3347.

[119] Tully, J. J.; Braxton, E.; Cobb, S. J.; Breeze, B. G.; Markham, M.; Newton, M. E.; Rodriguez, P.; Macpherson, J. V. Diamond membrane production: The critical role of radicals in the non-contact electrochemical etching of sp2 carbon. *Carbon* **2021**, *185*, 717–726.

[120] Lee, J. C.; Magyar, A. P.; Bracher, D. O.; Aharonovich, I.; Hu, E. L. Fabrication of thin diamond membranes for photonic applications. *Diamond and Related Materials* **2013**, *33*, 45–48.

[121] Basso, L.; Titze, M.; Henshaw, J.; Kehayias, P.; Cong, R.; Ziabari, M. S.; Lu, T.-M.; Lilly, M. P.; Mounce, A. M. Fabrication of thin diamond membranes by Ne^{+} implantation. *Giant* **2024**, *17*, 100238.

[122] Ziegler, J. F.; Ziegler, M. D.; Biersack, J. P. SRIM – The stopping and range of ions in matter (2010). *Nuclear Instruments and Methods in Physics Research Section B: Beam Interactions with Materials and Atoms* **2010**, *268*, 1818–1823.

[123] Naydenov, B.; Reinhard, F.; Lämmle, A.; Richter, V.; Kalish, R.; D'Haenens-Johansson, U. F. S.; Newton, M.; Jelezko, F.; Wrachtrup, J. Increasing the coherence time of single electron spins in diamond by high temperature annealing. *Applied Physics Letters* **2010**, *97*, 242511.

[124] Rose, B. C.; Huang, D.; Zhang, Z.-H.; Stevenson, P.; Tyryshkin, A. M.; Sangtawesin, S.; Srinivasan, S.; Loudin, L.; Markham, M. L.; Edmonds, A. M.; Twitchen, D. J.; Lyon, S. A.; de Leon, N. P. Observation of an environmentally insensitive solid-state spin defect in diamond. *Science* **2018**, *361*, 60–63.

[125] Xie, M.; Yu, X.; Rodgers, L. V. H.; Xu, D.; Chi-Durán, I.; Toros, A.; Quack, N.; de Leon, N. P.; Maurer, P. C. Biocompatible surface functionalization architecture for a diamond quantum sensor. *Proceedings of the National Academy of Sciences* **2022**, *119*, e2114186119.

[126] Ferrari, A. C. Raman spectroscopy of graphene and graphite: Disorder, electron-phonon coupling, doping and nonadiabatic effects. *Solid State Communications* **2007**, *143*, 47–57.

[127] Bray, K.; Regan, B.; Trycz, A.; Previdi, R.; Seniutinas, G.; Ganesan, K.; Kianinia, M.; Kim, S.; Aharonovich, I. Single Crystal Diamond Membranes and Photonic Resonators Containing Germanium Vacancy Color Centers. *ACS Photonics* **2018**, *5*, 4817–4822.

[128] John, P.; Stoikou, M. D. Hydrogen plasma interaction with (100) diamond surfaces. *Physical Chemistry Chemical Physics* **2011**, *13*, 11503.

[129] Robledo, L.; Childress, L.; Bernien, H.; Hensen, B.; Alkemade, P. F. A.; Hanson, R. High-fidelity projective read-out of a solid-state spin quantum register. *Nature* **2011**, *477*, 574–578.

[130] Randall, J.; Bradley, C. E.; van der Gronden, F. V.; Galicia, A.; Abobeih, M. H.; Markham, M.; Twitchen, D. J.; Machado, F.; Yao, N. Y.; Taminiau, T. H. Many-body–localized discrete time crystal with a programmable spin-based quantum simulator. *Science* **2021**, *374*, 1474–1478.

[131] Balasubramanian, G.; Neumann, P.; Twitchen, D.; Markham, M.; Kolesov, R.; Mizuochi, N.; Isoya, J.; Achard, J.; Beck, J.; Tissler, J.; Jacques, V.; Hemmer, P. R.; Jelezko, F.; Wrachtrup, J. Ultralong spin coherence time in isotopically engineered diamond. *Nature Materials* **2009**, *8*, 383–387.

[132] Sutula, M.; Christen, I.; Bersin, E.; Walsh, M. P.; Chen, K. C.; Mallek, J.; Melville, A.; Titze, M.; Bielejec, E. S.; Hamilton, S.; Braje, D.; Dixon, P. B.; Englund, D. R. Large-scale optical characterization of solid-state quantum emitters. *Nature Materials* **2023**, *22*, 1338–1344.

[133] Bolshakov, A.; Ralchenko, V.; Sedov, V.; Khomich, A.; Vlasov, I.; Khomich, A.; Trofimov, N.; Krivobok, V.; Nikolaev, S.; Khmelnitskii, R.; Saraykin, V. Photoluminescence of SiV centers in single crystal CVD diamond in situ doped with Si from silane. *physica status solidi (a)* **2015**, *212*, 2525–2532.

[134] Marchywka, M.; Pehrsson, P. E.; Vestyck, J., Daniel J.; Moses, D. Low energy ion implantation and electrochemical separation of diamond films. *Applied Physics Letters* **1993**, *63*, 3521–3523.

[135] Wang, C. F.; Hu, E. L.; Yang, J.; Butler, J. E. Fabrication of suspended single crystal diamond devices by electrochemical etch. *Journal of Vacuum Science & Technology B: Microelectronics and Nanometer Structures Processing, Measurement, and Phenomena* **2007**, *25*, 730–733.

[136] Zomer, P. J.; Guimarães, M. H.; Brant, J. C.; Tombros, N.; Van Wees, B. J. Fast pick up technique for high quality heterostructures of bilayer graphene and hexagonal boron nitride. *Applied Physics Letters* **2014**, *105*, 013101.

[137] Dibos, A. M.; Raha, M.; Phenicie, C. M.; Thompson, J. D. Atomic Source of Single Photons in the Telecom Band. *Phys. Rev. Lett.* **2018**, *120*, 243601.

[138] Lukin, D. M.; Dory, C.; Guidry, M. A.; Yang, K. Y.; Mishra, S. D.; Trivedi, R.; Radulaski, M.; Sun, S.; Vercruysse, D.; Ahn, G. H.; Vučković, J. 4H-silicon-carbide-on-insulator for integrated quantum and nonlinear photonics. *Nature Photonics* **2020**, *14*, 330–334.

[139] Suni, T.; Henttinen, K.; Suni, I.; Mäkinen, J. Effects of Plasma Activation on Hydrophilic Bonding of Si and SiO2. *Journal of The Electrochemical Society* **2002**, *149*, G348.

[140] Tong, Q.-Y.; Gösele, U. Semiconductor wafer bonding: recent developments. *Materials Chemistry and Physics* **1994**, *37*, 101–127.

[141] Chung, T. R.; Yang, L.; Hosoda, N.; Suga, T. Room temperature GaAs Si and InP Si wafer direct bonding by the surface activated bonding method. *Nuclear Instruments and Methods in Physics Research Section B: Beam Interactions with Materials and Atoms* **1997**, *121*, 203–206.

[142] Essig, S.; Moutanabbir, O.; Wekkeli, A.; Nahme, H.; Oliva, E.; Bett, A. W.; Dimroth, F. Fast atom beam-activated n-Si/n-GaAs wafer bonding with high interfacial transparency and electrical conductivity. *Journal of Applied Physics* **2013**, *113*, 203512.

[143] Bao, S.; Lee, K. H.; Chong, G. Y.; Fitzgerald, E. A.; Tan, C. S. AlN-AlN Layer Bonding and Its Thermal Characteristics. *ECS Journal of Solid State Science and Technology* **2015**, *4*, 200–205.

[144] Takigawa, R.; Asano, T. Thin-film lithium niobate-on-insulator waveguides fabricated on silicon wafer by room-temperature bonding method with silicon nanoadhesive layer. *Opt. Express* **2018**, *26*, 24413–24421.

[145] Matsumae, T.; Kurashima, Y.; Umezawa, H.; Tanaka, K.; Ito, T.; Watanabe, H.; Takagi, H. Low-temperature direct bonding of β-Ga2O3 and diamond substrates under atmospheric conditions. *Applied Physics Letters* **2020**, *116*, 141602.

[146] Matsumae, T.; Takigawa, R.; Kurashima, Y.; Takagi, H.; Higurashi, E. Low-temperature direct bonding of InP and diamond substrates under atmospheric conditions. *Scientific Reports* **2021**, *11*, 11109.

[147] Liang, J.; Masuya, S.; Kasu, M.; Shigekawa, N. Realization of direct bonding of single crystal diamond and Si substrates. *Applied Physics Letters* **2017**, *110*, 111603.

[148] Liang, J.; Masuya, S.; Kim, S.; Oishi, T.; Kasu, M.; Shigekawa, N. Stability of diamond/Si bonding interface during device fabrication process. *Applied Physics Express* **2018**, *12*, 016501.

[149] Huang, R.; Lan, T.; Li, C.; Wang, Z. Plasma-activated direct bonding at room temperature to achieve the integration of single-crystalline GaAs and Si substrate. *Results in Physics* **2021**, *31*, 105070.

[150] Pasternak, L.; Paz, Y. Low-temperature direct bonding of silicon nitride to glass. *RSC Adv.* **2018**, *8*, 2161–2172.

[151] Wang, F.; Yang, X.; Zhao, Y.; Wu, J.; Guo, Z.; He, Z.; Fan, Z.; Yang, F. Low-Temperature Direct Bonding of SiC to Si via Plasma Activation. *Applied Sciences* **2022**, *12*, 3261.

[152] Zhuang, B.; Li, S.; Li, S.; Yin, J. Ways to eliminate PMMA residues on graphene —— superclean graphene. *Carbon* **2021**, *173*, 609–636.

[153] Salvadori, M.; Araújo, W.; Teixeira, F.; Cattani, M.; Pasquarelli, A.; Oks, E.; Brown, I. Termination of diamond surfaces with hydrogen, oxygen and fluorine using a small, simple plasma gun. *Diamond and Related Materials* **2010**, *19*, 324–328.

[154] Yamamoto, M.; Matsumae, T.; Kurashima, Y.; Takagi, H.; Suga, T.; Itoh, T.; Higurashi, E. Comparison of Argon and Oxygen Plasma Treatments for Ambient Room-Temperature Wafer-Scale Au–Au Bonding Using Ultrathin Au Films. *Micromachines* **2019**, *10*, 119.

[155] Yeo, C. Y.; Xu, D. W.; Yoon, S. F.; Fitzgerald, E. A. Low temperature direct wafer bonding of GaAs to Si via plasma activation. *Applied Physics Letters* **2013**, *102*, 054107.

[156] Mezzi, A.; Kaciulis, S. Surface investigation of carbon films: from diamond to graphite. *Surface and Interface Analysis* **2010**, *42*, 1082–1084.

[157] Lesiak, B.; Kövér, L.; Tóth, J.; Zemek, J.; Jiricek, P.; Kromka, A.; Rangam, N. C sp2/sp3 hybridisations in carbon nanomaterials – XPS and (X)AES study. *Applied Surface Science* **2018**, *452*, 223–231.

[158] Talneau, A.; Roblin, C.; Itawi, A.; Mauguin, O.; Largeau, L.; Beaudouin, G.; Sagnes, I.; Patriarche, G.; Pang, C.; Benisty, H. Atomic-plane-thick reconstruction across the interface during heteroepitaxial bonding of InP-clad quantum wells on silicon. *Applied Physics Letters* **2013**, *102*, 212101.

[159] Chandrasekaran, N.; Soga, T.; Jimbo, T. GaAs film on Si substrate transplanted from GaAs/Ge structure by direct bonding. *Applied Physics Letters* **2003**, *82*, 3892–3894.

[160] Gösele, U.; Tong, Q.-Y. SEMICONDUCTOR WAFER BONDING. *Annual Review of Materials Science* **1998**, *28*, 215–241.

[161] Razek, N.; Neves, J.; Corre, P. L.; Rüedi, P.-F.; Quaglia, R.; Dasilva, Y. A. R.; von Känel, H. Low temperature covalent wafer bonding for X-ray imaging detectors. *Japanese Journal of Applied Physics* **2019**, *59*, SBBB06.

[162] Vogelgesang, R.; Ramdas, A. K.; Rodriguez, S.; Grimsditch, M.; Anthony, T. R. Brillouin and Raman scattering in natural and isotopically controlled diamond. *Phys. Rev. B* **1996**, *54*, 3989–3999.

[163] Lee, C. L.; Gu, E.; Dawson, M. D.; Friel, I.; Scarsbrook, G. A. Etching and micro-optics fabrication in diamond using chlorine-based inductively-coupled plasma. *Diamond and Related Materials* **2008**, *17*, 1292–1296.

[164] Tallaire, A.; Kasu, M.; Ueda, K.; Makimoto, T. Origin of growth defects in CVD diamond epitaxial films. *Diamond and Related Materials* **2008**, *17*, 60–65.

[165] Butcher, A.; Guo, X.; Shreiner, R.; Delegan, N.; Hao, K.; Duda, P. J.; Awschalom, D. D.; Heremans, F. J.; High, A. A. High-Q Nanophotonic Resonators on Diamond Membranes using Templated Atomic Layer Deposition of TiO2. *Nano Letters* **2020**, *20*, 4603–4609.

[166] Polyanskiy, M. N. Refractive index database. `https://refractiveindex.info`.

[167] Yang, N. In *Novel Aspects of Diamond*; Yang, N., Ed.; Topics in Applied Physics; Springer International Publishing, 2015; Vol. 121.

[168] Siew, Y. K.; Sarkar, G.; Hu, X.; Hui, J.; See, A.; Chua, C. T. Thermal Curing of Hydrogen Silsesquioxane. *Journal of The Electrochemical Society* **2000**, *147*, 335.

[169] Ding, S. W.; Haas, M.; Guo, X.; Kuruma, K.; Jin, C.; Li, Z.; Awschalom, D. D.; Delegan, N.; Heremans, F. J.; High, A.; Loncar, M. High-Q Cavity Interface for Color Centers in Thin Film Diamond. *arXiv preprint* **2024**, 2402.05811.

[170] Sun, L.; Petrenko, A.; Leghtas, Z.; Vlastakis, B.; Kirchmair, G.; Sliwa, K. M.; Narla, A.; Hatridge, M.; Shankar, S.; Blumoff, J.; Frunzio, L.; Mirrahimi, M.; Devoret, M. H.; Schoelkopf, R. J. Tracking photon jumps with repeated quantum non-demolition parity measurements. *Nature* **2014**, *511*, 444–448.

[171] Wallraff, A.; Schuster, D. I.; Blais, A.; Frunzio, L.; Huang, R. S.; Majer, J.; Kumar, S.; Girvin, S. M.; Schoelkopf, R. J. Strong coupling of a single photon to a superconducting qubit using circuit quantum electrodynamics. *Nature* **2004**, *431*, 162–167.

[172] Yoshihara, F.; Fuse, T.; Ashhab, S.; Kakuyanagi, K.; Saito, S.; Semba, K. Superconducting qubit-oscillator circuit beyond the ultrastrong-coupling regime. *Nature Physics* **2017**, *13*, 44–47.

[173] Bienfait, A.; Pla, J. J.; Kubo, Y.; Zhou, X.; Stern, M.; Lo, C. C.; Weis, C. D.; Schenkel, T.; Vion, D.; Esteve, D.; Morton, J. J.; Bertet, P. Controlling spin relaxation with a cavity. *Nature* **2016**, *531*, 74–77.

[174] Stockklauser, A.; Scarlino, P.; Koski, J. V.; Gasparinetti, S.; Andersen, C. K.; Reichl, C.; Wegscheider, W.; Ihn, T.; Ensslin, K.; Wallraff, A. Strong Coupling Cavity QED with Gate-Defined Double Quantum Dots Enabled by a High Impedance Resonator. *Phys. Rev. X* **2017**, *7*, 011030.

[175] Chu, Y.; Kharel, P.; Renninger, W. H.; Burkhart, L. D.; Frunzio, L.; Rakich, P. T.; Schoelkopf, R. J. Quantum acoustics with superconducting qubits. *Science* **2017**, *358*, 199–202.

[176] MacCabe, G. S.; Ren, H.; Luo, J.; Cohen, J. D.; Zhou, H.; Sipahigil, A.; Mirhosseini, M.; Painter, O. Nano-acoustic resonator with ultralong phonon lifetime. *Science* **2020**, *370*, 840–843.

[177] Palomaki, T. A.; Harlow, J. W.; Teufel, J. D.; Simmonds, R. W.; Lehnert, K. W. Coherent state transfer between itinerant microwave fields and a mechanical oscillator. *Nature* **2013**, *495*, 210–214.

[178] Santos, O. A.; van Wees, B. J. Magnon Confinement in an All-on-Chip YIG Cavity Resonator Using Hybrid YIG/Py Magnon Barriers. *Nano Letters* **2023**, *23*, 9303–9309.

[179] Clark, L. W.; Schine, N.; Baum, C.; Jia, N.; Simon, J. Observation of Laughlin states made of light. *Nature* **2020**, *582*, 41–45.

[180] Badolato, A.; Hennessy, K.; Atatüre, M.; Dreiser, J.; Hu, E.; Petroff, P. M.; Imamoğlu, A. Deterministic coupling of single quantum dots to single nanocavity modes. *Science* **2005**, *308*, 1158–1161.

[181] Vahala, K. J. Optical microcavities. *Nature* **2003**, *424*, 839–846.

[182] Vlasov, I. I. et al. Molecular-sized fluorescent nanodiamonds. *Nature Nanotechnology* **2014**, *9*, 54–58.

[183] Janitz, E.; Ruf, M.; Dimock, M.; Bourassa, A.; Sankey, J.; Childress, L. Fabry-Perot microcavity for diamond-based photonics. *Phys. Rev. A* **2015**, *92*, 043844.

[184] Rugar, A. E.; Lu, H.; Dory, C.; Sun, S.; McQuade, P. J.; Shen, Z.-X.; Melosh, N. A.; Vučković, J. Generation of Tin-Vacancy Centers in Diamond via Shallow Ion Implantation and Subsequent Diamond Overgrowth. *Nano Letters* **2020**, *20*, 1614–1619.

[185] Schröder, T.; Trusheim, M. E.; Walsh, M.; Li, L.; Zheng, J.; Schukraft, M.; Sipahigil, A.; Evans, R. E.; Sukachev, D. D.; Nguyen, C. T.; Pacheco, J. L.; Camacho, R. M.; Bielejec, E. S.; Lukin, M. D.; Englund, D. Scalable focused ion beam creation of nearly lifetime-limited single quantum emitters in diamond nanostructures. *Nature Communications* **2017**, *8*, 15376.

[186] Heebner, J.; Grover, R.; Ibrahim, T. *Optical Microresonators: Theory, fabrication, and applications*; Springer Series in Optical Sciences; 2008; Vol. 138; pp 1–266.

[187] Yariv, A. Universal relations for coupling of optical power between microresonators and dielectric waveguides. *Electronics Letters* **2000**, *36*, 321–322.

[188] Novotny, L.; Hecht, B. *Principles of Nano-Optics*; Cambridge University Press, 2006.

[189] Somaschi, N. et al. Near-optimal single-photon sources in the solid state. *Nature Photonics* **2016**, *10*, 340–345.

[190] Ruf, M.; Weaver, M. J.; van Dam, S. B.; Hanson, R. Resonant excitation and purcell enhancement of coherent nitrogen-vacancy centers coupled to a Fabry-Perot microcavity. *Phys. Rev. Applied* **2021**, *15*, 024049.

[191] Moreno, E.; Erni, D.; Hafner, C. Modeling of discontinuities in photonic crystal waveguides with the multiple multipole method. *Phys. Rev. E* **2002**, *66*, 036618.

[192] Cohen-Tannoudji, C.; Diu, B.; Laloë, F. *Quantum Mechanics*; A Wiley - Interscience publication; Wiley, 1977.

[193] Haroche, S.; Raimond, J.-M. *Exploring the Quantum: Atoms, Cavities, and Photons*; Oxford University Press, 2006.

[194] Burek, M. J.; Chu, Y.; Liddy, M. S.; Patel, P.; Rochman, J.; Meesala, S.; Hong, W.; Quan, Q.; Lukin, M. D.; Loncar, M. High quality-factor optical nanocavities in bulk single-crystal diamond. *Nature Communications* **2014**, *5*, 5718.

[195] Khanaliloo, B.; Mitchell, M.; Hryciw, A. C.; Barclay, P. E. High-Q/V Monolithic Diamond Microdisks Fabricated with Quasi-isotropic Etching. *Nano Letters* **2015**, *15*, 5131–5136.

[196] Zhang, J. L.; Sun, S.; Burek, M. J.; Dory, C.; Tzeng, Y.-K.; Fischer, K. A.; Kelaita, Y.; Lagoudakis, K. G.; Radulaski, M.; Shen, Z.-X.; Melosh, N. A.; Chu, S.; Lončar, M.; Vučković, J. Strongly Cavity-Enhanced Spontaneous Emission from Silicon-Vacancy Centers in Diamond. *Nano Letters* **2018**, *18*, 1360–1365.

[197] Kuruma, K.; Pingault, B.; Chia, C.; Renaud, D.; Hoffmann, P.; Iwamoto, S.; Ronning, C.; Lončar, M. Coupling of a single tin-vacancy center to a photonic crystal cavity in diamond. *Applied Physics Letters* **2021**, *118*, 230601.

[198] Lee, J. C.; Bracher, D. O.; Cui, S.; Ohno, K.; McLellan, C. A.; Zhang, X.; Andrich, P.; Alemán, B.; Russell, K. J.; Magyar, A. P.; Aharonovich, I.; Bleszynski Jayich, A.; Awschalom, D.; Hu, E. L. Deterministic coupling of delta-doped nitrogen vacancy centers to a nanobeam photonic crystal cavity. *Applied Physics Letters* **2014**, *105*, 261101.

[199] Devlin, R. C.; Khorasaninejad, M.; Chen, W. T.; Oh, J.; Capasso, F. Broadband high-efficiency dielectric metasurfaces for the visible spectrum. *Proceedings of the National Academy of Sciences* **2016**, *113*, 10473–10478.

[200] Nguyen, C. T.; Sukachev, D. D.; Bhaskar, M. K.; Machielse, B.; Levonian, D. S.; Knall, E. N.; Stroganov, P.; Chia, C.; Burek, M. J.; Riedinger, R.; Park, H.; Lončar, M.; Lukin, M. D. An integrated nanophotonic quantum register based on silicon-vacancy spins in diamond. *Phys. Rev. B* **2019**, *100*, 165428.

[201] Hasan, G. M.; Liu, P.; Hasan, M.; Ghorbani, H.; Rad, M.; Bernier, E.; Hall, T. J. Ring Resonator Gap Determination Design Rule and Parameter Extraction Method for Sub-GHz Resolution Whole C-Band Si3N4 Integrated Spectrometer. *Photonics* **2022**, *9*, 651.

[202] Kuruma, K.; Piracha, A. H.; Renaud, D.; Chia, C.; Sinclair, N.; Nadarajah, A.; Stacey, A.; Prawer, S.; Lončar, M. Telecommunication-wavelength two-dimensional photonic crystal cavities in a thin single-crystal diamond membrane. *Applied Physics Letters* **2021**, *119*, 171106.

[203] Burek, M. J.; Meuwly, C.; Evans, R. E.; Bhaskar, M. K.; Sipahigil, A.; Meesala, S.; Machielse, B.; Sukachev, D. D.; Nguyen, C. T.; Pacheco, J. L.; Bielejec, E.; Lukin, M. D.; Lončar, M. Fiber-Coupled Diamond Quantum Nanophotonic Interface. *Phys. Rev. Appl.* **2017**, *8*, 024026.

[204] Burek, M. J.; Cohen, J. D.; Meenehan, S. M.; El-Sawah, N.; Chia, C.; Ruelle, T.; Meesala, S.; Rochman, J.; Atikian, H. A.; Markham, M.; Twitchen, D. J.; Lukin, M. D.; Painter, O.; Lončar, M. Diamond optomechanical crystals. *Optica* **2016**, *3*, 1404–1411.

[205] Samutpraphoot, P.; Đorđević, T.; Ocola, P. L.; Bernien, H.; Senko, C.; Vuletić, V.; Lukin, M. D. Strong Coupling of Two Individually Controlled Atoms via a Nanophotonic Cavity. *Phys. Rev. Lett.* **2020**, *124*, 063602.

[206] Sergent, S.; Arita, M.; Kako, S.; Tanabe, K.; Iwamoto, S.; Arakawa, Y. High-Q AlN ladder-structure photonic crystal nanocavity fabricated by layer transfer. *physica status solidi c* **2013**, *10*, 1517–1520.

[207] Bracher, D. O.; Hu, E. L. Fabrication of High-Q Nanobeam Photonic Crystals in Epitaxially Grown 4H-SiC. *Nano Letters* **2015**, *15*, 6202–6207.

[208] Saber, I.; Boddeda, R.; Raineri, F.; Sanchez, D.; Beaudoin, G.; Sagnes, I.; Glorieux, Q.; Bramati, A.; Levenson, J. A.; Bencheikh, K. Photonic crystal nanobeam cavities with optical resonances around 800 nm. *J. Opt. Soc. Am. B* **2019**, *36*, 1823–1828.

[209] Evans, R. E.; Sipahigil, A.; Sukachev, D. D.; Zibrov, A. S.; Lukin, M. D. Narrow-Linewidth Homogeneous Optical Emitters in Diamond Nanostructures via Silicon Ion Implantation. *Phys. Rev. Appl.* **2016**, *5*, 044010.

[210] Riedel, D.; Lee, H.; Herrmann, J. F.; Grzesik, J.; Ansari, V.; Borit, J.-M.; Stokowski, H. S.; Aghaeimeibodi, S.; Lu, H.; McQuade, P. J.; Melosh, N. A.; Shen, Z.-X.; Safavi-Naeini, A. H.; Vučković, J. Efficient Photonic Integration of Diamond Color Centers and Thin-Film Lithium Niobate. *ACS Photonics* **2023**, *10*, 4236–4243.

[211] Maity, S.; Shao, L.; Bogdanović, S.; Meesala, S.; Sohn, Y.-I.; Sinclair, N.; Pingault, B.; Chalupnik, M.; Chia, C.; Zheng, L.; Lai, K.; Lončar, M. Coherent acoustic control of a single silicon vacancy spin in diamond. *Nature Communications* **2020**, *11*, 193.

[212] Kim, D.; Ibrahim, M. I.; Foy, C.; Trusheim, M. E.; Han, R.; Englund, D. R. A CMOS-integrated quantum sensor based on nitrogen–vacancy centres. *Nature Electronics* **2019**, *2*, 284–289.

[213] Sipahigil, A. et al. An integrated diamond nanophotonics platform for quantum-optical networks. *Science* **2016**, *354*, 847–850.

[214] Becker, J. N.; Pingault, B.; Groß, D.; Gündoğan, M.; Kukharchyk, N.; Markham, M.; Edmonds, A.; Atatüre, M.; Bushev, P.; Becher, C. All-optical control of the silicon-vacancy spin in diamond at millikelvin temperatures. *Phys. Rev. Lett.* **2018**, *120*, 053603.

[215] Trusheim, M. E.; Pingault, B.; Wan, N. H.; Gündoğan, M.; De Santis, L.; Debroux, R.; Gangloff, D.; Purser, C.; Chen, K. C.; Walsh, M., et al. Transform-limited photons from a coherent tin-vacancy spin in diamond. *Phys. Rev. Lett.* **2020**, *124*, 023602.

[216] Sohn, Y. I. et al. Controlling the coherence of a diamond spin qubit through its strain environment. *Nature Communications* **2018**, *9*, 2012.

[217] De Santis, L.; Trusheim, M. E.; Chen, K. C.; Englund, D. R. Investigation of the stark effect on a centrosymmetric quantum emitter in diamond. *Phys. Rev. Lett.* **2021**, *127*, 147402.

[218] Aghaeimeibodi, S.; Riedel, D.; Rugar, A. E.; Dory, C.; Vučković, J. Electrical tuning of tin-vacancy centers in diamond. *Phys. Rev. Applied* **2021**, *15*, 064010.

[219] Perdew, J. P.; Burke, K.; Ernzerhof, M. Generalized gradient approximation made simple. *Phys. Rev. Lett.* **1996**, *77*, 3865.

[220] Sun, J.; Ruzsinszky, A.; Perdew, J. P. Strongly constrained and appropriately normed semilocal density functional. *Phys. Rev. Lett.* **2015**, *115*, 036402.

[221] Hahn, T.; Kirby, R. Thermal Expansion of Fused Silica from 80 to 1000 K-Standard Reference Material 739. AIP Conference Proceedings. 1972; pp 13–24.

[222] Oikawa, N.; Maesono, A.; Tye, R. Thermal Expansion Measurements of Quartz Glass by Laser Interferometry. *Thermal Conductivity* **1999**, *24*, 405–416.

[223] Reeber, R. R.; Wang, K. Thermal expansion, molar volume and specific heat of diamond from 0 to 3000K. *Journal of Electronic Materials* **1996**, *25*, 63–67.

[224] McSkimin, H.; Andreatch Jr, P. Elastic moduli of diamond as a function of pressure and temperature. *Journal of Applied Physics* **1972**, *43*, 2944–2948.

[225] Lai, N. D.; Zheng, D.; Jelezko, F.; Treussart, F.; Roch, J.-F. Influence of a static magnetic field on the photoluminescence of an ensemble of nitrogen-vacancy color centers in a diamond single-crystal. *Applied Physics Letters* **2009**, *95*, 133101.

[226] Webb, R. H. Confocal optical microscopy. *Reports on Progress in Physics* **1996**, *59*, 427.

[227] Görlitz, J.; Herrmann, D.; Thiering, G.; Fuchs, P.; Gandil, M.; Iwasaki, T.; Taniguchi, T.; Kieschnick, M.; Meijer, J.; Hatano, M.; Gali, A.; Becher, C. Spectroscopic investigations of negatively charged tin-vacancy centres in diamond. *New Journal of Physics* **2020**, *22*, 013048.

[228] Narita, Y.; Wang, P.; Ikeda, K.; Oba, K.; Miyamoto, Y.; Taniguchi, T.; Onoda, S.; Hatano, M.; Iwasaki, T. Multiple Tin-Vacancy Centers in Diamond with Nearly Identical Photon Frequency and Linewidth. *Phys. Rev. Applied* **2023**, *19*, 024061.

[229] Arjona Martínez, J.; Parker, R. A.; Chen, K. C.; Purser, C. M.; Li, L.; Michaels, C. P.; Stramma, A. M.; Debroux, R.; Harris, I. B.; Hayhurst Appel, M.; Nichols, E. C.; Trusheim, M. E.; Gangloff, D. A.; Englund, D.; Atatüre, M. Photonic Indistinguishability of the Tin-Vacancy Center in Nanostructured Diamond. *Phys. Rev. Lett.* **2022**, *129*, 173603.

[230] Fuchs, P.; Jung, T.; Kieschnick, M.; Meijer, J.; Becher, C. A cavity-based optical antenna for color centers in diamond. *APL Photonics* **2021**, *6*, 086102.

[231] Torun, C. G.; Schneider, P.-I.; Hammerschmidt, M.; Burger, S.; Munns, J. H. D.; Schröder, T. Optimized diamond inverted nanocones for enhanced color center to fiber coupling. *Applied Physics Letters* **2021**, *118*, 234002.

[232] Tomm, N.; Javadi, A.; Antoniadis, N. O.; Najer, D.; Löbl, M. C.; Korsch, A. R.; Schott, R.; Valentin, S. R.; Wieck, A. D.; Ludwig, A.; Warburton, R. J. A bright and fast source of coherent single photons. *Nature Nanotechnology* **2021**, *16*, 399–403.

[233] Riedel, D.; Söllner, I.; Shields, B. J.; Starosielec, S.; Appel, P.; Neu, E.; Maletinsky, P.; Warburton, R. J. Deterministic enhancement of coherent photon generation from a nitrogen-vacancy center in ultrapure diamond. *Phys. Rev. X* **2017**, *7*, 031040.

[234] Pingault, B.; Jarausch, D. D.; Hepp, C.; Klintberg, L.; Becker, J. N.; Markham, M.; Becher, C.; Atatüre, M. Coherent control of the silicon-vacancy spin in diamond. *Nature Communications* **2017**, *8*, 15579.

[235] Knill, E.; Leibfried, D.; Reichle, R.; Britton, J.; Blakestad, R. B.; Jost, J. D.; Langer, C.; Ozeri, R.; Seidelin, S.; Wineland, D. J. Randomized benchmarking of quantum gates. *Phys. Rev. A* **2008**, *77*, 012307.

[236] Karapatzakis, I.; Resch, J.; Schrodin, M.; Fuchs, P.; Kieschnick, M.; Heupel, J.; Kussi, L.; Sürgers, C.; Popov, C.; Meijer, J.; Becher, C.; Wernsdorfer, W.; Hunger, D. Microwave Control of the Tin-Vacancy Spin Qubit in Diamond with a Superconducting Waveguide. *arXiv preprint* **2024**, 2403.00521.

[237] De Lange, G.; Wang, Z.-H.; Riste, D.; Dobrovitski, V.; Hanson, R. Universal dynamical decoupling of a single solid-state spin from a spin bath. *Science* **2010**, *330*, 60–63.

[238] Souza, A. M.; Alvarez, G. A.; Suter, D. Robust dynamical decoupling for quantum computing and quantum memory. *Phys. Rev. Lett.* **2011**, *106*, 240501.

[239] Souza, A. M.; Álvarez, G. A.; Suter, D. Robust dynamical decoupling. *Philosophical Transactions of the Royal Society A: Mathematical, Physical and Engineering Sciences* **2012**, *370*, 4748–4769.

[240] Fleischhauer, M.; Imamoglu, A.; Marangos, J. P. Electromagnetically induced transparency: Optics in coherent media. *Rev. Mod. Phys.* **2005**, *77*, 633.

[241] Orbach, R. Spin-Lattice Relaxation in Rare-Earth Salts. *Proceedings of the Royal Society of London. Series A, Mathematical and Physical Sciences* **1961**, *264*, 458–484.

[242] Wang, X.; Li, W.; Moran, B.; Gibson, B. C.; Hall, L. T.; Simpson, D. A.; Kealy, A. N.; Greentree, A. D. *Quantum Diamond Magnetometry for Navigation in GNSS Denied Environments*; Springer Berlin Heidelberg: Berlin, Heidelberg, 2023; pp 1–6.

[243] Rodgers, L. V. H. et al. Diamond surface functionalization via visible light–driven C–H activation for nanoscale quantum sensing. *Proceedings of the National Academy of Sciences* **2024**, *121*, e2316032121.

[244] Hong, S.; Grinolds, M. S.; Pham, L. M.; Le Sage, D.; Luan, L.; Walsworth, R. L.; Yacoby, A. Nanoscale magnetometry with NV centers in diamond. *MRS Bulletin* **2013**, *38*, 155–161.

[245] Barry, J. F.; Schloss, J. M.; Bauch, E.; Turner, M. J.; Hart, C. A.; Pham, L. M.; Walsworth, R. L. Sensitivity optimization for NV-diamond magnetometry. *Rev. Mod. Phys.* **2020**, *92*, 15004.

[246] Myers, B.; Das, A.; Dartiailh, M.; Ohno, K.; Awschalom, D.; Bleszynski Jayich, A. Probing Surface Noise with Depth-Calibrated Spins in Diamond. *Phys. Rev. Lett.* **2014**, *113*, 27602.

[247] Yamamoto, T. et al. Extending spin coherence times of diamond qubits by high-temperature annealing. *Phys. Rev. B* **2013**, *88*, 75206.

[248] Myers, B. A.; Ariyaratne, A.; Jayich, A. C. Double-Quantum Spin-Relaxation Limits to Coherence of Near-Surface Nitrogen-Vacancy Centers. *Phys. Rev. Lett.* **2017**, *118*, 197201.

[249] Childress, L.; Gurudev Dutt, M. V.; Taylor, J. M.; Zibrov, A. S.; Jelezko, F.; Wrachtrup, J.; Hemmer, P. R.; Lukin, M. D. Coherent dynamics of coupled electron and nuclear spin qubits in diamond. *Science* **2006**, *314*, 281–285.

[250] Fukami, M.; Candido, D. R.; Awschalom, D. D.; Flatté, M. E. Opportunities for Long-Range Magnon-Mediated Entanglement of Spin Qubits via On- and Off-Resonant Coupling. *PRX Quantum* **2021**, *2*, 040314.

[251] Candido, D. R.; Fuchs, G. D.; Johnston-Halperin, E.; Flatté, M. E. Predicted strong coupling of solid-state spins via a single magnon mode. *Materials for Quantum Technology* **2020**, *1*, 011001.

[252] Rowan, L. G.; Hahn, E. L.; Mims, W. B. Electron-Spin-Echo Envelope Modulation. *Phys. Rev.* **1965**, *137*, 61–71.

[253] Boss, J. M.; Chang, K.; Armijo, J.; Cujia, K.; Rosskopf, T.; Maze, J. R.; Degen, C. L. One- and Two-Dimensional Nuclear Magnetic Resonance Spectroscopy with a Diamond Quantum Sensor. *Phys. Rev. Lett.* **2016**, *116*, 197601.

[254] Mittiga, T.; Hsieh, S.; Zu, C.; Kobrin, B.; Machado, F.; Bhattacharyya, P.; Rui, N. Z.; Jarmola, A.; Choi, S.; Budker, D.; Yao, N. Y. Imaging the Local Charge Environment of Nitrogen-Vacancy Centers in Diamond. *Phys. Rev. Lett.* **2018**, *121*, 246402.

[255] Ovartchaiyapong, P.; Lee, K. W.; Myers, B. A.; Jayich, A. C. B. Dynamic strain-mediated coupling of a single diamond spin to a mechanical resonator. *Nature Communications* **2014**, *5*, 4429.

[256] Wang, Z. H.; Takahashi, S. Spin decoherence and electron spin bath noise of a nitrogen-vacancy center in diamond. *Phys. Rev. B* **2013**, *87*, 115122.

[257] Macklin, C. UC Berkeley UC Berkeley Electronic Theses and Dissertations. *DNA Mediated Assembly of Protein Heterodimers on Membrane Surfaces* **2020**, 67.

[258] Zhang, Z.-H.; Zuber, J. A.; Rodgers, L. V. H.; Gui, X.; Stevenson, P.; Li, M.; Batzer, M.; Grimau, M. l.; Shields, B.; Edmonds, A. M.; Palmer, N.; Markham, M. L.; Cava, R. J.; Maletinsky, P.; de Leon, N. P. Neutral silicon vacancy centers in undoped diamond via surface control. *arXiv preprint* **2022**, 2206.13698.

[259] Schreyvogel, C.; Polyakov, V.; Wunderlich, R.; Meijer, J.; Nebel, C. E. Active charge state control of single NV centres in diamond by in-plane Al-Schottky junctions. *Scientific Reports* **2015**, *5*, 12160.

[260] Janitz, E.; Herb, K.; Völker, L. A.; Huxter, W. S.; Degen, C. L.; Abendroth, J. M. Diamond surface engineering for molecular sensing with nitrogen—vacancy centers. *Journal of Materials Chemistry C* **2022**, *10*, 13533–13569.

[261] Qiu, Z.; Hamo, A.; Vool, U.; Zhou, T. X.; Yacoby, A. Nanoscale electric field imaging with an ambient scanning quantum sensor microscope. *npj Quantum Information* **2022**, *8*, 107.

[262] Lovchinsky, I.; Sushkov, A. O.; Urbach, E.; de Leon, N. P.; Choi, S.; Greve, K. D.; Evans, R.; Gertner, R.; Bersin, E.; Müller, C.; McGuinness, L.; Jelezko, F.; Walsworth, R. L.; Park, H.; Lukin, M. D. Nuclear magnetic resonance detection and spectroscopy of single proteins using quantum logic. *Science* **2016**, *351*, 836–841.

[263] Shi, F.; Zhang, Q.; Wang, P.; Sun, H.; Wang, J.; Rong, X.; Chen, M.; Ju, C.; Reinhard, F.; Chen, H.; Wrachtrup, J.; Wang, J.; Du, J. Single-protein spin resonance spectroscopy under ambient conditions. *Science* **2015**, *347*, 1135–1138.

[264] Glenn, D. R.; Bucher, D. B.; Lee, J.; Lukin, M. D.; Park, H.; Walsworth, R. L. High-resolution magnetic resonance spectroscopy using a Solid-State spin sensor. *Nature* **2018**, *555*, 351–354.

[265] Li, Z.; Guo, X.; Jin, Y.; Andreoli, F.; Bilgin, A.; Awschalom, D. D.; Delegan, N.; Heremans, F. J.; Chang, D.; Galli, G.; High, A. A. Atomic optical antennas in solids. *Submitted* **2024**,

[266] Bharadwaj, P.; Deutsch, B.; Novotny, L. Optical antennas. *Advances in Optics and Photonics* **2009**, *1*, 438–483.

[267] Schuller, J. A.; Barnard, E. S.; Cai, W.; Jun, Y. C.; White, J. S.; Brongersma, M. L. Plasmonics for extreme light concentration and manipulation. *Nature Materials* **2010**, *9*, 193–204.

[268] Taminiau, T.; Stefani, F.; Segerink, F. B.; Van Hulst, N. Optical antennas direct single-molecule emission. *Nature photonics* **2008**, *2*, 234–237.

[269] Acimovic, S. S.; Kreuzer, M. P.; González, M. U.; Quidant, R. Plasmon near-field coupling in metal dimers as a step toward single-molecule sensing. *ACS nano* **2009**, *3*, 1231–1237.

[270] Liu, N.; Tang, M. L.; Hentschel, M.; Giessen, H.; Alivisatos, A. P. Nanoantenna-enhanced gas sensing in a single tailored nanofocus. *Nature materials* **2011**, *10*, 631–636.

[271] Sobhani, A.; Knight, M. W.; Wang, Y.; Zheng, B.; King, N. S.; Brown, L. V.; Fang, Z.; Nordlander, P.; Halas, N. J. Narrowband photodetection in the near-infrared with a plasmon-induced hot electron device. *Nature communications* **2013**, *4*, 1643.

[272] Yu, N.; Blanchard, R.; Fan, J.; Wang, Q. J.; Pflügl, C.; Diehl, L.; Edamura, T.; Yamanishi, M.; Kan, H.; Capasso, F. Quantum cascade lasers with integrated plasmonic antenna-array collimators. *Optics Express* **2008**, *16*, 19447–19461.

[273] Novotny, L.; Van Hulst, N. Antennas for light. *Nature Photonics* **2011**, *5*, 83–90.

[274] Tang, L.; Kocabas, S. E.; Latif, S.; Okyay, A. K.; Ly-Gagnon, D. S.; Saraswat, K. C.; Miller, D. A. Nanometre-scale germanium photodetector enhanced by a near-infrared dipole antenna. *Nature Photonics* **2008**, *2*, 226–229.

[275] Schuller, J. A.; Taubner, T.; Brongersma, M. L. Optical antenna thermal emitters. *Nature Photonics* **2009**, *3*, 658–661.

[276] Novotny, L.; Stranick, S. J. Near-field optical microscopy and spectroscopy with pointed probes. *Annual Review of Physical Chemistry* **2006**, *57*, 303–331.

[277] Alaee, R.; Rockstuhl, C.; Fernandez-Corbaton, I. Exact Multipolar Decompositions with Applications in Nanophotonics. *Advanced Optical Materials* **2019**, *7*, 1800783.

[278] Fan, X.; Zheng, W.; Singh, D. J. Light scattering and surface plasmons on small spherical particles. *Light: Science & Applications* **2014**, *3*, e179.

[279] Feng, L.; Ma, R.; Wang, Y.; Xu, D.; Xiao, D.; Liu, L.; Lu, N. Silver-coated elevated bowtie nanoantenna arrays: Improving the near-field enhancement of gap cavities for highly active surface-enhanced Raman scattering. *Nano Research* **2015**, *8*, 3715–3724.

[280] Fischer, H.; Martin, O. J. F. Engineering the optical response of plasmonic nanoantennas. *Optics Express* **2008**, *16*, 9144–9154.

[281] Li, K.; Stockman, M. I.; Bergman, D. J. Self-similar chain of metal nanospheres as an efficient nanolens. *Phys. Rev. Lett.* **2003**, *91*, 227402.

[282] Dengchao, H.; Jun, W.; Qingxiu, D.; Binzi, X.; Xiang, W.; Kang, Y. Metal-Insulator-Metal Nanoislands with Enhanced Local Fields for SERS-Based Detection. *ACS Applied Nano Materials* **2023**, *6*, 16856–16863.

[283] Michaels, A. M.; Jiang, J.; Brus, L. Ag Nanocrystal Junctions as the Site for Surface-Enhanced Raman Scattering of Single Rhodamine 6G Molecules. *Journal of Physical Chemistry B* **2000**, *104*, 11965–11971.

[284] Miller, O. D.; Polimeridis, A. G.; Reid, M. H.; Hsu, C. W.; DeLacy, B. G.; Joannopoulos, J. D.; Soljačić, M.; Johnson, S. G. Fundamental limits to optical response in absorptive systems. *Optics express* **2016**, *24*, 3329–3364.

[285] Christiansen, R. E.; Michon, J.; Benzaouia, M.; Sigmund, O.; Johnson, S. G. Inverse design of nanoparticles for enhanced Raman scattering. *Optics Express* **2020**, *28*, 4444–4462.

[286] Mie, G. Beiträge zur Optik trüber Medien, speziell kolloidaler Metallösungen. *Annalen der Physik* **1908**, *330*, 377–445.

[287] Neves, A. A. R.; Cesar, C. L.; Garbos, M. K.; Euser, T. G.; Moreira, W. L. Expansion of arbitrary electromagnetic fields in terms of vector spherical wave functions. *Optics Express* **2016**, *24*, 2370–2382.

[288] Chen, Y.; White, S.; Ekimov, E. A.; Bradac, C.; Toth, M.; Aharonovich, I.; Tran, T. T. Ultralow-Power Cryogenic Thermometry Based on Optical-Transition Broadening of a Two-Level System in Diamond. *ACS Photonics* **2023**, *10*, 2481–2487.

[289] Subedi, S.; Fedorov, V.; Mirov, S.; Markham, M. Spectroscopy of GR1 centers in synthetic diamonds. *Opt. Mater. Express* **2021**, *11*, 757–765.

[290] Kuate Defo, R.; Kaxiras, E.; Richardson, S. L. How carbon vacancies can affect the properties of group IV color centers in diamond: A study of thermodynamics and kinetics. *Journal of Applied Physics* **2019**, *126*, 195103.

[291] Maity, S.; Shao, L.; Sohn, Y.-I.; Meesala, S.; Machielse, B.; Bielejec, E.; Markham, M.; Lončar, M. Spectral alignment of single-photon emitters in diamond using strain gradient. *Phys. Rev. Applied* **2018**, *10*, 024050.

[292] Baldwin Jr, J. A. Electron paramagnetic resonance investigation of the vacancy in diamond. *Phys. Rev. Lett.* **1963**, *10*, 220.

[293] Davies, G. Charge states of the vacancy in diamond. *Nature* **1977**, *269*, 498–500.

[294] Heremans, F.; Fuchs, G.; Wang, C.; Hanson, R.; Awschalom, D. Generation and transport of photoexcited electrons in single-crystal diamond. *Applied Physics Letters* **2009**, *94*, 152102.

[295] Wolfowicz, G.; Anderson, C. P.; Yeats, A. L.; Whiteley, S. J.; Niklas, J.; Poluektov, O. G.; Heremans, F. J.; Awschalom, D. D. Optical charge state control of spin defects in 4H-SiC. *Nature communications* **2017**, *8*, 1876.

[296] Tisler, J.; Reuter, R.; Lämmle, A.; Jelezko, F.; Balasubramanian, G.; Hemmer, P. R.; Reinhard, F.; Wrachtrup, J. Highly efficient FRET from a single nitrogen-vacancy center in nanodiamonds to a single organic molecule. *Acs Nano* **2011**, *5*, 7893–7898.

[297] Nelz, R.; Radtke, M.; Slablab, A.; Xu, Z.-Q.; Kianinia, M.; Li, C.; Bradac, C.; Aharonovich, I.; Neu, E. Near-Field Energy Transfer between a Luminescent 2D Material and Color Centers in Diamond. *Advanced Quantum Technologies* **2020**, *3*, 1900088.

[298] Kong, X.; Nir, E.; Hamadani, K.; Weiss, S. Photobleaching pathways in single-molecule FRET experiments. *Journal of the American Chemical Society* **2007**, *129*, 4643–4654.

[299] Roy, R.; Hohng, S.; Ha, T. A practical guide to single-molecule FRET. *Nature methods* **2008**, *5*, 507–516.

[300] Gottscholl, A.; Diez, M.; Soltamov, V.; Kasper, C.; Sperlich, A.; Kianinia, M.; Bradac, C.; Aharonovich, I.; Dyakonov, V. Room temperature coherent control of spin defects in hexagonal boron nitride. *Science Advances* **2021**, *7*, eabf3630.

[301] Anderson, C. P.; Glen, E. O.; Zeledon, C.; Bourassa, A.; Jin, Y.; Zhu, Y.; Vorwerk, C.; Crook, A. L.; Abe, H.; Ul-Hassan, J., et al. Five-second coherence of a single spin with single-shot readout in silicon carbide. *Science advances* **2022**, *8*, eabm5912.

[302] Bayliss, S.; Deb, P.; Laorenza, D.; Onizhuk, M.; Galli, G.; Freedman, D.; Awschalom, D. Enhancing spin coherence in optically addressable molecular qubits through host-matrix control. *Phys. Rev. X* **2022**, *12*, 031028.

[303] Moerner, W. E.; Kador, L. Optical detection and spectroscopy of single molecules in a solid. *Phys. Rev. Lett.* **1989**, *62*, 2535.